

الجمهورية الجزائرية الديمقراطية الشعبية
République Algérienne Démocratique Et Populaire
وزارة التعليم العالي والبحث العلمي
Ministère de L'Enseignement Supérieur et de La Recherche Scientifique
جامعة فرحات عباس - سطيف 1
Université Ferhat Abbas - Sétif 1

THÈSE

Présentée à l'Institut d'Optique et Mécanique de Précision pour l'obtention du
Diplôme de

DOCTORAT 3^{ème} Cycle LMD

Domaine : Sciences et Techniques
Filière : Optique et mécanique de Précision
Spécialité : Matériaux et Engineering

Par

Mohamed HAMIDOUCHE

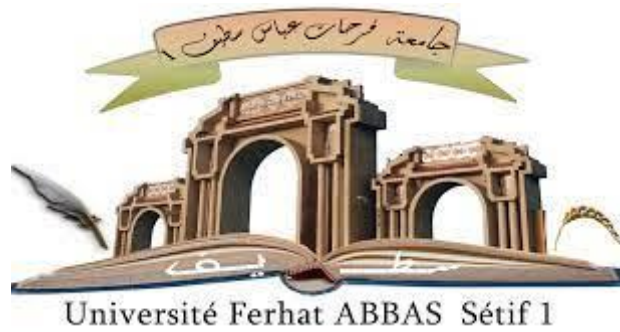
THÈME

**Caractérisation mécanique et tribologique des
dépôts élaborés par voie électrolytique**

Soutenue, le :

Devant le jury composé de:

Président du Jury	Kamel LOUCIF	Prof.	UFA Sétif 1
Directeur de thèse	Nafissa KHENNAFI	Prof.	UFA Sétif 1
Examineur	Loubna MENTER	Prof.	UFA Sétif 1
Examineur	Abderrazak BOUZID	Prof.	UMBI BBA
Examineur	Younes BENARIOUA	Prof.	UMB M'sila



Ferhat ABBAS University – Setif 1

THESIS

Presented at the Institute of Optics and Precision Mechanic for the obtaining of
the Diploma of

DOCTORATE 3rd Cycle LMD

Domain: Sciences and Techniques

Field: Optics and Precision Mechanic

Specialty: Materials and Engineering

By

Mohamed HAMIDOUCHE

THEME

**Mechanical and tribological characterization of
electrolytically elaborated (Ni and Ni-Co)
deposits**

Table of contents

Acknowledgments.....	I
Dedications	II
List of figures	III
List of tables.....	IV

GENERAL INTRODUCTION

1. OVERVIEW	1
2. BRIEF STATE OF THE ART	5
3. THESIS OBJECTIVES	6
4. THESIS NOVELTIES	7
5. THESIS OUTLINES.....	7

CHAPTER I: Literature review

I.1 INTRODUCTION	9
I.2 WEAR AND FRICTION	9
I.2.1 Tribological system	9
I.2.2 Friction.....	10
I.2.2.a) The different classifications of friction	11
I.2.2.b) The laws of friction.....	12
I.2.3 Wear.....	12
I.2.4 Wear mechanisms	13
I.2.4.a) Adhesive wear	13
I.2.4.b) Abrasive wear	13
I.2.4.c) Fatigue wear	14
I.2.4.d) Corrosive or tribochemical wear	15
I.2.5 Wear evaluation	15
I.2.6 Wear and friction tests	16
I.2.7 Wear prevention	17
I.3 ANTI-WEAR COATINGS	18
I.3.1 Methods of elaboration of coatings	19
I.3.2 Nanostructured coatings	19
I.4 ELECTRODEPOSITION OF NANOCRYSTALLINE COATINGS	21
I.4.1 Principle of electrodeposition.....	21
I.4.2 Advantages of electrodeposition	22
I.4.3 Applications of electrodeposition.....	23
I.4.3.a) Decoration	23
I.4.3.b) Protection	23
I.4.3.c) Enhancements	24
I.4.3.d) Electroforming.....	24
I.4.3.e) Synthesis of nanomaterials and nanostructures.....	24
I.4.4 Synthesis of nanocrystalline coatings by electrodeposition.....	24
I.5 NANOSTRUCTURED ELECTRODEPOSITED Ni AND Ni-Co COATINGS.....	25
I.5.1 Potentials of Ni and Ni-Co alloy as alternatives to hexavalent Cr coatings.....	25
I.5.2 Alloying of Ni with Co by electrodeposition.....	26

I.5.3 Electrodeposition baths of nanocrystalline Ni and Ni-Co coatings	28
I.5.3.a) Electrodeposition baths of nanocrystalline Ni coatings	28
I.5.3.b) Electrodeposition baths of nanocrystalline Ni-Co coatings	29
I.5.4 Applications of electrodeposited nanocrystalline Ni and Ni-Co coatings	30
I.5.4.a) Applications of electrodeposited nanocrystalline Ni coatings	30
I.5.4.b) Applications of electrodeposited nanocrystalline Ni-Co coatings	31
I.5.5 Properties of electrodeposited nanocrystalline Ni coatings	31
I.5.5.a) Microstructural properties	31
I.5.5.b) Mechanical properties	33
I.5.5.c) Tribological properties	34
I.5.6 Properties of electrodeposited nanocrystalline Ni-Co coatings	36
I.5.6.a) Microstructural properties	36
I.5.6.b) Mechanical properties	38
I.5.6.c) Tribological properties	40

CHAPTER II: Experimental methods

II.1 INTRODUCTION	42
II.2 COATINGS ELECTRODEPOSITION	42
II.2.1 Materials and chemicals	42
II.2.1.a) Type and chemical composition of the used substrates	42
II.2.1.b) Substrates preparation	42
II.2.2 Composition of the electroplating bath	44
II.2.3 Experimental parameters and setup	44
II.2.3.a) Experimental parameters	44
II.2.3.b) Experimental set-up	45
II.3 COATINGS CHARACTERISATIONS	46
II.3.1 Chronopotentiometry	46
II.3.2 Wavelength Dispersive X-ray Fluorescence Spectrometry (WD-XRF)	46
II.3.3 Metallographic observation	47
II.3.4 X-ray diffraction (XRD)	48
II.3.5 Scanning electron microscopy (SEM) and Microanalysis X	50
II.3.6 Profilometry	51
II.3.7 Confocal Microscopy	53
II.3.8 Atomic Force Microscopy	54
II.3.9 Micro and Nano indentation	55
II.3.9.a) Micro-indentation	55
II.3.9.b) Nano-indentation	56
II.3.10 Scratch test	58
II.3.11 Tribological tests	58

CHAPTER III: Study of the performances of nanocrystalline Ni-Co alloy as anti-wear coating

III.1 INTRODUCTION	61
III.2 EXPERIMENTAL DETAILS	61
III.2.1 Coatings electrodeposition	61
III.2.2 Compositional, morphological and microstructural characterizations	61
III.2.3 Mechanical and tribological characterizations	62
III.3 RESULTS AND DISCUSSIONS	63

III.3.1 Study of the performances of nanocrystalline Ni-Co alloy as anti-wear coating on mild steel substrate	63
III.3.1.a) Composition of the electrodeposited Ni-Co coating	64
III.3.1.b) Morphological and microstructural properties	65
III.3.1.c) Microhardness	70
III.3.1.d) Tribological behavior	72
III.3.2 Tribological performances of the nanocrystalline Ni-Co coating compared with nanocrystalline Ni coating	82
III.3.2.a) Composition of the electrodeposited Ni-Co coating	83
III.3.2.b) Morphological and microstructural properties	83
III.3.2.c) Microhardness	86
III.3.2.d) Tribological behavior	87
III.4 CONCLUSIONS	90

CHAPTER IV: Effect of the electrodeposition conditions on the properties of Ni-Co coatings

IV.1 INTRODUCTION	94
IV.2 EXPERIMENTAL DETAILS	94
IV.2.1 Coatings electrodeposition	94
IV.2.2 Compositional, morphological and microstructural characterizations	94
IV.2.3 Mechanical and tribological characterizations	95
IV.3 RESULTS AND DISCUSSIONS	96
IV.3.1 Effect of the bath Co content on the properties of the electrodeposited Ni-Co coatings ... 96	
IV.3.1.a) Effect on the composition of coatings	97
IV.3.1.b) Effect on the morphostructural properties of coatings	97
IV.3.1.c) Effect on the microhardness of coatings	101
IV.3.1.d) Effect on the tribological behavior of coatings	103
IV.3.2 Effect of the bath temperature on the properties of electrodeposited Ni-Co coatings 107	
IV.3.2.a) Effect on the deposition potential	107
IV.3.2.b) Effect on the composition of coatings	109
IV.3.2.c) Effect on the morphostructural properties of coatings	111
IV.3.2.d) Effect on the microhardness of coatings	114
IV.3.2.e) Effect on the tribological behavior of coatings	117
IV.3.3 Other parameters that seem to have a slight effect on the properties of the electrodeposited Ni-Co coatings	121
IV.3.3.a) Effect on the deposition potential	122
IV.3.3.b) Effect on the composition of coatings	122
IV.3.3.c) Effect on the thickness of coatings	124
IV.3.3.d) Effect on the microstructural properties of coatings	125
IV.3.3.e) Effect on the hardness of coatings	126
IV.3.3.f) Effect on the tribological behavior of coatings	127
IV.4 CONCLUSIONS	131

GENERAL CONCLUSIONS AND PERSPECTIVES

1. GENERAL CONCLUSIONS	134
2. PERSPECTIVES	136

Bibliographical references	138
---	-----

Acknowledgements

The realization of this thesis was possible thanks to the support of several people to whom I would like to express my sincere gratitude.

First of all, I would like to express my gratitude to my thesis director, Madame Nafissa KHENNAFI-BENGHALEM, professor at the University of Ferhat Abbas-Setif1, who gave me the opportunity to work on a very current subject. I would like to thank her sincerely for her patience, her availability and especially her judicious advices, which contributed to feed my reflection.

I would like to thank especially Pr. Amor AZIZI, who was the first to introduce me to the subject that guided my thesis.

The major part of this work was carried out at the Research Unit of Emerging Materials at the University of Ferhat Abbas-Setif 1. I would like to thank both the current director of the unit Dr. Abdelghani MERDAS and the previous director Pr. Mohamed HAMIDOUICHE for the facilities that were granted to me as well as to all the PhD students affiliated to this unit.

My great greetings also go to the persons in charge and members of the Laboratory of the Nonmetallic Materials (LMNM), for having facilitated, advised and assisted me. I quote in particular the ex-director of the laboratory, Pr. Noureddine BOUAOUADJA, and my dear friend the engineer Ahmed BENKHELIF.

A large part of the characterizations was performed at the Institute of Materials Research of the Slovak Academy of Sciences. My warmest thanks to the director of the institute, Dr. Pavol Hvizdos, for all the facilities offered to me during a two months internship in their center of excellence "PROMATECH". My thanks also go to the engineers and technicians of the institute who contributed to the success of my internship and who helped me during the realization of the characterizations, in particular Martin, David, Robert, Marek and Zuzana.

I am very grateful to Pr. Kamel LOUCIF for accepting the task of chairing the jury, as well as to Pr. Loubna MENTER, Pr. Younes BENARIOUA and my dear former teacher Pr. Abderrazak BOUZID who have gladly accepted to devote their time as reviewers of this manuscript. It is an honor for me to do so and I express my deep satisfaction to them.

These years of thesis have left behind a flood of friendships, joy, hope, sadness and frustration. I would like to thank all my friends who shared with me these difficult moments. I quote among them in particular, not in general, Aghiles BOUIBED, Abelghani KENZOUR, Abdelwahab AYADI, Oualid SADOON, Fateh MAYOUF and Elhadi OTMANI.

I appreciate very much the help of my friend and colleague, El Oualid Bounab, in the layout of the figures. I will never forget your support Oualid.

I would like to express my gratitude to all the researchers, specialists, speakers, and all the people who took the time to discuss my topic. Through their words, writings, advices and criticisms, they have guided my thoughts and helped me move forward in my analyses.

Finally, a very big THANK YOU to all my family who have flooded me with their love, prayers and motivations that have made my endeavors successful. My heartfelt gratitude goes out to them.

Dedication

TO

My teacher of passion, patience and perseverance ...My father

My eternal source of inspiration, motivation and blessing...My mother

Who share with me my unhappiness and my happiness...My sisters and brothers

My brothers whom my mother did not give birth to ...My friends

All those who love me and that I love them

List of figures

GENERAL INTRODUCTION

Figure 1: Some examples on the wear of industrial parts	2
--	---

CHAPTER I: Literature review

Figure I.1: Schematic representation of a tribosystem.....	10
Figure I.2: Necessity of a force F to overcome friction and cause motion by (a) rolling or (b) sliding	11
Figure I.3: Wear map according to Ashby and Lim.....	16
Figure I.4: Methods of wear prevention.....	18
Figure I.5: Causes of materials degradation showing a percentage estimate of the economic importance of each	19
Figure I.6: General classification of surface coating methods	19
Figure I.7: The benefits that can be gained using nanostructured materials	20
Figure I.8: Schematic representation of the atomic structure of nanocrystalline materials showing an important atomic percentage in grain boundaries.....	21
Figure I.9: Principle of an electrodeposition setup using dissoluble anode (a) and non-dissoluble anode (b).....	22
Figure I.10: The binary phase diagram of Ni-Co alloy according to ASM International	27
Figure I.11: The main applications areas of Ni coatings.....	31
Figure I.12: The main applications of electrodeposited Ni-Co coatings.....	32
Figure I.13: Morphologies of microcrystalline and nanocrystalline Ni coatings electrodeposited with DC (a) and (d) ; PC (b) and (e) ; PRC (c) and (f).....	33
Figure I.14: Comparaison of XRD pattern of nancrystalline Ni coating with annaealed Ni (a) and microcrystalline Ni coating (b).....	33
Figure I.15: Effect of current density and temperature on hardness (a)(b) and grains size of nanocrystalline Ni coatings (c)(d)	35
Figure I.16: Relationship between hardness and grain size of Ni electrodeposited coatings.....	35
Figure I.17: Wear rate vs. hardness (a) and friction coefficient vs. crystallites size of Ni electrodeposits (b)	36
Figure I.18: Worn surface morphology of electrodeposited Ni coatings with crystallites size of (a) 3 μm , (b) 250 nm and (c) 16 nm.....	36
Figure I.19: The effect of some electrodeposition parameters on the Co content of Ni-Co coatings: (a) bath Co content, (b) current density, (c) temperature and (d) pH	37
Figure I.20: SEM morphologies of microcrystalline Ni-Co coatings with different Co content: (a) 0 wt.%, (b) 7wt.%, (c) 66 wt.% and (d) 81 wt.%	37
Figure I.21: SEM morphologies of nanocrystalline Ni-Co electrodeposits with (a) 14 wt.%, (b) 39 wt.% and (c) 84 wt.% Co content.....	38
Figure I.22: XRD patterns of Ni-Co electrodeposits with different Co contents.....	39
Figure I.23: Microhardness of Ni-Co coatings as function of Co content (a) and d-0.5 (b)	39
Figure I.24: Friction coefficient (a) and wear rate (b) vs. Co content of Ni-Co coatings	40
Figure I.25: Wear tracks of pure Ni (a) and Ni-Co alloy electrodeposits with 27 wt.% Co (b) and 81 wt.% Co (c)	41

CHAPTER II: Experimental methods

Figure II.1: The geometry of the resin-embedded discs used as substrates	43
Figure II.2: The shape of the substrate prepared as cathode.....	43

Figure II.3: The experimental set-up used for the electrodeposition of different coatings	45
Figure II.4: Examples on the used current regimes (a) and on the obtained curves during Ni-Co electrodeposition (b).....	46
Figure II.5: The principle of X-ray fluorescence spectrometer (a) and the used Rigaku ZSX Primus IV X-Ray fluorescence spectrometer (b).....	47
Figure II.6: The used Axio metallographic microscope (a) and an example of metallographic observation on StW24 steel used as substrate (b)	48
Figure II.7: Schematic representation of the Bragg equation (a) and the operating principle of the x-ray diffractometer (b)	49
Figure II.8: The used Philips X'Pert X-ray diffractometer	50
Figure II.9: The principle scheme of scanning electron microscope (a) and the used JEOL JSM-7000 F scanning electron microscope (b).....	51
Figure II.10: The principle of sensor contact profilometer (a) and the used AlphaStep D-500 Stylus Profiler (b).....	52
Figure II.11: Example on the measurement of the coating thickness (a) and the wear track profile (b)	52
Figure II.12: Schematic diagram of the principle of confocal laser scanning microscopy (a) and the used Leica DCM8 confocal microscope (b).....	53
Figure II.13: A schematic representation of the AFM instrument (a) and the used MFP-3D atomic force microscope (b).....	54
Figure II.14: Principle of Vickers micro-indentation essay (a) and the used Tukon 2500 Vickers micro-durometer (b)	55
Figure II.15: Schematic description of nanoindentation testing (a) and an example of load-displacement curves obtained for Ni-Co alloy coating (b).....	57
Figure II.16: SEM micrograph of the performed nanoindentation imprints (a) and the used TTX NHT nano indenter (b)	57
Figure II.17: Representative diagram of the used scratch tester (a) and the used Bruker scratch tester (b)	58
Figure II.18: Representative diagram of the used pin-on-disc tribometer (a) and the used CSM THT tribometer (b).....	60

CHAPTER III: Study of the performances of nanocrystalline Ni-Co alloy as anti-wear coating

Figure III.1: Co and Ni mass percentages in the bath and in the electrodeposited Ni-Co coating	64
Figure III.2: Mechanism and steps of the anomalous codeposition of Ni-Co alloy	65
Figure III.3: Surface morphology of StW24 steel substrate (a) and Ni ₆₃ -Co ₃₇ coating (b).....	67
Figure III.4: XRD patterns of StW24 steel substrate and Ni ₆₇ -Co ₃₇ electrodeposited coating	68
Figure III.5: Schematic representation of the saccharin effect on the crystal growth of Ni-Co deposits	69
Figure III.6: SEM observation on the surface of Ni ₆₃ -Co ₃₇ coating (a) and optical microscopic observation on the surface of StW24 steel substrate (b)	70
Figure III.7: Schematic representation of the substitutional Ni-Co solid solution	71
Figure III.8: Microhardness values and indentation imprints of the StW24 steel substrate and the electroplated Ni ₆₃ -Co ₃₇ coating.....	72
Figure III.9: Friction coefficient of Ni ₆₃ -Co ₃₇ coated and uncoated StW24 steel substrate under 5N (a) and 10N (b).....	74
Figure III.10: Wear rate of Ni ₆₃ -Co ₃₇ coating and StW24 steel substrate under 5 and 10N	76
Figure III.11: SEM observations of the worn surfaces of uncoated (a) and Ni-Co coated StW24 steel substrate (b)	76

Figure III.12: SEM micrograph and EDS elemental mapping of the worn surfaces of uncoated StW24 substrate.....	78
Figure III.13: SEM micrograph and EDS elemental mapping of the wear track of Ni-Co coated substrate.....	79
Figure III.14: EDS spectrum of selected zones on the worn surfaces of uncoated StW24 substrate (a) and Ni-Co coated substrate (b).....	80
Figure III.15: EDS profile along the wear track widths of uncoated (a) and Ni-Co coated substrate (b).....	81
Figure III.16: Parameters influencing the tribological behavior of the studied materials, solid arrows indicate major effect while dashed arrows indicate slight effect.....	82
Figure III.17: Co and Ni mass percentages in the electrolyte and in the electroplated Ni ₁₃ -Co ₈₇ coating.....	83
Figure III.18: SEM observations on the surface of the nanocrystalline pure Ni coating (a) and Ni ₁₃ -Co ₈₇ coating (b).....	84
Figure III.19: 2D and 3D imaging of the surface of nanocrystalline Ni coating (a)-(b) and Ni-Co coating (c)-(d).....	85
Figure III.20: X-ray diffraction spectrums of Ni and Ni ₁₃ -Co ₈₇ nanocrystalline coatings.....	86
Figure III.21: The microhardness (a) and the crystallites size (b) of the electrodeposited Ni and Ni ₁₃ -Co ₈₇ coatings.....	87
Figure III.22: Friction coefficient of the electrodeposited Ni and Ni ₁₃ -Co ₈₇ coatings.....	88
Figure III.23: The wear rate of the electrodeposited Ni and Ni ₁₃ -Co ₈₇ coatings.....	89
Figure III.24: SEM observation with different magnifications on the wear tracks of pure Ni coating (a) (b) (c) and Ni ₁₃ -Co ₈₇ coating (d) (e) (f).....	91

CHAPTER IV: Effect of the electrodeposition conditions on the properties of Ni-Co coatings

Figure IV.1: Co content in the electrodeposited Ni-Co coatings and abnormality degree vs. the Co concentration in the electrolyte.....	98
Figure IV.2: SEM micrographs of the electrodeposited coatings: (a) and (b) pure Ni, (c) with 74 wt.% Co and (d) with 87 wt.% Co.....	99
Figure IV.3: XRD patterns of the electrodeposited Ni-Co coatings.....	100
Figure IV.4: The crystallites size vs. the Co content of the electrodeposited Ni-Co coatings.....	101
Figure IV.5: Microhardness vs. Co content of the electrodeposited Ni-Co coatings.....	102
Figure IV.6: Microhardness vs. the inverse square root of crystallites size of the electrodeposited Ni-Co coatings.....	103
Figure IV.7: Friction coefficient vs. sliding time of the electrodeposited Ni-Co coatings.....	104
Figure IV.8: Wear rate vs. Co content of the electrodeposited Ni-Co coatings.....	105
Figure IV.9: Worn surface morphologies of the electrodeposited Ni-Co coatings (a) (b) pure Ni coating, (c) (d) Ni-Co coating with 74 wt.% Co, (e) (f) Ni-Co with 87 wt.% Co.....	106
Figure IV.10: Wear tracks of the pins rubbed against (a) pure Ni coating, (b) Ni-Co coating with 63 wt.% Co, (c) Ni-Co coating with 87 wt.% Co.....	107
Figure IV.11: Cathodic potential as function of time at different electroplating bath temperatures..	109
Figure IV.12: Co and Ni contents in the electrodeposited Ni-Co coatings vs. the bath temperature.	110
Figure IV.13: SEM micrographs of the Ni-Co coatings electrodeposited at: (a) 25°C, (b) 45°C, (c) 65°C, (d) 85°C.....	112
Figure IV.14: XRD patterns of the Ni-Co coatings electrodeposited at different bath temperatures	113
Figure IV.15: Crystallites size of the electrodeposited Ni-Co coatings vs. the bath temperature.....	114
Figure IV.16: Microhardness of the electrodeposited Ni-Co coatings vs. the bath temperature.....	115
Figure IV.17: Microhardness vs. the inverse square root of crystallites size of the Ni-Co coatings electrodeposited at different bath temperatures.....	116

Figure IV.18: Friction coefficient of the Ni-Co electrodeposited at different bath temperatures vs. sliding time	118
Figure IV.19: Wear rate of the Ni-Co coatings electrodeposited at different bath temperatures.....	119
Figure IV.20: Worn surface morphologies of the Ni-Co coatings electrodeposited at: (a) 25°C, (b) 45°C, (c) 65°C and (d) 85°C	121
Figure IV.21: Deposition potential on the different used substrates as function of deposition time .	123
Figure IV.22: Co content in the electrodeposition bath and in the coatings deposited on different substrates (a) and during different deposition times (b)	123
Figure IV.23: Thickness of coatings as a function of type of substrate (a) and deposition duration (b)	124
Figure IV.24: XRD patterns of Ni-Co coatings electrodeposited on different substrates (a) and with different thicknesses (b)	125
Figure IV.25: Nanohardness of the coatings deposited at different substrates and with different thicknesses (a) (c) and their indentation load-displacements curves (b) (d)	126
Figure IV.26: FT vs. FN monitoring during the scratch test of Ni-Co coatings deposited on different substrates (a) and with different thicknesses (b)	128
Figure IV.27: Friction coefficient vs. FN monitoring during the scratch test of Ni-Co coatings deposited on different substrates (a) and with different thicknesses (b)	128
Figure IV.28: Optical micrographs of the scratches performed on the Ni-Co coatings deposited on StW24 steel, copper and brass.....	129
Figure IV.29: Optical micrographs of the scratches performed on Ni-Co coatings of different thicknesses.....	130
Figure IV.30: SEM micrographs of a scratch made on one of the electrodeposited Ni-Co coatings	130
Figure IV.31: Cross-sectional profiles on the largest width of the scratches made on the different studied coatings	131

GENERAL CONCLUSIONS AND PERSPECTIVES

Figure 1: Macroscopic observations of Ni-Co-SiO ₂ nanocomposite coatings deposited in the presence of different additives amounts	137
---	-----

Liste of tables

GENERAL INTRODUCTION

Table 1: Potential cost savings through an appropriate use of tribological knowledge (1.6% of Gross Domestic Product (GDP), 2008)	1
--	---

CHAPTER I: Literature review

Table I.1: Schematic representation and microscopic views of the main wear mechanisms	14
Table I.2: Some of the assays used for friction and wear testing	17
Table I.3: Nickel electroplating baths	28
Table I.4: Ni-Co electroplating baths	29
Table I.5: Bath additives used in Ni and Ni-Co electrodeposition.....	30

CHAPTER II: Experimental methods

Table II.1: The composition of the different metals used as substrates	42
Table II.2: The composition of the used electroplating baths	44
Table II.3: The experimental conditions used for the elaboration of the different coatings	45
Table II.4: Nature and composition of the different used substrates	48
Table II.5: The composition of the balls used as pins	59

CHAPTER III: Study of the performances of nanocrystalline Ni-Co alloy as anti-wear coating

Table III.1: The bath compositions and the experimental conditions used for the electroplating of the coatings.....	62
Table III.2: The parameters used for the microhardness and tribological measurements.....	63

CHAPTER IV: Effect of the electrodeposition conditions on the properties of Ni-Co coatings

Table IV.1: Experimental parameters and conditions used for the electrodeposition of the different coatings.....	95
Table IV.2: The experimental parameters used for the characterization of the mechanical and tribological properties of the electrodeposited coatings	96

General Introduction

GENERAL INTRODUCTION

1. OVERVIEW

The term “tribology” (coming from the Greek: “τριβος or tribo” which means “friction or attrition” [1]) is defined as the science and technology of interactions between solid surfaces in relative motion [1,2]. This term was first used in 1966 by a British government committee that examined the amount of annual losses due to friction and wear and actually refers to the study of friction, wear and lubrication [1–3]. Friction may be interpreted as a process of dissipation of energy, and wear as one of dissipation of a surface structure and/or mass. Lubrication may be considered as a process by which the load between two solid bodies moving relatively to each other is dissipated, with the dissipation of energy and mass concentrated more or less on the lubricant itself [4]. Tribology is therefore pluridisciplinary in nature and covers mechanical engineering, materials science, physics and chemistry, as well as the relatively young disciplines of tribology, namely biotribology and nanotribology [2,4].

In 1977, a report financed by the United States government suggested that up to US\$16.25 billion could be saved through the correct use of tribological knowledge [2]. Likewise, in 1986, Rabinowicz estimated that 6% of the United Kingdom's gross product was lost because of poor knowledge or misapplication of tribology [5]. Similar studies have also been carried out in other countries and similarly important potential savings have been estimated as shown in [Table 1](#) for the year 2008 [2]. It is then easy to imagine the economic impact of even a small improvement in this area.

Table 1: Potential cost savings through an appropriate use of tribological knowledge (1.6% of Gross Domestic Product (GDP), 2008) [2].

Country	Potential savings (US \$ billion)
European Union	303
United States	186
China	68
Japan	63
Germany	50
France	48
United Kingdom	36

Friction in machinery and mechanical applications is of considerable importance, as it is necessary for motion and motion translation systems such as gears, clutches, belts, pulleys and in the case of braking systems. However, the increased friction is one of the main causes of energy dissipation in mechanical systems where greater fuel consumption is required in the presence of friction to do the same work performed in its absence, especially under conditions of insufficient or no lubrication [6,7]. The energy losses caused by friction in industrial countries are estimated to be between 5 and 7% of their gross domestic product [8].

Most of the time, friction is accompanied by the wear phenomenon, which is one of the major causes of performance loss as well as component failure and equipment destruction (Figure 1). Where, 50 to 60% of all mechanical system failures worldwide are due to severe wear of these systems, and for industries with wear problems, the costs were typically 0.25% of their turnover [9]. Therefore, any reduction in wear leads to significant material savings, but also contributes to the protection of the environment by limiting the emission of particles that can be harmful, and by limiting equipment waste on the other hand. Reduced wear also means that the interval between maintenance or even replacement of expensive machines will be longer. In addition to saving scarce and valuable natural resources, this also means fewer production stoppages [10]. The conclusions of all the estimation studies are broadly consistent that at least 1% of gross domestic product could be saved with a minimum of additional investment in tribological research [1], and the potential for even greater savings could exist with further research. Based on all the foregoing, it can be concluded that research in the field of tribology is of great importance, whether for the resources, the economy or the environment.

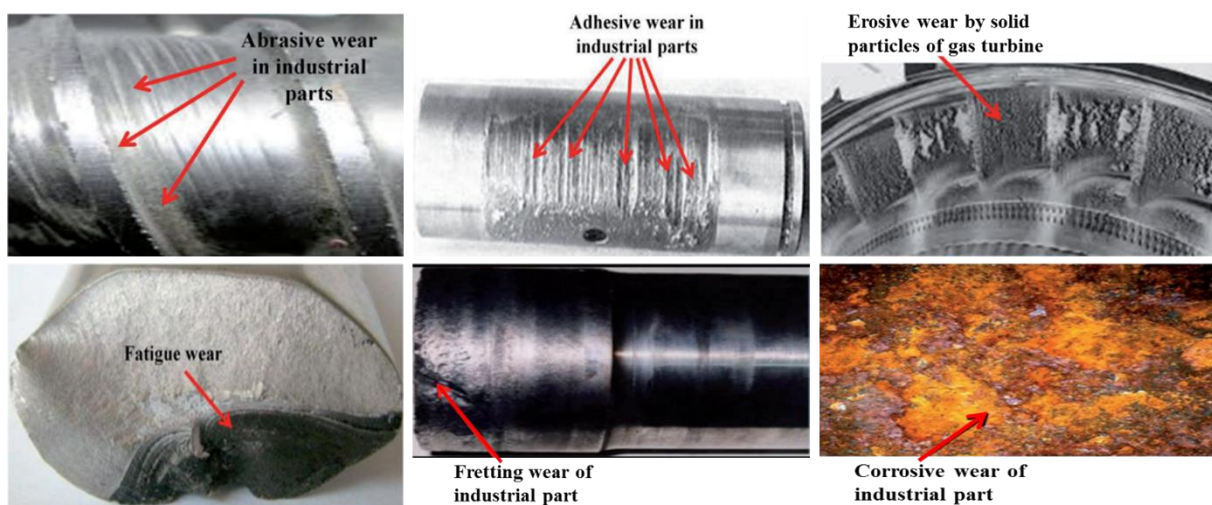


Figure 1: Some examples on the wear of industrial parts [11].

Historically, many of the wear and friction problems have been solved by modifying part design, selecting high-performance bulk materials or using lubrication techniques [6]. Nevertheless, these solutions are limited and also have some drawbacks. Modifications performed on base materials may affect some of their desirable intrinsic properties or involve the application of other expensive materials. While lubrication systems include the use of liquid lubricants such as synthetic and mineral oils or solid lubricants, the problem lies in the manufacture of these materials, which are often based on the use of petroleum derivatives. Companies are seeking to reduce the use of non-renewable petroleum and the carbon dioxide and nitrogen oxide emissions resulting from the use of its derivatives. The environmental pollution resulting from the spilling and release of oils into nature is also frightening and cannot be taken lightly [7]. In addition, the lubrication systems may be inadequate or ineffective in many cases.

Tribologists have put into practice recently a new approach to control friction and wear, using surface treatments and coatings. This resulted, and to some extent was fueled, by the growth of a new field known as "Surface Engineering" [12]. This growth was driven by two principal factors. The first was the development of new treatments processes (thermal and thermochemical) and coating methods (physical and chemical), which allow to obtain tribological and tribo-chemical surface properties that were not previously available. The second factor in the growth of this field was the recognition by materials scientists and engineers that the surface is the most important part of many engineering elements. It is on the surface that the majority of failures originate, through either wear, corrosion or fatigue. Therefore, the surface has a dominant effect on cost and performance over the lifetime, including the serviceability of the machines [13]. It is in this context that new surface treatments and coating processes are being developed and are already having a significant impact. However, surface transformation treatments offer very limited properties due to the limited materials that can be treated and due to the limitations of surface transformation treatment methods. Whereas coating treatments can provide very diverse and high properties as desired, due to the diversity of materials that can be applied in coatings, whether pure, alloys or composites, and also due to the diversity of coating processes. Given this background, the industrial strategy is often to use surface engineering through coatings to improve the performance and extend the life of mechanical and tribological systems.

Surface engineering by coatings is a technically and economically advantageous method compared to other surface treatment processes. It offers a wide range of possibilities to improve

the resistance of surfaces to stresses involving several phenomena simultaneously (friction, abrasion, corrosion, shocks, etc.), while maintaining the intrinsic properties of the base materials, which are less expensive and easier to implement [14]. By decreasing the coating structure scale from micrometer to nanometer size, the mechanical properties of the materials such as toughness, hardness, wear resistance and fracture strength may further improved [15,16]. Many surface treatment processes [17] can be used to produce so-called nanostructured coatings, such as thermal spraying, electrodeposition, PVD, Sol-Gel, etc. Among these methods, electrodeposition has received much attention in the recent years because it has several advantages in the development of based metal coatings, since it ensures uniform deposits on substrates with complex geometries, low cost, low energy consumption, industrial applicability, versatility and low wastes [18]. It also offers some distinctive features for wear applications. As electroplating processes operate below 100°C, it is sometimes the only coating process that can be applied to deposit hard coatings on substrates subject to deformation without considering the metallurgical details of solubility of solids and the associated high temperature problems that exist with the majority of other processes. Since it can produce coatings without causing deformation, it is often used to restore worn parts and to coat small holes and other cavities that are difficult to coat by other processes [19].

Hard chromium coatings are one of the best-known electrodeposits in tribological applications to improve the life of wear parts in industry. However, the toxicity of chrome plating baths is a major environmental defect that justifies the search for its replacement [20,21]. Nickel and electrodeposits are one of the coatings developed to replace toxic hard chrome coatings [22]. The reduction of the crystallites size of these coatings to the nanometer scale contributes greatly to the improvement of their hardness and tribological properties [23]; however, their properties are still weaker than those of hard chrome coatings. Hence, other approaches are being developed to further improve the properties of nanocrystalline Ni coatings, including reinforcing these coatings with hard micro and nano hard-particles [24,25] or alloying Ni with other metals [26,27].

One of the most interesting binary Ni alloy coatings, whose tribological performances can be better than pure Ni and comparable or even better than chromium coatings [28,29], is Ni-Co alloy. Ni-Co nanostructures can be obtained through electrodeposition by a very easy and economical approach that is very suitable for industry [29], which consists in adding to the electrodeposition bath organic additives such as saccharin and 2-butyne-1,4-diol (BD) that can inhibit the growth of crystallites and maintain their size at the nanoscale [30,31].

Nanocrystalline Ni-Co alloys coatings exhibit good mechanical and tribological characteristics [32,33]. However, their mechanical applications are related directly to their microstructure and morphology which influenced strongly by their Co content. Typically, the effect of Co content on the mechanical properties of Ni-Co coatings has aroused great interests for researchers. Where the investigations showed that Co content of coatings can be controlled by the control of bath composition [34] and the physical parameters of electroplating such as current density [35], pH [36], temperature [37], agitation [38], etc.

2. BRIEF STATE OF THE ART

Many studies have been conducted on nanocrystalline Ni-Co coatings in the recent years. They show that the tribological properties of Ni-Co coatings are better than that of nanocrystalline Ni coatings [28,39], where the lubricity and hardening which can cobalt add on Ni coatings properties are very attractive characteristics. Therefore, the most of studies were focused on the effect of Co content on the tribological properties and anti-wear applications of nanocrystalline Ni-Co coatings. L. Wang et al. [40] investigated the microstructure and tribological behavior of Ni-Co coatings with different Co contents, they have been concluded that hcp crystal structure in Co-rich coatings lead to the remarkable friction-reduction effect and better wear resistance when compared with Ni-rich coatings with fcc crystal structure. C. Ma et al study [39] has dealt with the effect of tribofilms formation on the wear behavior of Ni-Co alloy coatings with different Co contents. They have found that tribofilms were formed on the worn surface of the Ni-rich coatings (≤ 60 at.% Co), which translated by high friction coefficients and wear rates, while no tribofilm or iron transfers from the counterpart were found on the Co-rich coatings (≥ 70 at.% Co content). Thus, a very important reduction in friction and improved wear resistance were experienced. Some studies were interested in improving of Ni-Co tribological properties by various methods. Sh. Hassani et al. [41] focused on the improving of tribo-corrosion resistance of Ni-Co nanocrystalline coatings in NaOH medium by the optimization of current density and by the addition of saccharin and sodium lauryl sulphate, they have found that increasing in current density and addition of saccharin improved tribocorrosion resistance, while addition of sodium lauryl sulphate improved corrosion resistance but not tribocorrosion resistance. On their part L. Wang et al. [33] tried the elaboration of Ni-Co coatings with graded composition and structure for the reduction of internal stress and the amelioration of tribological behavior of electrodeposited coatings. They have concluded that graded Ni-Co alloys coatings presented a much lower friction coefficient and a remarkably improved wear resistance compared with the uniform structured Ni-Co coatings under the same dry sliding wear

conditions. Nevertheless, other studies focused only on hardness without or with other mechanical properties and did not care about friction and wear behavior. Y. Li et al. [42] have studied the effects of saccharin and cobalt content in the bath on the microhardness of nanocrystalline Ni-Co deposits. They stated that the additions of appropriate amount of cobalt and saccharine could lead to finer structure and higher hardness of coatings but further increase of their concentrations in the bath could lead to the decrease of the deposit hardness. They focused in another paper [35] on the effects of peak current density on microhardness and tensile strength of nanocrystalline Ni-Co coatings elaborated by pulsed electrodeposition, and they concluded that the increase in current density makes the grain size of deposits finer, and the tensile strength and the hardness higher. Whereas N. Feninech et al. [43] have studied the effect of some electrodeposition parameters (current density, pH and temperature) on the microstructure, brittleness, tensile strength and hardness of Co-Ni alloys, and they have found that the harder deposits can be obtained at room temperature with current density of 3Adm^{-2} and pH of 3.5.

3. THESIS OBJECTIVES

From the overview and the state of the art presented above, it can be seen that most of the current work on Ni-Co coatings aims to improve their mechanical and tribological properties as economical and eco-friendly alternatives to the eco-damaging hard chrome coatings commonly used in anti-wear applications. The objectives of this thesis project are not out of this context where we aim to:

- Study of the effect of saccharin and 2-butyne-1,4-diol (BD) as grain refiners on the morphostructural characteristics of Ni-Co coatings.
- Understand the reasons for the improved properties of Ni-Co coated steel compared to its uncoated counterpart.
- Evaluation of the anti-wear performances of nanocrystalline Ni-Co coatings by comparing them with those of pure nanocrystalline Ni coatings.
- Make a good correlation between the morphostructural properties of Ni and Ni-Co coatings and their mechanical and anti-wear performances.
- Understand the wear mechanisms and the effect of wear debris and tribofilms on the wear behavior of the different studied materials.

- Optimize the electrodeposition conditions such as bath Co content and bath temperature through the study of their effects on the compositional, morphostructural, mechanical and tribological properties of Ni-Co coatings.
- Study of the maintainability of the properties of electrodeposited Ni-Co coatings on different substrates and with different thicknesses.
- Study of the adhesion of electrodeposited Ni-Co coatings on different substrates and with different thicknesses.

4. THESIS NOVELTIES

- Investigation of the reasons behind the improved mechanical and wear performances of the Ni-Co coated substrate compared to an uncoated substrate.
- In-depth analyses of the effect of tribofilm formation on the wear behavior of Ni and Ni-Co coatings.
- A focused study on the relationship between morphostructural properties, hardness and anti-wear performances of Co-Ni coatings (>50 wt.% Co).
- Investigate for the first time the effect of bath temperature, metal substrate type and deposition duration on the tribological properties of Ni-Co coatings.
- Study for the first time the adhesion capacity and the maintenance of the properties of Ni-Co coatings on different substrates and with different thicknesses.

5. THESIS OUTLINES

- In the general introduction section, we present the subject of the thesis with the context, the problematic, the state of the art, the objectives and the novelties of this thesis.
- Chapter I discusses the mechanisms of friction and wear phenomena, their evaluation and measurement methods as well as the main processes implemented to reduce their negative effects, including the surface engineering process by electrodeposition. A brief literature review is also provided on the work that has been done on the subject of electrodeposition and the characterization of microstructural, mechanical and tribological properties of nanocrystalline coatings of pure Ni and Ni-Co alloys.
- Chapter II presents the protocols for the preparation of the substrates, the formulation of the baths, the design of the electrodeposition setup, the elaboration of the coatings as well as the applied characterization methods.
- Chapter III is devoted to the study of the performances of the nanocrystalline Ni-Co alloy as an anti-wear coating, comparing their performances with the uncoated StW24

steel substrate and the pure nanocrystalline Ni coating. An attempt is also made in this chapter to understand the wear mechanisms and the role of debris and tribofilms on the tribological behavior of the studied materials.

- Chapter IV is focused on the study of the effect of certain electrodeposition conditions, namely the bath Co content, the bath temperature, the type of metal substrate and the deposition duration, on the composition and on the morphostructural, mechanical and tribological properties of the Ni-Co coatings. The maintenance of the properties of the Ni-Co coatings, in particular their tribological performances, is also tested on different substrates, namely StW24 steel, copper and brass and using different coating thicknesses (43.2, 79.8 and 110.6 μm).
- The last section states the general conclusions of this study as well as the perspectives of our future work.

Chapter I:

Literature review

CHAPTER I: LITERATURE REVIEW

I.1 INTRODUCTION

Despite their presence in our daily life, tribological manifestations such as friction and wear are not phenomena that most people consider in their everyday activities. Nevertheless, they are responsible for many problems and significant costs in a modern civilization. That is why engineers and designers are always required to consider these factors when designing technical equipment. This chapter relates to the general context of our research stating the mechanisms of friction and wear phenomena, their evaluation and measurement methods and the main processes implemented to reduce their negative effects, in particular the process of surface engineering by coating. The electrodeposition “or also electroplating” will be presented as one of the processes for the elaboration of high performance tribological and nanocrystalline coatings. A brief literature review will also be given on the works that have been done on the subject of the electrodeposition and the characterization of the microstructural, mechanical and tribological properties of nanocrystalline coatings of pure Ni and Ni-Co alloys as well as the experimental parameters that can affect these properties. This could well pave the way for the research topic addressed in this thesis.

I.2 WEAR AND FRICTION

I.2.1 Tribological system

In general, friction and wear are considered as losses in tribological systems. They depend not simply on the properties of different materials, but also on the interactions that occur and the magnitude of stresses in the system [44]. Under certain conditions, even small changes in the tribological system can have large impacts on friction and wear. Thus, friction and wear are the properties of an entire tribological system, not just the characteristics of the materials in contact. As shown in [Figure I.1](#), a tribological system (tribosystem) is defined as being composed of three main elements [44,45]:

- **The first bodies:** the main and the opposite bodies.
- **The intermediate matter (third body):** The origin of this interfacial medium can be external (solid or liquid lubricant) or internal by in situ formation (detachment of particles from the first bodies). This third body can partially or totally separates the two first bodies in contact.

- **The surrounding environment:** Where the interactions between this environment and the contact can thus take place according to its composition, its temperature and its possible pollution.

These, combined with the sum of all the stresses involved (the stress system) allow to determine the friction coefficient, the wear mechanism and the wear rate that will occur. The stress system consists of the physical and technical parameters of the normal force (F_N), velocity (v), temperature (T), stress duration (t), modes of movement and the evolution of these parameters in the course of time [44]. Practically speaking, tribological systems can be classified as follows:

- **Closed tribological systems:** such as bearings and seals.
- **Open tribological systems:** such as chutes and pipe systems [44]. In this case, the opposite body is absent but its function is provided by the intermediate material.

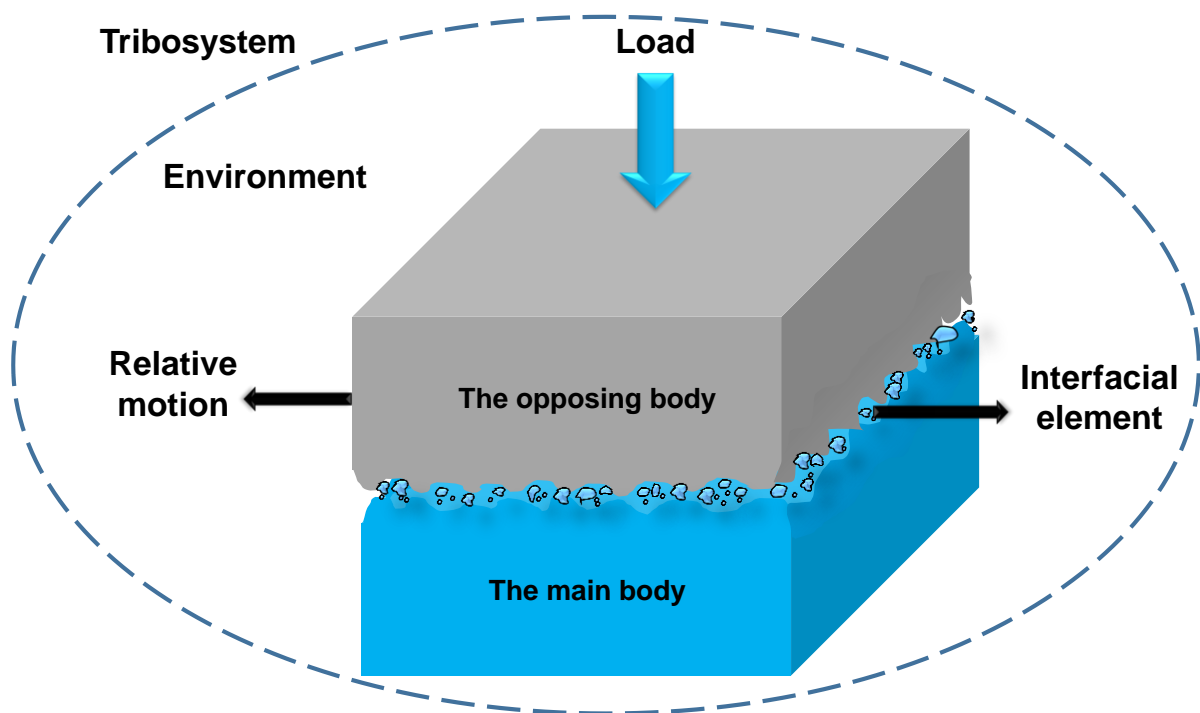


Figure I.1: Schematic representation of a tribosystem.

I.2.2 Friction

Friction is the resistance to movement produced when a body moves tangentially to another body with which it is in contact [1,2,12]. Friction is therefore not a property of the material, but a response of a whole tribological system [12]. This broad definition includes two important classes of relative motion namely sliding and rolling. The distinction between sliding and rolling is useful one, but the two are not mutually exclusive, and even apparently pure rolling

almost always implies some sliding [1]. Ideally, for both rolling and sliding, a tangential force F is required to displace the upper body on the fixed counter face, as shown in Figure I.2. The relationship between this frictional force and the normal load W is known as the friction coefficient (μ), and can be calculated using the formula (eq.I.1 [12]):

$$\mu = \frac{F}{W} \quad (\text{I.1})$$

The magnitude of the frictional force is usually quantified by the friction coefficient value that can vary over a broad range, from around 0.001 in a lightly loaded ball bearing to more than 10 for two identical clean metallic surfaces sliding under vacuum. However, for the most usual materials that slide in the air without lubricant, the μ value varies from about 0.1 to 1 [1].

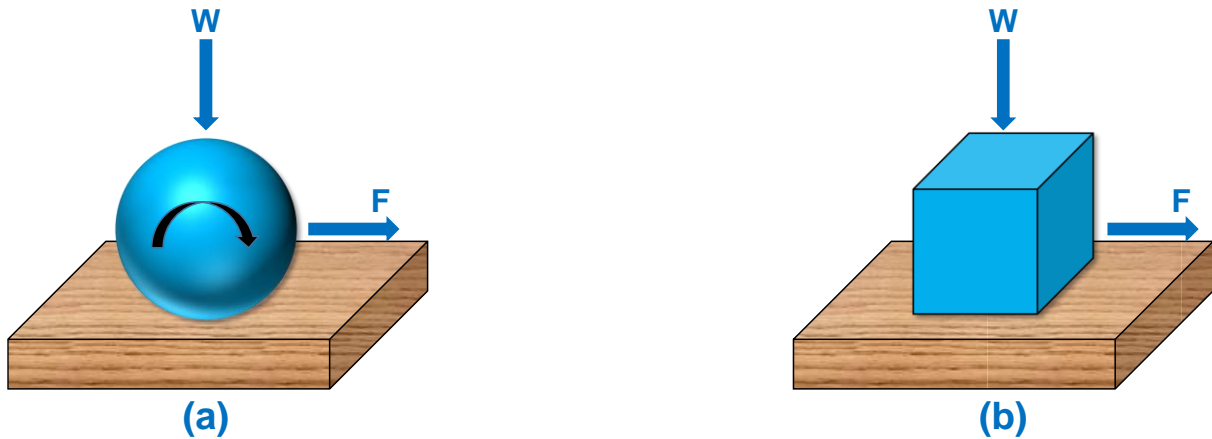


Figure I.2: Necessity of a force F to overcome friction and cause motion by (a) rolling or (b) sliding.

I.2.2.a) The different classifications of friction

Depending on the amplitude, we distinguish:

- **The dynamic or kinetic friction:** which resists the movement without totally preventing it.
- **Static friction:** which completely prevents movement between the sliding or rolling surfaces [46].

Depending on the movement of the rubbing device, we can distinguish:

- **A sliding friction:** where the wiper slides on the opposing surface such as in the case of brake/disc plates, curtain/slide, cutting tool/piece, shaft/bearing, etc.
- **A rolling and swivel friction:** where the wiper rolls on the contact surface as in the case of bearing ball/ring, car/road wheel, train/rail wheel, etc. [47].

Depending on the presence of lubrication, we distinguish:

- **Dry friction:** when two solids rub directly against each other without the use of a lubricant. This type of friction is very present all around us: rails and wheels of railways, brushes and collectors of electrical machines, pantographs and catenaries, brakes, reading heads and magnetic tapes, etc.
- **Lubricated friction:** when using liquid or viscous lubricants (oils, greases) or solid lubricants (graphite, molybdenum disulphide...). One of the surfaces can also be conditioned to make it self-lubricating [46].

I.2.2.b) The laws of friction

The laws of friction can be summarized as follows:

- The frictional force is proportional to the normal load.
- The frictional force is independent of the apparent contact surface.
- The frictional force is independent of the sliding speed.

These three laws of friction are more or less reliable, but except in some important cases, they offer useful syntheses of empirical observations [1].

I.2.3 Wear

The definition of wear is a difficult problem as well as a subject of debate. For this reason, many definitions of wear can be found in the literature. According to the most glossaries in the specialized technical literature, wear is defined as “the progressive loss of substance from the working surface of a body resulting from relative movement at the surface” [2,4,48]. Nevertheless, the large range of technical problematics of interest to the tribologist need to be served by a larger definition. For this, a larger definition of wear may include the loss of material from one surface, the transfer of material from one surface to another, or the movement of material within the same surface [49]. Another simple statement is that the wear is “damage to a solid surface, generally involving progressive loss of material, due to relative movement between that surface and one or more contacting substances” [50]. There is no standard unit of wear, but the most commonly used unit is the wear rate, generally expressed as the mass or volume lost per the distance traveled or the contact area. The wear rate is given as a function of the normal load by Archard's wear formula (eq.I.2 [51]):

$$Q = KN/H \quad (\text{II.2})$$

Where Q is the worn volume from the surface per unit of sliding distance (m^3/m), N is the normal load applied to the surface (N), H is the hardness of the worn surface (N/m^2) and K is the wear coefficient.

I.2.4 Wear mechanisms

A non-exhaustive list of wear mechanisms can be drawn up. In theory, these mechanisms identified in different cases of contacts can all be applied at the same time, some being more important than others depending on the imposed conditions. The forth principles wear mechanisms are described in detail in the following paragraphs and represented schematically in [Table I.1](#).

I.2.4.a) Adhesive wear

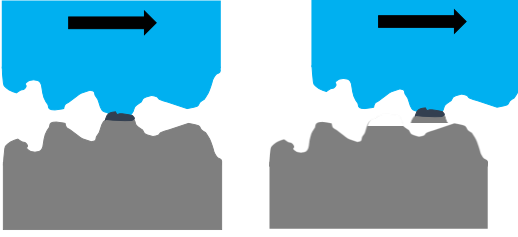
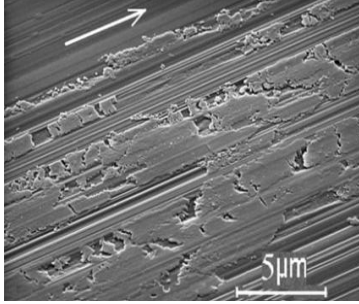
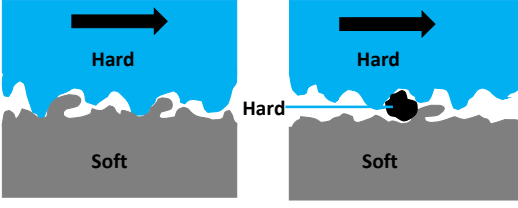
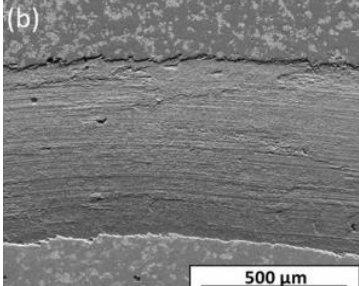
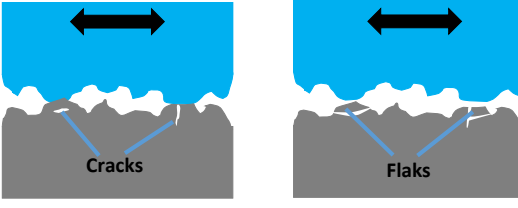
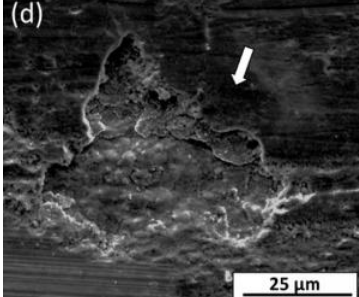
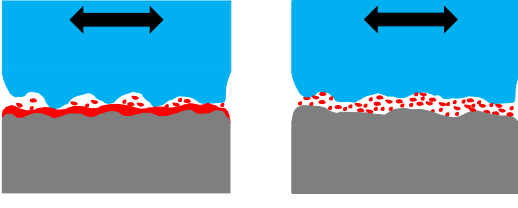
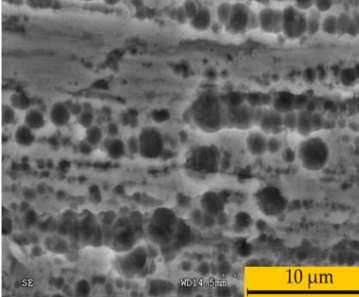
Adhesive wear is associated with the formation of adhesion joints at contact points located on the surface asperities. The material of one part is transferred and solidly welded to the other. Adhesive wear is the wear that always occurs first, even in the absence of abrasives or wear products. It is divided into two classes:

- **Soft wear** (the interface is less hard than the parts): it produces debris that is small, flat, thin and composed mainly by oxides. Soft wear leaves smooth and polished surfaces and increases the load capacity.
- **Severe wear** (the interface is harder than one of the two parts): it is characterized by coarse, angular and numerous debris consisting of a mixture of oxides and the base material that create roughness. Severe wear and tear may lead to seizure of the mechanism [\[7,55\]](#).

I.2.4.b) Abrasive wear

Abrasive wear is defined as the displacement of matter produced by hard particles or protrusions striking or sliding against a solid surface [\[7,55\]](#). Abrasive wear is the result of sliding friction due to ploughing or plastic deformation [\[56\]](#). The abrasion wear mechanism naturally follows the adhesion wear mechanism as soon as wear debris are formed. It is the wear mechanism that prevails in all machines, the most severe and the one that causes the most material loss. Abrasive wear can occur either in two or three bodies: two-body, directly from the contacting solids, or three-body, as a result of the action of hard solid particles between the two surfaces in relative motion ([Table I.1](#)). These types of wear are manifested by scratching, scraping, polishing and the removal of microchips due to the action of particles that attack solid surfaces.

Table I.1: Schematic representation and microscopic views of the main wear mechanisms.

Wear mechanism	Graphical representation	Microscopic view
Adhesive wear	 <p>Cold welding of asperities</p> <p>Breaking of asperity and formation of a wear fragment</p>	 <p>Example on the adhesive wear [52]</p>
Abrasive wear	 <p>Hard</p> <p>Soft</p> <p>Two-body wear</p> <p>Hard</p> <p>Soft</p> <p>Three-body wear</p>	 <p>(b)</p> <p>500 μm</p> <p>Example on the abrasive wear [53]</p>
Fatigue wear	 <p>Cracks</p> <p>Cracks propagation</p> <p>Flaks</p> <p>Formation of flakes</p>	 <p>(d)</p> <p>25 μm</p> <p>Example on the fatigue wear [53]</p>
Corrosive wear (tribocorrosion)	 <p>Formation of a rust layer</p> <p>Deterioration of the rust layer</p>	 <p>10 μm</p> <p>Example on the corrosive wear [54]</p>

I.2.4.c) Fatigue wear

The phenomenon of fatigue is most frequently of a mechanical nature. Mechanical fatigue is the phenomenon of the formation and propagation of cracks under the repeated action of alternating stresses. The degradations are manifested by pitting, cracks, flaking and structural

modifications. Depending on the friction coefficient value, the stresses in the contacting solids are localized either on or below the contact surface. In the first case, the crack forms on the surface (Table I.1). As it propagates, it first moves towards the interior of the solid, then returns to the surface to form a wear fragment. In the second case, the crack is first created below the surface (Table I.1). Moving towards the surface, this crack forms a wear fragment. This type of wear is mainly encountered in gears and bearings, where it constitutes the normal mode of destruction [55].

I.2.4.d) Corrosive or tribochemical wear

In the presence of a reactive environment, a number of complex phenomena can occur, in particular the reactions with this environment (e.g. tribooxidation by oxygen). Depending on the nature and characteristics of the formed compounds, these reactions can be beneficial to the contact or conversely be the cause of material loss. Friction can accelerate corrosion if it removes films of poorly resistant oxides or salts; conversely, corrosion can destroy the rubbing qualities of surfaces. Hard surface films can improve wear resistance, but if they peel off, they can promote abrasion. The asperities of the denuded surfaces due to the rupture of the oxide layers are subject to very high pressures and temperatures that results in microweldings identical to those that produce seizing [55].

I.2.5 Wear evaluation

To be more general and especially more predictive than all the laws, Ashby and Lim [57] have established wear maps, representations of “pion-disk” type test results (Figure I.3), to define domains of identical behavior and transitions between different wear regimes. The aim here is to build a database equivalent, for example, to existing catalogs for the elasticity characteristics of materials. In order to facilitate extrapolation to other types of contacts, the results given in terms of degradation, can be used as a basis for the development of a new database. Soft wear, severe wear, delamination and seizure are provided according to the speed and of the contact pressure that has been adjusted to the right size [58]. This approach quickly took on an international dimension, but was eventually abandoned due to numerous operational problems. Parameters not taken into account until then appear to be very important: the contact stiffness imposed by the test bench (tribometer), the contact geometry (horizontal or vertical, i.e. whether or not it favors the loss of wear particles), etc.

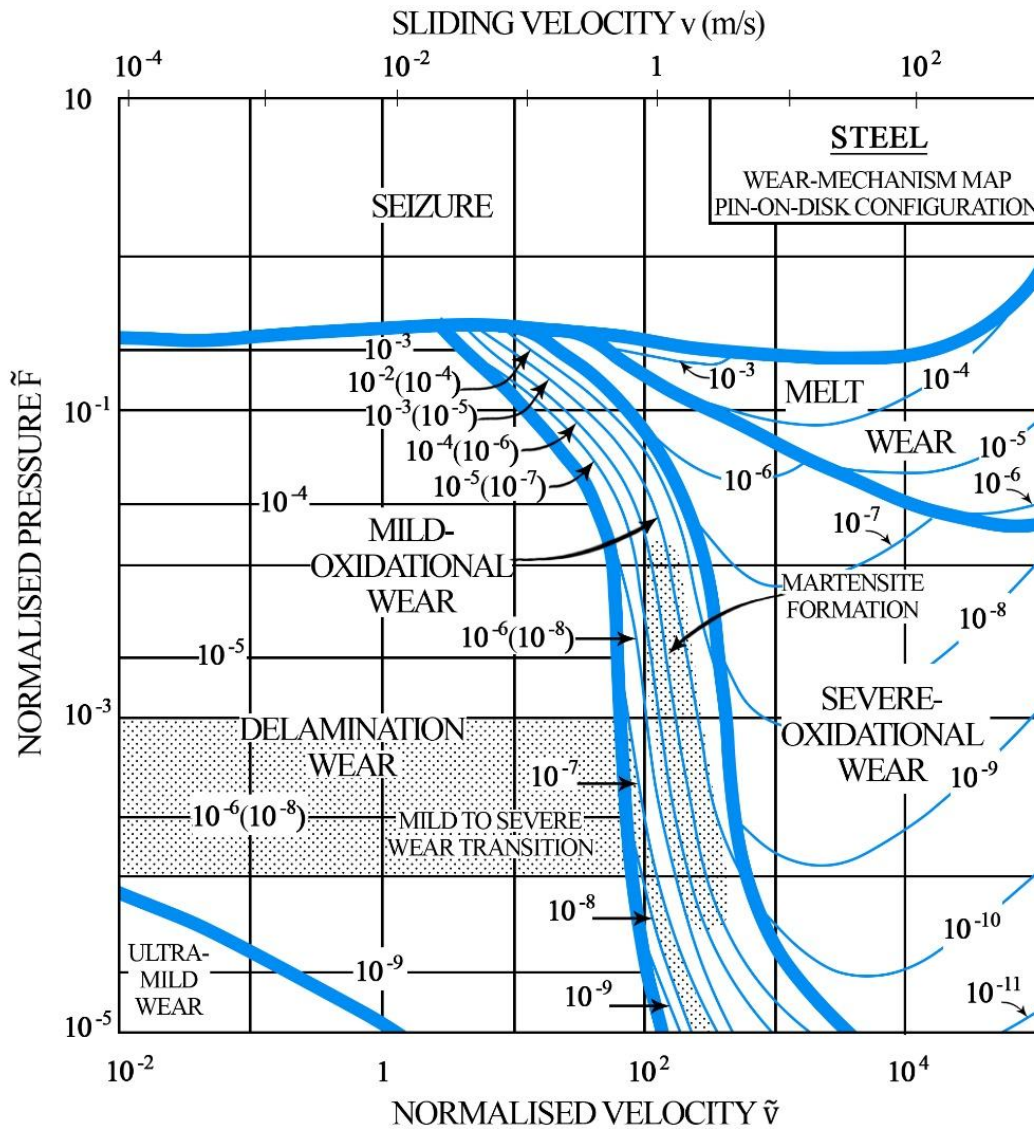
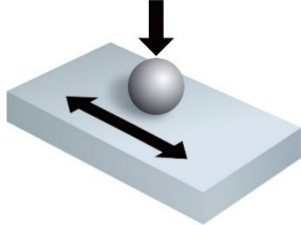
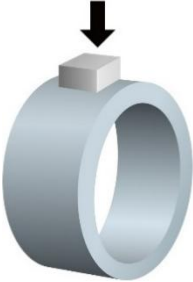
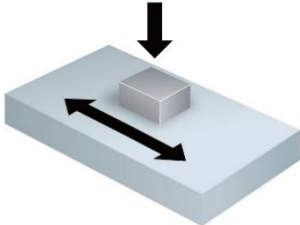
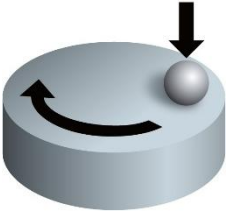
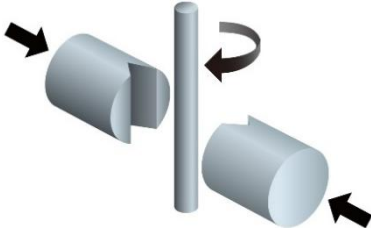
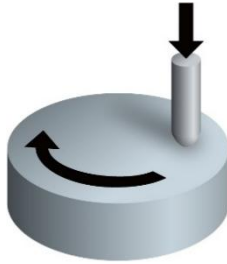


Figure I.3: Wear map according to Ashby and Lim [57].

I.2.6 Wear and friction tests

The principle of all wear and friction tests is the relative movement of one or two bodies that are in continuous contact, this contact can be punctual, linear or flat (Table I.2). The choice of a wear test is mainly related to the intended application by the analyzed materials or parts. For this reason many wear tests can be obtained in research and industrial laboratories, some of them are standards, while others designed for very specific applications. The most commonly tests that can be found are sliding motion tests, rolling motion tests, abrasion, erosion and scratch tests. Table I.2 summarizes some of the most common methods used for friction and wear testing.

Table I.2: Some of the assays used for friction and wear testing [59].

Point contact	Linear contact	Plane contact
 <p>Ball on Plate</p>	 <p>Block on Ring</p>	 <p>Block on Plate</p>
 <p>Ball on Disk</p>	 <p>Pair v-blocks on Pin</p>	 <p>Pin on Disk</p>

I.2.7 Wear prevention

The most commonly used methods for controlling friction and wear damages are summarized in [Figure I.4](#). In modern industrialized societies, reducing or controlling friction and wear is increasingly necessary for several reasons, such as extending the life of machines and biosystems, improving the efficiency of motors and devices, developing innovative and advanced products, conserving material resources, saving energy, and improving security. Historically, these goals were accomplished through design modifications, selection of more performing bulk materials, or through the use of lubrication techniques. Modifications of bulk materials may imply applications of ceramics and polymers. Lubricating systems should involve the use of liquid lubricants such as synthetic and mineral oils or solid lubricants such as molybdenum disulfide (MoS_2). Tribologists have put into practice recently a new approach to control friction and wear, using surface treatments and coatings. This resulted, and to some extent was fueled, by the growth of a new field known as "Surface Engineering" [12]. This growth was driven by two principal factors. The first was the development of new treatments processes (thermal and thermochemical) and coating methods (physical and chemical), which allow to obtain tribological and tribo-chemical surface properties that were not previously

available. The second factor in the growth of this field was the recognition by materials scientists and engineers that the surface is the most important part of many engineering elements. It is on the surface that the majority of failures originate, through either wear, corrosion or fatigue. The surface has a dominant effect on cost and performance over the lifetime, including the serviceability of the machines [13]. It is in this context that new surface treatments and coating processes are being developed and are already having a significant impact. Bearing systems and the devices that work in near-vacuum environments, such as in aerospace mechanisms, satellites, or engine components that operate under corrosive and erosive hot conditions, such as in aero gas turbines, could not operate effectively without advanced tribological coatings [60].

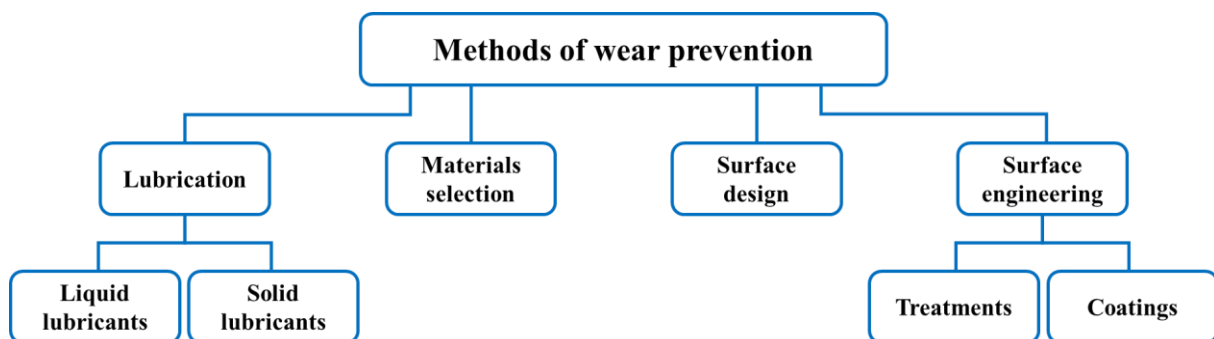


Figure I.4: Methods of wear prevention.

I.3 ANTI-WEAR COATINGS

From an economic point of view, surface deterioration is the predominant factor in materials deterioration as shown in Figure I.5 [61], and since the major problem is concentrated in surfaces, surface engineering, especially material coating is considered one of the most effective modern solutions to friction and wear problems. These coatings provide surfaces with satisfactory resistance to the types of stresses and external physico-chemical factors to which the materials are exposed. They also make it possible to preserve the satisfactory properties of the coated materials such as the low cost and the ease of shaping. Over the last few decades, numerous coating techniques have been developed and modified, making it possible to offer a wide range of options for improving the mechanical and tribological properties of components. Among the developed coatings, nanostructured coatings are among the main ones that have demonstrated high anti-wear performances. In the following, we will try to summarize the most important techniques used for coatings as well as the most important properties of nanostructured coatings.

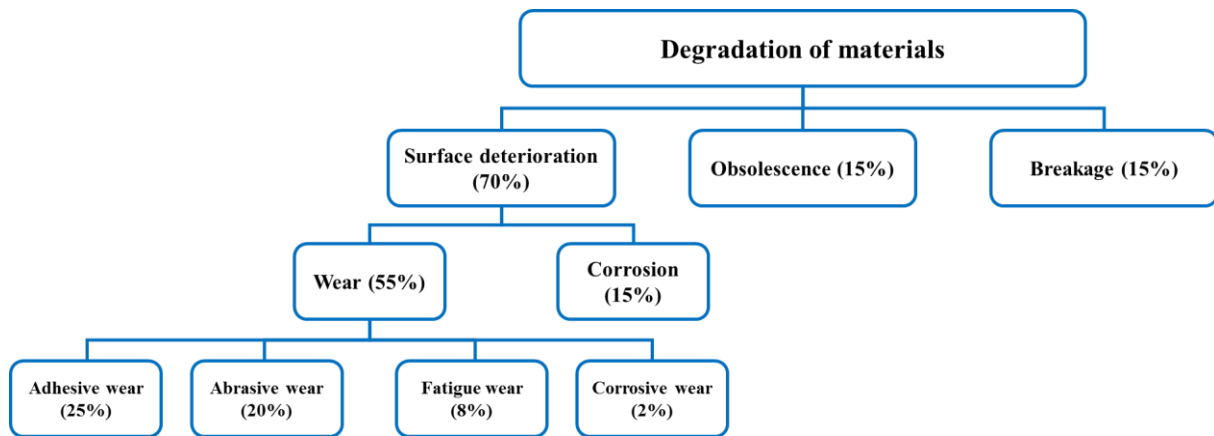


Figure I.5: The causes of materials degradation showing a percentage estimate of the economic importance of each [61].

I.3.1 Methods of elaboration of coatings

The rapid development of tribological and anti-wear coatings over the last decades is mainly due to the development of new coating methods, which would have good control over the properties of the resulting coatings such as composition, morphology, homogeneity, structure, cohesion and adhesion, which were previously unavailable. Referring to the well-known general classification of deposition processes prepared by Rickerby and Matthews [12], coating processes can be divided into four classes, namely, gaseous, solution, molten and semi-molten state processes. Figure I.6 below illustrates all the coating techniques included in this general classification.

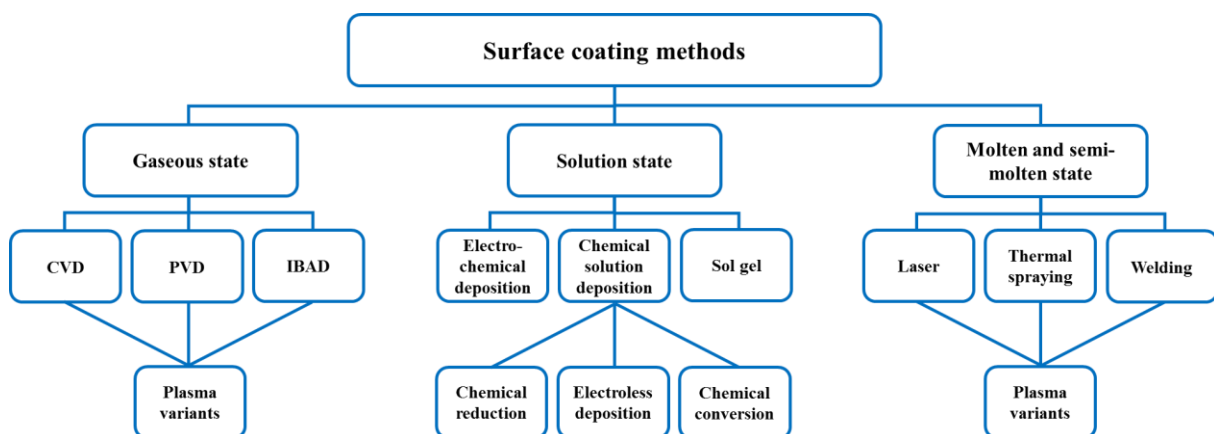


Figure I.6: A general classification of surface coating methods [12].

I.3.2 Nanostructured coatings

In the last years, nanostructures have attracted a growing interest from the scientific and industrial community of materials [16]. Nanocrystalline materials with a crystallites size below

100 nm have unique chemical, physical and mechanical properties (Figure I.7). Mechanically, nanocrystalline coatings have the potential to significantly improve capacities by offering, in numerous cases, extraordinary strength and hardness, unsurpassed protection against tribological contact damage, and enhancements in many other functional properties.

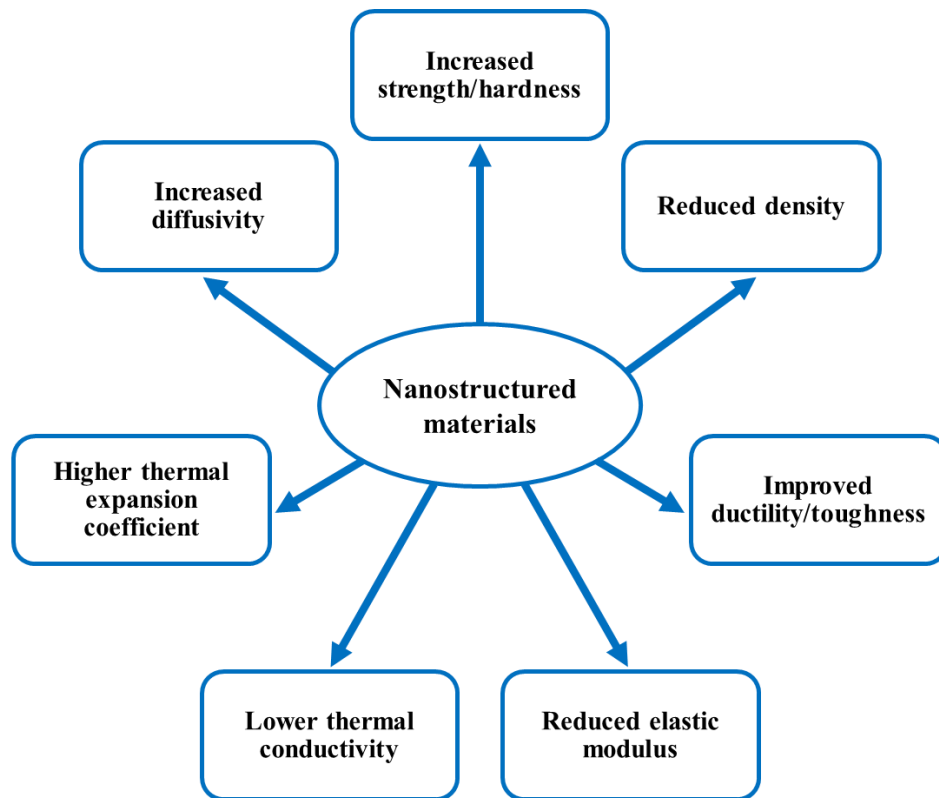


Figure I.7: The benefits that can be gained using nanostructured materials [6].

The unique characteristics of nanocrystalline materials result from the higher number of grain boundaries in comparison to their coarse polycrystalline counterparts. A high proportion of the atoms (up to 49%) are boundary atoms (Figure I.8), thus grain boundaries play a major role in the deformation of these materials. Nanocrystalline materials are characterized by superior creep and plasticity under lower temperatures compared to their conventional coarse polycrystalline counterparts. Likewise, the plastic deformation of nanocrystalline coatings is related to the sliding of the grain boundaries by means of diffusion or rotation of the grain boundaries [16]. Nanocrystalline surfaces can be produced by several processes, the most important of which is surface coating using various techniques such as PVD, CVD, sputtering and electrochemical processes. The adhesion between the coating and the substrate is crucial for the properties of the coating [62]. At the meantime, optimizing the properties of nanocrystalline coatings, with tolerance to defects and other non-mechanical considerations,

poses critical problems and challenges, depending on the coating methods and application areas [16].

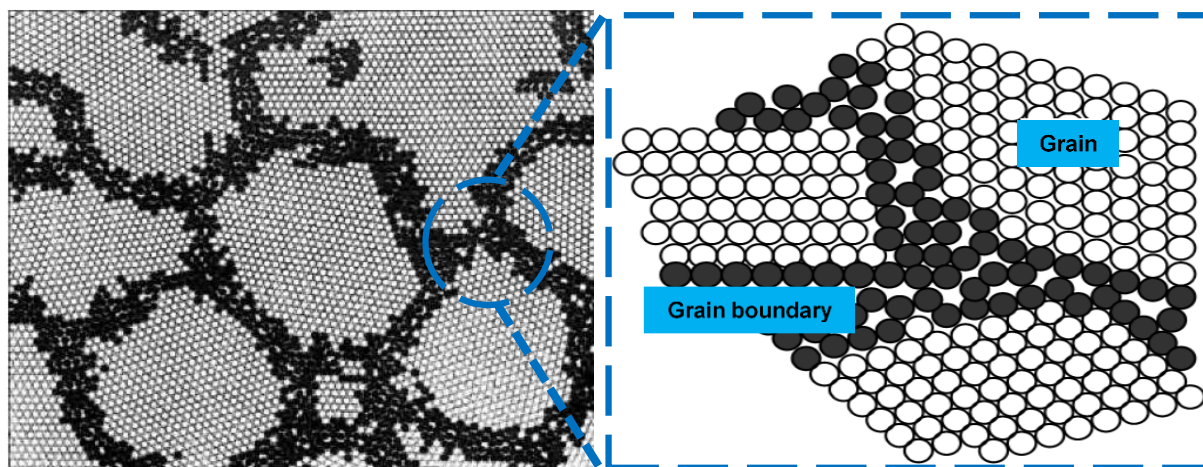


Figure I.8: Schematic representation of the atomic structure of nanocrystalline materials showing an important atomic percentage in grain boundaries.

I.4 ELECTRODEPOSITION OF NANOCRYSTALLINE COATINGS

In recent years, the importance of electrodeposition in nanosciences and nanotechnologies has become clear to researchers, particularly with regard to the development of nanostructured layers and coatings. Further progress is also inevitable and nanocrystalline coatings are expected to benefit from increased exploitation and development of their performances by the academic and industrial sectors, especially in the field of anti-wear and anti-corrosion applications. Bath composition, temperature, pH, type of power supply, current density are the key parameters which influences the deposition process and hence the properties of the deposited materials.

I.4.1 Principle of electrodeposition

The word "electrodeposition" generally refers to the principle of the electrolysis process. One of the historical approaches to this process is electroplating, which mainly allows the production of metal or alloy coatings for decorative or protective applications [63]. It consists essentially in the immersion of the conductive or semi-conductive material to be coated (termed as a cathode) in an electrolytic cell containing ions of the material to be deposited, a support solution (electrolyte) and a counter electrode or anode. In an electrolytic cell, there are no spontaneous electrochemical reactions [63]. Therefore, for a reaction to take place, the two electrodes must be connected to an external power supply to make the current flow possible as represented in Figure I.9. The object to be coated is linked to the negative pole of the energy source, so that

the metal ions M^{n+} present in the electrolyte are reduced to metal atoms M , which will ultimately form the coating on the cathodic surface, a gaseous evolution also taking place on the cathode [64]. In contrast, the oxidation reaction, involving the dissolution of the metal or the release of gas, occurs at the anode. There are two types of electroplating cells, namely cells with dissoluble and with non-dissoluble anodes. In the cells with dissoluble anode (Figure I.9 (a)), the anodic half-reaction involves the dissolution of the anode (eq.I.3), while the cathodic half-reaction involves the reduction of dissolved ions of anode and electrolyte (eq.I.4) [63]. In the cells with non-dissoluble anode (Figure I.9 (b)), the anodic half-reaction not involves the dissolution of anode and the cathodic half-reaction limited only to the reduction of ions present in the electrolyte (eq.I.4).

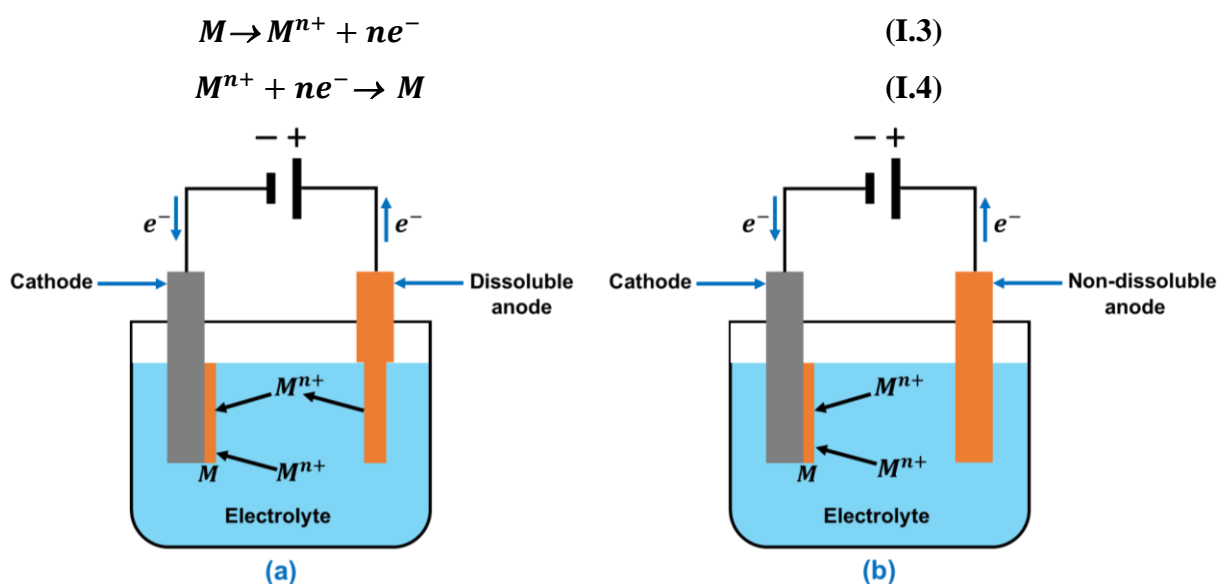


Figure I.9: Principle of an electrodeposition setup using dissoluble anode (a) and non-dissoluble anode (b).

I.4.2 Advantages of electrodeposition

Electrodeposition has gotten an extensive consideration in the last years thanks to its several advantages over the conventional and the recent deposition processes, the main advantages can be summarized in the following lines [9,65,66]:

- Industrial applicability thanks to the low cost, the high production rates, the low induced energy and the reduced wastes.
- Easy functioning, as the process parameters can be easily adjusted to achieve the required composition, morphology and microstructure.

- Versatility, as the process can be used to produce a wide variety of materials, films and coatings.
- Deposits with grain sizes ranging from hundreds of micrometers to a few nanometers can be developed simply by properly controlling the electrodeposition parameters such as the bath composition, the current density, the pH, the temperature, etc.
- Different electrodeposits geometries can be achieved such as homogeneous, multilayer, gradient, patterned, etc.
- The electrodeposits can be performed under ambient conditions of temperature and pressure.
- Uniform electrodeposits can be applied to substrates with complex geometries.
- In the most cases, there is no need for the post-treatment of the electrodeposits.

I.4.3 Applications of electrodeposition

Electroplating has seen many applications in the industrial field, particularly in coating technology, since its invention in 1805 by the Italian chemist Luigi V. Brugnatelli. The main applications of this technique can be summarized as follows [67–70]:

I.4.3.a) Decoration

Electroplating is used in jewelry, furniture, building hardware and tableware to improve aesthetics. High value metal coatings are electroplated onto a less expensive base metal surface to give them a flawless appearance.

I.4.3.b) Protection

- **Corrosion protection:** Electroplating is a way to prevent corrosion, especially when the metals to be plated are naturally corrodible. Coating the corrosive metal with a thin layer of a more noble metal prevents and delays its corrosion. Several electrolytic anticorrosion coatings have achieved unparalleled success in the industry, such as nickel and chromium coatings on automotive parts and appliances, zinc and cadmium coatings on nuts, screws and electrical components.
- **Wear protection:** Electrodeposited coatings of hard or self-lubricating materials such as nickel, chromium, copper and their alloys are widely used in the automotive, aeronautic and machinery industries as anti-wear coatings for the surface protection of wear parts such as bearings and worn shafts.

- **Radiations protection:** Many metals have no inherent protection against artificial or natural radiations. To remedy this situation, these metals are electroplated with a thin layer of protective metal as an additional defense against such radiation.

I.4.3.c) Enhancements

- **Enhancement of electrical conductivity:** Integrated circuits in electronic devices are made from cheap metals that do not conduct electricity efficiently. To improve their conductivity, the parts are coated with a thin layer of expensive metals like gold and silver.
- **Enhancement of adhesion:** Electrodeposited coatings are widely used as a primer for better adhesion between the substrate and other coatings such as paints and varnishes.
- **Enhancement of other properties:** Electrodeposited coatings are also used to improve other surface properties such as thermal conductivity, lubricity, solderability, reflectivity, hydrophobicity, wettability, catalytic properties, etc.

I.4.3.d) Electroforming

Electroforming is one of the main techniques used to manufacture micro tools such as micro parts for MEMS, sieves, screens, dry shaving heads, registration stamps, molds and dies.

I.4.3.e) Synthesis of nanomaterials and nanostructures

Due to their advantages mentioned above, electrodeposition is an attractive method for the development of nanomaterials and nanostructured materials with special magnetic and electronic properties for applications in soft and hard magnets, semiconductors, high efficiency transformers, energy storage, power supplies, motors, etc.

I.4.4 Synthesis of nanocrystalline coatings by electrodeposition

Electroplating is one of the most ancient methods used to produce nanocrystalline materials. In which the grain size of the deposits is controlled to obtain nanostructures with specific physical, chemical and mechanical characteristics [71]. The result is a bulk material, which does not need further treatment, as defined by Gleiter [72]. In this respect, electrolytically deposited nanocrystals are very different from those built from consolidated particles. It is possible to electrodeposit a huge number of metals, alloys, ceramics and composites whose crystallites size is down to less than 100 nm. They can be electrodeposited as thin layers (1 to 100 μm) or in bulk (several millimeters in thickness). Furthermore, the codeposition of ceramics with metals

and polymers has opened the way to the development of new hybrid nanostructured materials that cannot be obtained by any other technique.

Basically, crystallites size in the nanometer range can be achieved when the electroplating parameters such as current density, pH, bath composition, temperature, etc. are selected to favor the nucleation of new grains over the growth of existing grains. Practically, this could be done through several approaches such as increasing the deposition rate, forming the appropriate complexes in the bath, adding the suitable surfactants to limit the surface diffusion of the adatoms, etc. The two main mechanisms that were recognized as the key steps controlling the rate of generation of nanocrystals are charge transfer at the electrode surface and diffusion of adions at the crystal surface [73]. Therefore, the diffusion of the adions on the surface must be inhibited; this is achieved for example by adsorption of foreign species such as grain refiners on the growth surface. The effectiveness of these grain refiners depends on their adsorption behavior on the surface, their compatibility with the electrolyte and their stability at different temperatures. Several chemical species have been found to inhibit crystal growth and reduce grain size down to the nanometric order such as saccharin [42], BD [31] and coumarin [74] in the case of electrodeposition of nickel and its alloys. The second key factor in the formation of nanocrystals during the electrocrystallisation is the overpotential [17,75]. With lower potentials and high surface diffusion rates, grain growth is favored. Conversely, high overpotentials and low diffusion rates favor new nucleus formation.

A non-exhaustive number of nanocrystalline and nanocomposite materials have been successfully developed by electrodeposition, such as pure nanocrystalline metals (Ni, Co, Pd, Cu, etc.), binary alloys (Ni-Co, Ni-P, Zn-Ni, Pd-Fe, Co-W, etc.) and ternary alloys (Ni-Co-P, Ni-Fe-Cr, etc.), metal matrix composites (Ni-SiC, Ni-Co-TiO₂, etc.), ceramics (ZrO₂, SiO₂, etc.) and ceramic nanocomposites [68,71,76–81]. These nanocrystalline and nanocomposite coatings can be produced either by direct current electrodeposition, where the presence of grain refiners in the electrolyte is required, or by pulsed current electrodeposition, where the addition of grain refiners is an option.

I.5 NANOSTRUCTURED ELECTRODEPOSITED Ni AND Ni-Co COATINGS

I.5.1 Potentials of Ni and Ni-Co alloy as alternatives to hexavalent Cr coatings

Conventional electrolytic chromium coatings obtained from hexavalent chromium electrolytes have been used for more than 120 years. However, over the past two decades, there has been increasing pressure from health and environmental organizations to abandon the use of

hexavalent chromium. It is well known by the scientific community that hexavalent chromium is carcinogenic and can cause serious health damage in case of inhalation over a long period. For this reason, the U.S. Environmental Protection Agency (EPA) classifies hexavalent chromium and its compounds among 17 chemicals as extremely hazardous substances [20]. As for nickel and its compounds, their damage is largely related to their solubility and also to the route of exposure. For example, the EPA classifies nickel refinery dust in Group A as a human carcinogen [20], while soluble nickel salts are not classified as a potential human carcinogen. With respect to the nickel sulfate widely used in this work, it was found not to be carcinogenic by inhalation to rats and mice [82]. It is classified as category 2 or even category 3 as a suspected carcinogen according to the European Commission (EC) regulation No. 1272/2008 [83]. However, there is no clear evidence that inhalation of nickel-containing mists during electroplating can cause cancer. As for cobalt sulfate used less frequently in this work, it is not included in the list of carcinogenic chemicals by the EPA, whereas it is classified in category 2 as a substance capable of causing cancer to humans according to EC regulation No.1272/2008 [83]. Although the classifications are not completely consistent, it is accepted that the nickel and cobalt salts used in electroplating are much less hazardous than hexavalent chromium. Thus, it is currently very reasonable, in the absence of alternative materials for hexavalent chromium that are non-hazardous and inexpensive, to consider using nickel, cobalt and their alloy as alternatives to hexavalent chromium in electroplating. In addition to environmental friendliness, numerous studies [29,84,85] have shown that Ni-Co alloy coatings can replace and even be better than hexavalent chromium coatings in anti-corrosion and anti-wear applications.

1.5.2 Alloying of Ni with Co by electrodeposition

Nickel is a transition metal with a face-centered cubic (fcc) crystal structure in the solid state. It has a molar mass of 58.69 gm⁻¹, a density of 8.90 gcm⁻³ at 25 °C and melts at 1453 °C. It is chemically inactive under normal conditions, but its corrosion resistance decreases under oxidative conditions. However, it is resistant to corrosion and oxidation at moderate to high temperatures. Its electrical resistance is very low at low temperatures. The specific properties make it a very versatile metal and easily alloyable with most metals. Cobalt is located adjacent to nickel in the periodic table of elements. Its molar mass and density are close to those of Ni, 58.93 gmol⁻¹ and 8.85 gcm⁻³, respectively. As a function of temperature, Co can take two different crystal structures: the Co (ϵ) with a hexagonal close-packed structure (hcp) at temperatures below 417 °C; and the Co (α) with fcc structure from 417 °C to the melting temperature (1493 °C). Alloying Ni with Co allows for improvements in physicochemical and

mechanical properties especially corrosion and wear resistance [29,40,86]. For this reason, Ni-Co alloys are applied as technical coatings in the fields of wear and corrosion protection, electrocatalysis, magnetism, etc. [40,87]. The binary phase diagram of Ni-Co alloy system is shown in Figure I.10, the very important aspect of this system is that Ni and Co can form total solid solutions at any Co/Ni ratio, which allows producing alloys having any chemical composition [88].

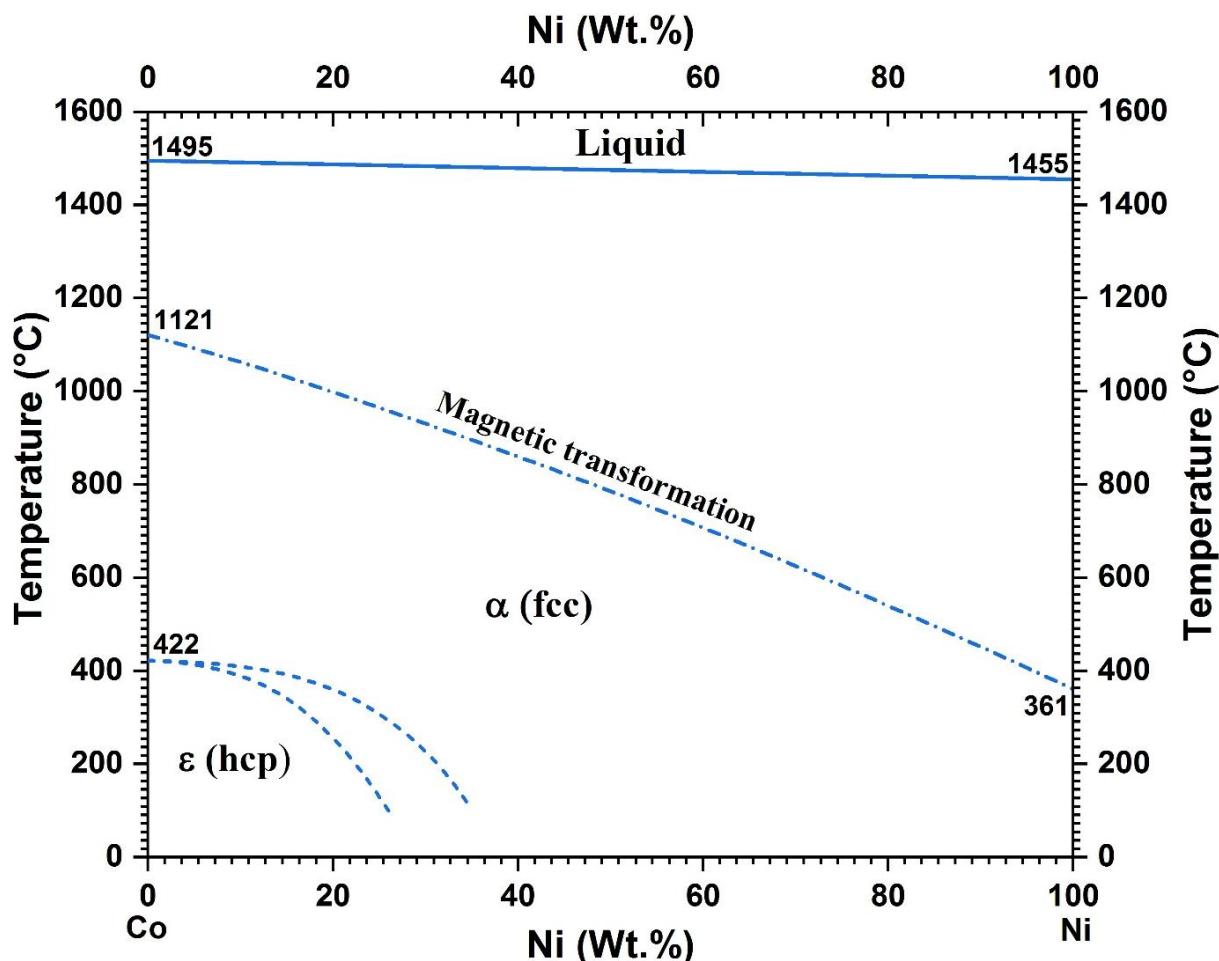


Figure I.10: The binary phase diagram of Ni-Co alloy according to ASM International [91].

Electrodeposition is a simple, controllable, and economically effective method to produce Ni-Co alloys. Moreover, these alloy systems are among the easiest alloys to be electrodeposited because Ni and Co have close standard potentials ($E^\circ_{\text{Ni}} = -0.250 \text{ V}$ and $E^\circ_{\text{Co}} = -0.277 \text{ V}$ vs. SHE) [89]. However, it must be taken into consideration that deposition of Ni with Co is an anomalous codeposition [89]. Where Ni and Co with Fe form the iron group metals that codeposit abnormally [90]. An anomalous codeposition (as discussed extensively in section III.3.1.a) means that the less noble metal is deposited preferentially compared to the more noble metal. As in our case, the less noble metal Co is deposited preferentially over Ni. Therefore, it is not easy to control the Co/Ni ratio in the deposits by the ratio of the ions concentration in the bath

($\text{Co}^{2+}/\text{Ni}^{2+}$). On the other hand, according to the Ni-Co alloy phase diagram (Figure I.10), the codeposition of Ni with Co under electrodeposition conditions (generally ambient pressure and temperature < 200°C) provides a monophasic α (fcc) solid solution extending from pure Ni to ~64 wt% Co, with a biphasic α (fcc) + ε (hcp) region extending from ~64 to ~74 wt. % Co, and a monophasic ε (hcp) region continuing to pure Co.

I.5.3 Electrodeposition baths of nanocrystalline Ni and Ni-Co coatings

I.5.3.a) Electrodeposition baths of nanocrystalline Ni coatings

The first electrolytic nickel-plating bath was formulated by Watts in 1916. This bath contained nickel sulfate to provide nickel ions, nickel chloride or sodium chloride to help dissolve the nickel anode and boric acid as a buffering agent. The deposition parameters can be controlled (current density, pH, temperature, etc.) and specific additives can be added to this bath to control grain size and characteristics of deposits. Three other nickel electroplating baths were then experimented, namely a nickel sulfate bath, a nickel chloride bath and a nickel fluoborate bath. Each of them showed many advantages in addition to some inconveniences, which are listed in Table I.3.

Table I.3: Nickel electroplating baths [92].

Bath type	Sources of Ni^{2+}	Advantages	Inconveniences
Sulphate bath (Watts bath)	<ul style="list-style-type: none"> • NiSO_4 with a small amount of NiCl_2 	<ul style="list-style-type: none"> • Less expensive • Less corrosive to equipment • Easy to use • Lower internal stress in deposits 	Not available
Sulphamate bath	<ul style="list-style-type: none"> • $\text{Ni}(\text{NH}_2\text{SO}_3)_2$ with small quantities of NiCl_2 	<ul style="list-style-type: none"> • High rate of deposition • Lower internal stress in deposits 	<ul style="list-style-type: none"> • High sensitivity to impurities • High cost of chemicals
Chloride bath	<ul style="list-style-type: none"> • NiCl_2 	<ul style="list-style-type: none"> • Higher electrical conductivity 	<ul style="list-style-type: none"> • High cost of chemicals. • High corrosion • Higher internal stress in deposits
Fluoborate bath	<ul style="list-style-type: none"> • $\text{Ni}(\text{BF}_4)_2$ 	<ul style="list-style-type: none"> • Deposits obtained similar to those from nickel sulphate bath 	<ul style="list-style-type: none"> • High cost of chemicals.

I.5.3.b) Electrodeposition baths of nanocrystalline Ni-Co coating

Many different baths are used for the electrodeposition of Ni-Co coatings. These baths differ mainly in the sources of Ni and Co ions. The most popular are sulfate (Watts bath), sulphamate and chloride baths. Recently, other baths with specific additives have also been introduced, such as ionic liquid baths, citrate baths, pyrophosphate baths, gluconate baths, etc. [Table I.4](#) lists the advantages and disadvantages of the three most common baths.

Table I.4: Ni-Co electroplating baths [88].

Bath type	Chemicals	Advantages	Inconveniences
Modified Watts bath	<ul style="list-style-type: none"> • NiSO₄ and CoSO₄ as sources of Ni and Co ions. • NiCl₂ for enhance solution conductivity and solubility of Ni anodes. 	<ul style="list-style-type: none"> • Low cost. • Smooth and bright deposits. • Good corrosion resistivity of deposits. • Lower internal stress. 	Not available
Sulphamate bath	<ul style="list-style-type: none"> • Ni(NH₂SO₃)₂ and Co(NH₂SO₃)₂ as main sources of Ni and Co ions. • NiCl₂ and CoCl₂ to help dissolve anodes uniformly and to prevent anode polarization. 	<ul style="list-style-type: none"> • Lower internal stress in deposits. • Higher solubility. • Higher deposition rate. • Higher stability at pH range from 2 to 4 and temperatures up to 60°C. 	<ul style="list-style-type: none"> • Very sensitive to impurities. • High expensive. • Possibility of hydroxides precipitation.
Chloride bath	<ul style="list-style-type: none"> • NiCl₂ and CoCl₂ as sources of Ni and Co ions. • NaCl or NH₄Cl as supporting agents to enhance the cathodic current efficiency. 	<ul style="list-style-type: none"> • Higher electrolyte conductivity. • High hardness of deposits. 	<ul style="list-style-type: none"> • High cost of chemicals. • Higher internal stress of deposits. • High corrosively.

In addition to the main constituents mentioned above, additives are frequently added to pure Ni and Ni-Co alloy electroplating baths in order to control the electrocrystallisation process for various purposes, such as achieving the appropriate composition, structure and morphology and

for improving the different properties [93]. The principal additives commonly added to Ni and Ni-Co electrodeposition baths and their roles are summarized in Table I.5.

Table I.5: Bath additives used in Ni and Ni-Co electrodeposition [88].

Additive	Role
<ul style="list-style-type: none"> • Boric acid • Ammonium sulfate • Sodium dodecyl sulfate (SDS) • Thiosemicarbazide hydrochloride • Thiourea • Sodium saccharin • Saccharin • Dextrin • Gum Arabic • Gelatin • Sodium acetate • Citric acid • L-ascorbic acid • Triton X-100 • 1,4 butyne diol • Coumarin • 1,3-naphthalene sulphonic acid • Formaldehyde • Glycine • Crotonaldehyde • Glycolic acid • Oxalic acid • 2-butin-1,4-diol (BD) • FC 95TM • Sodium gluconate • Dodecyltrimethylammonium chloride (DTAC) 	<ul style="list-style-type: none"> • Buffer • Buffer • Surfactant • Surfactant • Surfactant, brightener • Stress reducing, grain refinement • Surface roughness reducing, brightener • Stress reducing, grain refinement, • Surface roughness reducing, improving the brightness and quality of coatings • Surfactant • Surfactant • Surfactant • Internal stress reducer, complexant, stablbing the structure and properties • Internal stress reducer, stablbing the structure and properties • Surface smoother • Anti- pitting agent • Brightener • Reducing the current efficiency • Stress reducer • Complexing agent • Complexant • Complexant • To control the internal stress; and grain size and texture • Wetting agent • Complexing agent • Cationic surfactant

I.5.4 Applications of electrodeposited nanocrystalline Ni and Ni-Co coatings

I.5.4.a) Applications of electrodeposited nanocrystalline Ni coatings

Due to their good properties such as corrosion resistance [94], high hardness [95], wear resistance [28] and superplasticity [96], Ni is used as a coating material in many fields such as decoration [97], surface protection [98], electronics [94], micro/nano electromechanical

systems [99], etc. Figure I.11 shows the main areas of use of Ni coatings and the percentage of their use in each area.

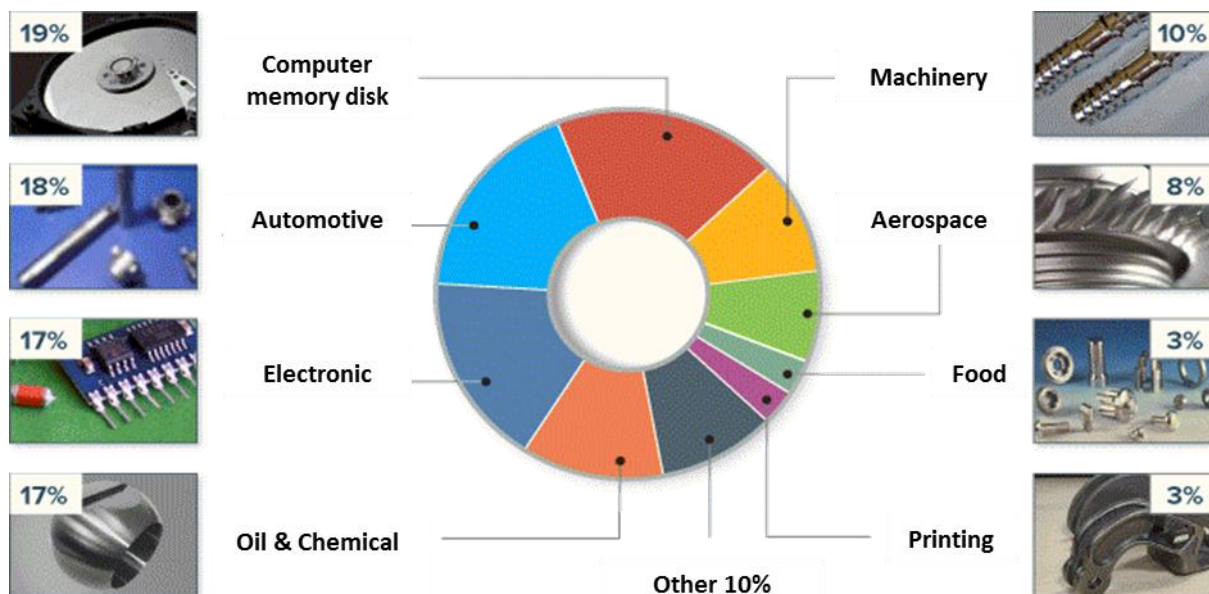


Figure I.11: The main applications areas of Ni coatings [100].

I.5.4.b) Applications of electrodeposited nanocrystalline Ni-Co coatings

Alloying Ni with Co through electrodeposition allows obtaining physicochemical and mechanical properties better than those of pure Ni [86,101]. Ni-Co alloy coatings exhibit better adhesion, higher hardness, enhanced thermal stability, better anti-corrosion and anti-wear properties as well as improved magnetic properties [28,40,102–104]. Which offers opportunities for more and more applications. Figure I.12 summarizes the main applications of Ni-Co coatings.

I.5.5 Properties of electrodeposited nanocrystalline Ni coatings

I.5.5.a) Microstructural properties

It is well known that the morphology of electrodeposited coatings can be strongly influenced by the type and composition of the electrolyte as well as the electrodeposition parameters (current density, pH, temperature, stirring, etc.). However, it is accepted that the morphology of electrodeposited nanocrystalline Ni coatings is dense, very smooth and generally tends to be colony-like [105–107] compared to their counterpart, microcrystalline Ni coatings which generally exhibit a pyramidal rough surface morphology [105,108–111]. Figure I.13 [112] provides a comparison between the morphology of microcrystalline and nanocrystalline Ni coatings elaborated at Watts bath with different electrodeposition techniques, namely direct current (DC), pulsed current (PC) and pulsed reverse current (PRC) electrodeposition. It is clear

that all microcrystalline Ni coatings are characterized by a pyramidal rough surface morphology (Figure I.13 (a)-(c)). However, the saccharin (as grain growth inhibitor) adsorbs on the active sites of pyramids, inhibits their growing [41,66,105], and leads to very smooth granular morphology in the case of nanocrystalline Ni coatings (Figure I.13 (d)-(f)).

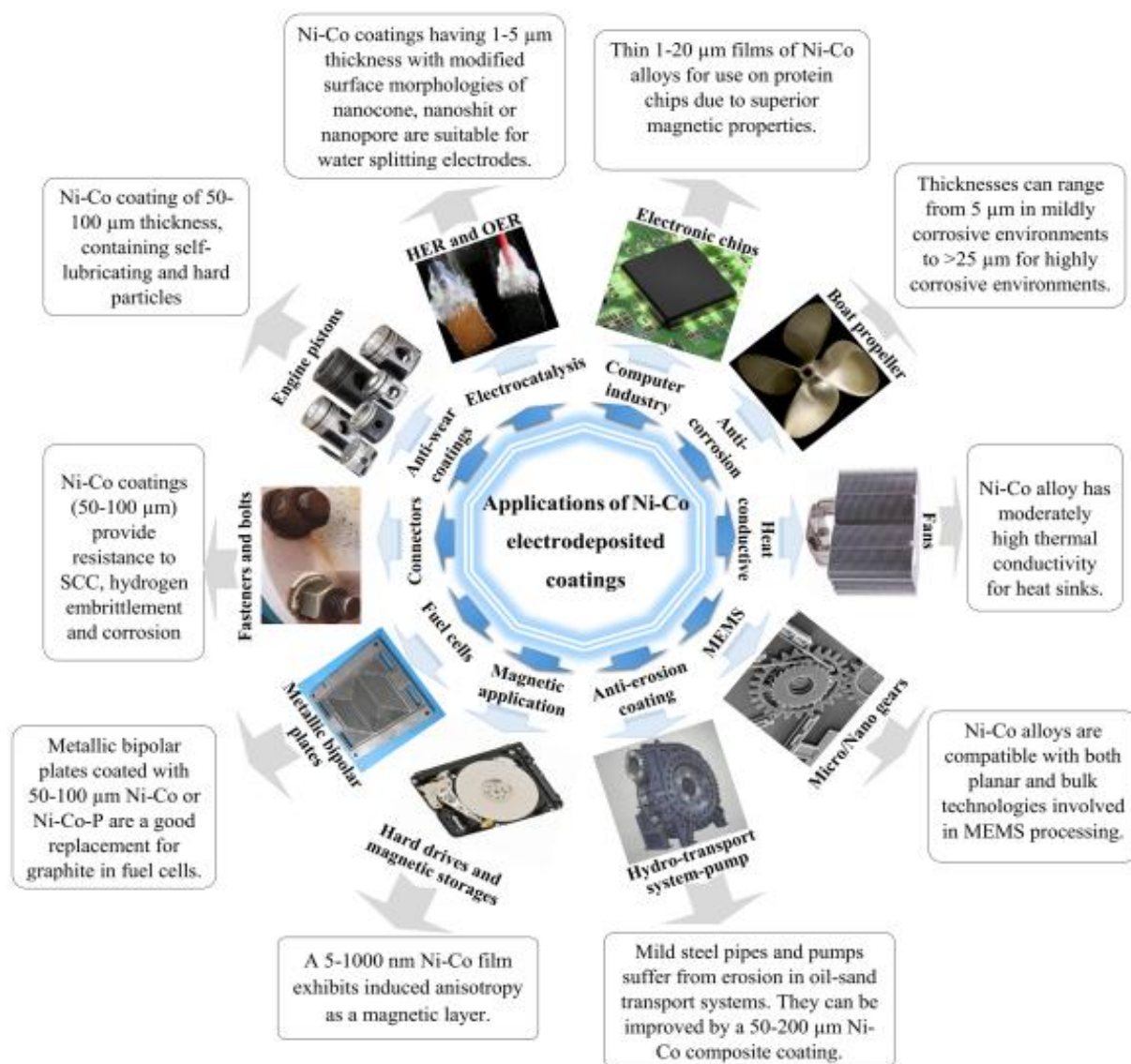


Figure I.12: The main applications of electrodeposited Ni-Co coatings [88].

The DRX analysis of pure Ni coatings shows that they are consistently characterized by a pure face-centered cubic (fcc) crystal structure. On the other hand, the texture of the nanocrystalline Ni coatings is influenced by the used electrolytes and the electrodeposition conditions. However, the (111) and (200) crystallographic orientations were found to be predominant in the texture of pure nanocrystalline Ni coatings [105–107,113,114]. Figure I.14 (a) [113], provides a comparison between the annealed microcrystalline Ni coating and the electrodeposited nanocrystalline Ni coating, while Figure I.14 (b) [106] provides a comparison

between the microcrystalline Ni coating electrodeposited in the absence of saccharin and the nanocrystalline Ni coating electrodeposited in the presence of saccharin as grain refiner. The first observation that can be drawn is that the all the coatings showing fcc crystal structure with (111) and (200) as preferred orientations, while the second observation is that the nanocrystalline Ni coatings show broad peaks compared to their microcrystalline counterparts, which can be explained by the grain refinement [106,107,113].

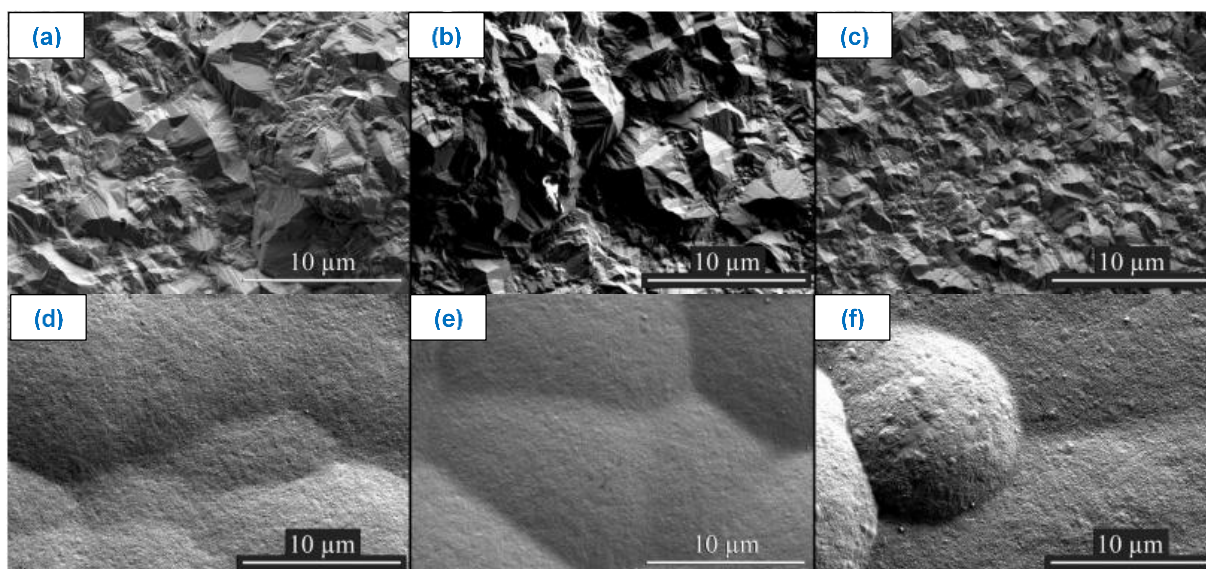


Figure I.13 : Morphologies of microcrystalline and nanocrystalline Ni coatings electrodeposited with DC (a) and (d) ; PC (b) and (e) ; PRC (c) and (f).

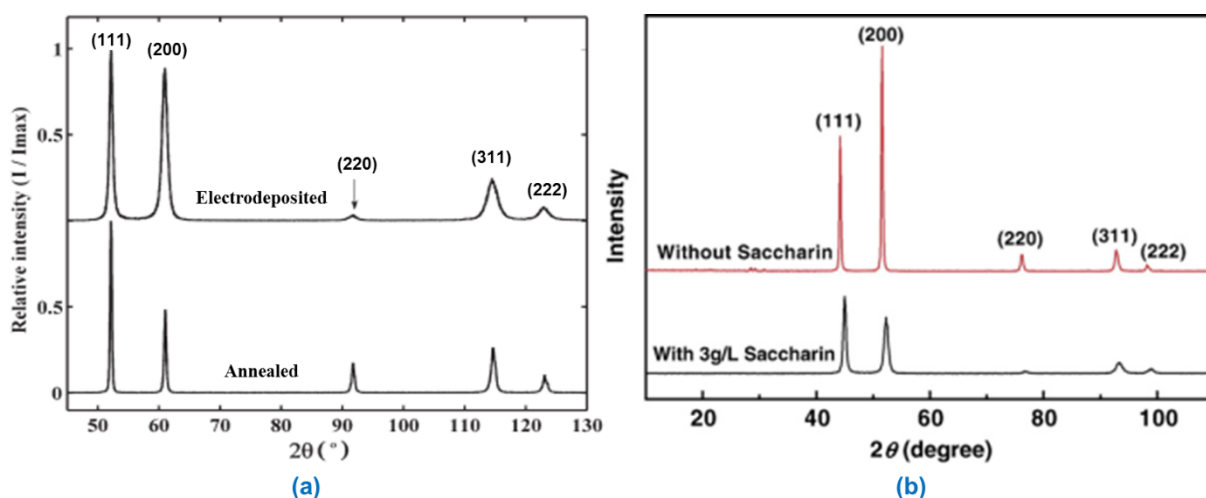


Figure I.14 : Comparation of XRD pattern of nanocrystalline Ni coating with annealed Ni (a) and microcrystalline Ni coating (b).

I.5.5.b) Mechanical properties

The hardness of electrodeposited nanocrystalline Ni coatings can be strongly affected by the applied electrodeposition parameters as shown in Figure I.15 (a) and (b) [115] in the case of

different current densities and different bath temperatures, respectively. Compared with Figure I.15 (c) and (d), it can be observed that these changes in the hardness are inversely proportional to the variation in the grain size of the electrodeposits. Where the hardness of the coatings increases with the decrease of the grain size, which is known as the Hall-Petch effect (detailed in section III.3.1.c). Many studies have reported that the microhardness of Ni coatings increases as the grain size decreases from micrometer to nanometer, as can be seen in Figure I.16 (a) [23]. This microhardness increase also continues by grain size decreasing in the nanometer order [23,77,107,116], as can be seen in Figure I.16 (a) and (b). However, a deviation from the Hall-Petch relation is noticed in the nanometer scale as can be seen in Figure I.16 (a) and (b). The grain size value of deviation or even failure of the Hall-Petch relation is not consistent between studies. This value was found below 62 nm by Jeong et al [23], below 8 nm by Mishra et al [116] and below 45 nm by Wang et al [107]. While Erb et al [77] claimed that the Hall-Petch relationship fell apart at a grain size of less than 30 nm. The mechanism of deviation and failure of Hall-Petch relationship is also not clear. Several factors have been proposed in the literature as being responsible for this deviation, such as suppression of dislocation stacking [116], diffusional creep [77], larger grain boundary fraction [117], and increased porosity of deposits with small grain sizes [118].

I.5.5.c) Tribological properties

The tribological performances of electrodeposited Ni coatings are found to be influenced mainly by their hardness related to their grain size. Jeong et al [23] and Wang et al [107] recorded that the wear rate of Ni coatings decreases with increasing their hardness (Figure I.17 (a)), which is in agreement with Archard's law (detailed in IV.3.1.d). It is also revealed that the friction coefficient is strongly influenced by the decrease in grain size of the electrodeposited Ni coatings. Wang et al [107] found that the friction coefficient decreases from 0.75 to about 0.62 when the grain size reduces from 3 μm to 16 nm (Figure I.17 (b)). Similarly, Mishra et al [116] reported that the friction coefficient decreased from about 0.75 to about 0.15 when the grain size of Ni electrodeposits went from 61 μm to 8 nm. Meanwhile, SEM observations of the worn surface morphologies of Ni electrodeposits (Figure I.18 (a)-(c) [107]) showed that the wear mechanism gradually transforms from a severe adhesive wear accompanied by plastic deformation and delamination to a mixed abrasive-oxidative wear, as a result of hardness increase following the decrease in crystallite size from the micrometric to the nanometric order.

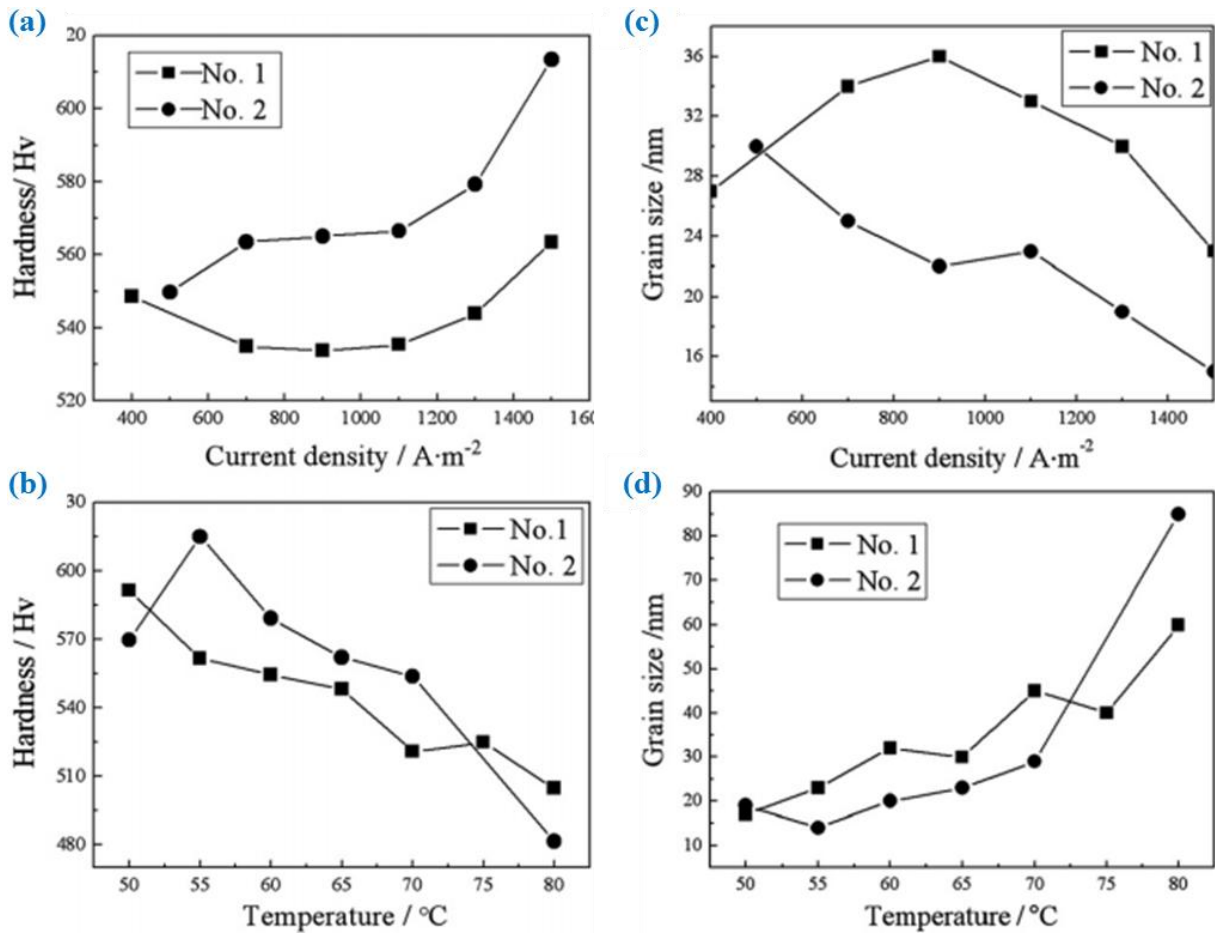


Figure I.15: Effect of current density and temperature on hardness (a)(b) and grains size of nanocrystalline Ni coatings (c)(d) [115].

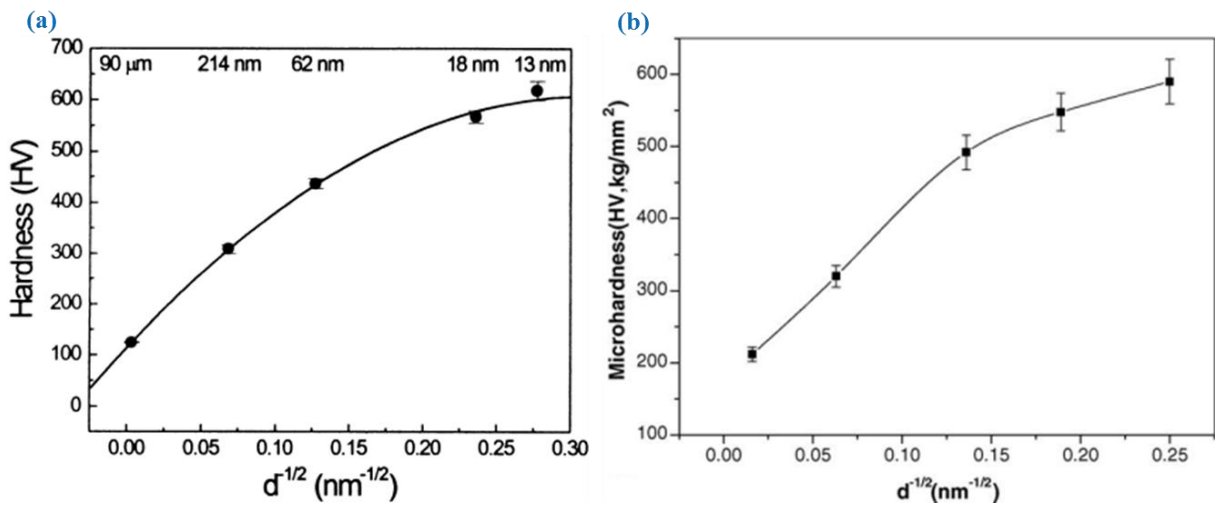


Figure I.16: Relationship between hardness and grain size of Ni electrodeposited coatings.

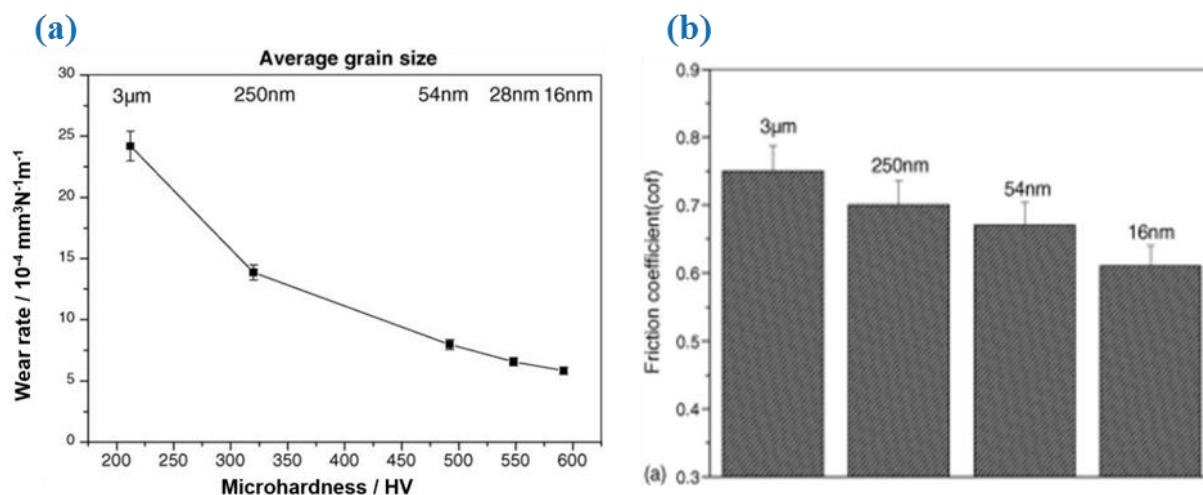


Figure I.17: Wear rate vs. hardness (a) and friction coefficient vs. crystallites size of Ni electrodeposits (b).

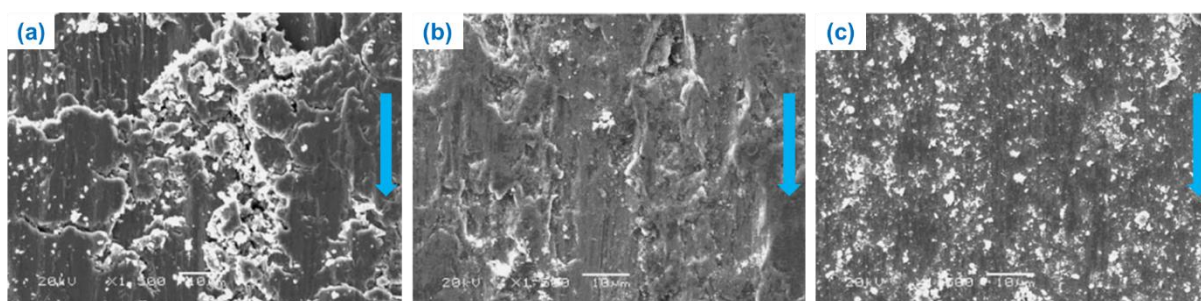


Figure I.18: Worn surface morphology of electrodeposited Ni coatings with crystallites size of (a) 3 μ m, (b) 250 nm and (c) 16 nm.

I.5.6 Properties of electrodeposited nanocrystalline Ni-Co coatings

I.5.6.a) Microstructural properties

The morphology of nanocrystalline Ni-Co coatings can be affected essentially by their cobalt content, which can be controlled by the conditions of electrodeposition such as the bath composition [42,111], the current density [35,119], pH [36,120], agitation [108,121] and the bath temperature [122,123], etc. Figure I.19 depicts the effect of some electrodeposition parameters and experimental conditions on the Co content of Ni-Co alloy coatings. While, Figure I.20 [40] and Figure I.21 [124] illustrate the effect of Co content on the morphology of microcrystalline and nanocrystalline Ni-Co electrodeposits, respectively. Remarkably, the morphology of Ni-Co coatings exhibits almost the same behavior in both scales with the increase of Co content. Where, the morphology change gradually from polyhedral crystallites like those of pure Ni electrodeposits to a branched structure similar to that of pure Co coatings. Regarding nanocrystalline Ni-Co alloy coatings, as can be seen in Figure I.21, the Ni-rich ones (≥ 39 wt.% Co) exhibit generally polyhedral crystallites of nanometric dimensions. As the Co

content in the coatings increases from about 7 to 66 wt.%, the crystallite size gradually decreases and the structure takes the form of smaller, less compact spherical clusters. Whereas, Co-rich nanocrystalline Ni-Co coatings (≥ 80 wt.% Co) exhibiting a branched structure (fiber-like structure) with acicular crystallites of about $1\mu\text{m}$ in length.

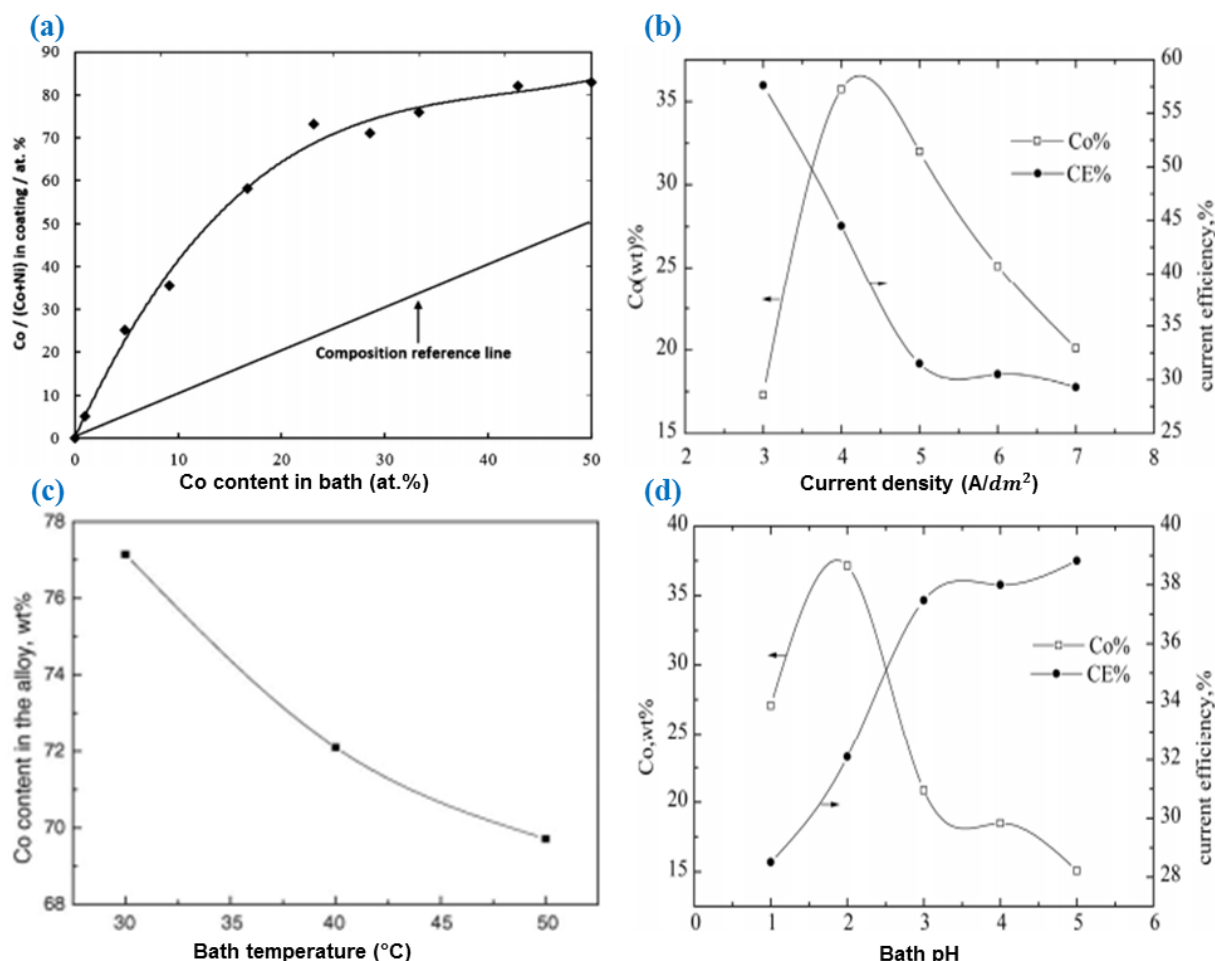


Figure I.19: The effect of some electrodeposition parameters on the Co content of Ni-Co coatings: (a) bath Co content [39], (b) current density [125], (c) temperature [126] and (d) pH [125].

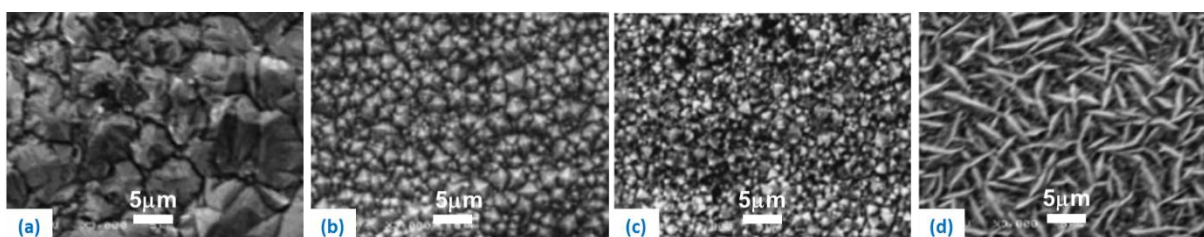


Figure I.20: SEM morphologies of microcrystalline Ni-Co coatings with different Co content: (a) 0 wt.%, (b) 7wt.%, (c) 66 wt.% and (d) 81 wt.% [40].

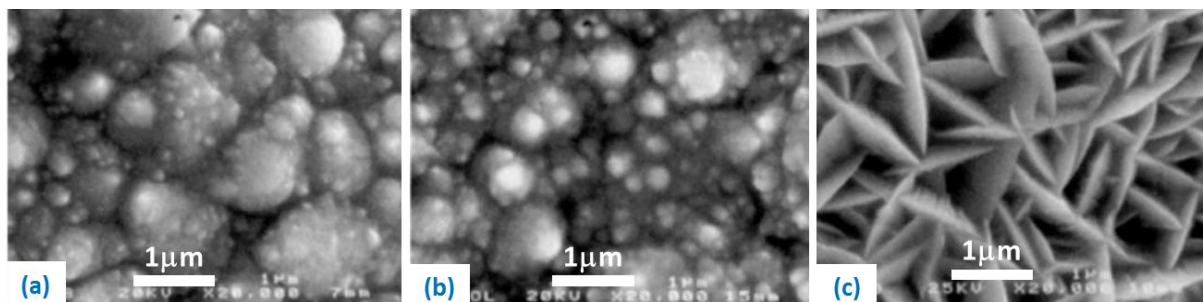


Figure I.21: SEM morphologies of nanocrystalline Ni-Co electrodeposits with (a) 14 wt.%, (b) 39 wt.% and (c) 84 wt.% Co content [124].

The crystal structure of Ni-Co electrodeposits also changes gradually from α (fcc) to ϵ (hcp) phase with increasing Co content [29,127,128]. Figure I.22 shows two examples about the XRD patterns of Ni-Co coatings with different Co content, taken from the study of Ma et al [29] (a) and Lupi et al [129] (b). It can be seen that, Ni and Ni-Co rich coatings (65 wt.% Co) exhibit a single-phase α (fcc) crystal structure. Ni-Co coatings with Co content between 65 and 78 wt.% contain a mixture of α (fcc) and ϵ (hcp) phases, while Co-rich Ni-Co coatings (≥ 78 wt.% Co) are characterized by a single-phase ϵ (hcp) structure similar to that of pure Co coatings. These changes in crystal structure are in good agreement with the changes in the phase structure depicted in the binary phase diagram of Ni-Co alloys at ambient temperature (Figure I.10). On the other hand, the nanocrystalline Ni-Co alloy electrodeposits in the major cases exhibit two preferred crystallographic orientations (111) and (200) [30,33,42,130,131], however others orientations can be more dominants in some cases [132,133]. These differences are generally due to the different baths and electrodeposition parameters used.

I.5.6.b) Mechanical properties

The microhardness of nanocrystalline Ni-Co electrodeposits is strongly influenced by the electrodeposition conditions such as the bath Co content [29,42], the current density [35,119], the bath temperature [33,43], the bath pH [43], etc. The latter parameters mainly influence the Co content and the crystallites size of Ni-Co coatings. Figure I.23 illustrates the effect of Co content and crystallites size on the microhardness of Ni-Co coatings. It can be observed that the microhardness of Ni-Co initially increases with increasing Co content from 0 to about 49 wt%, but gradually decreases with further increase of Co content in the coating. A similar evolution of microhardness has been reported by Srivastava et al [102] and Golodnitsky et al [124]. This decrease in hardness when the Co content exceeds 50 wt.% coincided with the formation of a branched (fiber-like) structure and the transformation of the crystal structure from fcc to hcp [29,40,102]. Furthermore, it can be observed that the evolution of the microhardness of Ni-Co

coatings with the variation of grain size follows a quasi Hall-Petch gradient (Figure I.23 (b)), which is the same finding reported by [108]. However, an anomalously deviation from Hall-Petch gradient were reported by Ma et al [134] for the electrodeposited nanocrystalline Ni-Co coating with grain size below 15 nm, which was attributed to the loose microstructures and the high porosity of such coatings.

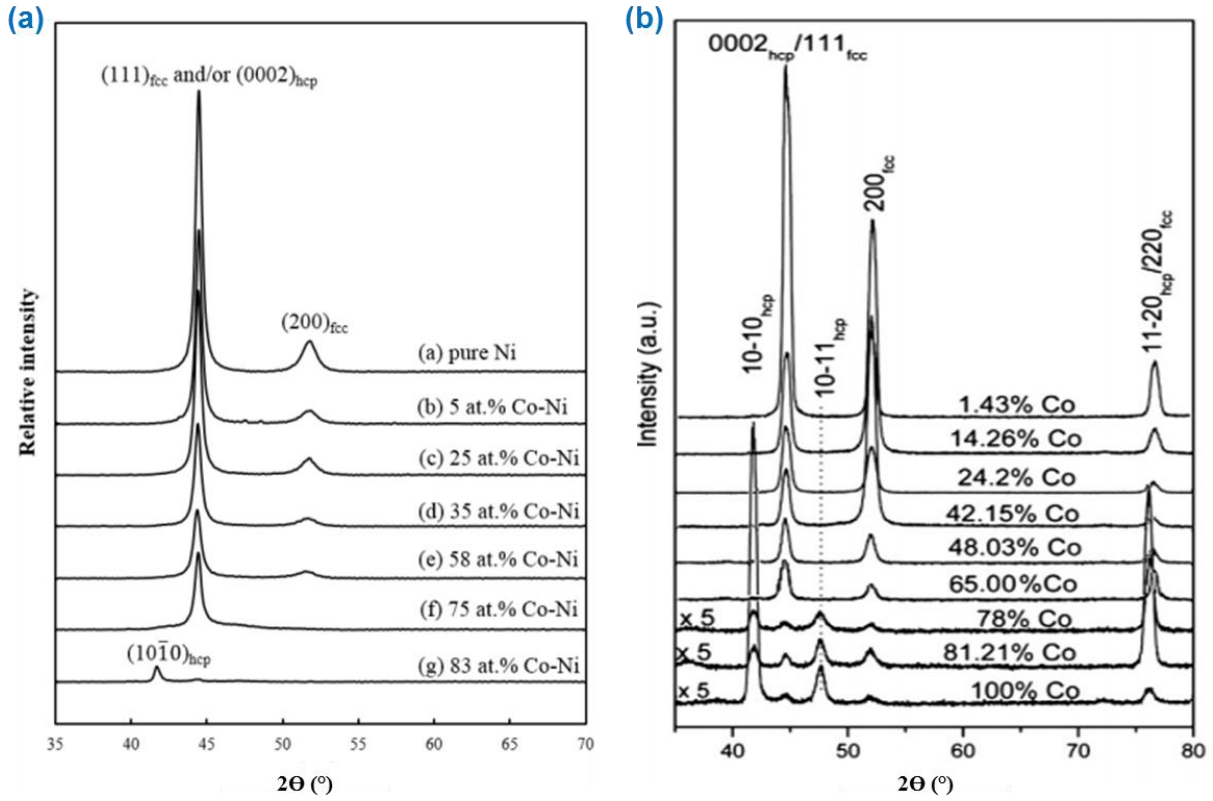


Figure I.22: XRD patterns of Ni-Co electrodeposits with different Co contents.

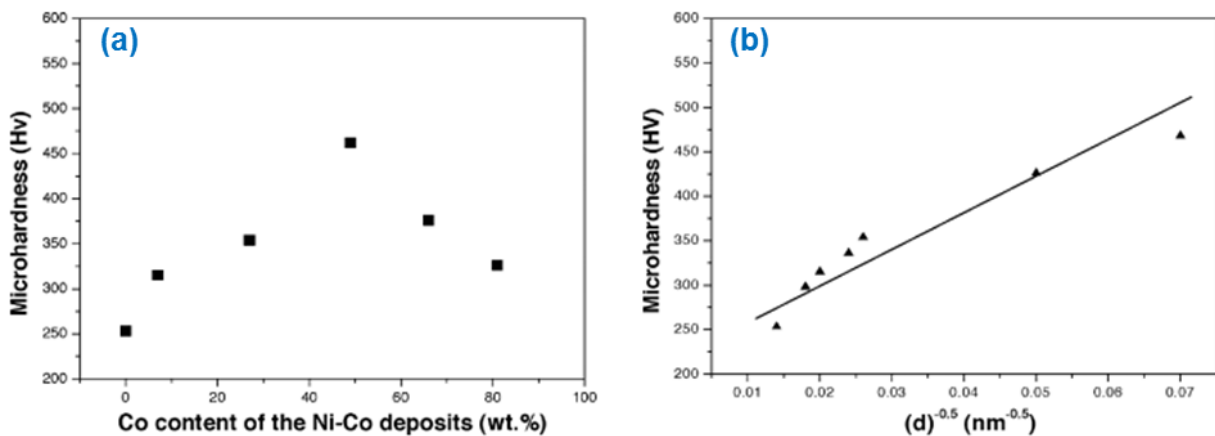


Figure I.23: Microhardness of Ni-Co coatings as function of Co content (a) and $d^{-0.5}$ (b).

I.5.6.c) Tribological properties

According to the study of Ma et al [79], the Ni-Co coatings showed tribological and anti-wear performances comparable to those of hard chromium. Nevertheless, the tribological behavior of Ni-Co coatings depends on their Co content [39,40]. Wang et al [40] revealed that Co-rich Ni-Co coatings (≥ 50 wt.% Co) were characterized by better tribological properties than Ni and Ni-rich Ni-Co coatings (< 50 wt.% Ni). As can be seen in Figure I.24 (a), Ni and Ni-rich coatings with α (fcc) crystal structure show almost the same friction coefficient. The friction coefficient of Ni-Co coatings starts to decrease significantly when the Co content exceeds 50 wt.% and experiences a dramatic reduction when the Co content is above 80 wt.%. These changes in the friction coefficient of the coatings with increasing Co content coincide well with the phase transformations from α (fcc) to α (fcc) + ϵ (hcp) and subsequently ϵ (hcp). At the same time, it can be seen that the wear rate of Ni-Co coatings (Figure I.24 (b)) decreases with increasing Co content. The decrease in wear rate with increasing Co content from 0 to 49 wt.% was attributed to the increase in hardness from 253 to 462 HV, which is consistent with Archard's law (eq.II.2) that relates wear rate proportionally to the inverse microhardness of materials. However, despite the hardness decrease, a dramatic decrease in wear rate is observed when the Co content is greater than 50 wt.% what contradicts the Archard's law. Thus, this inverse Archard's law can be thought to be attributed to the hcp crystal structure of Co-rich coatings. Where some studies [135,136] have reported that hcp structured Co-based alloys (Co-Re, Co-Mo and Co-Cr) exhibit superior tribological performance compared to their fcc structured counterparts.

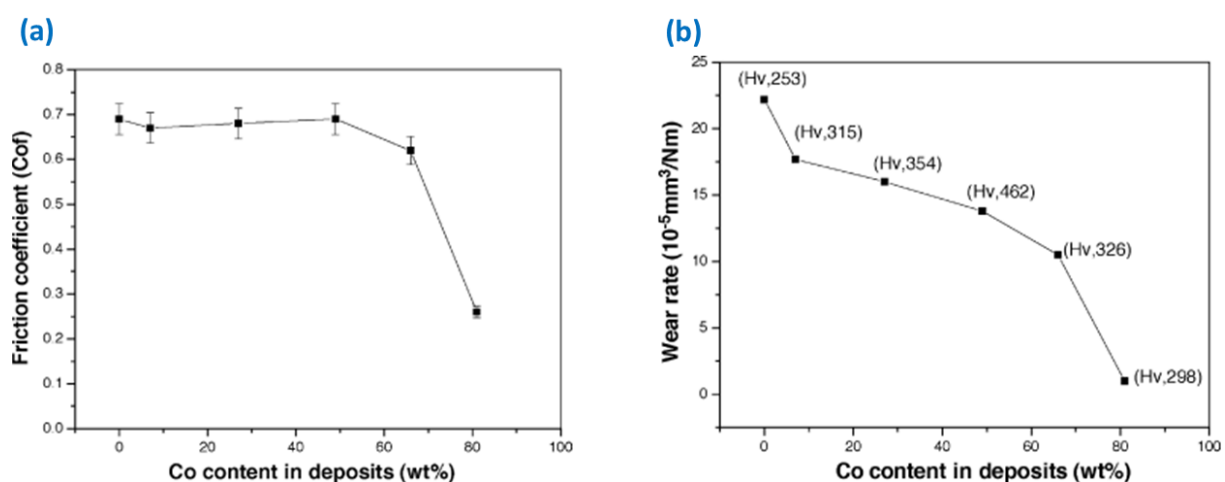


Figure I.24: Friction coefficient (a) and wear rate (b) vs. Co content of Ni-Co coatings [40].

Furthermore, SEM observations of the worn surface morphologies (Figure I.25 (a)-(b)) revealed that the pure Ni and Ni-rich Ni-Co (27 wt.%) coatings with fcc structure exhibited an adhesive

wear mechanism with significant plastic deformation in the friction direction. Conversely, the hcp-structured Co-rich coating (81 wt.%) showed a smooth wear pattern with smaller damaged regions and very slight adhesions; almost the same observations regarding the effect of Co content on the wear behavior of Ni-Co electrodeposits were reported by Ma et al [39].

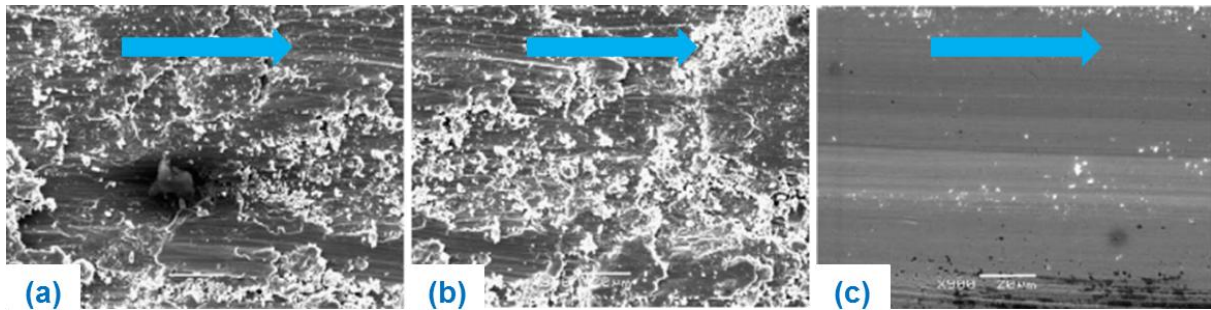


Figure I.25: Wear tracks of pure Ni (a) and Ni-Co alloy electrodeposits with 27 wt.% Co (b) and 81 wt.% Co (c) [40].

Chapter II:

Experimental methods

CHAPTER II: EXPERIMENTAL METHODS

II.1 INTRODUCTION

In this chapter, we focus on the experimental means used during our work. It is divided into two parts that present successively the tools used during the various stages of electrodeposition and analysis of coatings. The first part gives an overview of the materials and equipment used during the electrodeposition process, such as the composition of different substrates and their specific surface preparations, the composition of the electrolytes. The experimental setup is also detailed, as well as the plating conditions. A second part is dedicated to the description of the different characterization techniques used to analyze the composition as well as the electrochemical, microstructural, morphological, mechanical and tribological properties of the substrates and the elaborated coatings.

II.2 COATINGS ELECTRODEPOSITION

II.2.1 Materials and chemicals

II.2.1.a) Type and chemical composition of the used substrates

Three metallic materials of different compositions are used in this work as substrates for the electroplating of the various coatings. The chemical compositions of the three metals used as substrates are summarized in [Table II.1](#).

Table II.1: The composition of the different metals used as substrates.

Substrates	Chemical composition					
StW24 Steel	C	Si	P	S	Mn	Fe
	0.08	0.0435	0.0143	0.0146	0.354	99.5
Copper	Si		P	S		Cu
	0.251		0.0291	0.0198		99.7
Brass	Si	Fe	Pb	Zn	Cu	
	0.0589	0.121	1.57	38.5	59.7	

II.2.1.b) Substrates preparation

- **Cutting:** StW24 Steel, copper and brass discs with a diameter of 20 mm are cut by the use of the STRUERS ACCUTOM-100 laboratory chainsaw to obtain discs of identical thickness (4 mm).

- **Resin-embedding:** The steel, copper and brass discs (substrates) obtained after the cutting operation are hot-embedded with a phenolic resin using the STRUERS CITOPRESS-30 to delimit a surface of 3.14 cm². The embedded substrates are shown in [Figure II.1](#).

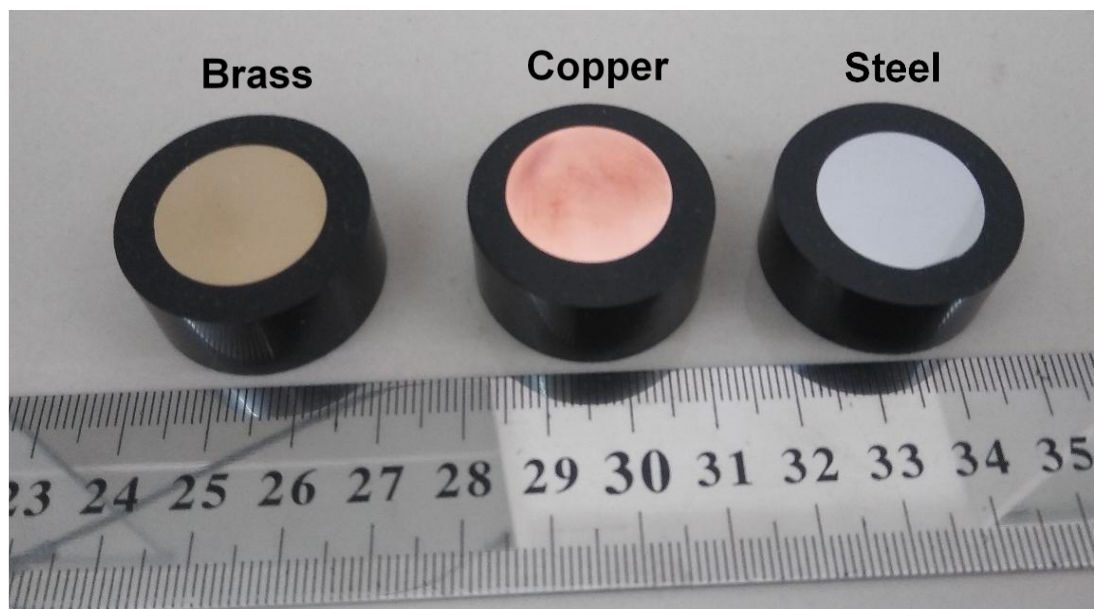


Figure II.1: The geometry of the resin-embedded discs used as substrates.

- **Mechanical polishing:** After the resin-embedding, the substrates are mechanically polished with STRUERS TegraPol-35 mechanical polisher using Si-C abrasive papers (220, 500, 800, 1200, 2400 and 4000 grade).
- **Chemical degreasing:** After the polishing operation, the polished substrates are chemically degreased in a special commercial solution of pH= 11 (Fisher scientific) using an ultrasonic bath.
- **Electrical connecting:** To ensure electrical contact with the substrate, the resin-embedded substrates are then pierced laterally and soldered with copper electrical contact wires as shown in [Figure II.2](#).

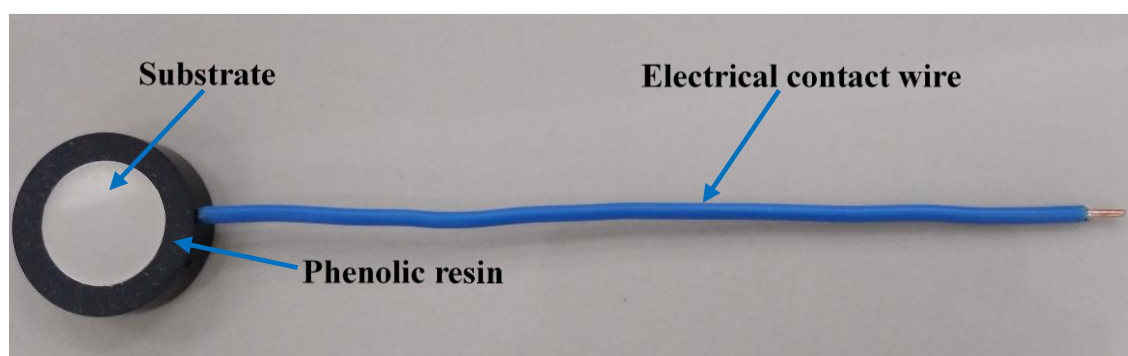


Figure II.2: The shape of the substrate prepared as cathode.

- **Chemical Polishing:** Finally, the substrates are activated in HCl acid solution (10% per volume) for 20s, rinsed with distilled water and immersed directly in the electroplating bath.

II.2.2 Composition of the electroplating bath

In this work, the different coatings are electrodeposited from a modified Watts bath. The names, the chemical formulations, the roles and the marks of all products used in this study for the formation of the various electroplating baths are summarized in [Table II.2](#).

Table II.2: The composition of the used electroplating baths.

Product name	Chemical formulation	Role	Mark and Purity
Nickel sulfate hexahydrate	$\text{NiSO}_4 \cdot 6\text{H}_2\text{O}$	As first source of metallic nickel	Sigma-Aldrich (99%)
Nickel chloride hexahydrate	$\text{NiCl}_2 \cdot 6\text{H}_2\text{O}$	As second source of metallic nickel and to improve the conductivity in the bath	Sigma-Aldrich ($\geq 98\%$)
Cobalt sulfate heptahydrate	$\text{CoSO}_4 \cdot 7\text{H}_2\text{O}$	As source of metallic cobalt	Sigma-Aldrich Reagent Plus [®] ($\geq 99\%$)
Boric Acid	H_3BO_3	As a buffering agent to fix the solution pH and to limit the alkalization and the formation of metal hydroxides near the substrate [137]	Sigma-Aldrich ($\geq 99.5\%$)
Saccharin	$\text{C}_7\text{H}_5\text{NO}_3\text{S}$	As grain refiner and stress reliever agent [79]	Sigma-Aldrich ($\geq 99\%$)
Sodium dodecylsulfate (SDS)	$\text{CH}_3(\text{CH}_2)_{11}\text{OSO}_3\text{Na}$	As surfactant [138]	Sigma-Aldrich $\geq 98.5\%$
2-butyne-1,4-diol (BD)	$\text{HOCH}_2\text{C}\equiv\text{CCH}_2\text{OH}$	As grain refiner and stress reliever agent [31]	Sigma-Aldrich (99%)

II.2.3 Experimental parameters and setup

II.2.3.a) Experimental parameters

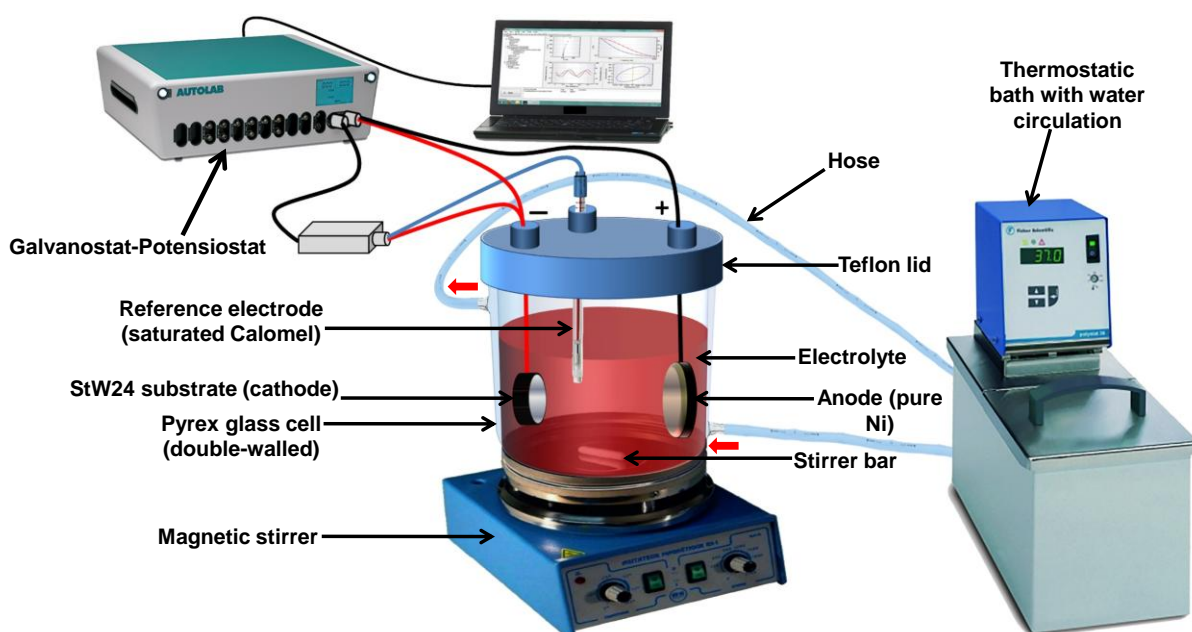
The different coatings are electrodeposited in this study by the use of direct current electroplating process (DC). The experimental parameters used in the electrodeposition of the different coatings are summarized in [Table II.3](#).

Table II.3: The experimental conditions used for the elaboration of the different coatings.

Parameters	Values
Current density	3-4 A/dm ²
Temperatures	25-85°C
Electrolyte pH	3-4
Agitation	Magnetic stirrer with a speed of 300 rpm
Electrodeposition duration	30-120 min

II.2.3.b) Experimental set-up

The electrodeposition experimental set-up used in this work is shown in Figure II.3. A double-walled pyrex glass cell with a total volume of 150ml is used as a container for the electrolyte solution. Previously prepared steel, copper and brass substrates are used as cathodes. A pure nickel disc with high purity (99.99%) is used as a soluble anode. All the potential values are measured against a Calomel reference electrode saturated with potassium chloride (SCE). The bath temperature is controlled by the use of a thermostatic bath with water circulation (Fisher scientific-Polystat 36). During all the electroplating process, the solution is continuously stirred by a magnetic stirrer bar (6mm diameter × 30mm length) at a speed of 300rpm. The current intensity and the potential in the electrochemical cell are supplied and controlled by the use of 302N Autolab galvanostat-potentiostat piloted by a computer using Nova 1.7 software.

**Figure II.3:** The experimental set-up used for the electrodeposition of different coatings.

II.3 COATINGS CHARACTERISATIONS

II.3.1 Chronopotentiometry

Chronopotentiometry (CP) is one of the simplest electrochemical methods. It consists in carrying out constant current electrolysis at the electrode and monitoring the variation of the potential as a function of time. The variation in potential is related to the change in concentration of the electroactive species at the electrode. In this work, all the deposits are made by imposed current mode. The intensity of the current flowing between the working electrode (substrate) and the anode (nickel disc) is kept constant by 302N Autolab galvanostat-potentiostat (see Figure II.3). The variations in the potential of the working electrode are recorded as a function of time over the entire duration of the deposition. Figure II.4 (a) shows the most used regimes in the present work (3 and 4 A/dm²), while Figure II.4 (b) presents some examples on chronopotentiometric curves obtained during the electrodeposition of Ni-Co coating at different bath temperatures.

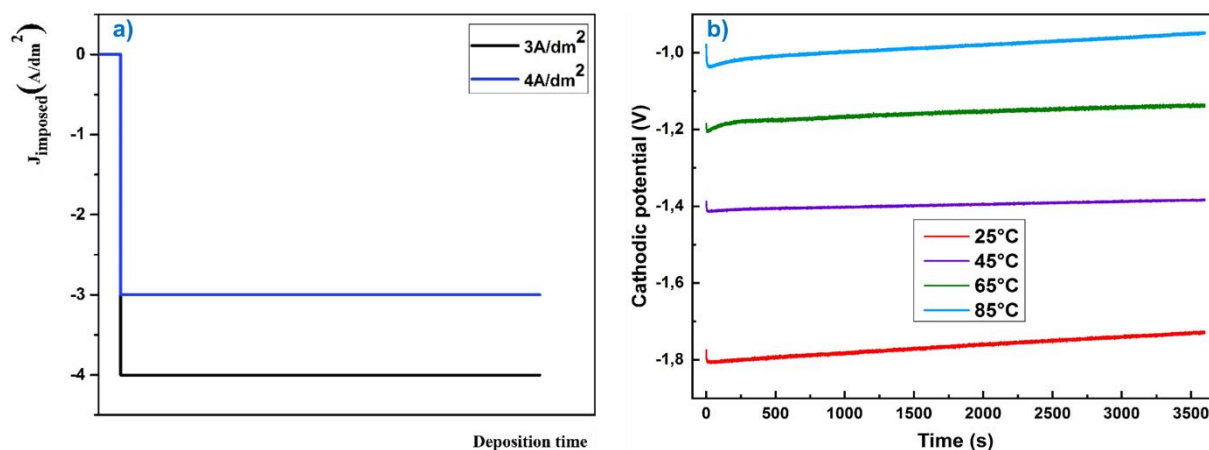


Figure II.4: Examples on the used current regimes (a) and on the obtained curves during Ni-Co electrodeposition (b).

II.3.2 Wavelength Dispersive X-ray Fluorescence Spectrometry (WD-XRF)

X-ray fluorescence spectrometry is a global elemental analysis technique for identifying and determining most of the chemical elements that constitute a sample. This technique can be used for a wide variety of materials: minerals, ceramics, cements, metals, oils, water, glass, etc., in solid or liquid form. It allows the analysis of all chemical elements from Beryllium (Be) to Uranium (U) in concentration ranges from a few ppm to 100%, with precise and reproducible results. In X-ray fluorescence spectrometry, the sources of X-rays usually used are X-ray tubes or radioactive sources (especially for portable devices but which are tending to disappear with the development of mini-tubes). Because of their high energy, the X-photons emitted by the

tube have the capacity to extract electrons located on the layers close to the atomic nucleus. The atom then ionized will tend to return to a state of equilibrium, an electron of a more external layer will come to fill the gap left by the electron that has been ejected. This electronic transition is accompanied by a release of energy in the form of an X-photon of energy (Figure II.5 (a) [139]). It is the phenomenon of X-ray fluorescence, which is a secondary emission of X-rays characteristic of the atoms that constitute the sample. The analysis of this secondary X-radiation makes it possible to know the nature of the chemical elements present in a sample as well as their mass concentration.

For the analysis of X-ray fluorescence radiation emitted by the sample, there are two main types of equipment: Wavelength Dispersive X-ray Fluorescence Spectrometers (WD-XRF) and Energy Dispersive X-ray Fluorescence Spectrometers (ED-XRF). In the present work, the composition of substrate and deposits is determined using Rigaku ZSX Primus IV wavelength dispersive X-Ray fluorescence spectrometer (WD-XRF), equipped with a 3/4 kW sealed X-ray tube and a 48-position auto-sampler, allows the vacuum analysis from Be to U.

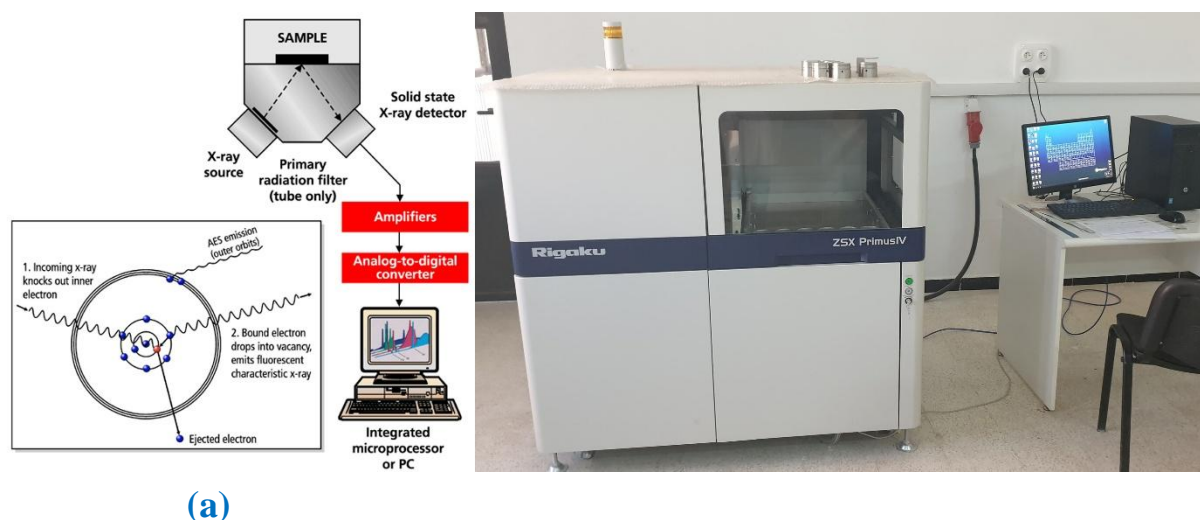


Figure II.5: The principle of X-ray fluorescence spectrometer (a) and the used Rigaku ZSX Primus IV X-Ray fluorescence spectrometer (b).

II.3.3 Metallographic observation

After the specimens preparation processes (embedding, pre-polishing and polishing), we resort to chemical etching. Chemical etching is often applied to differentiate and improve the contrast of existing phases in order to reveal their micro or macrostructure. Two reagents are used in this work for chemical etching, the first reagent is technically known as Nital 3%. It is used for the chemical etching of StW24 steel (the metal used as a substrate in the majority of this work). The second reagent is used for etching of Ni-Co alloy coatings. The composition of the two

chemical reagents used for etching is shown in Table II.4. The duration of the etching is about 15 to 20 seconds at room temperature. Once the effect of the etching is clearly visible on the sample (a small variation in the color of the etched surface), a washing of the surface with a water jet is carried out to stop any reaction. In order to leave no water traces on the surface, the samples are dried with hot air. After chemically etching of the samples, we use optical microscopy to observe the microstructure of different samples. The optical microscope used in the observation is an inverted metallographic microscope type, with a magnification capacity ranges from 25x to 1000x, operating in bright and dark field and equipped with a device for taking photos (HD camera + PC). Figure II.6 provides a photo of the used Axio Observer 1M optical microscope and an example of metallographic observation on StW24 steel used as substrate.

Table II.4: Nature and composition of the different used substrates.

Attacked metal	Etching solution composition per volume	
StW24 steel substrate	Nitric acid (3%)	Ethyl alcohol (97%)
Ni-Co coating	Nitric acid (20%)	Chlorohydric acid (80%)

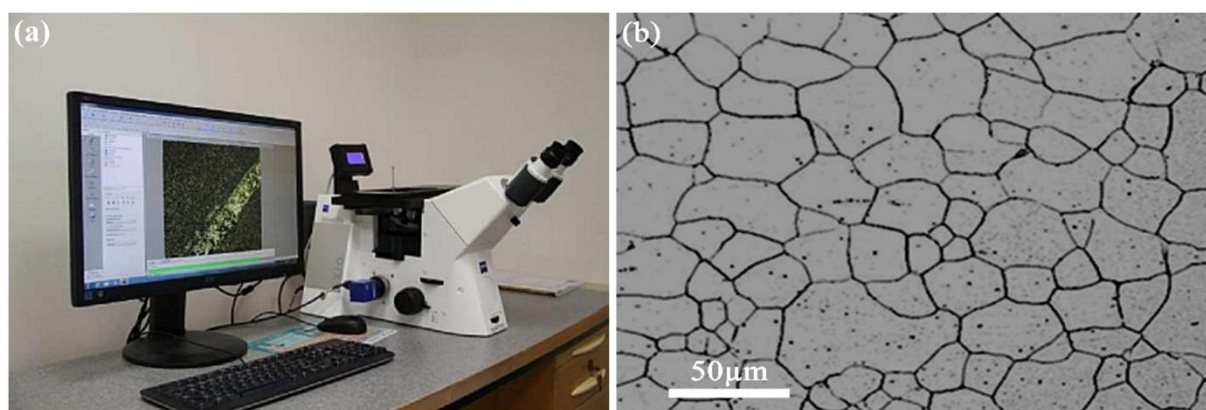


Figure II.6: The used Axio metallographic microscope (a) and an example of metallographic observation on StW24 steel used as substrate (b).

II.3.4 X-ray diffraction (XRD)

X-ray diffraction is a technique whose use ranges from the simple identification of crystals to the determination of their atomic structure. It can provide very valuable crystallographic information (atoms arrangement, lattice parameters, etc.) on a wide variety of materials (metals, polymers, ceramics and composites). It makes possible to identify the composition of the phases in presence as well as their evolution and transformations, the quantitative portions of the phases

in some cases (within the precision limits of the technique), the size of the crystallites (grains) and their orientation on the surface layers of the material (about 10 μm), as well as the macro/micro stresses. The X-ray diffraction technique is based on the fact that a crystal lattice consists of a stack of families of parallel and equidistant reticular planes. The incident x-ray beam is partially reflected from the foreground. The unreflected beam "falls" onto the second plane to be partially reflected again and so on and so forth. In order for the waves scattered by the different planes to be in phase and for the total intensity of the scattered wave to be significant, the Bragg's law [140] in relation (eq.II.1) must be verified:

$$n\lambda = 2d \sin\theta \quad (\text{II.1})$$

Where d is the distance of the reticular planes, λ is the wavelength and n the order of reflection. This relationship shows that it is sufficient to measure the Bragg angles θ to determine the dimensions and shape of the crystal's elementary lattice (Figure II.7 (a)). The amplitudes of the reflected waves are used to determine the atomic structure of the pattern. The operating principle of the x-ray diffractometer is shown in Figure II.7 (b) [141].

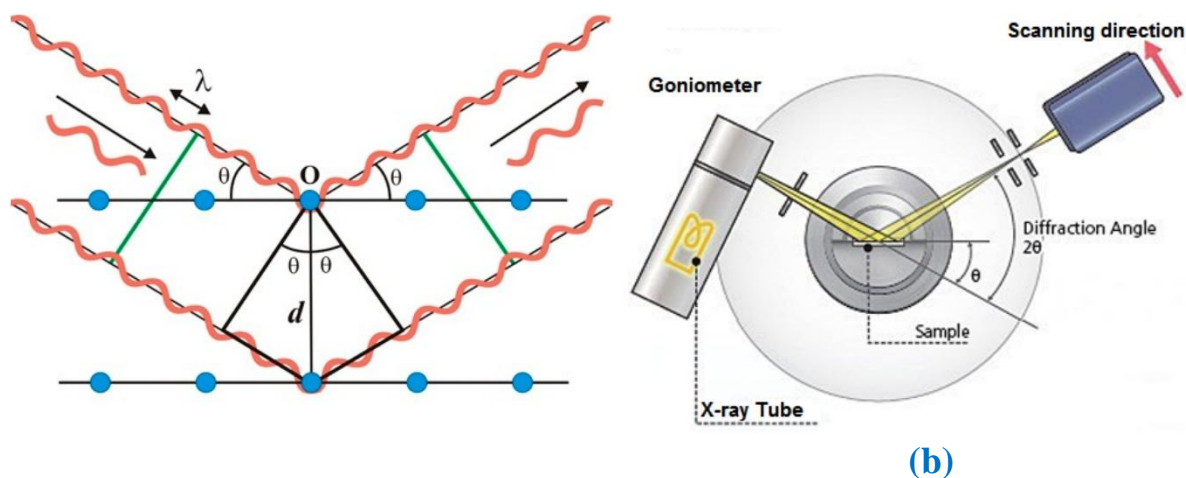


Figure II.7: Schematic representation of the Bragg equation (a) and the operating principle of the x-ray diffractometer (b).

In the present work, the X-ray diffraction was performed with a Philips X'Pert Pro MPD type apparatus (see Figure II.8) equipped with a copper anti cathode ($\lambda = 1.54 \text{ \AA}$). This diffractometer is based on a Bragg Brentano mounting for which the sample-detector distance is constant whatever the angle θ between the incident beam and the diffracting planes. The identification of the phases was done by comparing the X-ray diffraction patterns with the international

database (ICDD: International Centre for Diffraction Data) using HighScore Plus software (PANalytical X'Pert).



Figure II.8: The used Philips X'Pert X-ray diffractometer.

II.3.5 Scanning electron microscopy (SEM) and Microanalysis X

SEM allows to study the surface morphology of practically all solid materials, at scales ranging from that of the magnifying glass (x10) to that of the transmission electron microscope (x500,000 or more). The operation principle of scanning electron microscopy is based on an electron beam (electron sonde) scanning the surface of the sample to be analyzed. [Figure II.9 \(a\) \[142\]](#) illustrates the principle scheme of SEM, where the interaction between the electron beam and the sample generates secondary low-energy electrons that are accelerated towards a secondary electron detector that amplifies the signal. At each point of impact, there is an electrical signal. The intensity of this electrical signal depends both on the nature of the sample at the point of impact which determines the secondary electron yield and on the topography of the sample at the point under consideration. It is thus possible, by scanning the beam over the sample to obtain a cartography of the scanned area. For conventional SEM, the analyzed material must be conductive in order to avoid charging phenomena due to electrons, so the metallization must be carried out for example with carbon or gold for the insulations. SEM at controlled pressure (known as environmental or low vacuum) allows observation in a vacuum of up to 30 mbar, thus making it possible to examine wet or greasy samples and insulators without prior metallization (ceramics, polymers and corroded metals), or even in the presence of liquid. The association of the microscope with a microanalyzer allows the detection of

continuous background characteristic X-rays ($1\mu\text{m}$) to establish the X-mapping of the analyzed sample: this is the EDS (X Energy Dispersive Spectroscopy) mode. This mode establishes a cartography of the distribution of the elements present over a chosen range. As many X-cartographies are edited as there are elements to analyze.

In the present work, the morphology and the microstructure of the elaborated coatings were observed with a high-resolution scanning electron microscope (SEM) JEOL JSM-7000 F (see Figure II.9 (b)). It allows to work with an acceleration voltage ranging from 0.1 to 30 kV and at an adequate resolution (1 nm to 15 kV) discriminating the main structural elements (less than 500 nm). The instrument is equipped with an Oxford Instruments X-ray Energy Dispersion Analyzer (EDS), allowing the analysis and the identification of the chemical/elemental composition of each phase within the material from a sub-micron volume. Different EDS analysis techniques are used in this study to determine the elements present in the elaborated coatings, the wear tracks and in the wear debris such as: spot analyses in judiciously chosen areas, concentration profiles along the wear tracks, elements distribution cartographies and spectral maps.

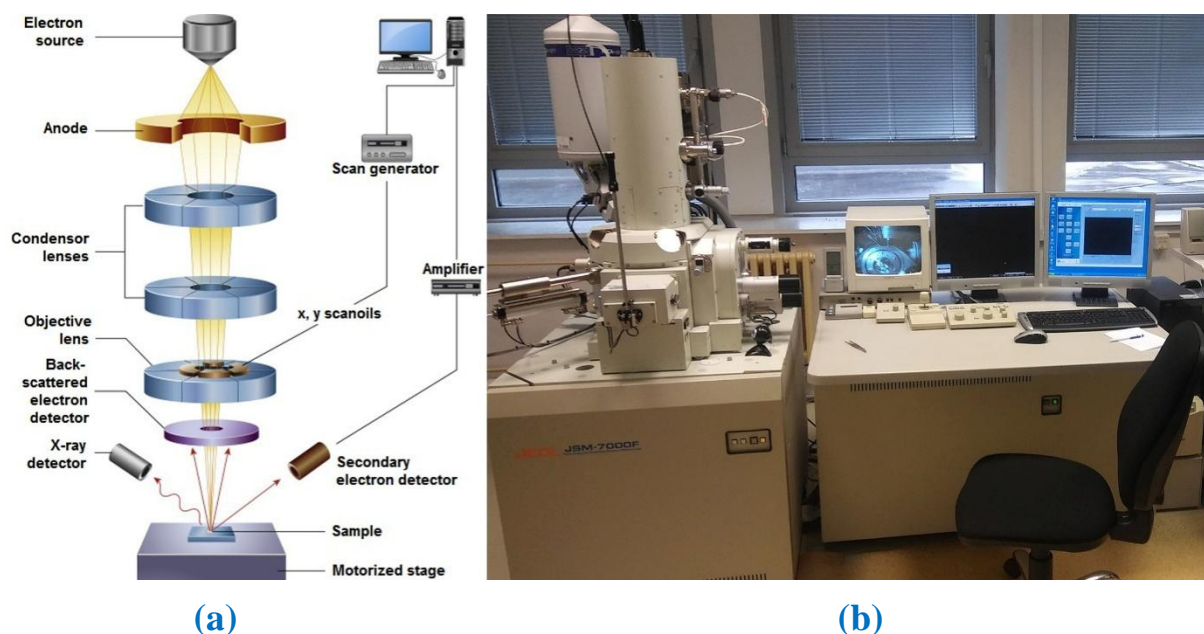


Figure II.9: The principle scheme of scanning electron microscope (a) and the used JEOL JSM-7000 F scanning electron microscope (b).

II.3.6 Profilometry

The profilometer is a high-precision instrument used to analyze topography and surface roughness. The resolution of this instrument is lower than that of the AFM, but the analysed surfaces can have a high relief (up to 1.5 mm). To perform the measurement, a stylus gently

scans the surface while the vertical deflection is measured continuously. This data is used to generate 2D or 3D profiles of the sample topography.



Figure II.10: The principle of sensor contact profilometer (a) and the used AlphaStep D-500 Stylus Profiler (b).

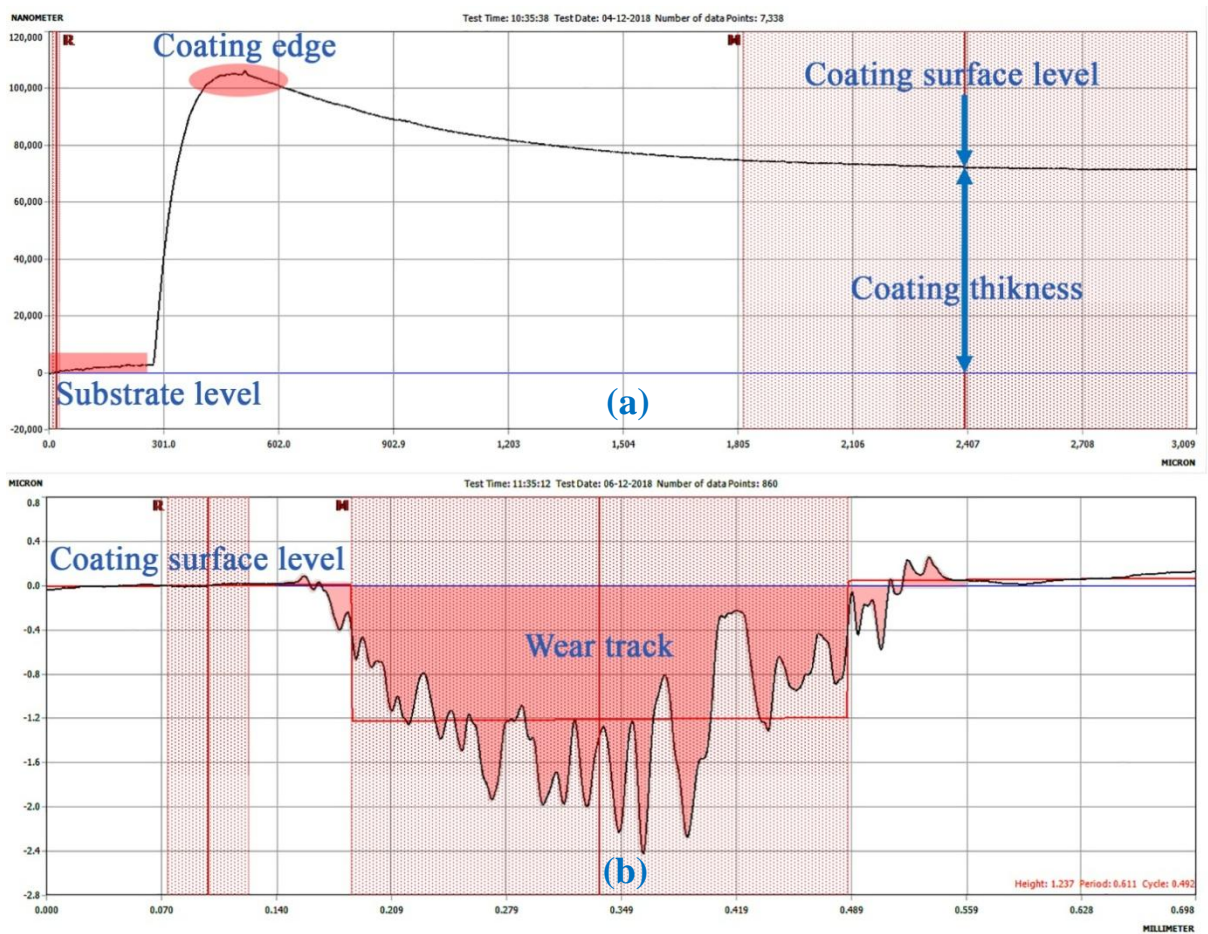


Figure II.11: An example on the measurement of the coating thickness (a) and the wear track profile (b).

In the present work, the acquisition of surface profiles and roughness, coating thicknesses and wear grooves was carried out with a high-sensitivity computerized AlphaStep D-500 Stylus Profiler (KLA-TENCOR) (see [Figure II.10](#)) equipped by a stylus with a radius of 2 μm . It is capable of precisely measuring step heights ranging from less than 10 angstroms to 1.2 millimeters. An example of how to measure the coating thickness and the wear track profile is shown in [Figure II.11](#).

II.3.7 Confocal Microscopy

Confocal microscopy is a non-destructive optical technique for obtaining optical sections not only in the (X,Y) plane but also in a (X,Z) plane parallel to the optical axis, which can be reconstructed in three dimensions. These "virtual" optical sections do not affect the entire sample as opposed to the physical sections required in electron microscopy. The latest developments in confocal fluorescent microscopy make it possible to observe remarkable 3D structures using marking means based on the use of fluorescent products. A CCD sensor thus gives an XZ image. Only one scan is then necessary (in Y) to make the 3D measurement. The principle of confocal microscopy is illustrated in [Figure II.12 \(a\)](#) [143].

2D and 3D microscopic observations of the surface topography and wear grooves, the measurement of roughness and total worn volume were carried out in this work using a Leica DCM8 confocal microscope ([Figure II.12 \(b\)](#)).

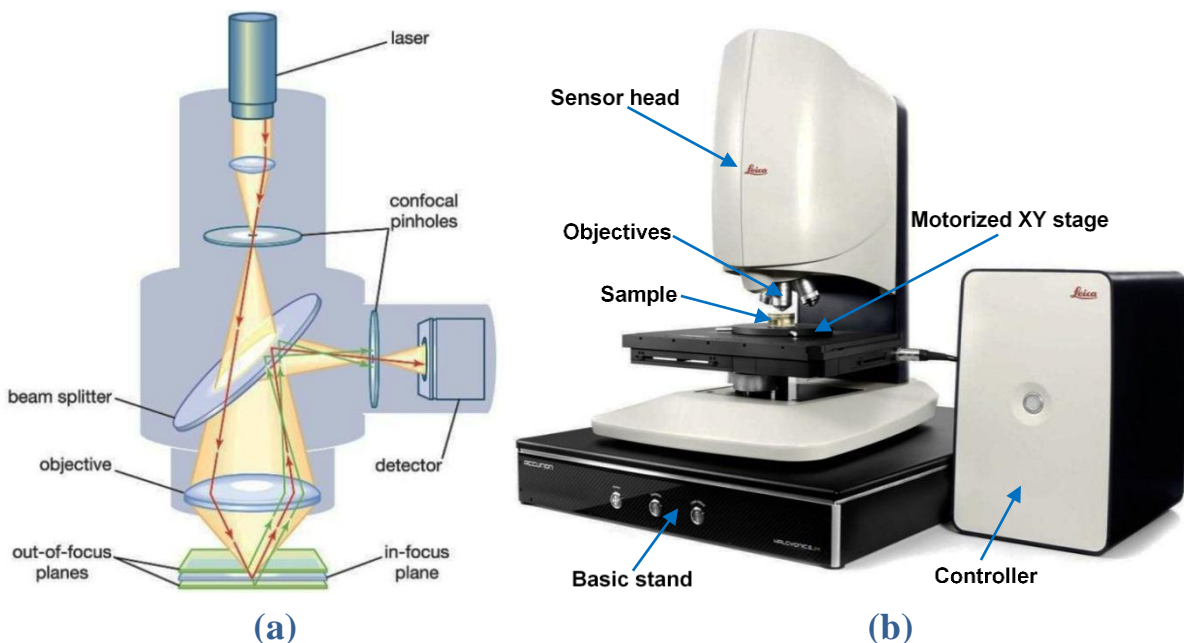


Figure II.12: Schematic diagram of the principle of confocal laser scanning microscopy (a) and the used Leica DCM8 confocal microscope (b).

II.3.8 Atomic Force Microscopy

Atomic force microscopy (AFM) is a technique of choice for the detailed analysis of surface morphology, and the observation of eventual pores or coating defects. Contrary to the scanning electron microscope, it can be used with non-conductive samples without the need to metallize the surface. This technique is based on the detection of variations in force between a very small probe and a surface. A point placed at the extremity of a flexible lever, called a micro-lever (or cantilever) scans the surface. The forces between the point and the surface cause deflections of the micro-lever, which are detected by a laser optical system. The sample under study is mounted on a piezoelectric tube that allows movement in the three spatial directions. As the interaction force varies from point to point, there are variations in the deflection of the micro-lever. A retroaction loop maintains the position of the micro-lever constant by acting on the piezoelectric tube whose voltage variations are used to construct the images (Figure II.13 (a) [144]).

The analysis of the surface morphology was carried out in the present work with a MFP-3D Classic AFM (Asylum Research, see Figure II.13 (b)) equipped with AC240TS cantilevers, which are manufactured by Olympus. The AC240TS has a spring constant of $\sim 2\text{N/m}$ and a resonant frequency of $\sim 70\text{ kHz}$, with very small bending radii ($\sim 2\text{ nm}$) in intermittent contact mode (tapping mode) in order to detect eventual small pores in the coating. In this mode, the point is driven to oscillate at a frequency close to its resonant frequency with a large vibration amplitude. The point hits the surface periodically changing from an attractive regime (Van der Waals) to a repulsive regime (due to the covering of electronic clouds).

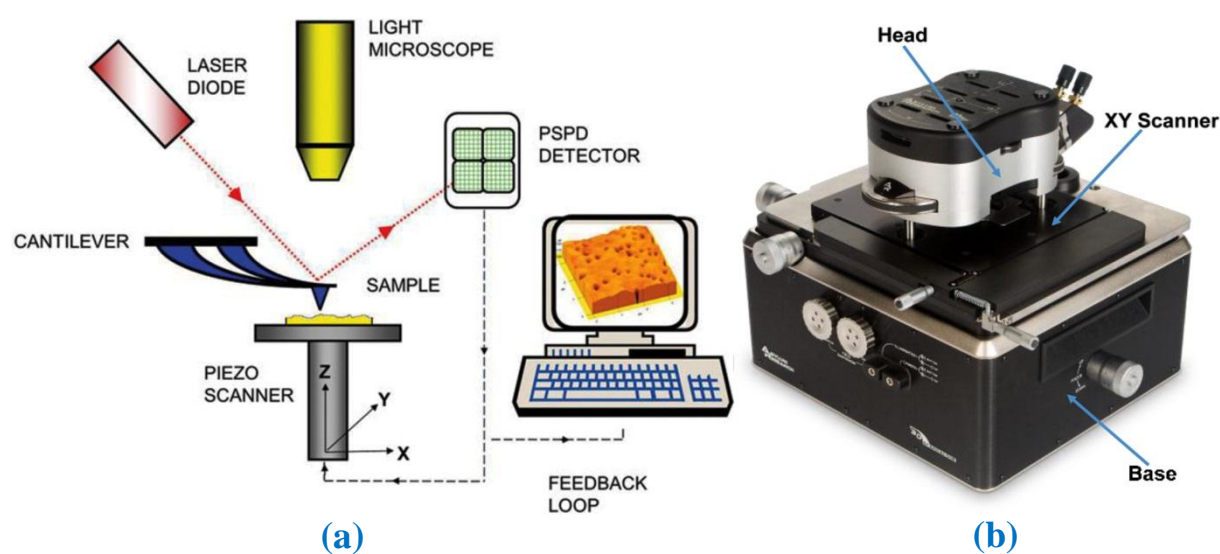


Figure II.13: A schematic representation of the AFM instrument (a) and the used MFP-3D atomic force microscope (b).

II.3.9 Micro and Nano indentation

The determination of the mechanical characteristics, hardness and elastic modulus, was carried out for each sample by means of micro and nanoindentation tests.

II.3.9.a) Micro-indentation

The general principle of the indentation test is to apply an indenter to the surface of the material to be tested. Under the effect of a load, the indenter sinks into the material causing elastic and plastic deformations. The imprint size is related to the applied force. In fact, the greater the force, the larger the size of the residual imprint. The general relationship of hardness is [145]:

$$H = \frac{P}{A} \quad (\text{II.2})$$

Where P = the applied load and A = the representative surface of the imprint.

The micro-indentation test has greatly extended the capabilities of the indentation test because it allows very low forces to be applied and hardness measurements to be taken on thin layers and coatings of at least ten microns in thickness. According to the geometrical shape of the indenter we can distinguish: Vickers micro-hardness (HV), Brinell micro-hardness (HB) and Rockwell micro-hardness (HRB and HRC). Vickers microhardness is characterized by an indenter in the form of a diamond pyramid with a square base and a vertex angle of 136° between two opposite faces. A load F is applied to the indenter (Figure II.14 (a) [146]). Because the size of the square indentation left by the indenter is usually very small, its diagonals are measured by optical microscopy to calculate the hardness of the sample. The Vickers hardness (HV) is calculated by equation (II.3) [147]:

$$HV = \frac{2F \sin\left(\frac{136^\circ}{2}\right)}{g \cdot D^2} = 1.854 \frac{F}{D^2} \quad (\text{II.3})$$

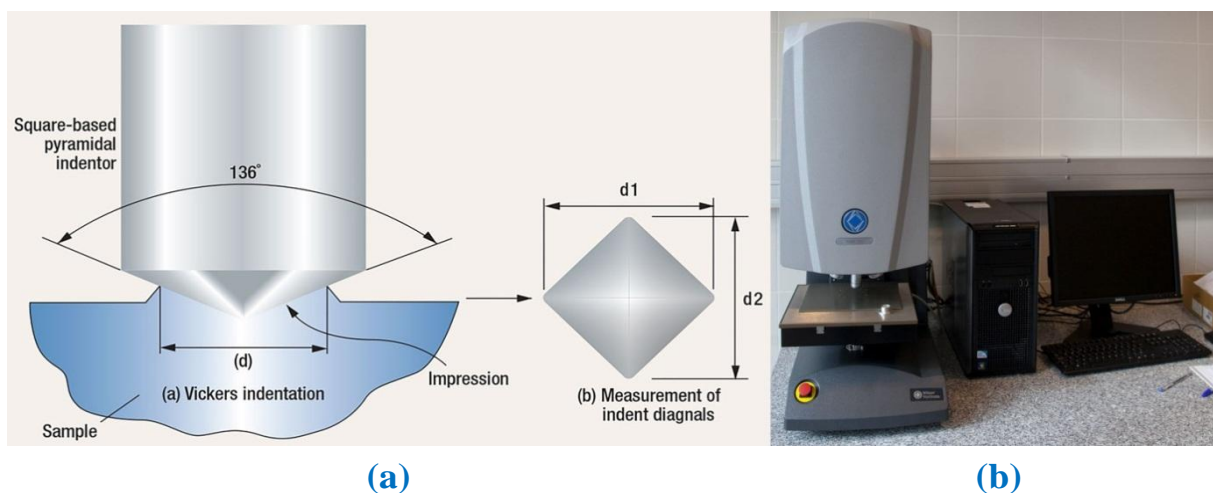


Figure II.14: Principle of Vickers micro-indentation essay (a) and the used Tukon 2500 Vickers micro-durometer (b).

Where F is the applied load (in N) and D is the average of the two diagonals of the imprint in millimetres.

$$D = (d_1 + d_2/2) \quad (\text{II.4})$$

In this work, a branded Vickers micro durometer (BUEHLER, model Tukon 2500, [Figure II.14 \(b\)](#)) is used to qualify the hardness of substrates and elaborated coatings. Different charges are applied and the holding time for each test is 15s.

II.3.9.b) Nano-indentation

Nano-indentation is a technique that is attracting considerable interest in the field of thin films and coatings. During the mechanical characterization of coatings, characteristic values may be distorted as a result of the deformation of the substrate caused by the high load applied to it. In order to avoid this phenomenon, the maximum penetration of the indenter tip must be very small compared to the thickness of the deposit. When using this method, the load applied is of the order of a few tens of micro-newtons (μN) and the penetration depth of the indenter varies from a few tens of nanometers (nm) to a few micrometers (μm). Nano-indentation is used to determine several mechanical properties such as hardness, Young modulus, toughness, adhesion, creep, etc.

The principle of this test consists of driving the indenter tip onto the surface of the deposit. The evolution of the indenter tip penetration under the load applied during loading and unloading makes it possible to determine the elastic and plastic response of the deposit. After this, the charge/discharge curve as a function of depth is determined. This curve is divided into two parts ([Figure II.15](#)). The loading part, which shows the penetration of the indenter up to the maximum penetration (h_{max}). In this part, there is a contribution of elastic and plastic deformations. The second part of the discharge represents the removal of the indenter tip that leads to a residual imprint with a depth (h_f). The real penetration depth of the indenter at maximum load is h_c . The slope of the charge/discharge curve represents the stiffness S of the material. The hardness and the elasticity modulus of the deposit can be determined from the following equations [[145,148](#)]:

$$H = \frac{P_{\text{max}}}{A} \quad (\text{II.5})$$

$$E = \frac{\sqrt{\pi} S}{2 \sqrt{A}} \quad (\text{II.6})$$

$$S = \frac{dP}{dh} \quad (\text{II.7})$$

Where P_{max} is the maximum indentation load in mN, h is the penetration depth of the indenter in nm, A is the area of indentation projection on the coating surface in nm^2 , E is the elasticity modulus in (GPa) and S is the contact stiffness in mN/nm.

To perform the nano-indentation tests we used a TTX NHT Micro-nano indenter "CSM Instrument". This latter is equipped with a Berkovich type indenter (pyramid-shaped diamond tip with a triangular base). For each sample, we have made a matrix of 9 equidistant indentations (Figure II.16 (a)). The parameters retained for the nano-indentation tests are normal load = 200 mN, loading rate = 400 mN/min, pause at maximum load = 10s, unloading speed: 400 mN/min.

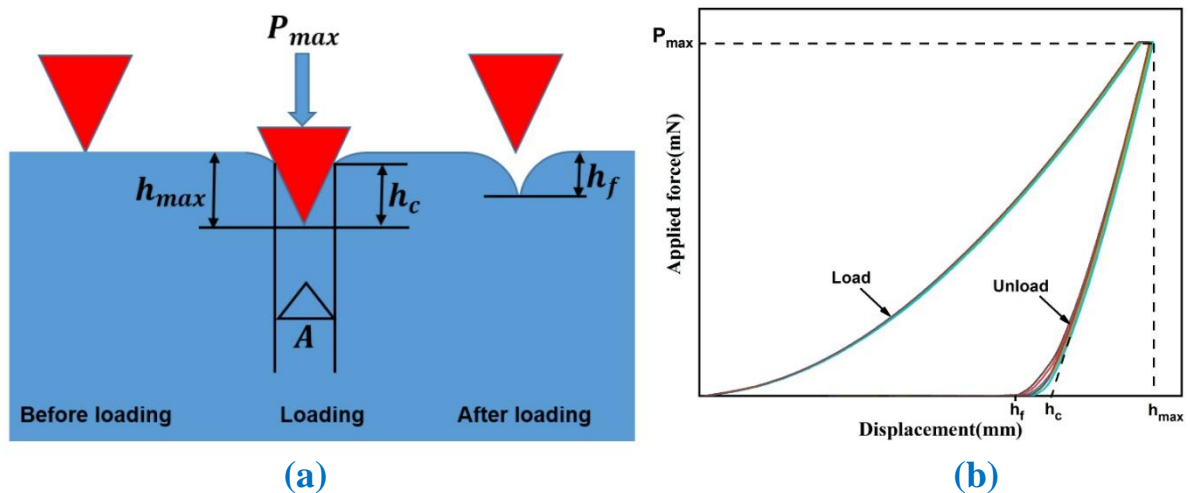


Figure II.15: Schematic description of nanoindentation testing (a) and an example of load-displacement curves obtained for Ni-Co alloy coating (b).

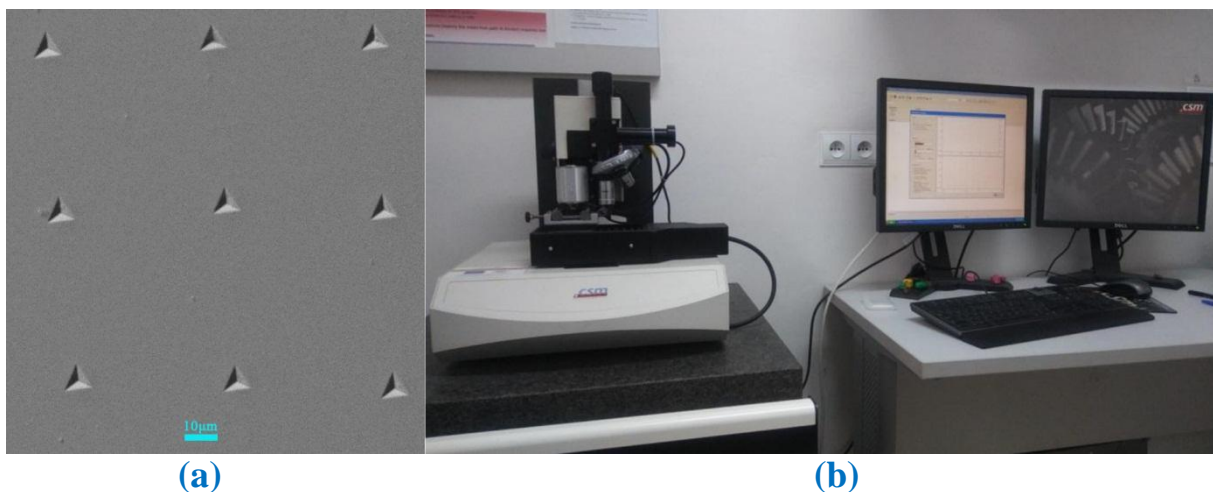


Figure II.16: SEM micrograph of the performed nanoindentation imprints (a) and the used TTX NHT nano indenter (b).

II.3.10 Scratch test

The scratch test is a generalization of the two-dimensional indentation test. A diamond indenter (cone, pyramid or sphere) is moved parallel to the sample surface at a constant speed. The normal force F_N applied at the stylus can be constant or linearly increasing from zero to a maximum value F_{zmax} . The penetration of the point into the sample as well as the lateral force is measured throughout the test. This test allows us to highlight the behavior of the coating in friction and to study the resistance of the coating to wear. Several physical phenomena (deformation, damage, delamination...) can also be highlighted during this test.

The scratch test was performed in this work to determine the coating adhesion to the different substrates. Where the critical load (L_c) for which delamination is obtained, which is an indication of the mechanical strength of the coating. The applied load is increasing (from 0 to 100 N) with a rate of $1.66\text{N}\cdot\text{s}^{-1}$ and the critical load (L_c) is determined by three different means: optical observation of the imprint left by the stylus, measurement of the acoustic emission during the test and friction coefficient monitoring. It is thus possible to determine the substrate/coating adhesion energy from the critical load measured in the scratch test. [Figure II.17](#) represents the principle of the scratch test (a) and the used Bruker scratch tester. (b).

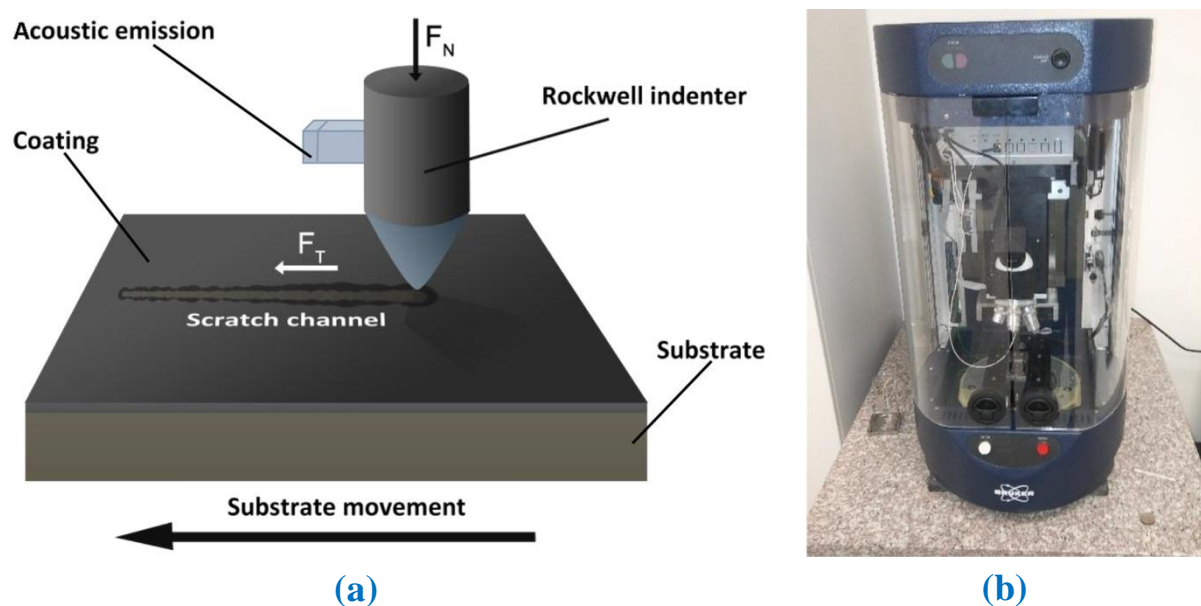


Figure II.17: Representative diagram of the used scratch tester (a) and the used Bruker scratch tester (b).

II.3.11 Tribological tests

The tribological tests were carried out with a ball on disc type tribometer from CSM Instruments (High temperature tribometer CSM THT) (see [Figure II.18](#)). The principle consists in rubbing a calibrated ball on a rotating sample. A displacement sensor located in the lever arm measures

the deflection due to the ball friction. The test can be subject to several variables: the load applied on the sample, the rotation speed of the sample, the radius of the rubbing track and the length of the test or the number of cycles, the nature and diameter of the antagonist ball chosen according to the nature of the sample to be tested, the sample surface condition and the test conditions (dry or lubricated friction, with or without wear debris evacuation). The test parameters were chosen after a literature review, although some of the works present very different conditions.

Table II.5: The composition of the balls used as pins.

Ball type	Diameter (mm)	Hardness (HV)	Composition (wt. %)						
Alumina 	6	1900	Al₂O₃						
			99.99						
AISI 1040 hard steel 	6	700	C	Cr	Si	Mn	Mo	Cu	Fe
			1.05	1.60	0.15	0.25	0.1	0.3	Rest

In the present work, the tribological behavior of the samples is studied under dry sliding wear conditions (without lubrication). The representative diagram of the used tribometer is illustrated in [Figure II.18 \(a\)](#). All tribometric analyses are performed at room temperature under 40-50% humidity. 3-5 and 10N loads are applied with a sliding speed of 0,5 to 5cms⁻¹, this should be specified for each case. The corresponding total wear time will depend on the selected radius. It is between 10 and 30min which correspond to a sliding length of 25 to 100 meters. The sliding length is chosen so that the friction coefficient has time to stabilize. AISI 1040 hard steel and alumina balls were used as a pins (counter body). The properties and the chemical composition of the used balls are listed in [Table II.5](#). The friction coefficient in function of time is automatically computed during the test. The morphology and composition of worn surfaces are studied by SEM and EDS respectively; however the wear rate is evaluated by the measurement of the mass loss using Sartorius digital precision balance with an accuracy of ± 0.1mg. The wear rate of samples was calculated either by measuring the wear track surface ([eq. II.8 \[149\]](#)) or by measuring the variation in the sample mass ([eq. II.9 \[150\]](#)) as a function of the load applied and the travelled distance. For the measurement of profiles, five random measurements are taken by the profilometer (see [Figure II.11 \(b\)](#)).

$$Q = \frac{V}{F_N L} = \frac{2\pi R A}{F_N L} \quad (\text{II.8})$$

$$Q = \frac{\Delta m}{\rho F_N L} \quad (\text{II.9})$$

Where A is the wear track surface by m^2 in the sliding direction, R is the wear track radius, F_N is the applied load in N, L is the sliding distance in meter, Δm is the weight loss measured in grams and ρ is the worn material density in g/mm^3 .

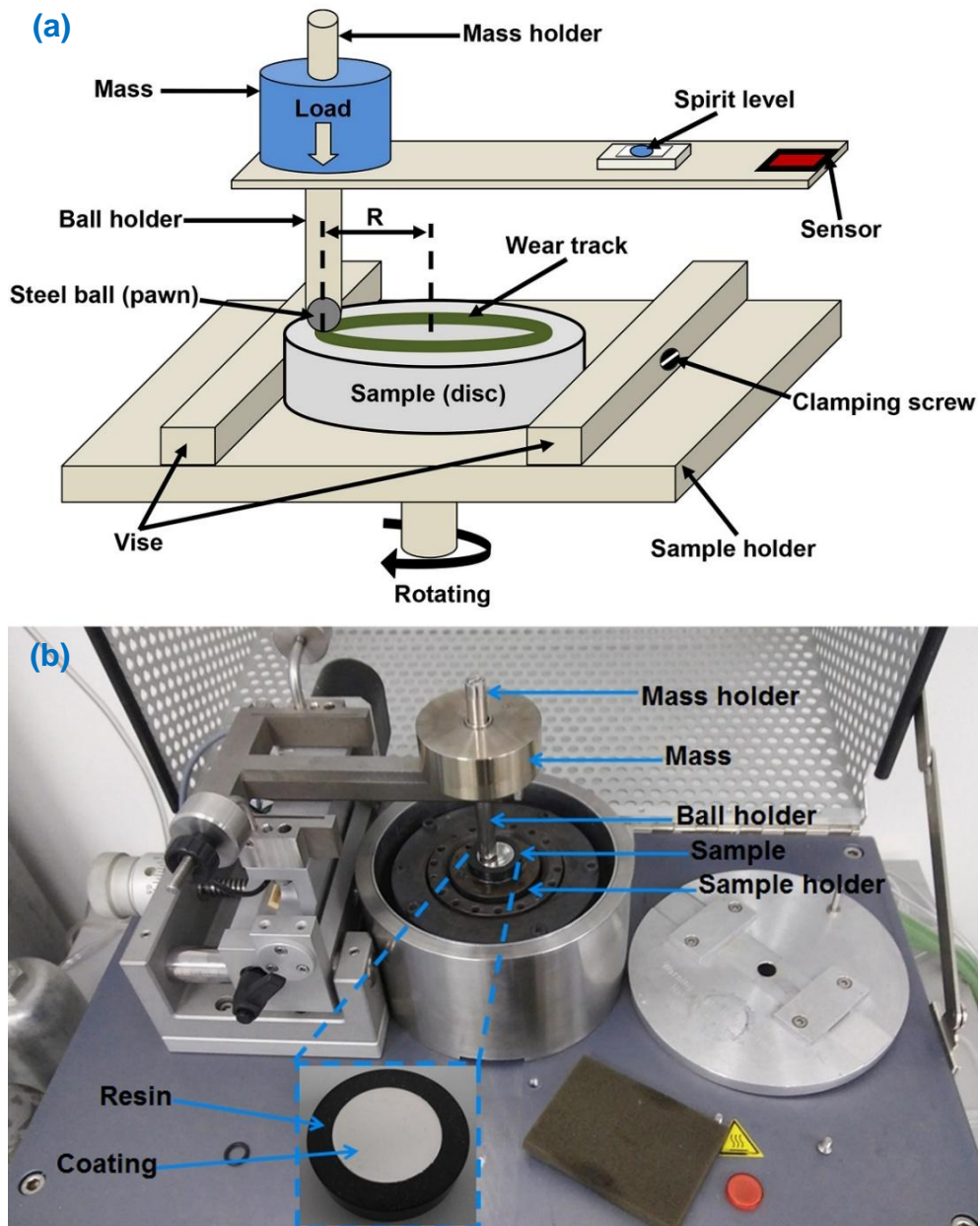


Figure II.18: Representative diagram of the used pin-on-disc tribometer (a) and the used CSM THT tribometer (b).

Chapter III:

*Study of the performances of
nanocrystalline Ni-Co alloy
as anti-wear coating*

CHAPTER III: Study of the performances of nanocrystalline Ni-Co alloy as anti-wear coating

III.1 INTRODUCTION

The recent studies have shown that the electroplated microcrystalline Ni-Co alloys coatings exhibited better tribological properties than the microcrystalline pure Ni coatings. However, the microhardness needs to be further increased by decreasing the crystallites size. Moreover, the role of tribofilms and debris on the varied tribological behaviors is contested and poorly understood. In this chapter of the work, we will try to address these issues. Therefore, Ni and Ni-Co coatings with reduced nanometric crystallites size are electrodeposited on StW24 mild steel substrate in the presence of saccharin and 2-butyne-1,4-diol (BD) as grain refiners, here a special attention is given to the effect of saccharin on the morphostructural characteristics of these coatings. Chemical, morphological, structural and mechanical characterizations on the worn and unworn surfaces of the substrates and electroplated coatings are conducted by different surface analysis techniques. The performances of the nanocrystalline Ni-Co coatings as anti-wear coating on StW24 mild steel is examined. The anti-wear performances of these coatings are compared also with a commonly used coating for such applications, namely the electrodeposited nanocrystalline pure Ni coating. Furthermore, the wear mechanisms, the tribofilm formation and their roles on the tribological behavior of all the studied materials are discussed in detail.

III.2 EXPERIMENTAL DETAILS

III.2.1 Coatings electrodeposition

In this work part, the as prepared StW24 mild steel disc with 3.14cm² exposed surface area is used as a cathode (substrate). The nanocrystalline Ni and Ni-Co coatings are deposited from a modified Watts bath by the use of direct courant (DC) electrodeposition process. The composition of the electroplating baths and the experimental conditions used for the elaboration of different coatings are listed in [Table III.1](#).

III.2.2 Compositional, morphological and microstructural characterizations

The surface microstructure of coatings is investigated using a scanning electron microscope (SEM), while the microstructure of StW24 steel substrate is studied by the use of a metallographic microscope after etching of the substrate with Nital solution for about 20s, the

obtained images are then processed by ImageJ software for further clarification. A confocal microscope is used for characterize the surface morphology of the substrate and Ni₆₃-Co₃₇ coating. The composition of substrate and deposits is determined using X ray fluorescence spectrometer (XRF). The roughness of the coated and uncoated substrate and the thickness of coatings are measured using mechanical profiler; five measurements are made on each sample. The crystal structures of substrate and coatings are studied by the use of X-ray diffractometer (XRD).

Table III.1: The bath compositions and the experimental conditions used for the electroplating of the coatings.

Composition of the electroplating bath							
Components Coatings	NiSO ₄	NiCl ₂	CoSO ₄	H ₃ BO ₃	Saccharin	BD	SDS
Ni coating	200g/l	20g/l	-	30g/l	2g/l	0.5g/l	0.2g/l
Ni₆₃-Co₃₇ coating	200g/l	20g/l	20g/l	30g/l	2g/l	0.5g/l	0.2g/l
Ni₁₃-Co₈₇ coating	200g/l	20g/l	200g/l	30g/l	2g/l	0.5g/l	0.2g/l
Experimental conditions							
Current density	Temperature	Electrolyte pH	Agitation rate	Duration			
4A/dm ²	45°C	4.2±0.05	200 rpm	1 hour			

III.2.3 Mechanical and tribological characterizations

The microhardness of the substrate and deposits is determined by Vickers indenter using the parameters listed in Table III.2. Five measurements are taken on each sample. The tribological behavior of the samples is studied using pin on disc tribometer under dry sliding wear conditions using the sliding parameters mentioned in Table III.2. All the tribometric analyses are performed at room temperature under 28-44% of humidity. AISI 1040 hard steel ball (Ø = 6mm, hardness = 700HV) is used as a pin (counter body). The friction coefficient in function of time is automatically computed during the test. The morphology and the composition of the worn surfaces are studied by SEM and EDS respectively, whereas, the wear rate is evaluated by the measurement of the mass loss using digital precision balance having an accuracy of ± 0.1mg.

Table III.2: The parameters used for the microhardness and tribological measurements.

Microhardness measurements				
Samples Conditions	Stw24 steel substrate	Ni₆₃-Co₃₇ coating	Pure Ni coating	Ni₁₃-Co₈₇ coating
Applied load (g)	10	10	50	50
Holding time (s)	15	15	15	15
Tribological measurements				
	Stw24 steel substrate	Ni₆₃-Co₃₇ coating	Pure Ni coating	Ni₁₃-Co₈₇ coating
Applied load (N)	5 and 10	5 and 10	3	3
Sliding time (min)	17	17	10	10
Sliding speed (mms⁻¹)	5	5	5	5

III.3 RESULTS AND DISCUSSIONS

III.3.1 Study of the performances of nanocrystalline Ni-Co alloy as anti-wear coating on mild steel substrate

To demonstrate the importance of a coating for anti-wear applications, it must first be deposited on a material widely used, but suffers from friction such as low carbon steel and then prove the wear resistance of the coated substrate compared to the bare substrate. The tribological performance of the nanocrystalline Ni-Co alloy coatings electrodeposited on steels has been demonstrated in some previous studies, but unfortunately, the reasons behind the improved properties of Ni-Co coated substrates compared to bare steel substrates did not get much attention. This is what will be well displayed in this work through the investigation of the compositional, microstructural, morphological, mechanical and tribological characteristics of Ni-Co coated and uncoated StW24 mild steel substrate. One also tries to understand the wear mechanisms and the role of debris and tribofilms formation on the tribological behavior of the studied materials.

III.3.1.a) Composition of the electrodeposited Ni-Co coating

Figure III.1 represents cobalt and nickel masse percentages in the electrolyte and in the Ni-Co coating. It is clear that cobalt percentage in the coating (37%) higher than those in the bath (8%). On the contrary, nickel percentage in the coating (63%) is less than those in the bath (92%). This refers to the anomalous codeposition mechanism of Ni-Co alloys. The anomalous co-deposition term as introduced by Brenner [89] refers to the preferential electrodeposition of the less noble metal (Co) rather than the more noble metal (Ni). Many models were proposed to explain this anomalous codeposition [90,151,152]. However, a generally accepted explanation proposed for this anomalous phenomenon is the formation of metal hydroxides Co(OH) and Ni(OH) caused by a local increase of the near cathode pH. The mechanism and steps of the anomalous co-deposition of Ni-Co alloy are expressed by the following equations and well-illustrated graphically by Figure III.2.

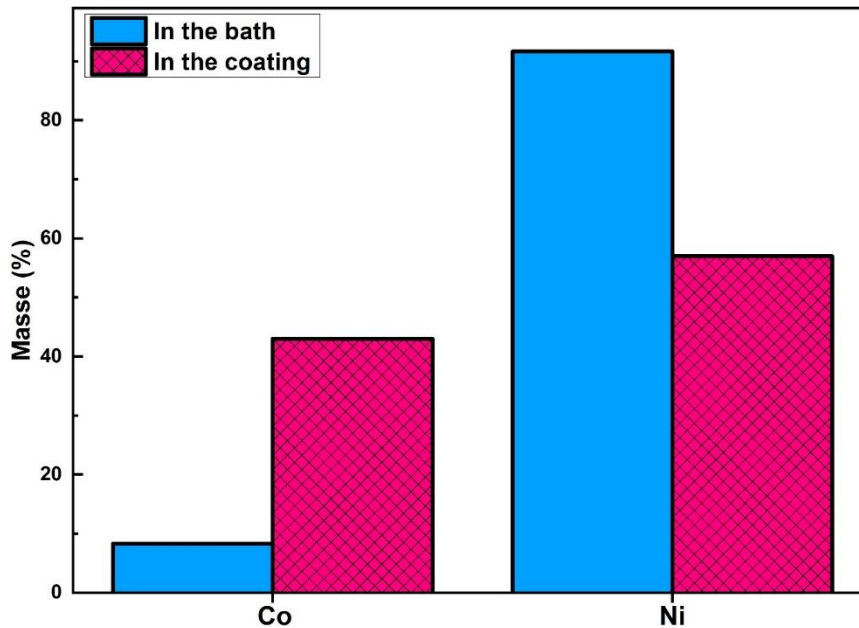
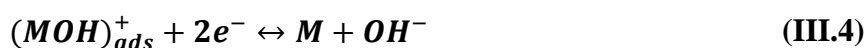


Figure III.1: Co and Ni mass percentages in the bath and in the electrodeposited Ni-Co coating.



Where M represents Ni and Co metal atoms and M_{ads} represents adsorbed metal atoms. The formation of $(CoOH)^+$ precipitate at the cathode may inhibits the adsorption of $(NiOH)^+$. Therefore, the adsorption ability of $(CoOH)^+$ is considered to be higher than $(NiOH)^+$ [153], consequently the reduction of cobalt is promoted. It is worth mentioning that, almost the same

coating composition as this study (37% Co vs. 67% Ni) was obtained in some previous studies by using a bath with almost the same composition (7.55% Co vs. 92.45% Ni) in the study [125] and (10% Co vs. 90% Ni) in the study [39].

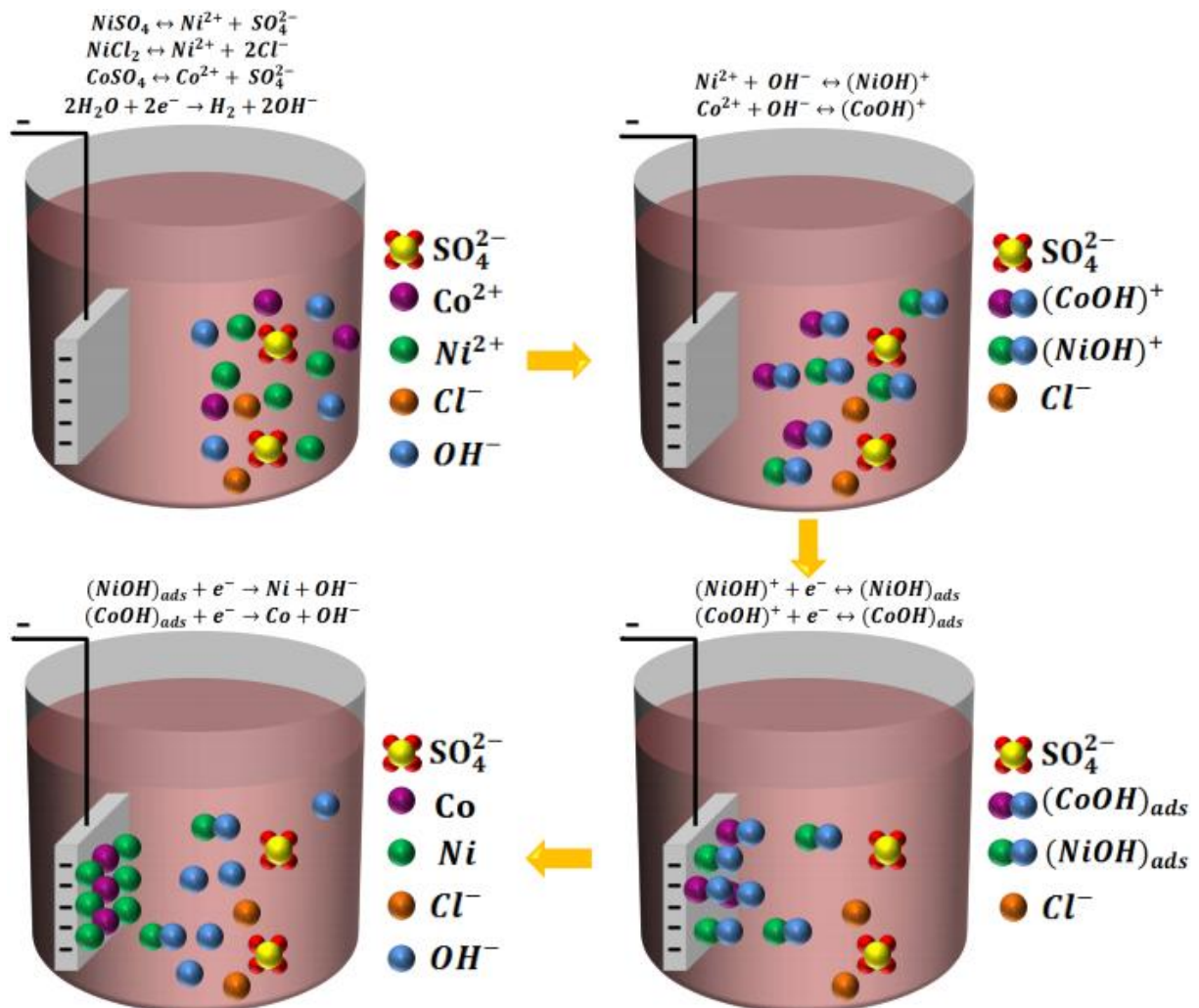
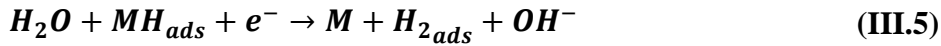


Figure III.2: Mechanism and steps of the anomalous codeposition of Ni-Co alloy.

III.3.1.b) Morphological and microstructural properties

Microscopic observations of the surface morphologies of the uncoated and Ni-Co coated substrate are shown in Figure III.3. The surface of the bare substrate is apparently smooth with the existence of certain grooves due to the mechanical polishing of the substrate by the abrasive paper, the presence of these grooves can increase the roughness of the Ni-Co coated substrate but their presence is necessary for a good adhesion of coating to the substrate by mechanical fastening. On the other hand, the grooves are totally covered in Ni-Co coated substrate but its surface exhibits a bigger roughness value, which is evident by the roughness values measurement, where it is found that the surface roughness value of Ni₆₃-Co₃₇ coating ($R_{ms} \approx 0.28\mu m$) is greater when compared to that of the bare substrate ($R_{ms} \approx 0.085\mu m$). Moreover,

several pores can be observed on the surface of Ni-Co coatings (Figure III.3 (b)); these pores are mainly due to the hydrogen evolution reaction (HER) on the cathodic substrate surface. In view of previous studies [154,155], a generally accepted explanation for HER is the increase of the near electrode pH caused by the water electrolysis leading to the formation of hydroxides and to the hydrogen evolution reaction, as follows:



The hydrogen molecules produced during the simultaneously HER process can adsorbed on the substrate surface which influences strongly the quality of deposits especially their density. Therefore, this problem must be taken into consideration. Because of that, many approaches have been applied in this study to reduce the hydrogen adsorption and its negative effects on the Ni-Co elaborated coatings. Among them, the addition of boric acid (H₃BO₃) in the electroplating bath as buffer agent to prevent the near cathode pH variation and to inhibit the formation of hydroxide ions [156,157]; the addition of sodium dodecyl sulfate (SDS) as surfactant to reduce the surface tension which can facilitate the release of hydrogen bubbles and prevent their trapping within the deposit [138,158], the use of low current density for enhance the cathodic current efficiency and reduce the predominance of the hydrogen reduction reaction [125], and the continuously stirring of solution during all the electroplating process to assist the release of hydrogen molecules trapped in the deposit surface [159]. Consequently, the coatings are compacts and there are no cracks at the coatings surfaces due to the internal stresses caused by the hydrogen trapping compared to some studies that obtained cracked Ni-Co electrodeposits [34,79,160]. Furthermore, the rate of pores is decreased very importantly but the pores cannot be completely eliminated (Figure III.3 (b)).

XRD patterns of StW24 steel substrate and the electrodeposited Ni₆₃-Co₃₇ coating are displayed in Figure III.4. As can be seen from the patterns, it is obvious that StW24 substrate is characterized only by a body centered cubic crystal structure (bcc) with crystallographic orientations (111), (200), (211), (220) and (310) with the dominance of (111) as preferred orientation. The peaks of bcc phase structured StW24 steel are in accordance with their composition as given in Table II.1.

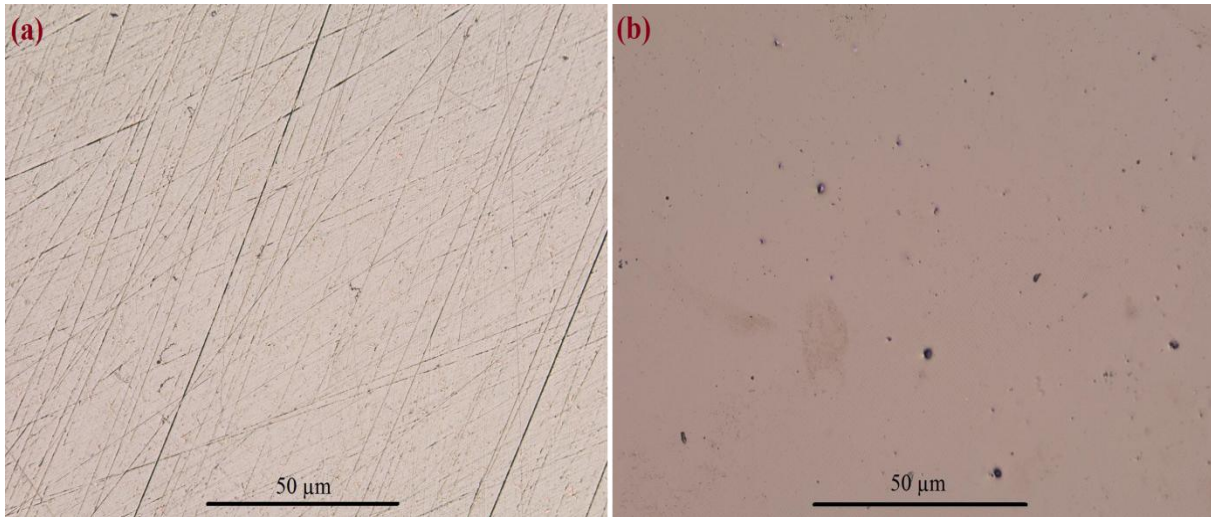


Figure III.3: Surface morphology of StW24 steel substrate (a) and Ni₆₃-Co₃₇ coating (b).

According to Fe-C phase diagram [161], at room temperature a steel like StW24 with a carbon content less than 0.08 mass.% and about 99.5 mass.% Fe can only presents a bcc structured α -ferrite grains which is compatible with (JCPDS 03-065-4899) XRD data. By considering the width of the XRD peaks, we can directly conclude that the diffraction peaks of StW24 steel used as substrate in this study corresponds to micrometric α -ferrite grains (eq.III.8 [162]), which is in good agreement with its SEM micrograph (Figure III.6 (b)). On the other hand, it is clear that the deposited Ni-Co alloy with 37% Co content having very good crystallinity. Figure III.4 also reveals that the diffraction peaks of Ni-Co are significantly more broaden than those of StW24. The width of all Ni₆₃-Co₃₇ alloy peaks corresponds to crystallites with nanometric size (≈ 12.08 nm), which is very smaller than that of the StW24 steel substrate. Furthermore, it can be seen that all the four identified peaks of the Ni₆₃-Co₃₇ alloy coating are in good concordance with the face-centered cubic structured Ni peaks (JCPDS 15-0806 and 004-0850). XRD patterns of the deposited coating do not contain any diffraction peaks corresponding to the hexagonal close packed structure (hcp) of Co phase, which confirmed that Ni-Co coatings under study form a total solid solution in there the atoms of the crystal lattice of Ni matrix had been replaced by Co partly [163]. Crystallographic orientations (111), (200), (311) and (222) are remarked in the XRD patterns of Ni-Co coatings in this study as many previous researches [41,42,125]. To assess the texture formation of the coatings, the relative peak intensities of the diffraction peaks are considered and it is seen that the electrodeposited Ni-Co coating have (111) preferential orientation.

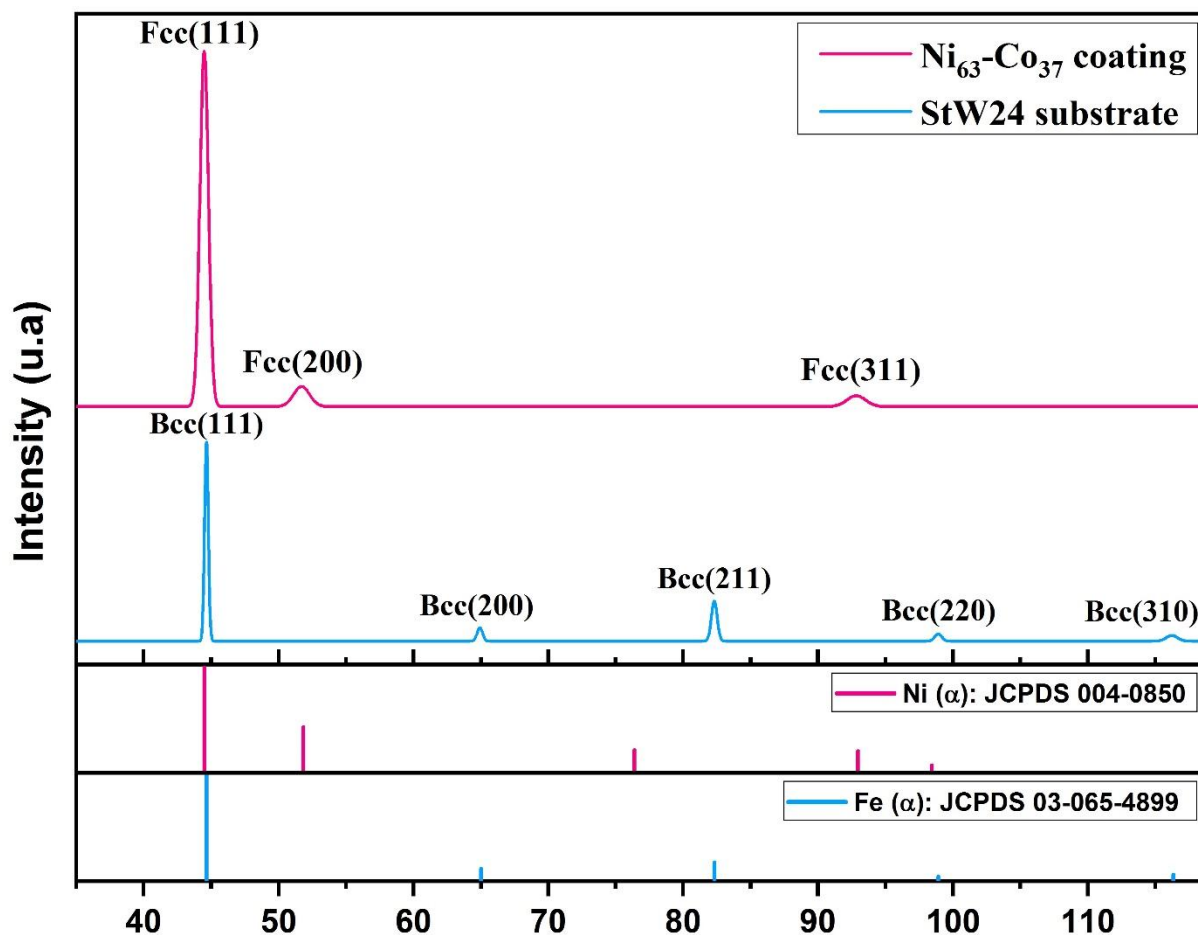


Figure III.4: XRD patterns of StW24 steel substrate and $\text{Ni}_{63}\text{-Co}_{37}$ electrodeposited coating.

Our proposed explanation in this study regarding the very small grain size of $\text{Ni}_{63}\text{-Co}_{37}$ coatings and the consolidation of (111) texture is related to the effect of organic additives, mainly the saccharin (where the inhibition effect of BD is negligible because of its very low concentration (0.5g/l), therefore the saccharin inhibition effect is considered to be dominant). It has been proposed that a charge transfer during electrodeposition is carried out in three steps: (1) transfer of ions to the terrace sites, (2) surface diffusion of adions on terrace sites and (3) displacement of adions through step-edge sites towards the active sites of growth [41,164]. It can be assumed that the decrease in surface diffusion would retard their flux to the active growth sites and thus inhibit the grain growth. According to the literature, saccharin as molecules or decomposed species containing sulfide can be adsorbed onto the surface of crystals during the electrodeposition [41], by filling its non-shared electron pair with the electrons of 3d orbit of Ni and Co atoms to form stable coordinated bonds [106] as can be seen in Figure III.5. As a result, it can play the role of a barrier to slow the surface diffusion of adions towards the active growth sites [41], in view of the fact that, the growth of the electrodeposits is a competition between the nucleation and the growth of crystals. Saccharin molecules provide more sites of

nucleation and thus delay the growth of crystals, resulting in finer grains. Otherwise, saccharin adsorbed molecules change not only the grain size but also the crystallographic orientation of Ni-Co electrodeposits. Amblard et al. [165] reported that the preferred crystal orientation of electrodeposited nickel could be attributed to the inhibition of the electrocrystallisation process by adsorbed chemical species like NiOH_{ads} and H_{ads} . Moreover, Li et al. [166] reported that the adsorption capacity of the species by different crystallographic plans was different. Therefore, the highest coverage with adsorbed species leads to the slowest growth rate of the crystal face. As mentioned above, the Ni-Co deposits prepared without adding saccharin has a strong (200)fcc texture. However, in the present research (200)fcc plans has preferential adsorption of saccharin molecules than (111)fcc as shown in Figure III.5. By implication, the crystal growth only leaves the (111)fcc plans.

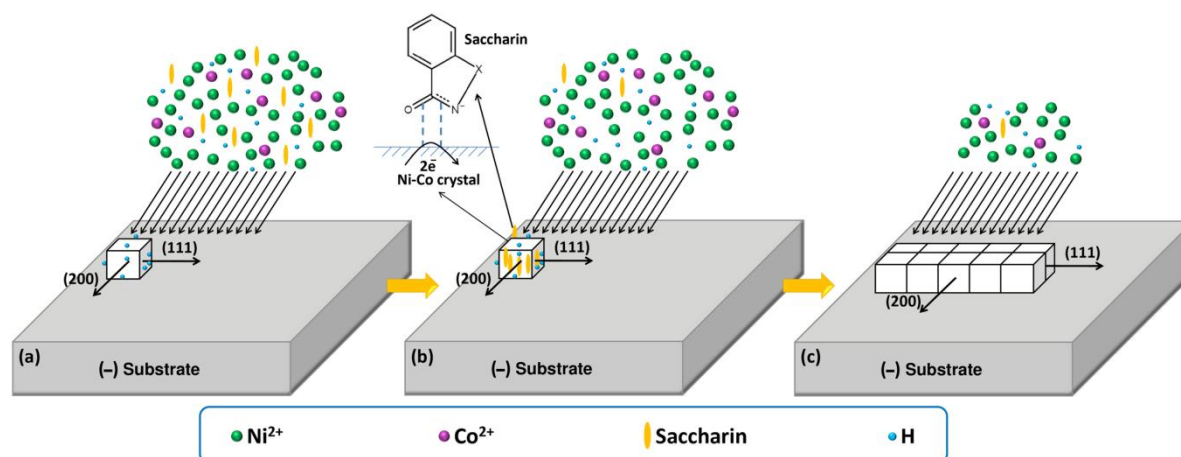


Figure III.5: Schematic representation of the saccharin effect on the crystal growth of Ni-Co deposits.

Figure III.6 displays the microstructure of StW24 steel substrate and the morphology of $\text{Ni}_{63}\text{-Co}_{37}$ coating. The micrograph of low carbon StW24 steel substrate depicted in Figure III.6 (b) reveals that is characterized only by ferrite micrometric grains, which confirms the DRX analysis results (Figure III.4). On the other hand, $\text{Ni}_{63}\text{-Co}_{37}$ alloy coatings are characterized by colony-like morphology in the form of orange peels whose nanometric grains. Almost similar granular morphology was also observed for Ni-Co films with almost the same Co content and in the presence of saccharin in some earlier studies [108,160,167]. Although that the pyramidal structure is a common morphology for Ni-Co electrodeposits with single fcc phase structure [30,35,41] which have approximately rough surfaces. However, a colony-like surface morphology consist of different sizes of grain colonies have been observed in $\text{Ni}_{63}\text{-Co}_{37}$ electrodeposited coatings in this study, this because of the addition of organic additives, namely, saccharin and BD. The adsorption of saccharin and BD molecules on the growing peaks of

pyramids (active sites) as shown in Figure III.5, inhibits the surface diffusion of adions, blocks the active sites and prevents the growth of pyramids [41,111]. Consequently, the morphology of the Ni-Co deposit becomes a colony-like instead of the typical pyramidal morphology of the fcc structured Ni-Co alloys [105,111]. It is noteworthy that the grain size of Ni₆₃-Co₃₇ deposits is too fine to be resolved exactly using conventional SEM images, but it can be estimated. The crystallites of the Ni₆₃-Co₃₇ coatings that appears nanometric are very small compared to that of StW24 mild steel substrate appears to be in the micrometer order. In the other hand, the SEM micrographs prove the possibility of elaboration of smooth, homogeny and compact coatings by electrodeposition, where the elaborated Ni₆₃-Co₃₇ coatings show a dense surface morphology free from micro-cracks (Figure III.6 (a)) which is in good concordance with the observations by confocal microscope (Figure III.3 (b)). The absence of macro and microcracks in this study compared to other studies [34,36] is due to the additions of stress relievers (saccharin and BD) which can raise the compressive stress in order to recompense the tensile stress introduced by large Co atoms (Figure III.7). Moreover, no hydroxides or foreign particles can be observed on the Ni-Co coating surface, which is consisted with the coating homogeneity demonstrated by XRF and XRD analyses (Figure III.1 and III.4).

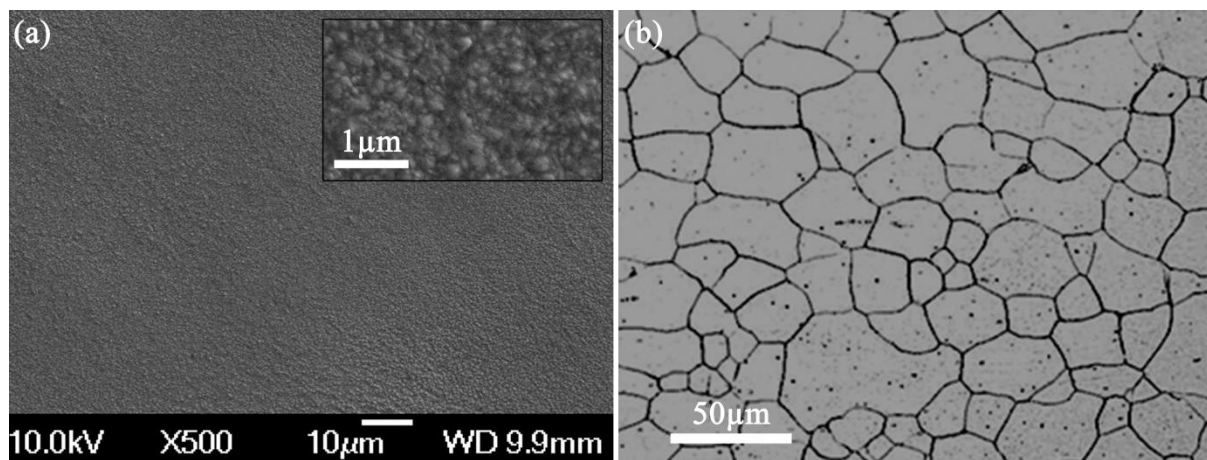


Figure III.6: SEM observation on the surface of Ni₆₃-Co₃₇ coating (a) and optical microscopic observation on the surface of StW24 steel substrate (b).

III.3.1.c) Microhardness

Figure III.8 presents the microhardness of the StW24 mild steel substrate and Ni₆₃-Co₃₇ coating (with average thickness $\approx 50\mu\text{m}$), measured at room temperature. It is clear that the microhardness of ferritic low allied StW24 steel substrate multiplies and increases from 256 to reach a value of 761HV0.01 after its coating by the nanocrystalline Ni-Co alloy. According to the Mohs hardness scale, there is no big difference between the hardness of unalloyed

polycrystalline nickel and iron (3.5-5 for Ni vs. 3.5-4.5 for Fe [168]) and by Vickers hardness measurement, unalloyed polycrystalline Ni shows a slightly higher hardness than polycrystalline Fe (65.06HV for Ni vs. 62HV for Fe [169]). This small difference in hardness cannot be explains the multiplication of the mild steel substrate microhardness about three times after their coating by Ni-Co alloy in this study. This big difference in microhardness is attributed to the improvement of Ni hardness thanks to the solid solution hardening (SSH) by Co. Where, the large Co atoms (atomic radius = 152pm [170]) replace partially the small atoms of the Ni (atomic radius =149pm [170]) in the crystal lattice as shown in [Figure III.7](#), leading to localized distortions in the Ni lattice, these distortions interact with dislocations, resulting in a strengthening effect [171].

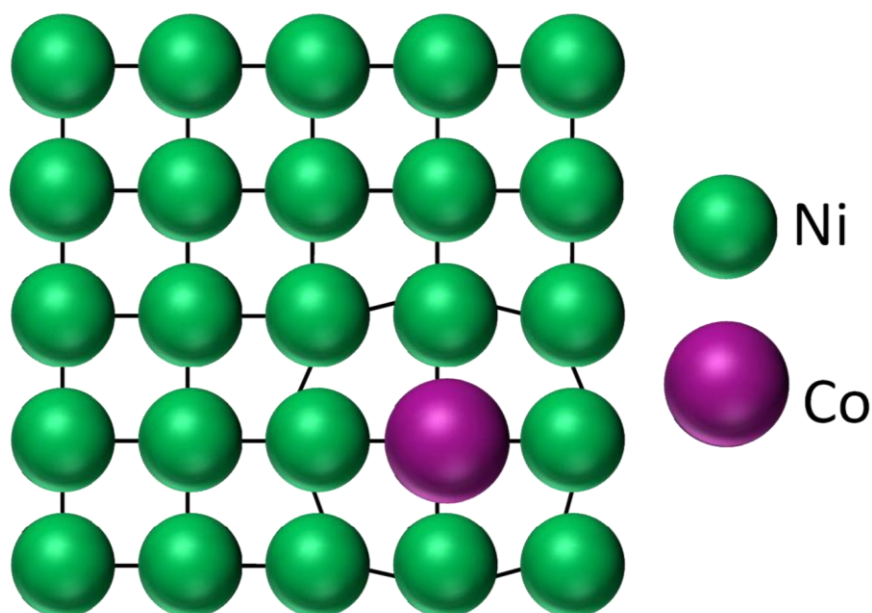


Figure III.7: Schematic representation of the substitutional Ni-Co solid solution.

The high hardness of Ni-Co electrodeposits is caused also by the grain boundary strengthening (Hall-Petch hardening). The electrodeposited Ni-Co coating shows nanometric crystallites sizes, which means the presence of a high volume fraction of grain boundaries, these grains boundaries acting as efficient obstacles preventing the propagation of dislocations. Since the lattice structure of the adjacent grains differs in orientation, more energy is needed for a dislocation to change direction and move into the adjacent grain. The grain boundary is also more disordered than inside the grain, which prevents dislocations from moving in a continuous sliding plane. The inhibition of dislocation movement by the grain boundaries will prevent the material to behave plastically and thus enhance the hardness of the coating. The increase of

hardness of polycrystalline materials with the refinement of crystallites known as the Hall-Petch effect, which can be described mathematically by the Hall-Petch relationship [172]:

$$H = H_0 + \frac{k}{\sqrt{d}} \quad (\text{III.6})$$

Where H_0 is the intrinsic hardness, k is a constant for a specific material and d is the crystallite size. Figure III.8 shows also that no crack propagation or delamination from the substrate noticed around the imprint of indentation. That is proves that the elaborated Ni₆₃-Co₃₇ coating has good adherence on the substrate, and in other hand it has low internal stress and good toughness and ductility despite its relatively high hardness, which is attributed to the fcc crystalline structure of the coating, where fcc structured metals are extremely ductile [173]. Additionally, the not big distribution of hardness values measured at different places on Ni₆₃-Co₃₇ coating is another sign about its good homogenization.

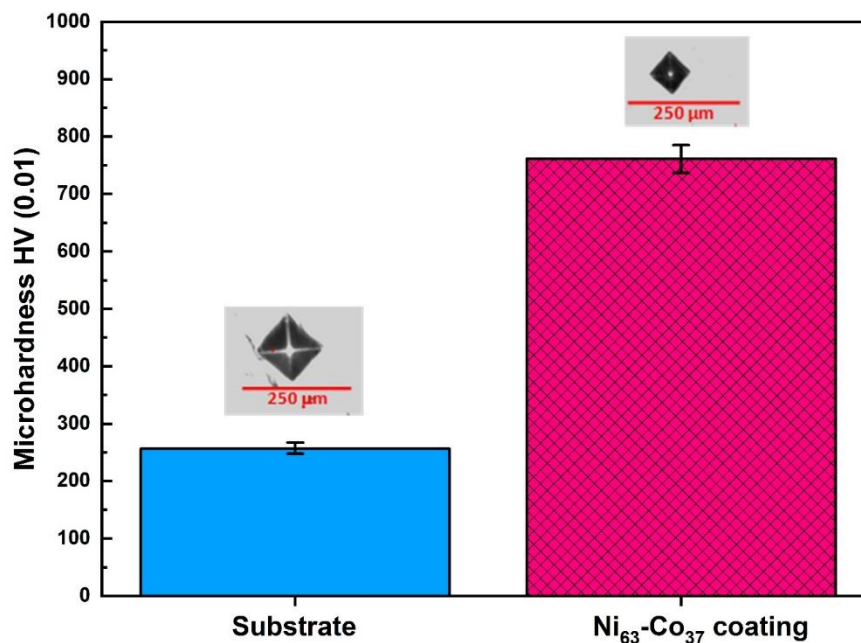


Figure III.8: Microhardness values and indentation imprints of the StW24 steel substrate and the electroplated Ni₆₃-Co₃₇ coating.

III.3.1.d) Tribological behavior

Figure III.9 shows as function of time the friction coefficient response of Ni-Co coated and uncoated StW24 steel substrate sliding against 100C6 steel ball in unlubricated conditions and under two loads 5 and 10N, respectively. It is obvious that the friction coefficient varies with rubbing duration. Generally, when the applied load is not big, the initial stage of rubbing is governed by the surface roughness of materials due to the contact between the superficial layer of disc and pin [174,175]. Under a low load such as 5N, the friction coefficient (μ) of the

nanocrystalline Ni₆₃-Co₃₇ alloy coating increases rapidly with the time in the initial stage to reach over 0.56 at around 2min of sliding due to the effect of their relatively high roughness which can be reduced by the polishing of the coatings surface. However, the surface roughness effect is removed in the first few cycles of sliding, consequently after 4min of sliding, the friction coefficient become governed only by the abrasive-adhesive wear mechanism of Ni-Co alloy. The friction coefficient experiences in this phase a little decrease to an average value ($\mu_{\text{moy}} = 0.38$) and remain unstable fluctuates between (0.25 and 0.45) because the effect of wear debris as shown in [Figure III.11](#), it remains at this range up to the end of the experiment. On the other hand, the friction coefficient of uncoated StW24 steel reaches in the initial stage of sliding an average value ($\mu_{\text{moy}} = 0.08$) smaller than that of Ni-Co coated substrate because of its relatively lower surface roughness. The removing of surface roughness effect of StW24 steel lasts time very shorter than that of Ni₆₃-Co₃₇ coating surface because of its lower hardness, it remains just about forty seconds. Then, it starts to increase gradually with the pin penetration until the third minute of rubbing, after that the friction coefficient becomes governed only by the abrasive oxidative wear mechanism of the substrate. It increases slowly to reach an average value ($\mu_{\text{moy}} = 0.35$) because the transition from mild to severe wear and it maintains at this range until the end of the analysis. Moreover, the coefficient of friction for both Ni-Co coated and uncoated substrate show a strong change with increasing the applied load. By increasing applied load to 10N, the effect of surface roughness on Ni₆₃-Co₃₇ coating friction behavior is still because of its high surface hardness. The friction coefficient rises rapidly in the early stage of sliding to reach a value ($\mu_{\text{moy}} = 0.4$), it maintains at this level, and after 2min, a friction transition from moderate to severe wear appears, leading to a very high and much more unstable friction coefficient reaches a value ($\mu_{\text{moy}} = 0.82$) toward the end of the test. This abrupt variation of friction coefficient is typical of galling processes. On the other hand, the course of the friction coefficient of uncoated substrate under 10N applied load becomes much more stable and lower than that of Ni-Co coated substrate. With the exception of the initial stage of sliding, which cannot governed by the surface roughness of the substrate in this case, because of the low substrate surface hardness and because of the high applied load that induces a severe wear at the first step of rubbing. The rapidly rising of friction coefficient of substrate in the early stage of sliding in this case is due to the easy pin penetration in substrate surface because the low hardness of substrate and the relatively high applied load, the worn surface is smoothed easily by the abrasive oxidative wear resulting in the reduction of friction coefficient after about 1.5min. Compared with the Ni-Co coated substrate, the average friction coefficient of uncoated substrate is not much increases by applying of 10N load, where it reaches only $\mu_{\text{moy}} = 0.42$ due

to the inexistence of tribofilm on its worn surface (Figure III.12). A comparable variation range of the friction coefficient as well as the variation of the friction coefficient with the applied load have been reported by other authors [175,176].

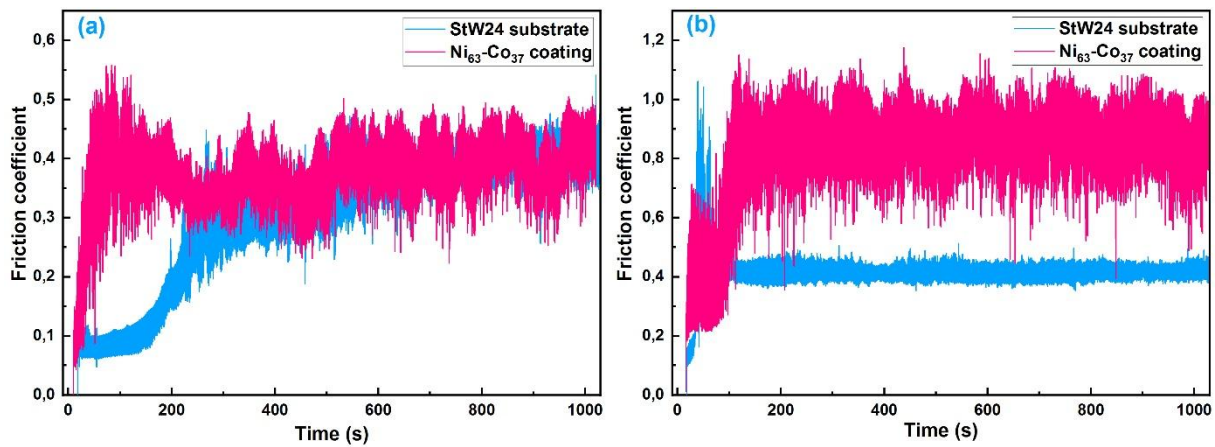


Figure III.9: Friction coefficient of Ni₆₃-Co₃₇ coated and uncoated StW24 steel substrate under 5N (a) and 10N (b).

Figure III.10 shows the wear rate of Ni-Co coated and uncoated StW24 steel substrate under 5 and 10N loads. The wear rate (Q) of the two materials, under identical wear test conditions is calculated by the use of the equation (II.9 [150]). It is quite evident that under a charge of 5N, the wear rate of Ni₆₃-Co₃₇ coating is approximately 51% of that of StW24 steel substrate (1.84 vs. $3.57 \cdot 10^{-4} \text{mm}^3/\text{Nm}$). However, with the increase of the applied load to 10N, there is an increase of 316% in the wear rate of Ni-Co coated substrate which multiplies to reach a value of $7.6 \cdot 10^{-4} \text{mm}^3/\text{Nm}$, while the wear rate of StW24 increases about 158% to reach a value of $9.21 \cdot 10^{-4} \text{mm}^3/\text{Nm}$ for an 100 % increase in the applied charge value. Hence, under the two loads 5 and 10 N, Ni-Co coated substrate exhibits a wear rate lower than the bare StW24 steel substrate. Referring to Figure III.8, it can be concluded that the wear rates of the Ni-Co coated and uncoated substrates are inversely proportional to the hardness values, when a higher wear resistance occurs at Ni-Co coated substrate that exhibits the much higher hardness. Since the wear is due to the accumulation of plastic deformation and the measure of resistance of a material against the plastic deformation is the hardness, therefore, it is essential to understand the relationship between them. The relationship between the wear rate and the hardness can be expressed well using the traditional Archard's law (eq.III.7) mostly used in abrasive and adhesive wear conditions [177]:

$$Q = \frac{KLN}{H} \quad (\text{III.7})$$

Where Q is the volumetric wear loss, L is the sliding distance, K is the dimensionless wear constant, N is the normal load and H is the hardness of the worn surface. According to this law, there is an inverse correlation between the wear rate and the hardness of the worn surface, where the materials wear rate decreases as its surface hardness increases, which can explain the results of the present study. Moreover, it is important to mention that the higher rising in the wear rate of Ni₆₃-Co₃₇ coating under the increased load (10N) compared to that of the substrate can be justified by the nearly two times higher friction coefficient of Ni-Co coated substrate compared with the uncoated substrate. This is despite the fact that the hardness of the uncoated substrate is much lower than that of the Ni₆₃-Co₃₇ coating. Hence, it can be concluded that the wear resistance of materials depends not only by its hardness, but in many cases is mainly affected by its friction coefficient, which related in turn to the phase structure, surface roughness and the wear mechanism of materials.

The difference in the wear properties of uncoated and Ni-Co coated substrate can be further verified by the study of the worn surfaces morphologies. The selected SEM images of the wear tracks morphologies of the uncoated and Ni-Co coated substrate sliding against AISI 1040 hard steel ball under 10N load are shown in [Figure III.11 \(a\)](#) and [\(b\)](#), respectively. According to the images, the worn surface of the uncoated substrate reveals various abrasive grooves and scratches parallel to the sliding direction and shows a severe plastic deformation in the direction of rubbing. This results in the larger damaged regions and the appreciable removal of material ([Figure III.11 \(a\)](#)), indicating that the uncoated substrate experienced a usual abrasive wear under these conditions. Compared with the uncoated steel substrate, a densification of the worn surface of Ni-Co coated substrate seems to take place. The worn surface in this case is relatively smooth featured with fatigue wear and slight adhesion, the presence of the debris particles and some detachments could be seen scattered on the smooth worn surface which is a typical proof for the slight plastic deformation and hence the abrasive-adhesive wear ([Figure III.11 \(b\)](#)).

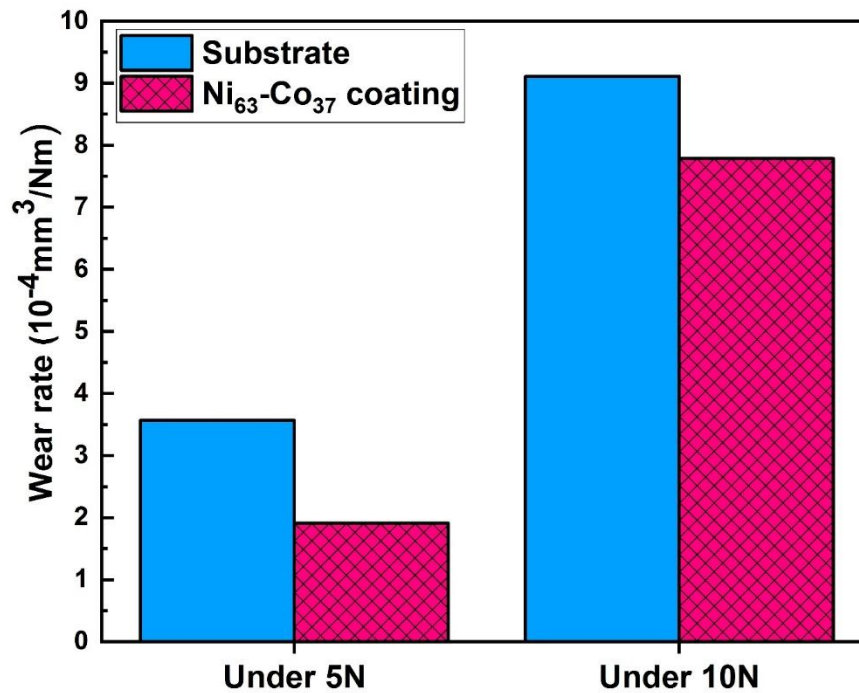


Figure III.10: Wear rate of Ni₆₃-Co₃₇ coating and StW24 steel substrate under 5 and 10N.

In the other hand, it is quite evident that the wear track of the Ni-Co coated substrate is much narrower and shallower than that of the uncoated substrate, which confirms further the significantly lowest wear rate and the better wear resistance of the Ni-Co coated substrate.

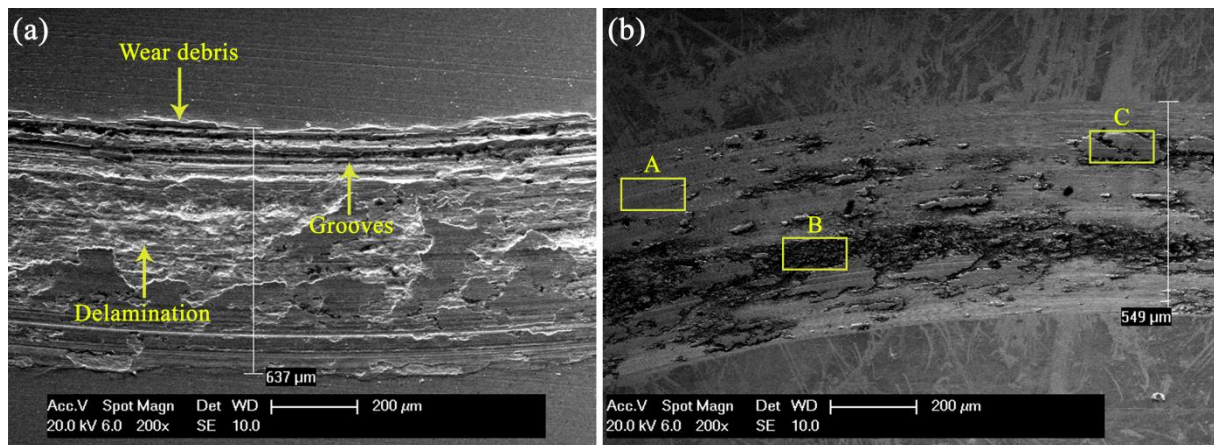


Figure III.11: SEM observations of the worn surfaces of uncoated (a) and Ni-Co coated StW24 steel substrate (b).

SEM observations of the wear track with elements map on the surface of StW24 steel substrate are shown in Figure III.12. It is quite evident that the unworn surface of substrate (red area) contains almost only iron which is compatible with its composition analysis (Table II.1). However, the wear track area has not a similar composition as the unworn surface, it includes iron with a high amount of oxygen (Figure III.12 (b) and (c)), whereby, the steel substrate was

oxidized during the wear process because of the elevated local temperature in the contact area which is a sign of an oxidative wear mechanism. It is believed that, the increase in friction coefficient of the steel substrate in the first stage of friction resulted from the formation of this iron oxide on the worn surface; especially with the increased charge (10N). Nevertheless, the iron oxide particles could not form a stable tribofilm on the worn surface of substrate to eliminate the metallic contact between the pin and the substrate (disk). The most of oxidized debris delaminated easily, pushed by the pin to the sides of the contact zone, and accumulated in the edges of the wear track (Figure III.12 (a)). Moreover, in these conditions of much lower adhesion and less frictional heating no observed transfers from the pin to the worn surface. The analysis of the wear debris by EDS as it can be seen in Figure III.14 (a) confirms that, where the wear debris of substrate contains just iron and about 29wt.% of oxygen. The removing of this iron oxide film by the pin leads to the smoothing of the worn surface. Consequently, the friction coefficient of StW24 steel substrate decreases and becomes more stable after about three minutes of sliding (Figure III.9 (b)). Although the diminution of friction coefficient can improve the wear resistance of the steel substrate but the inexistence of the tribofilm as third body that can act as separator of the two surfaces in contact is among the reasons behind the large surface damage and the high wear rate of the uncoated steel substrate compared with Ni-Co coated substrate.

The wear track of Ni-Co coated substrate and its elemental mapping are shown in Figure III.13. The existence of iron and oxygen with Ni-Co alloy signal in the analysis of attached debris indicates the presence of the tribofilm as none of them are noticed in the unworn surface of as-deposited coatings (Figure III.13 (b), (d), (e) and (f)). Furthermore, the EDS spectrum of the debris attached on the wear scar (Figure III.13 (b)) shows that the debris contains Ni, Co and oxygen with small amount of foreign elements (Fe, Cr and Mo). These elements are components of the steel ball used as pin (Table II.5) and transferred from the pin to the worn surface because of the relatively high adherence between the coating and the pin. Where a tribofilm constituted by the oxides of the two surfaces is favored to be generated due to the oxidation of transfers from the counterpart and the detachments from the coating under the high local temperature in the contact area [178]. However, the small amount of the transferred oxidized debris is not enough to form a complete and stable tribofilm which can totally covered the worn surface.

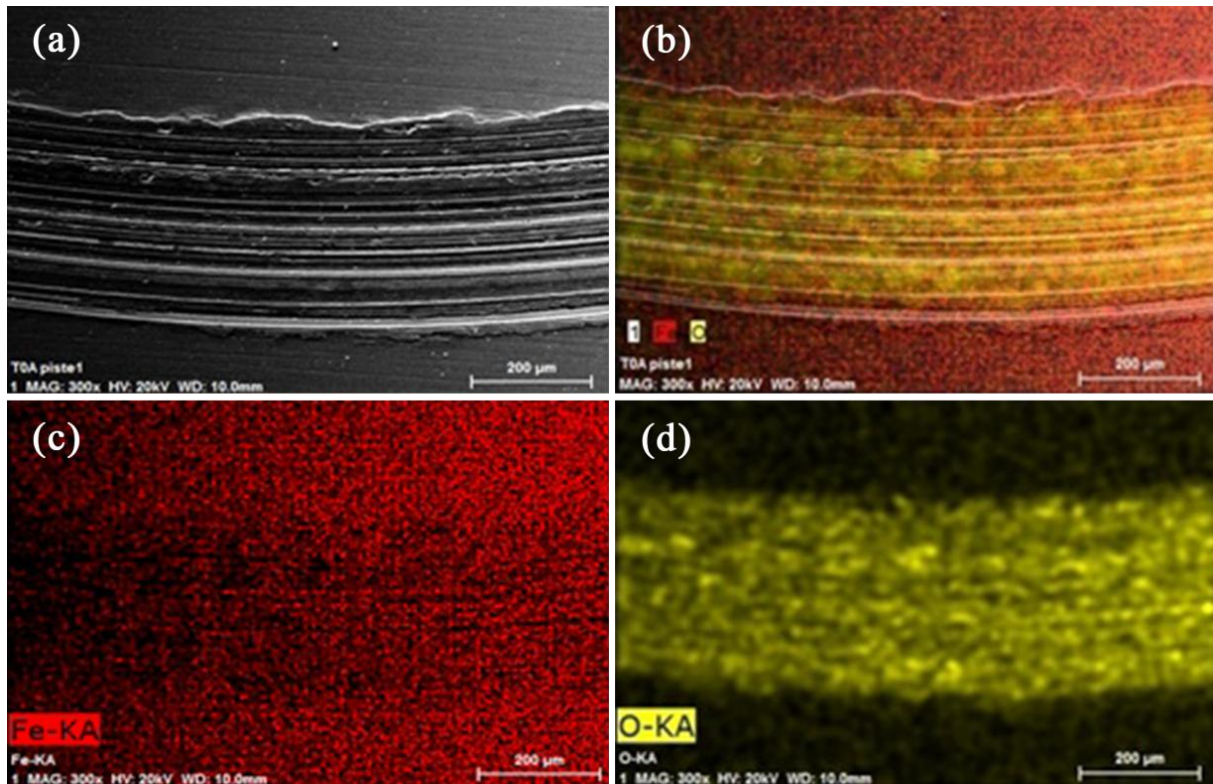


Figure III.12: SEM micrograph and EDS elemental mapping of the worn surfaces of uncoated StW24 substrate.

Where it can be seen evidently in [Figure III.11 \(b\)](#) that the worn surface of the Ni₆₃-Co₃₇ coating presents three different zones: the smooth zone (A) indicative for the typical polishing wear in which the worn surface becomes relatively smooth under the combined effects of load and shear [179]. The transition area with fine particles on it (B) and the zone covered by the tribofilm (C) resulted by the chemical and physical interactions between the pin and the disk [180]. As this tribofilm is discontinued and unstable, it cannot play the role of an efficient barrier to promote separation between the contact surfaces. Moreover, the higher ductility of the fcc structure and the absence of a lubricant component with low shear strength in the tribofilm [39] are the reasons behind the friction coefficient of Ni₃₆-Co₃₇ coating much more unstable and higher compared to that of the bare substrate under the high load (10N). Existing studies [181,182] show that the formation of a tribofilm leads to the same bad effect on the tribological behavior of the worn materials as this study. While other studies [183,184] have found that the tribofilm acted as good solid lubricant resulted in significant decrease in the friction coefficient and the wear rate of the worn materials at room temperature. We believe that this difference is due to the stability of the tribofilm, its coverage of the worn surface and its components, as a stable tribofilm with a complete coverage and lubricant components can improve the tribological characteristics of the worn surface while the partial coverage by unstable tribofilm may lead to

completely opposite results. Therefore, it is interesting to study the effect of tribofilms on the tribological behavior of Ni-Co coatings under varied conditions for more comprehension of the tribofilm impact mechanism that remains misunderstood. This is what we will be contributing to, as can be seen in Chapter IV.

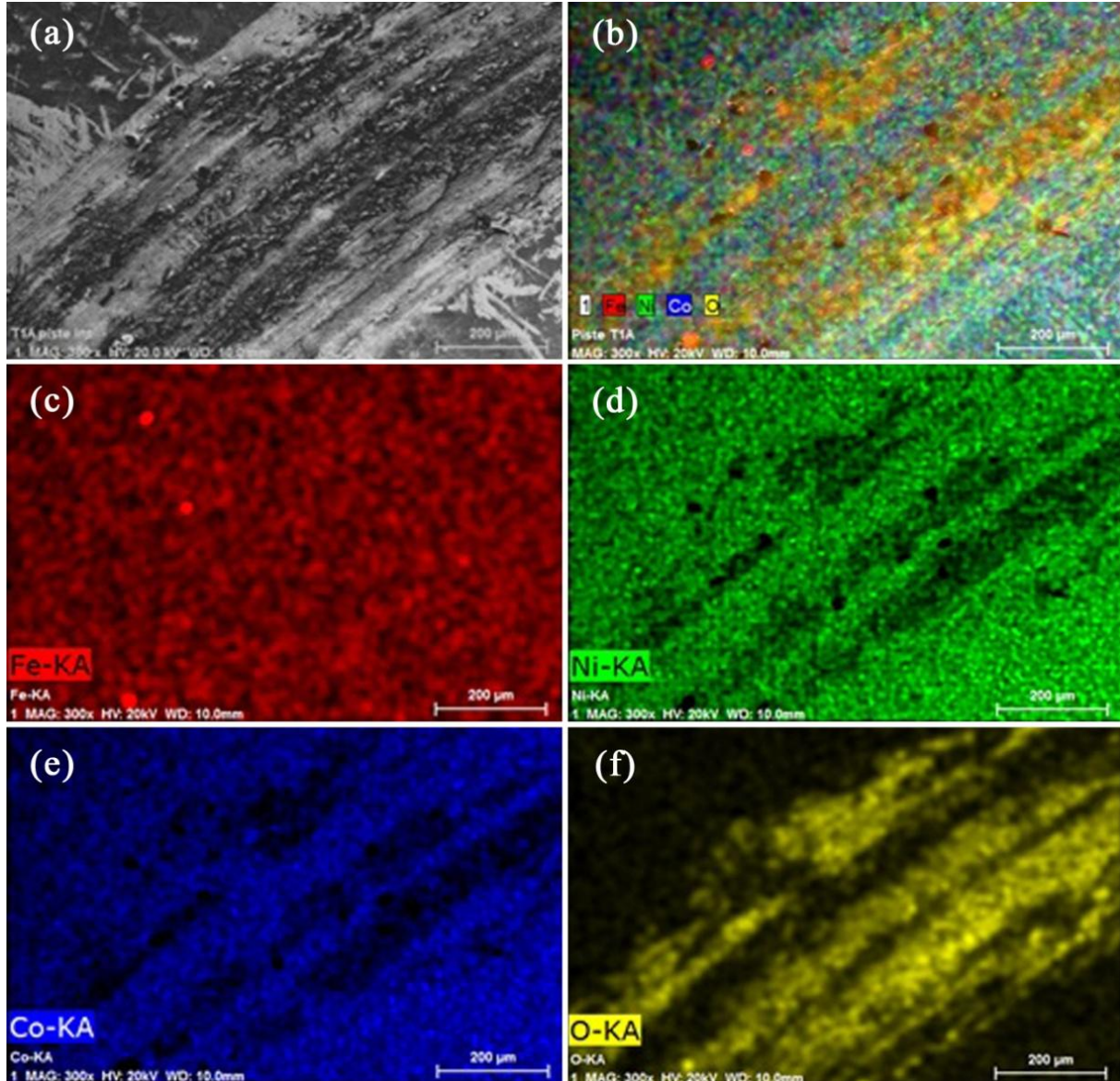


Figure III.13: SEM micrograph and EDS elemental mapping of the wear track of Ni-Co coated substrate.

EDS profile along the wear track widths of uncoated and Ni-Co coated substrates are shown in [Figure III.15 \(a\)](#) and [\(b\)](#), respectively. According to [Figure III.15 \(a\)](#), the amount of Fe is decreased significantly in the worn surface of substrate compared with the unworn surface, which confirms the abrasive mechanism nature of wear, while the amount of oxygen is increased which confirms the oxidative nature of wear. Moreover, the oxygen and iron amounts are almost constants and not much fluctuate along the width of wear track except in the gray

untouched zones, confirming that the predominant mechanism in the wear of uncoated substrate is the abrasive oxidative mechanism.

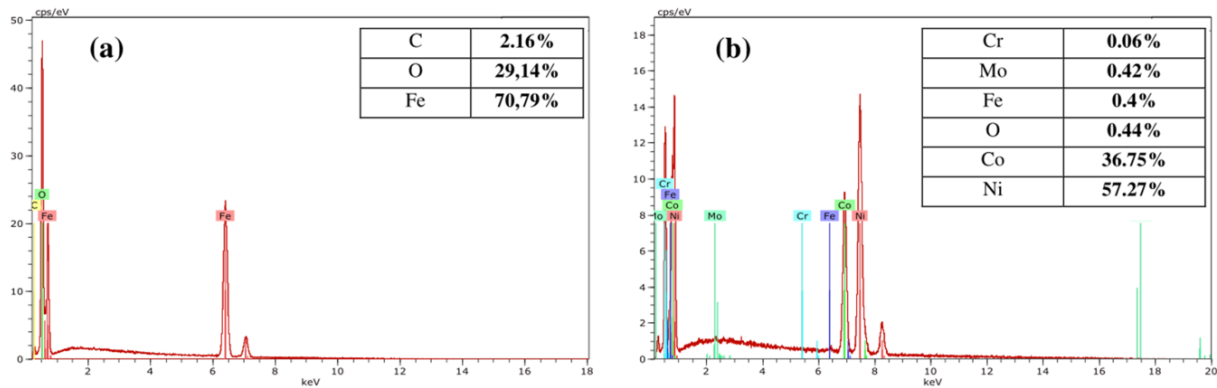


Figure III.14: EDS spectrum of selected zones on the worn surfaces of uncoated StW24 substrate (a) and Ni-Co coated substrate (b).

According to [Figure III.15 \(b\)](#), the amounts of Ni, Co and O are fluctuated along the width of the wear track of Ni-Co coated substrate while the percentage of iron is constant. The fluctuation in Ni, Co and O contents is another sign for the discontinuous tribofilm containing oxygen that is attributed to the mixed mode of adhesive-abrasive oxidative wear mechanism of Ni-Co alloy. In contrast, the EDS elements profiles and SEM images are characterized by two areas appear alternately on the worn surface ([Figure III.15 \(b\)](#)). The abrasive oxidative wear leads to the diminution of Ni, Co contents and the increasing of O content (smooth white areas). While the adhesive oxidative wear due to the oxidation of Ni₆₃-Co₃₇ coating without the diminution of Ni and Co percentages (dark areas covered by debris). In the other hand, [Figure III.15 \(b\)](#) shows that the cobalt percentage exhibits much slow decreasing compared with Ni percentage, indicating that the introduced Co has much more resistance to wear compared with Ni lattice. It is believed that there are two reasons behind the better wear resistance of Co. The first one is the forced accommodation of Co atoms with the greater atomic radius in the fcc nickel lattice ([Figure III.7](#)) which leads to a larger mismatch of the nickel lattice engenders higher internal stress, making the ejection of cobalt much more difficult. The second reason suggested that in the present research cobalt has a higher oxidation resistance than nickel. Therefore, nickel debris has been fully oxidized prior to the completely cobalt oxidation. The NiO film produced by the superficial diffusion of Ni prevented the cobalt oxidation. The above results confirm the results of our previous study [28], concluding that the addition of cobalt on the nickel lattice leads to the enhancement of its wear resistance.

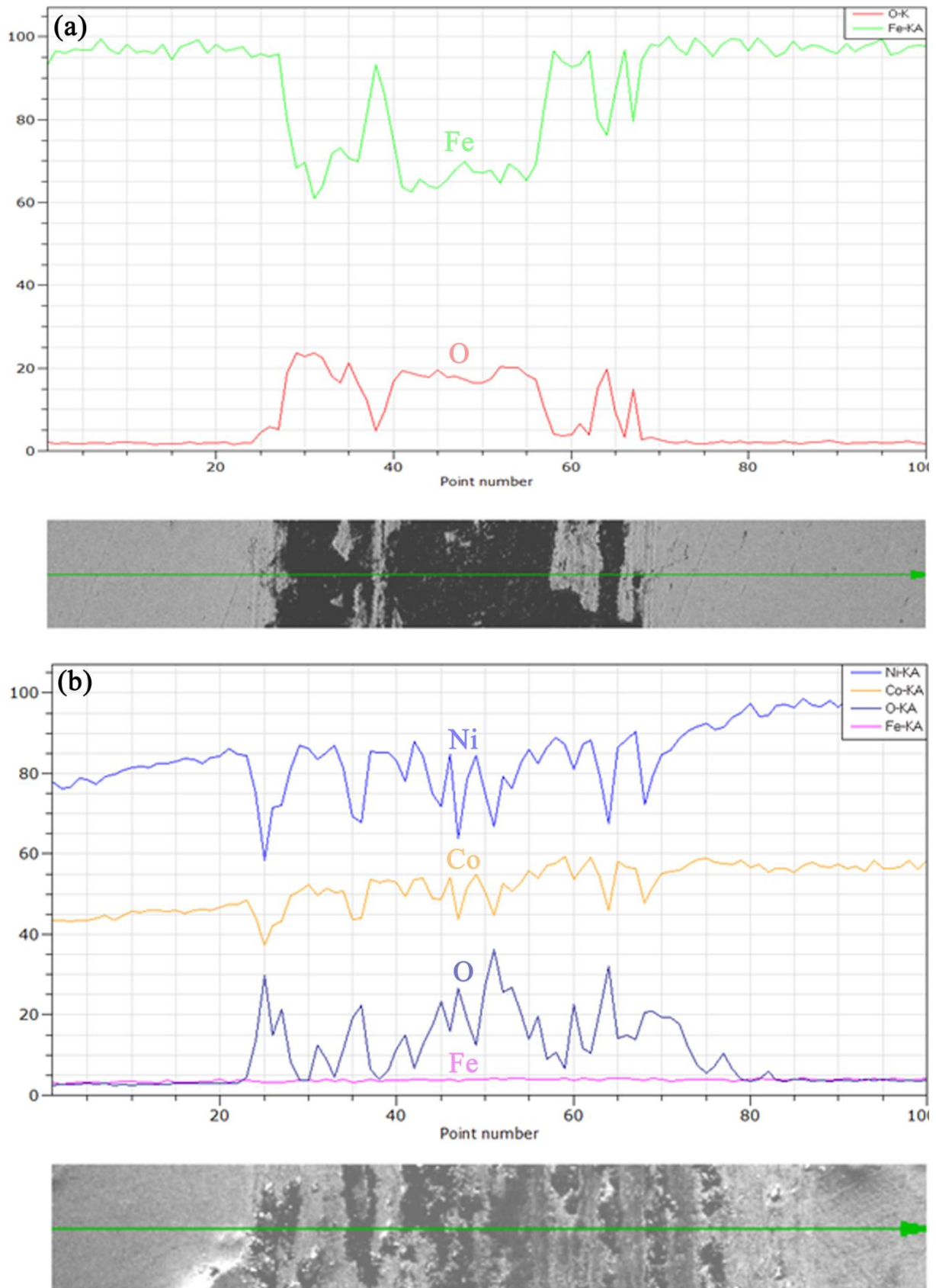


Figure III.15: EDS profile along the wear track widths of uncoated (a) and Ni-Co coated substrate (b).

The above discussions show that the wear rate, the coefficient of friction and the worn surface morphology show considerably different characteristics for the uncoated and Ni-Co coated substrate. The composition, the grain size, the surface roughness, the phase structure and the environmental conditions (temperature, oxidation, humidity, lubrication, etc.) have a significant influence on the wear characteristics of uncoated and Ni-Co coated substrate through the determination of the hardness and the physico-chemical interaction on the worn surface during the rubbing process. Consequently, the variations noticed in the wear characteristics of uncoated and Ni-Co coated substrate can be explained in terms of the composition, the morpho-structural characteristics and the environmental conditions. The correlation between the tribological behavior (friction and wear resistance) of the studied materials with the different affecting parameters in this study can be schematically summarized as shown in [Figure III.16](#).

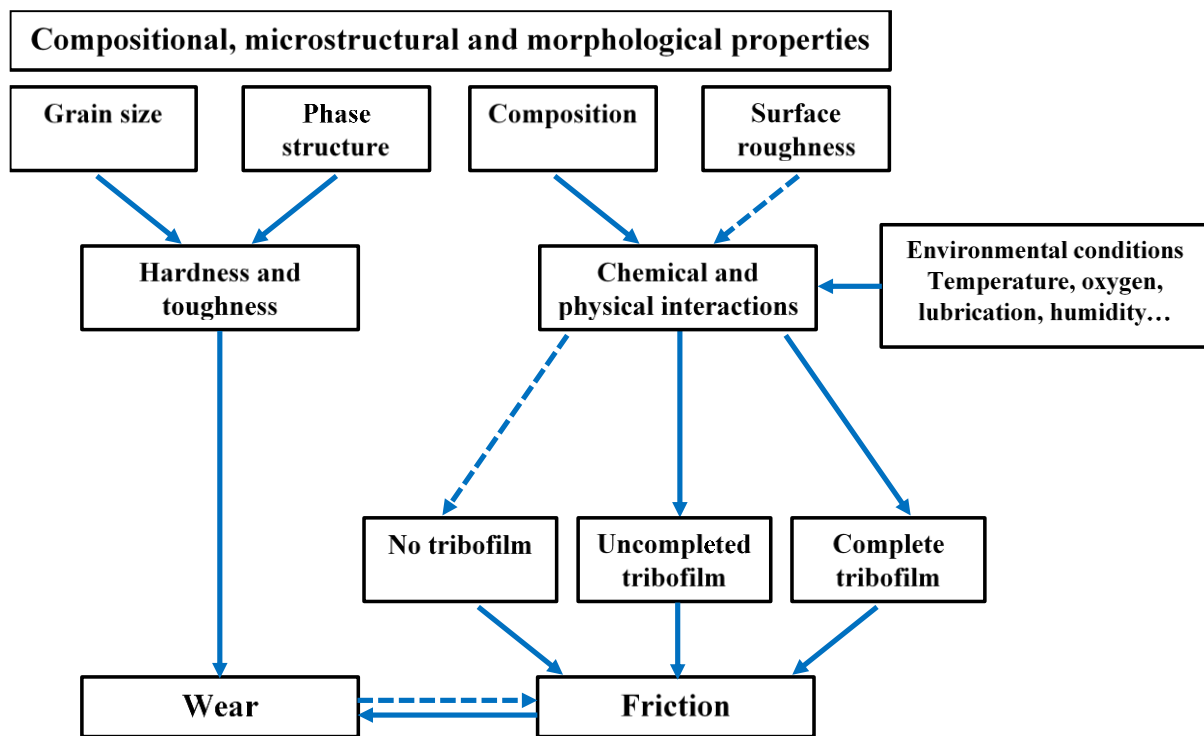


Figure III.16: Parameters influencing the tribological behavior of the studied materials, solid arrows indicate major effect while dashed arrows indicate slight effect.

III.3.2 Tribological performances of the nanocrystalline Ni-Co coating compared with nanocrystalline Ni coating

To prove the anti-wear performances of the electrodeposited Ni-Co coatings, it is necessary to compare its tribological properties with those of coatings commonly used for this purpose, namely, the pure electrodeposited Ni coating. That is done in the present study. Moreover, a correlation between the tribological properties and the morpho-structural characteristics is

established to understand the reasons behind the tribological behavior of each coating. Ni-Co coating with high cobalt content (87% Co) are electroplated for this purpose in this section, because Ni-Co coatings with small Co content (<50% Co) can exhibit properties close to those of pure Ni coatings.

III.3.2.a) Composition of the electrodeposited Ni-Co coating

Figure III.17 shows the masse percentage of cobalt and nickel in the electrolyte and in the electroplated Ni-Co coating. It is clear that the cobalt percentage in the coating (87%) is higher compared to that in the bath (47%), this despite that the concentration of Ni^{2+} ions in the bath is greater than that of Co^{2+} ions. This means that the anomalous co-deposition mechanism of Ni-Co alloys still exists, even at high cobalt concentration in the electrolyte. However, by referring to the section (III.3.1.a), it can be noted that the ratio $\text{Co}_{\text{deposit}}/\text{Co}_{\text{electrolyte}}$ decreased from 4.62 in $\text{Ni}_{63}\text{-Co}_{37}$ deposition to 1.83 for $\text{Ni}_{13}\text{-Co}_{87}$ deposition, which means that the abnormality degree is decreased by the increase of Co content in the bath. It should be mentioned that, a detailed discussion regarding the effect of the electrolyte cobalt content on the abnormality degree is given in CHAPTER IV.

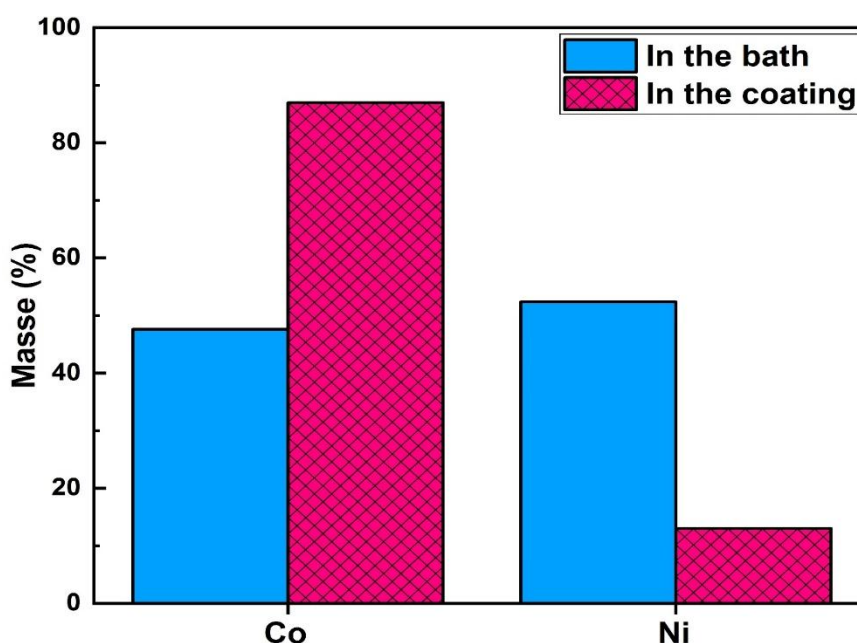


Figure III.17: Co and Ni mass percentages in the electrolyte and in the electroplated $\text{Ni}_{13}\text{-Co}_{87}$ coating.

III.3.2.b) Morphological and microstructural properties

SEM observations on the surfaces of the electroplated nanocrystalline Ni and $\text{Ni}_{13}\text{-Co}_{87}$ coatings are shown in Figure III.18. The nanocrystalline pure Ni coating is characterized by a dense and relatively smooth surface with a pyramidal grains structure (Figure III.18 (a)), which is a

common morphology for Ni and Ni rich coatings with a single fcc phase structure [30,35,41]. While Ni₁₃-Co₈₇ coating is characterized by a branched-porous (fiber-like) morphology with acicular crystallites between 0.3 and 0.8 μm in length, where the presence of a microscopic porosity in this later can be clearly observed (Figure III.18 (b)). Similar branched-porous morphology was observed for Ni-Co electrodeposits with high Co content (>50% Co) in some previous studies [134,177,185]. As can see in the XRD spectrums of the two coatings in Figure III.20, the change of the surface morphology from pyramidal in pure Ni coatings to branched-porous in Ni-Co coating is related to the change of the crystal phase structure from fcc to hcp phase following the addition of high cobalt content (87%) to the Ni coating. This indicates that the addition of cobalt has a significant influence on the surface morphology and structure of the nanocrystalline Ni deposits.

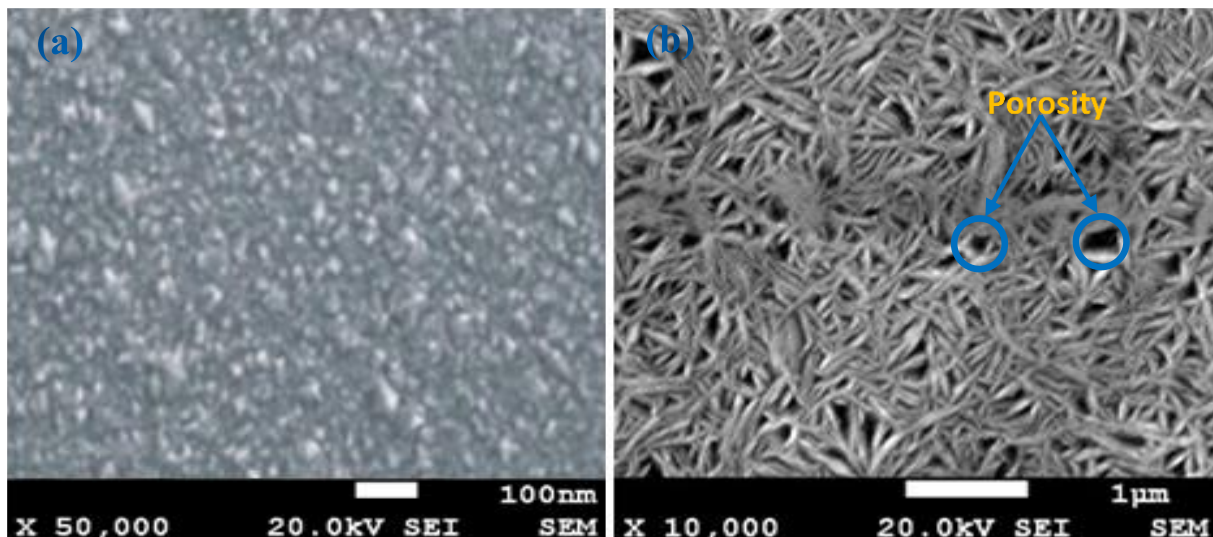


Figure III.18: SEM observations on the surface of the nanocrystalline pure Ni coating (a) and Ni₁₃-Co₈₇ coating (b).

Moreover, Ni₁₃-Co₈₇ coating shows a surface morphology very different to colony-like morphology of Ni₆₃-Co₃₇ (Figure III.6 (a)), which means that the cobalt content in the coating has also a great effect on the morphostructural properties of Ni-Co coatings. This, in addition to other clearly observed differences in the microstructural and mechanical characteristics of the two coatings, prompted us to study in detail the effect of cobalt content on the properties of Ni-Co coatings in the next chapter. On the other hand, despite the existence of a significant porosity rate in the Ni₁₃-Co₈₇ coating structure but no macro-cracks can be observed on the surface of these deposits, this may be due to the role of saccharin and BD as anti-stress agents as clearly explained in section (III.3.1.b).

Despite the fact that the scanned surface is not the same, but the atomic force microscopy (AFM) imaging results are consistent with the SEM results. It can be clearly seen in [Figure III.19 \(a\) \(c\)](#) that the morphology changes from a smooth granular structure to a fiber-like one when 87 wt.% Co is added to the nanocrystalline pure Ni coatings. This change in the morphology with the addition of high Co content to pure Ni coatings leads in turn to the increase in the roughness of the coatings as can be seen in [Figure III.19 \(b\) \(d\)](#).

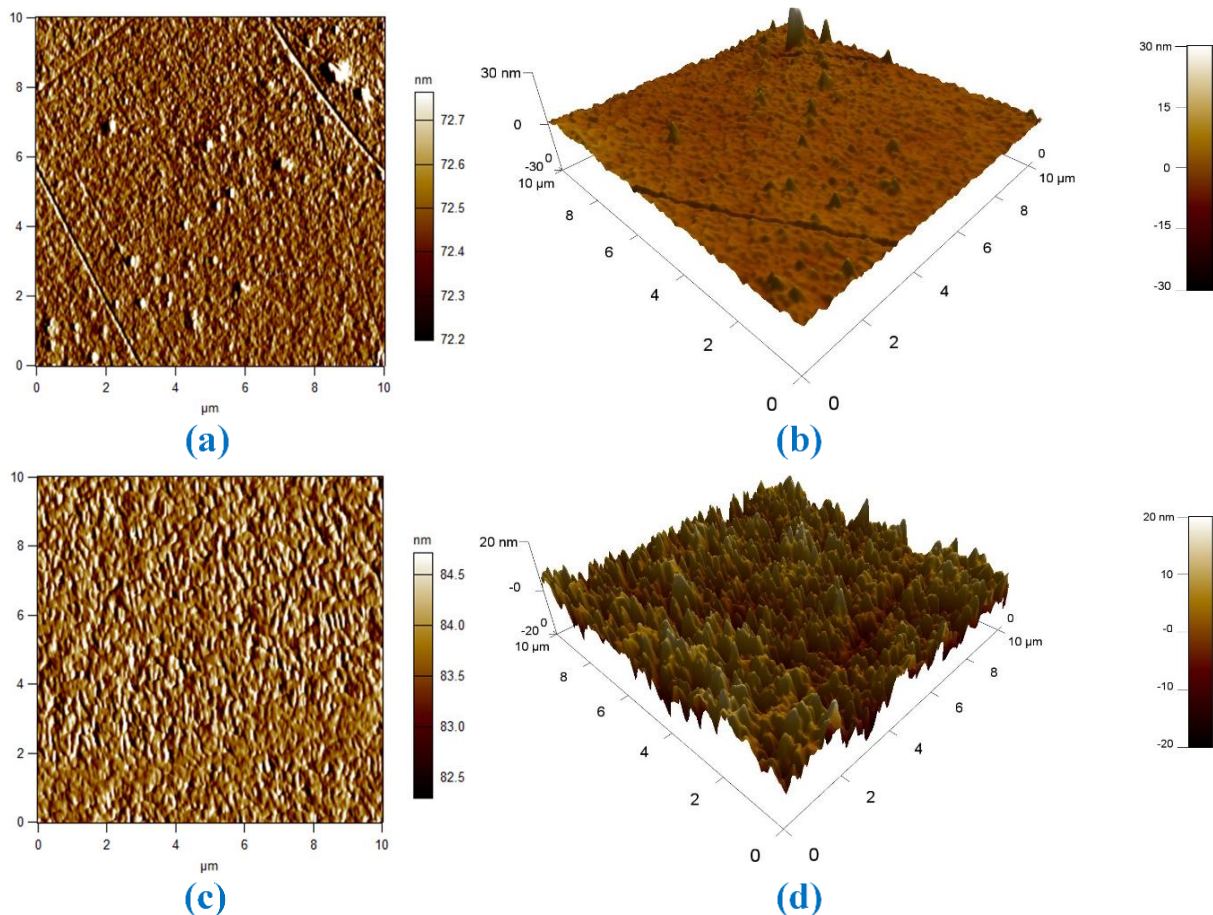


Figure III.19: 2D and 3D imaging of the surface of nanocrystalline Ni coating (a)-(b) and Ni-Co coating (c)-(d).

XRD patterns of the electrodeposited Ni and Ni₁₃-Co₈₇ coatings presented by [Figure III.20](#) show that the addition of high cobalt concentration changes completely the crystal structure of nanocrystalline Ni coatings. It can be seen that the pure Ni deposits are characterized by a single α (fcc) phase structure which is a common structure of Ni and Ni-rich Ni-Co alloy coatings ([Figure I.10 \[91\]](#)). However, the addition of high cobalt content leads to a complete disappearing of the fcc phase and a new ϵ (hcp) phase which is a common structure of nanocrystalline Co and Co rich alloys coatings is appeared ([Figure I.10](#)). Similar changes in the crystal structure by the addition of high Co amounts were noted in the previous studies

[32,130,186]. It is worth noting that the effect of Co content on the crystal structure of Ni-Co coatings is studied and discussed extensively in Chapter IV. On the other hand, the consolidation of (111) and (100) crystallographic orientations instead (200) and (101) directions commonly found in the massifs of Ni and Co rich Ni-Co alloys is clearly noted in the XRD patterns of the elaborated Ni and Ni₁₃-Co₈₇ coatings, respectively. This is may be explained by the role of the adsorbed organic additive molecules, namely the saccharin as shown in the section (III.3.1.b).

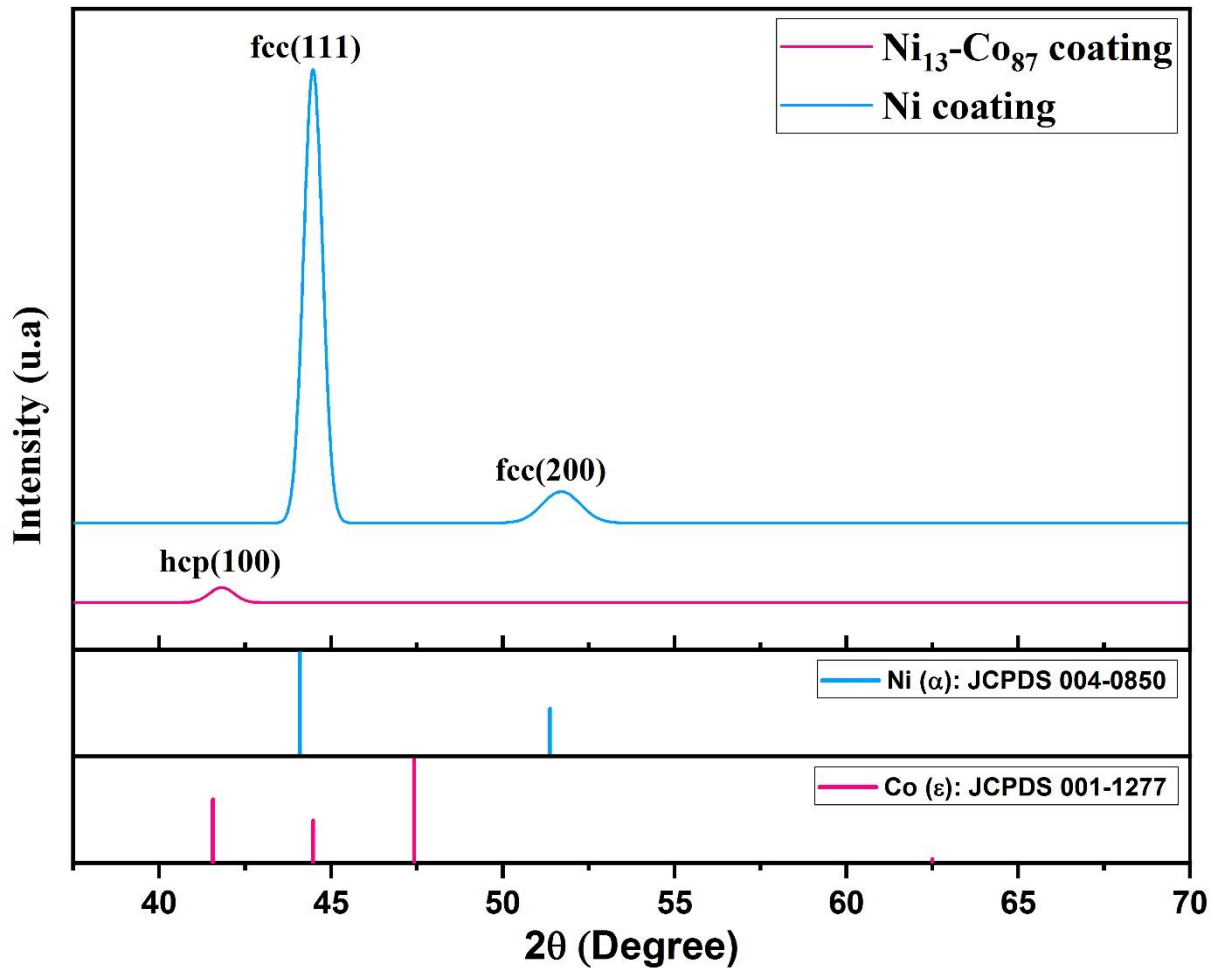


Figure III.20: X-ray diffraction spectrums of Ni and Ni₁₃-Co₈₇ nanocrystalline coatings.

III.3.2.c) Microhardness

Figure III.21 (a) shows the microhardness of the nanocrystalline Ni and Ni₁₃-Co₈₇ alloy coatings, whereas Figure III.21 (b) shows the grains size of the two coatings deduced from XRD peak broadening analysis using the following Scherrer formula [162]:

$$D = \frac{k\lambda}{\beta \cos\theta} \quad (\text{III.8})$$

Where D is the average crystallites size, λ is the X-rays wavelength in nanometer, $\lambda_{CuK\alpha_1} = 0.15405\text{nm}$ in our case, β is the peak width of the most intense diffraction peak profile at half maximum height in radians, k is a numerical factor related to the crystallites shape, normally taken as 0.9 and θ is the Bragg angle. According to Figure III.21 (a) Ni coating with a microhardness of about 580 HV0.05 is relatively hard; however, the microhardness reduces following the addition of high amount of Co to reach a value of about 305 HV0.05 in Ni₁₃-Co₈₇ coating. This hardness decrease is mainly due to the crystallites size of the Ni-Co coating higher nearly twice than that of pure Ni electrodeposits as can be seen clearly in Figure III.21 (b). Where, the decrease of the hardness of the electrodeposited coatings with the increase of crystallites size can well described mathematically using the classical Hall-Petch relationship (eq.III.6 [172]). Furthermore, the decrease in microhardness of Ni coating after its alloying with high cobalt amount is attributed also to the significantly porosity rate can be seen clearly in their branched-porous morphology as shown in Figure III.18 (b).

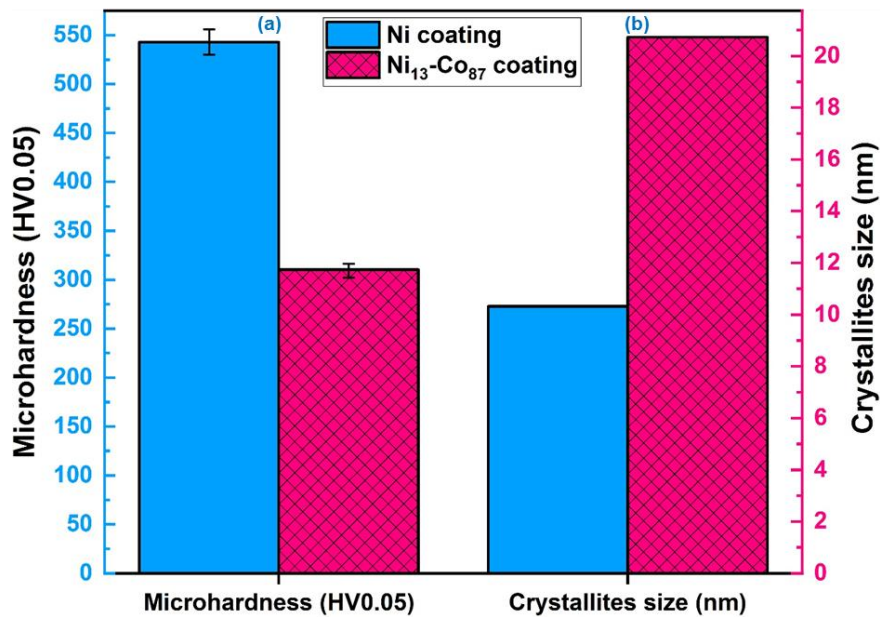


Figure III.21: The microhardness (a) and the crystallites size (b) of the electrodeposited Ni and Ni₁₃-Co₈₇ coatings.

III.3.2.d) Tribological behavior

The friction coefficient as function of time of the nanocrystalline Ni and Ni₁₃-Co₈₇ coatings measured under dry sliding conditions (without lubrication) is shown in Figure III.22. It is clear that the friction coefficient of Ni-Co alloy coating is lower by about five times than that of pure Ni coatings. Otherwise, the friction coefficient of Ni-Co alloy coating is much more stable than that of the pure Ni deposit. Combined with the morphostructural properties of the elaborated

coatings, the excellent friction-reduction behavior can be explained by the changes in the morphology and crystal structure of the Ni coating following its alloying with Co; especially, the total transition of the crystal structure from α (fcc) to ϵ (hcp) crystal phase. This later phase gives the material a lubrication effect and very good anti-wear performances according to several previous studies [39,177,187].

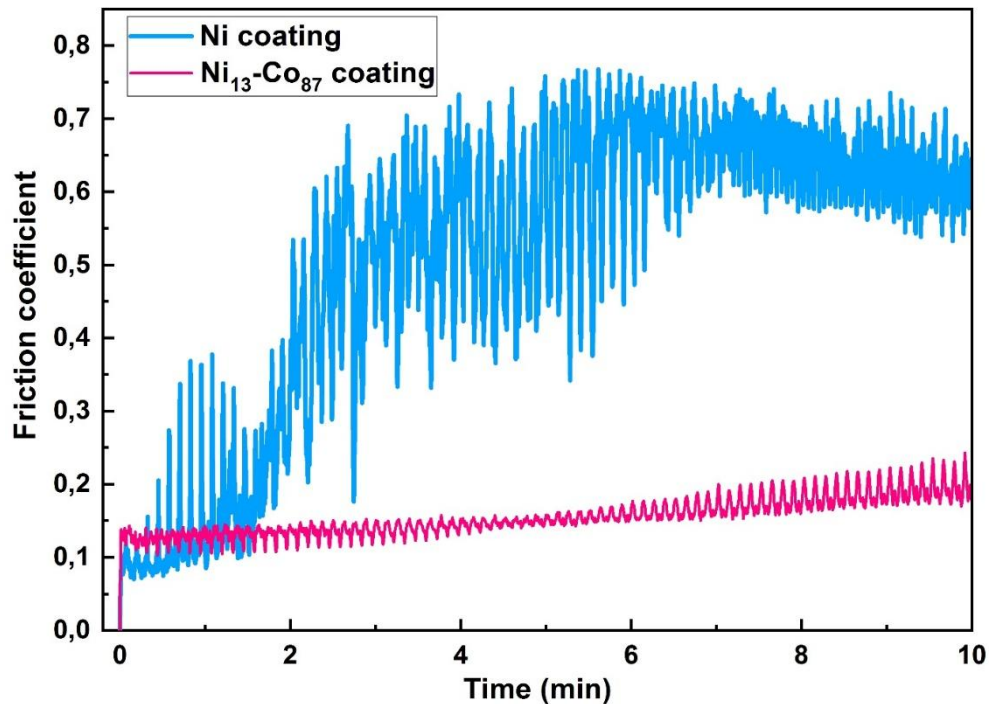


Figure III.22: Friction coefficient of the electrodeposited Ni and Ni₁₃-Co₈₇ coatings.

The wear rates of the two electroplated coatings under identical sliding conditions evaluated using the equation (II.9 [150]) are represented in Figure III.23. It can be noted that the Ni-Co alloy deposit have a wear rate about eight times lower compared to the pure Ni deposit, which is a sign of a very significant improvement in the wear resistance of Ni coating after its alloying with 87% of Co. This improvement is happened despite the decrease in the microhardness to almost the half following the cobalt addition on Ni coating as shown in Figure III.21, what contradicts the Archard's law expressed by the equation (eq.III.7 [177]). This reversed Archard's law can be attributed essentially to the special excellent anti-wear ϵ (hcp) crystal phase of the Co-rich Ni-Co coating. This effect can be explained also by the role of debris and tribofilm on the wear behavior of the coatings. Where existing research results [39,107,177] show the negative effect of the formation of tribofilms on the anti-wear performances of Ni and nickel-rich coatings. This undesirable debris film leads to a high and unstable friction coefficient, consequently to a high wear rate. A tribofilm of compacted wear debris can be

observed clearly in the worn surface of pure Ni coating, while there is no evidence of a tribofilm on the worn surfaces of the electrodeposited cobalt-rich Ni-Co coating (Figure III.24).

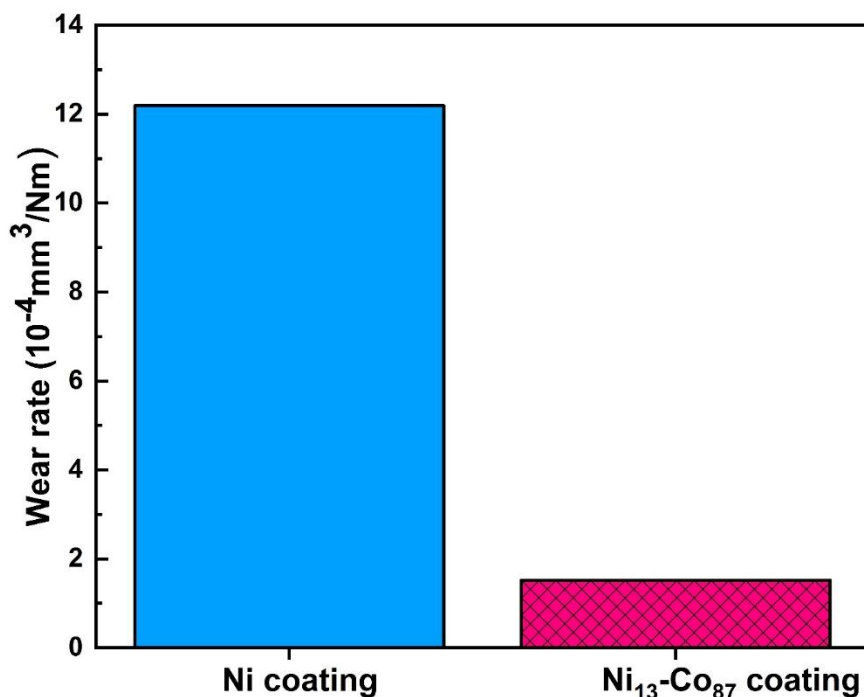


Figure III.23: The wear rate of the electrodeposited Ni and Ni₁₃-Co₈₇ coatings.

To understand and explain more the diversity between the wear behavior of pure Ni and Ni₁₃-Co₈₇ coatings, the worn surface morphologies can be observed microscopically as shown in Figure III.24. The appearance of a tribofilm that leads to a wide wear rate of pure Ni coatings is clearly observed in the worn surface of α (fcc) structured Ni coating subjected to the wear constraints (Figure III.24 (a), (b) and (c)). The appearance of tribofilm in this case is due to the harsh deformation in the sliding direction under the compression and shear constraints and the adhesive-oxidative wear mechanism of the pure Ni coating (the mechanism of a partial tribofilm formation is the same as explain for Ni₆₃-Co₃₇ in the section (III.3.1.d)). Moreover, Ni coating with the ductile α (fcc) phase shows a big tendency to plastic deformation resulting in high formation of asperity spots which leading in turn to a high and unstable friction coefficient of pure as shown in Figure III.22. In comparison with pure Ni deposit, there is no tribofilm appearance in the worn surface of Ni₁₃-Co₈₇ coating with ϵ (hcp) crystal structure; the worn surface in this case becomes dense and reveals less adhesion wear and smooth surface with very smaller smashed spots, where just some scars are remarked on the worn surface (Figure III.24 (d), (e) and (f)). This came out with better wear resistance of Ni₁₃-Co₈₇ alloy coating compared with Ni coating. That is also the cause behind the friction coefficient of Ni-Co alloy coating

much more stable and about five times lower than that of Ni coatings. The above tribological analyses results are in good agreement with the study of C. Ma et al [39] and L. Wang et al [177] regarding the influence of high Co addition on the tribological behavior of nanocrystalline and microcrystalline Ni coatings, respectively. Otherwise, it can be seen clearly that the Ni-Co wear tracks are much narrower and shallower compared to those of the pure nickel coating. That is another sign about the wear rate of Ni-Co coating very lower compared the pure Ni coating. These observations well coincide with the obtained results of wear rates evaluated by the weight loss (Figure III.23).

III.4 CONCLUSIONS

In the present chapter of the study, homogenous nanocrystalline Ni, Ni₆₃-Co₃₇ and Ni₁₃-Co₈₇ coatings with very good hardness-toughness combination and high adhesion to substrate was successfully electrodeposited on StW24 mild steel. The compositional, morphological, structural and tribological characteristics of StW24 mild steel substrate and the electrodeposited coatings were investigated. The performances of Ni-Co coatings as anti-wear coating on the Stw24 mild steel substrate were examined and compared with that of the pure Ni coating. The following important conclusions can be drawn from the different characterizations and comparisons:

- (1) XRF analysis showed that the electrodeposition of Ni-Co alloys follows an anomalous co-deposition mechanism where the less noble metal (Co) deposited preferentially compared to the more noble metal (Ni). This anomalous co-deposition mechanism of Ni-Co alloys still exists, even at high cobalt concentration in the electrolyte ($\approx 48\%$ Co) but with a reduced abnormality degree in this case.
- (2) The XRD patterns of the electroplated Ni and Ni-Co coatings showed that the addition of organic additives, namely, saccharin and BD in the electrolyte leads to crystallites size in the nanometric order. It leads also to the predominance of (111) as preferential crystallographic orientation instead of the (200) direction normally found in Ni and Ni-rich Ni-Co coatings, and the consolidation of (100) instead of the (101) direction usually existing in Co-rich Ni-Co coatings. Furthermore, the XRD patterns showed that Ni and Ni₆₃-Co₃₇ coatings characterized by a single α (fcc) phase structure. However, the addition of high cobalt amount leads to the transformation total of the phase structure to ϵ (hcp) structure as shown in the XRD pattern of Ni₁₃-Co₈₇ coating.

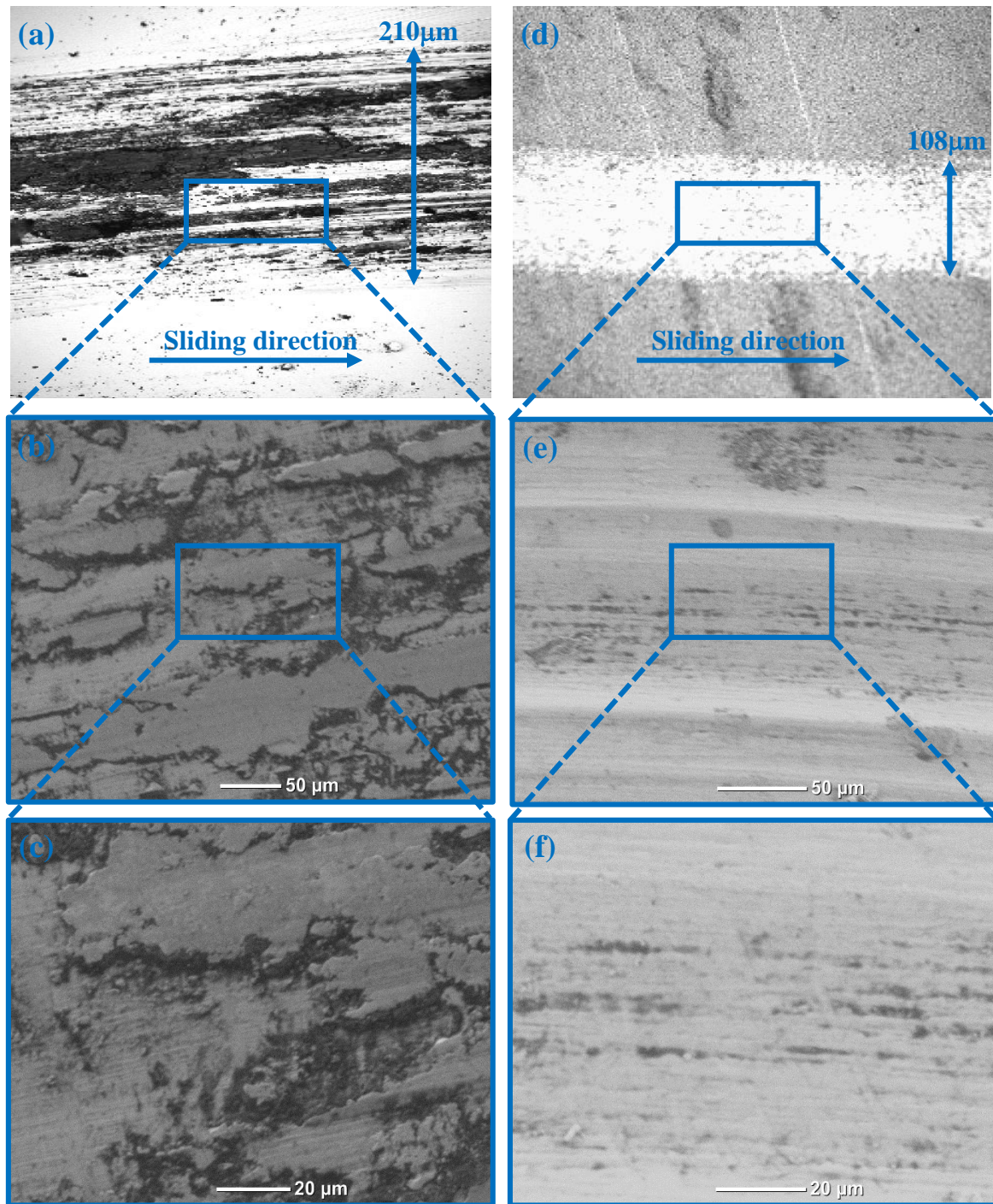


Figure III.24: SEM observation with different magnifications on the wear tracks of pure Ni coating (a) (b) (c) and Ni₁₃-Co₈₇ coating (d) (e) (f).

(3) SEM observations on the surfaces of the elaborated Ni and Ni-rich (Ni₆₃-Co₃₇) coatings revealed that these later are characterized by a pyramidal and colony-like morphologies, respectively. However, the addition of high cobalt content causes the change of these smooth morphologies to relatively rough branched-porous morphology in Ni₁₃-Co₈₇ coating; which is related to the change of the crystal phase from α (fcc) to ϵ (hcp) structure.

(4) Despite that the hardness of Ni is not very much higher than that of StW24 steel but the coating of this latter by the nanostructured Ni₆₃-Co₃₇ alloy led to the multiplication of its hardness about three times, which is attributed to the solid solution hardening of nickel by cobalt. The relatively high hardness of Ni-Co deposit is due also to the grain boundary strengthening (Hall-Petch hardening) thanks to the nanometric crystallites size of the coating. In the other hand, the microhardness of nanocrystalline Ni coatings reduced with the increase of the grains size of the coatings following the addition of high cobalt content, indicating that the microhardness of these electrodeposits follows the Hall-Petch effect.

(5) Ni-Co coated StW24 steel substrate showed less wear rate and high wear resistance compared with the uncoated substrate under the two applied loads 5 and 10N and this despite its relatively higher friction coefficient, this can be explained by the very high hardness of Ni-Co alloy coating compared with StW24 steel substrate, which is corresponding to Archard law. On the other hand, Ni₁₃-Co₈₇ alloy coating showed much lower friction coefficient and higher wear resistance compared with pure Ni coating. The decrease in the wear rate is happened regardless the decrease in the microhardness to almost the half what contradicts the Archard law. It is believed that this inversed Archard law effect was due to the significant friction-reduction following the total phase transition to ϵ (hcp) phase in Co-rich Ni-Co alloy coatings.

(6) The analyses of worn surface morphologies of uncoated and Ni-Co coated StW24 steel substrate by SEM and EDX showed that no tribofilm exists in the wear tracks of the uncoated and Ni₁₃-Co₈₇ coated substrates. Nevertheless, a partial tribofilm contains oxygen, resulting from the mixed abrasive-adhesive wear mechanism was observed clearly on the worn surfaces of Ni and Ni-rich Ni₆₃-Co₃₇ coating. It is worth noting that the tribofilm formation on the worn surface have a negative influence on the friction and wear behavior of the studied materials. Where, the absence of this debris film in the worn surfaces of uncoated and Ni₁₃-Co₈₇ coated substrate was translated by very low and stable friction coefficients. However, the partial tribofilm observed on the worn surfaces of Ni and Ni₆₃-Co₃₇ coating is responsible for their high and unstable friction coefficients that influence negatively on their anti-wear performances.

Chapter IV:

*Effect of the
electrodeposition conditions
on the properties of Ni-Co
coatings*

CHAPTER IV: Effect of the electrodeposition conditions on the properties of Ni-Co coatings

IV.1 INTRODUCTION

From the previous chapter, it was demonstrated that Ni-Co coatings have excellent anti-wear properties, however, it was clearly noticed that the morphostructural, mechanical and tribological properties of the Ni-rich coating (Ni₆₃-Co₃₇) and the Co-rich coating (Ni₁₃-Co₈₇) are very different. For this purpose, we plan in this chapter to study the effect of the cobalt content on the morphological, microstructural, mechanical and tribological properties of Ni-Co coatings. As discussed in chapter I, the Co content of coatings can be controlled not only by the Co content of the electrodeposition bath. Indeed, previous studies show that other electrodeposition parameters such as bath additives, current type and density, pH, temperature, agitation, etc. can have a significant effect on the composition and on all the properties of Ni-Co alloy coatings. In addition to the cobalt concentration, we are interested in this chapter in the effect of other parameters which are not covered in the previous studies, namely the effect of bath temperature, the nature of the substrate and the deposition time on the mechanical and anti-wear properties of Ni-Co coatings. Such a study can allow us to optimize the electrodeposition parameters to obtain an efficient Ni-Co anti-wear coating and to test the maintainability of its performances on different substrates and with different thicknesses.

IV.2 EXPERIMENTAL DETAILS

IV.2.1 Coatings electrodeposition

For the study of the effect of electrodeposition conditions and parameters on the different characteristics of Ni-Co coatings, various parameters and conditions are applied for this purpose in this chapter. The standard and varied parameters used for the electrodeposition of Ni-Co coatings in this study are summarized in [Table IV.1](#).

IV.2.2 Compositional, morphological and microstructural characterizations

The morphological properties of the electrodeposited Ni-Co coatings are investigated using a scanning electron microscope (SEM) and a confocal microscope. The composition of the coating is determined using X ray fluorescence spectrometer (XRF) and Energy-dispersive X-ray spectrometer (EDS). The roughness and the thickness of coatings are measured using a

mechanical profiler; five measurements are made on each sample. The crystal structure of coatings is studied by the use of X-ray diffractometer (XRD).

Table IV.1: Experimental parameters and conditions used for the electrodeposition of the different coatings.

THE STANDARD CONDITIONS						
Composition of the electroplating bath (g/l)						
NiSO₄	NiCl₂	CoSO₄	H₃BO₃	Saccharin	BD	SDS
200	20	20	30	2	0.5	0.2
Electrodeposition parameters						
Current density	Temperature	Electrolyte pH	Agitation rate	Duration		
4 A/dm ²	45 °C	4.2±0.05	200 rpm	60 min		
THE VARIED CONDITIONS						
Study of the Co content effect						
Co content in the bath (g/l)	0	40	80	120	160	200
Study of the temperature effect						
Bath temperature (°C)	25	45	65	85		
Study of the electrodeposition duration effect						
Electrodeposition duration (min)	30	60	90	120		
Study of the substrate nature effect						
Substrate nature	Steel		Copper		Brass	

IV.2.3 Mechanical and tribological characterizations

The microhardness and the nanohardness of the electroplated coatings are determined using Vickers micro-indenter and Berkovich nano-indenter, respectively. The different parameters used for the micro and nano indentations tests are listed in Table IV.2. The tribological behavior of the coating is studied using pin on disc tribometer under dry sliding wear conditions using the sliding parameters mentioned in Table IV.2. All the tribometric analyses are performed at room temperature under 28-44% of humidity. AISI 1040 hard steel ball (Ø = 6mm, hardness =

700HV) and alumina ball ($\varnothing = 6\text{mm}$, hardness = 1900HV) are used as a pins. The friction coefficient in function of time is automatically computed during the test. The morphology and the composition of the worn surfaces are studied by SEM and EDS, respectively, while the wear rate is evaluated by measuring the mass loss using digital precision balance having an accuracy of $\pm 0.1\text{mg}$. The adhesion of the coating to substrate is evaluated by the use of scratch tester; the parameters applied for the scratch tests are listed in Table IV.2. The critical load (L_c) is surveyed by two different means.

Table IV.2: The experimental parameters used for the characterization of the mechanical and tribological properties of the electrodeposited coatings.

Microhardness measurements				
Applied load (g)		Holding time (s)		Number of indentations
10 to 50		15		5
Nanohardness measurements				
Applied load (mN)	Loading rate (mN/min)	Pause at maximum load (s)	Unloading speed (mN/min)	Number of indentations
200	400	10	400	9
Pin on disk tests				
Applied load (N)		Sliding time (min)		Sliding speed (mms^{-1})
3 to 10		15 to 30		5
Scratch tests				
Applied load (N)		Loading rate (mNs^{-1})		Loading mode
From 0 to 100		1.66		Progressive

IV.3 RESULTS AND DISCUSSIONS

IV.3.1 Effect of the bath Co content on the properties of the electrodeposited Ni-Co coatings

In the previous chapter, it was concluded that cobalt-rich Ni-Co alloy coatings ($\geq 50\text{ wt.}\% \text{ Co}$) exhibit better tribological properties compared to Ni and nickel-rich Ni-Co coatings. Moreover, previous studies have shown that the main factor that manages the different properties of Ni-Co alloy electrodeposits is their Co content that can be controlled mainly by the Co

concentration in the electrodeposition bath. For this purpose, in the present part, Co-rich Ni-Co coatings (or also Co-Ni coatings) are electrodeposited on StW24 steel substrate in baths containing different concentrations of Co^{2+} . The effect of Co concentration in the baths used to deposit them on their compositional, morphostructural, mechanical and tribological properties is examined. The variations of structure and morphology with the variation of Co content are correlated with the change in mechanical and tribological behavior of the coatings in order to well understand all these changes.

IV.3.1.a) Effect on the composition of coatings

The relationship between the concentration of cobalt in the electrolyte and in Ni-Co coatings electrodeposited at a fixed concentration of Ni^{2+} in the bath is shown in [Figure IV.1](#), it is clear that the Co content in the coatings increases gradually with increasing the concentration of Co^{2+} ions in the electrolyte. Thus, the percentage of Co in the deposits is always higher than that in the electrolyte, which means that the mechanism of anomalous codeposition of the Ni-Co alloy, explained extensively in section [\(III.3.1.a\)](#), is still valid regardless the concentration of Co^{2+} and Ni^{2+} ions in the bath. On the other hand, the abnormality degree is defined as the $M_{\text{deposit}}/M_{\text{electrolyte}}$ ratio, where M_{deposit} and $M_{\text{electrolyte}}$ are the percentages of Co in the deposit and in the corresponding electrolyte, respectively. According to [Figure IV.1](#), the abnormality degree is significantly reduced with increasing cobalt content in the electrolyte, meaning that the anomalous codeposition is favored in the baths with the lower Co content. These results are important insofar as reducing the degree of abnormality can lead to a decrease in the rate of codeposition and consequently to a decrease in the thickness of the deposits. It is worth noting that Dolati et al [\[188\]](#) and Tian et al [\[160\]](#) have obtained results comparable to those of this study.

IV.3.1.b) Effect on the morphostructural properties of coatings

SEM micrographs of the Ni-Co coatings electrodeposited at baths with different Co contents are shown in [Figure IV.2](#). The pure Ni electrodeposit is characterized by a granular smooth surface morphology [Figure IV.2 \(a\)](#). The surface morphology of the Ni-Co coating with a Co content of 74 wt.% is a mixture of smooth granular areas with branched (fiber-like) morphology, with a predominance of the latter [Figure IV.2 \(b\)](#). However, with further increasing of Co content, pores replace the smooth granular areas and the morphology becomes branched-porous in the Ni-Co coating with 87 wt.% Co content [Figure IV.2 \(c\)](#).

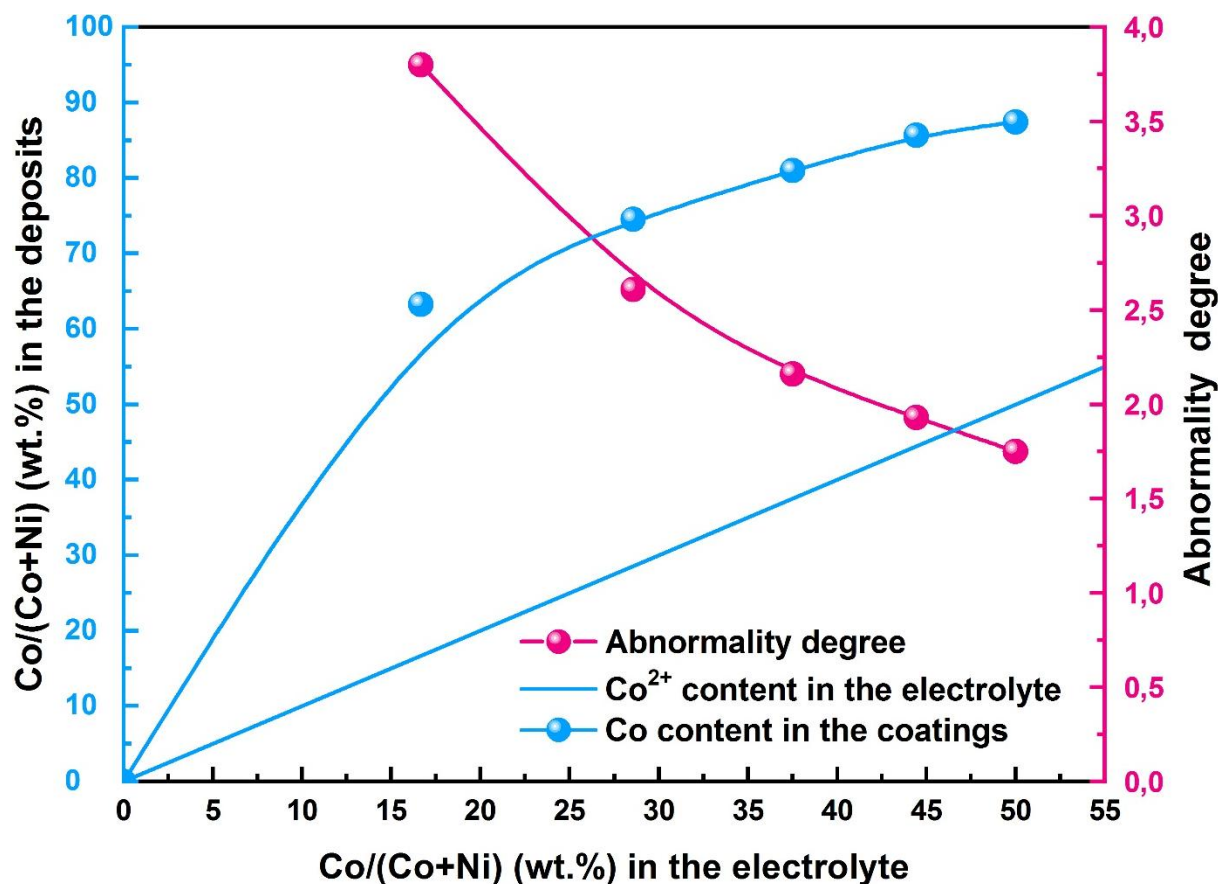


Figure IV.1: Co content in the electrodeposited Ni-Co coatings and abnormality degree vs. the Co concentration in the electrolyte.

The appearance of the fibrous morphology in the Co-rich Ni-Co coatings coincides well with the appearance of the ϵ (hcp) crystal structure, as can be clearly seen in the XRD patterns of the prepared Ni-Co coatings (Figure IV.3). The disappearance of the smooth granular zones is also associated with the total disappearance of the α (fcc) crystal structure and the transformation of the mixed structure (fcc + hcp) within the Ni-Co coating with 74 wt.% Co to a single ϵ (hcp) crystal structure within the Ni-Co coating with 87 wt.% Co. The increase in Co content in the coatings as a result of increasing the amount of Co added to the bath not only influences the morphology and structure of the coatings but also their thickness. The measurement of the thicknesses of the electrodeposited coatings by a mechanical profiler shows that the thickness of the Ni-Co coatings decreases from $55 \pm 5 \mu\text{m}$ to a value of about $42 \pm 5 \mu\text{m}$ with the increase of their Co content from 0 to 87 wt.%. This is probably due to the decrease in the codeposition rate following the decrease of abnormality degree as shown in Figure IV.1.

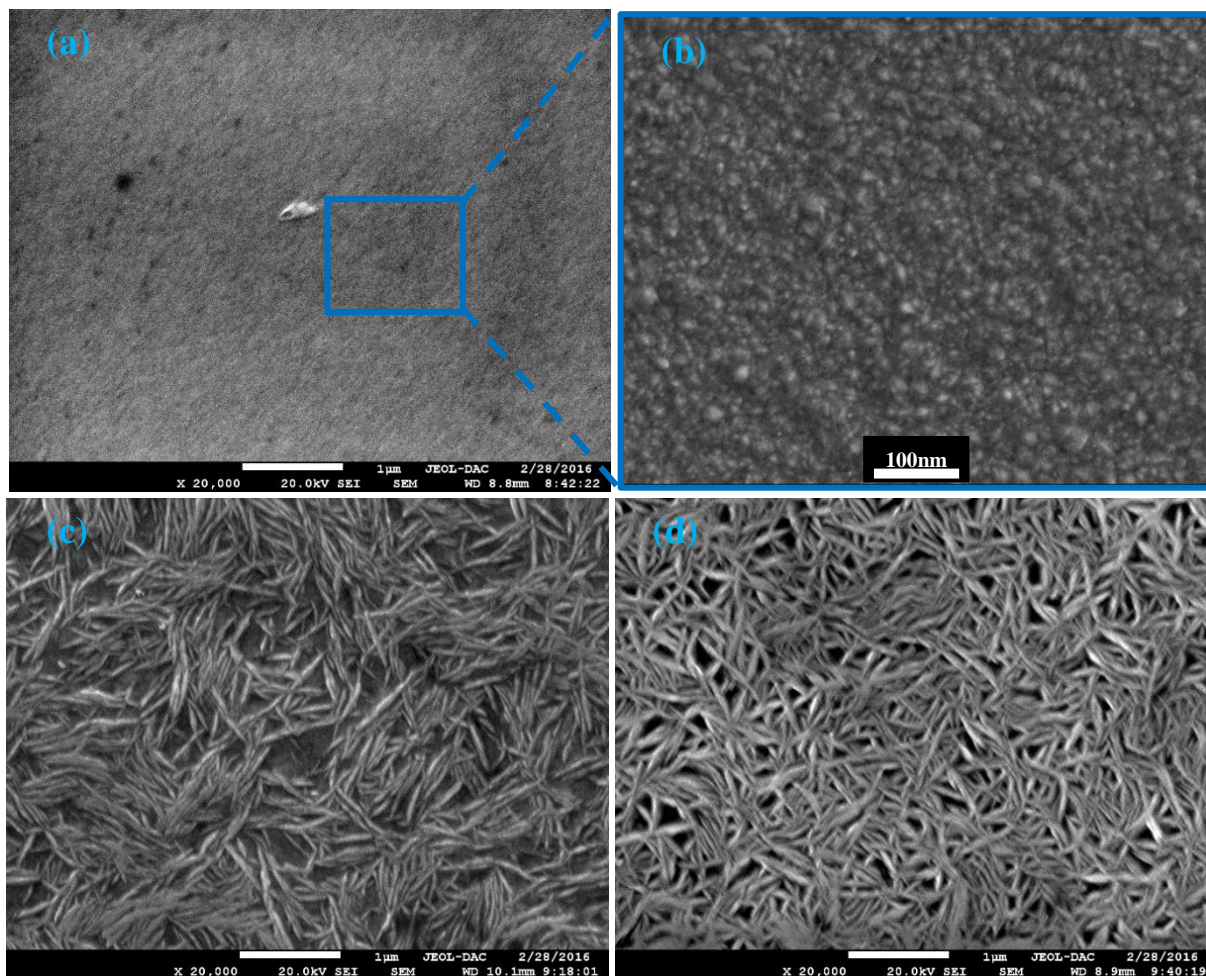


Figure IV.2: SEM micrographs of the electrodeposited coatings: (a) and (b) pure Ni, (c) with 74 wt.% Co and (d) with 87 wt.% Co.

XRD patterns of the electrodeposited Ni-Co coatings are presented in [Figure IV.3](#). It is clear that the Co content has a great influence on the crystal structure of the electrodeposited coatings. It can be seen that the pure Ni coating is characterized by a single α (fcc) phase structure. The Ni-Co deposit with 63 wt.% Co also displays the same single α (fcc) structure but with a remarkable decrease in peak intensity. The Ni-Co coating with 74 wt.% Co shows both α (fcc) and ϵ (hcp) phases but with a complete disappearance of the fcc (200) peak. While a complete disappearance of α (fcc) phase and a consolidation of ϵ (hcp) phase is noticed in the Ni-Co coating with 87 wt.% Co. This suggests that the crystal structure of Ni-Co coatings gradually changes from a full (fcc) lattice similar to that of pure Ni to a full (hcp) lattice similar to that of pure Co by increasing the Co content from 63 to 87 wt.%. Similar changes in the crystal structure by the addition of high amounts of Co to Ni electrodeposits have been noted in previous studies [32,130,186].

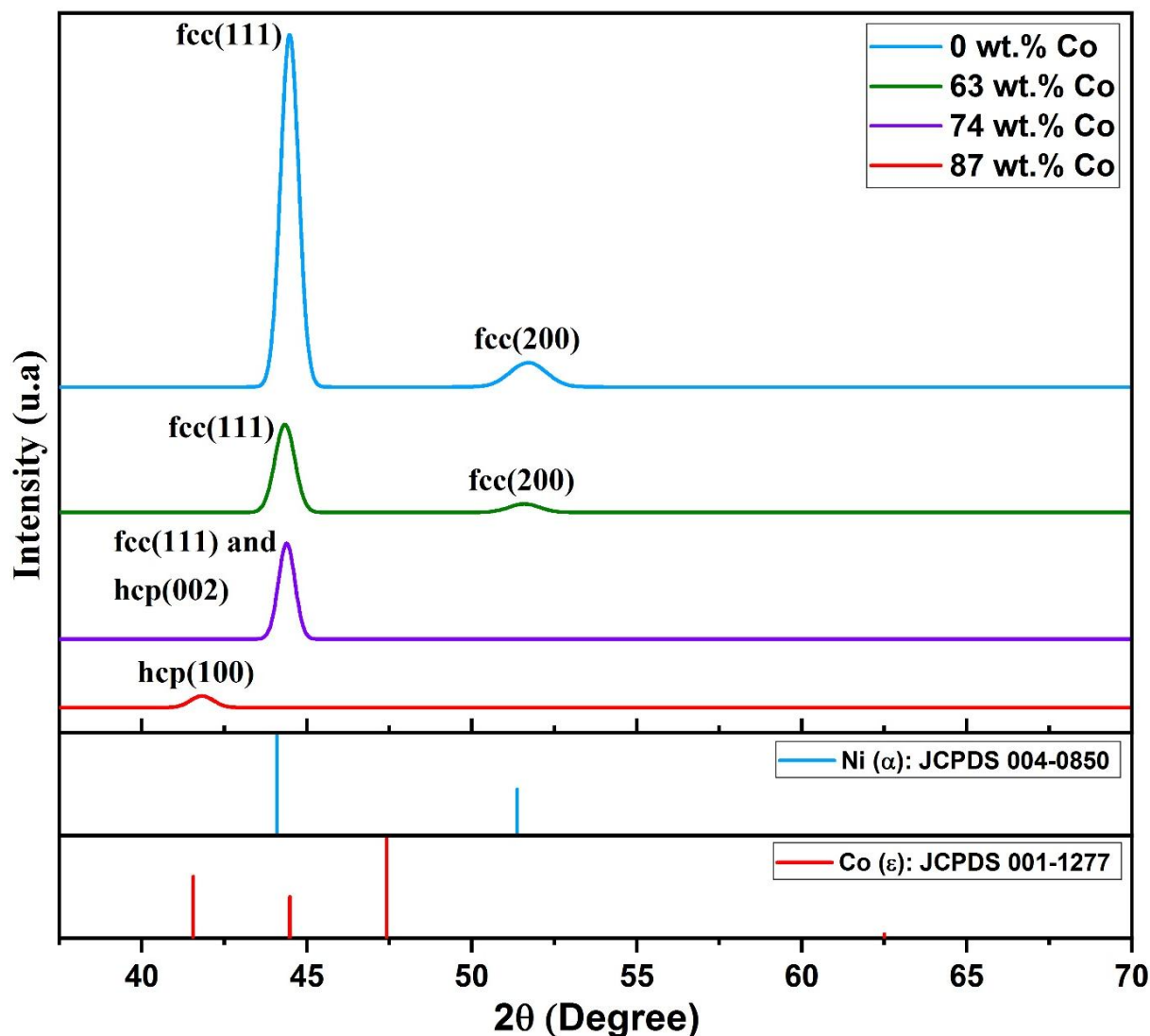


Figure IV.3: XRD patterns of the electrodeposited Ni-Co coatings.

These phase changes are also consistent with the equilibrium phase diagram of the Ni-Co alloy (Figure II.10), which exhibits a single α (fcc) phase along the range from 0 to about 65 wt.% Co, both ($\alpha + \epsilon$) phases in the interval extending from 65 to about 75 wt.% Co, and a single ϵ (hcp) phase continuing to 100 wt.% Co. All the electrodeposited coatings show preferred crystallographic orientations. Ni-Co with 63 wt.% have a double fiber textures (111) and (200) like those of pure Ni. Ni-Co with 74 wt.% Co has a single fiber texture (111)/(002), while Ni-Co with 87 wt.% Co takes a single fiber texture (100), which are almost the same results for Ni-Co coatings with different Co contents, obtained by Hibbard et al. [130] Lupi et al [129] and Ma et al [29]. In contrast, these preferred crystallographic orientations are different from those of the Ni-Co polycrystalline coatings found by [177]. These differences can be explained by the

effect of organic additives in the electrolyte bath, especially saccharin, as explained in detail in section (III.3.1.b).

The crystallites size of the elaborated coatings, calculated from the full width at mid-height (FWHM) of the XRD peaks using Scherrer's formula (eq.III.8) is presented in Figure IV.4. As can be seen from this figure, the crystallites size increases with the increase of Co content in the coatings, which is explained by the gradual change of the surface morphology of the coatings from smooth granular structure to fibrous branched structure, as shown in Figure IV.2. Somewhat similar to the morphology changes reported by Wang et al [177] and Golodnitsky et al [124] (Figures II.20 and II.21).

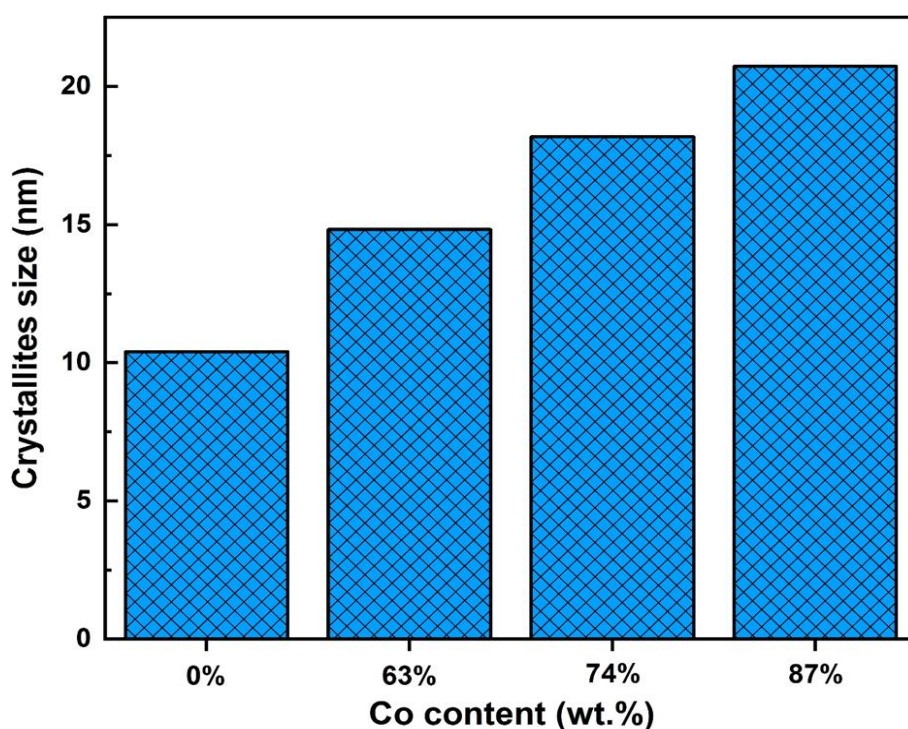


Figure IV.4: The crystallites size vs. the Co content of the electrodeposited Ni-Co coatings.

IV.3.1.c) Effect on the microhardness of coatings

Figure IV.5 shows the microhardness as a function of Co content of the electrodeposited Ni-Co coatings. It can be seen that the microhardness gradually decreases with increasing Co content of the coatings. The explanation for this gradual decrease in microhardness is the gradual increase in crystallites size of the Ni-Co coatings with the increase of their Co content, as shown in Figure IV.4. This decrease in hardness with increasing crystallites size of materials known as the Hall-Petch effect and can be described mathematically by the classical Hall-Petch

relationship (eq. III.7). To further clarify the effect of crystallites size on the microhardness of the electroplated Ni-Co coatings, the microhardness as function of the inverse square root of average crystallites size ($d^{-1/2}$) is represented in Figure IV.6 in the form of Hall-Petch plot. It is clear that the microhardness of the electrodeposited Ni-Co coatings is quasi-linearly proportional to $d^{-1/2}$. The measured microhardness fit well Hall-Petch plot with a correlation coefficient ($R^2 = 0.95$). Such a relationship has also been observed for pure Ni [23,107], pure Co [107] and Ni-Co coatings [108,177]. However, a small deviation from the Petch Hall gradient can be observed when the crystallite size was smaller than about 14 nm.

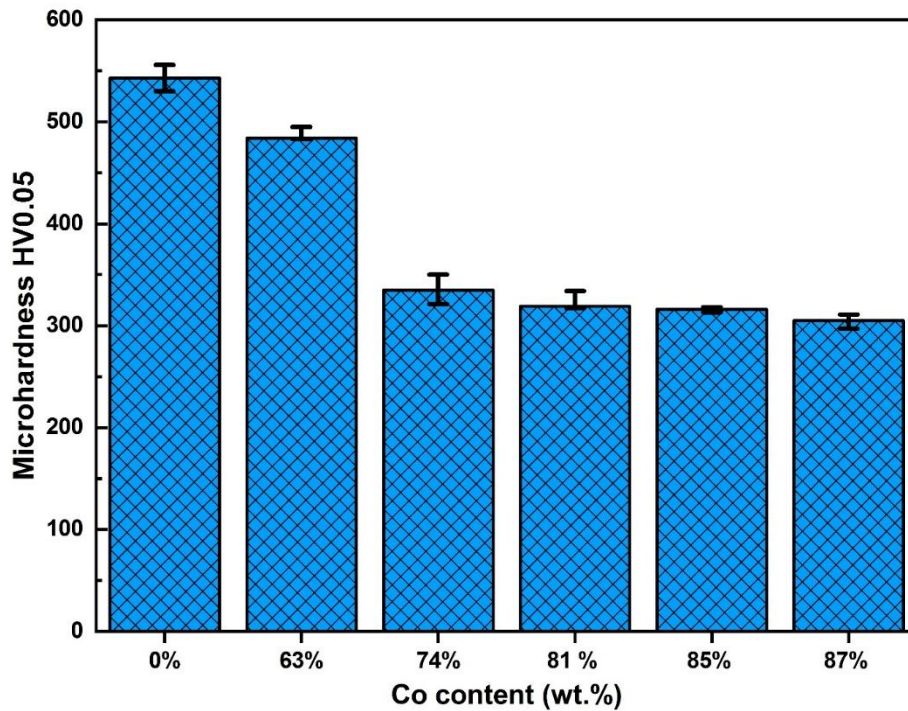


Figure IV.5: Microhardness vs. Co content of the electrodeposited Ni-Co coatings.

The deviation from Hall-Petch gradient is a common phenomenon in the nanomaterials generally [15,172,189]. It has also been reported for nanocrystalline Ni and Ni-Co coatings below different crystallites size values in many previous studies [23,107,134]. The mechanism of deviation and failure of Hall-Petch relationship is not clear, since there is a conflict of opinion on the causes of this phenomenon in the literature as shown in section (I.5.5.b).

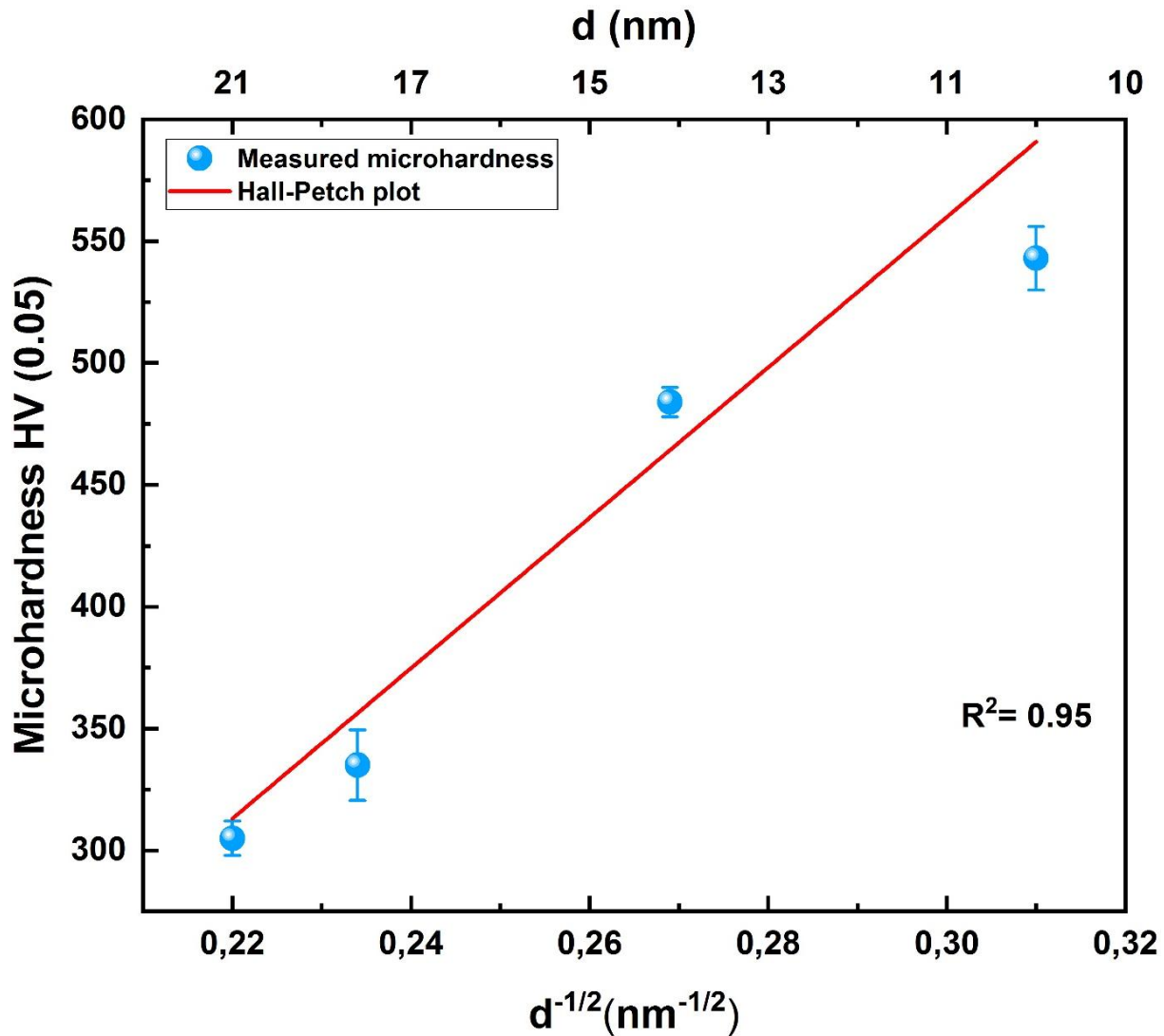


Figure IV.6: Microhardness vs. the inverse square root of crystallites size of the electrodeposited Ni-Co coatings.

IV.3.1.d) Effect on the tribological behavior of coatings

The friction coefficients of the elaborated Ni-Co coatings as function of time are shown in [Figure IV.7](#). It is obvious that the friction coefficient gradually decreases and becomes more stable with increasing Co content in the coating. Pure Ni and, to a lesser extent, Ni-Co (63 wt.% Co) coatings with a single α (fcc) crystal structure exhibit a relatively high and unstable coefficient of friction. However, a further increase of the Co content in the coatings leads to a drastic decrease of the friction coefficient. Combined with the XRD patterns ([Figure IV.3](#)), the gradual decrease in the friction coefficient with increasing Co content in the coatings can be explained by the gradual change of the crystal structure from the full (fcc) phase to a mixed (fcc+hcp) phase and then to a full (hcp) phase that exhibits excellent friction reduction behavior

according to some previous studies [39,107,177]. Furthermore, the high and unstable friction coefficient of the pure Ni coating and, to a lesser degree, Ni-Co with 63 wt.%, can be explained by the formation of tribofilms on their worn surfaces, as can be clearly seen in Figure IV.9 (a-d).

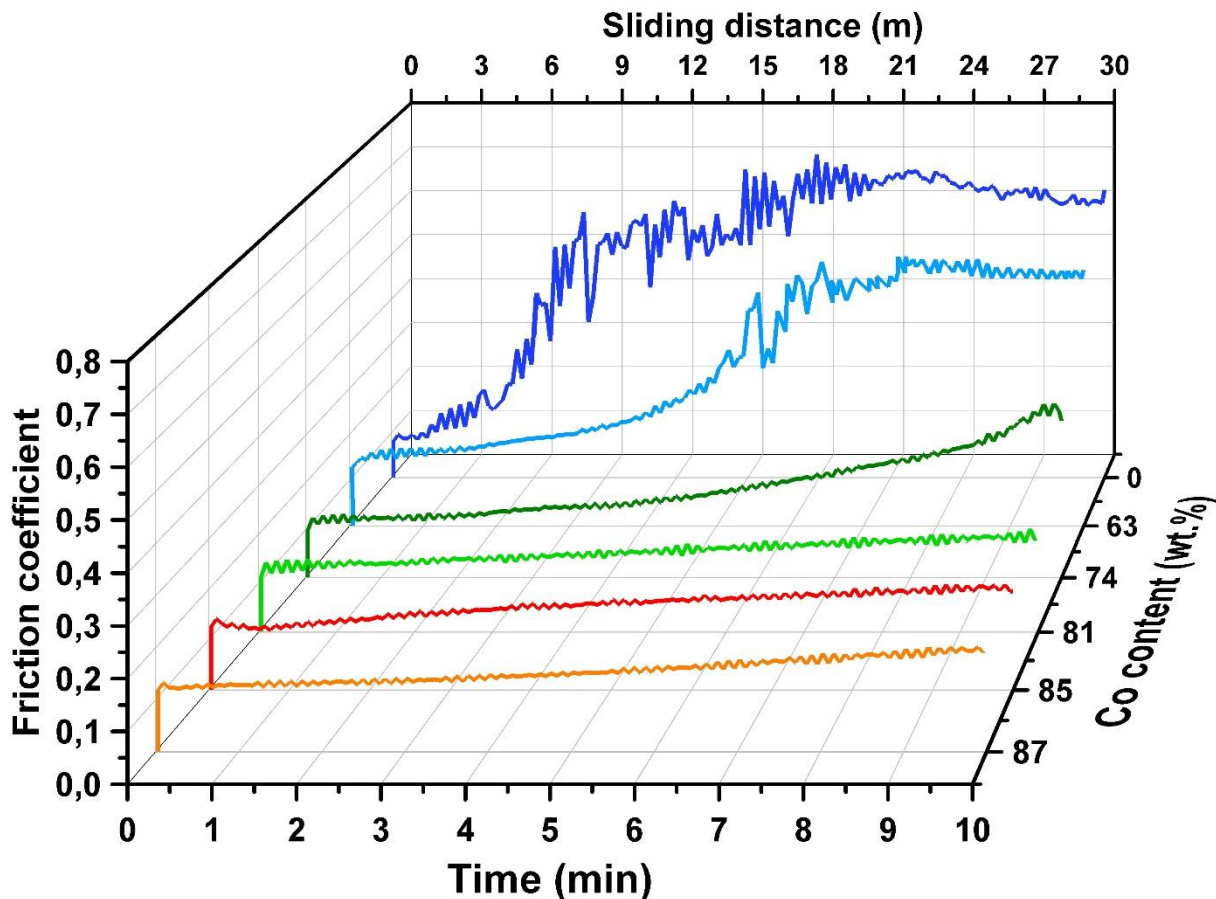


Figure IV.7: Friction coefficient vs. sliding time of the electrodeposited Ni-Co coatings.

The wear rate of the electroplated Ni-Co coatings as function of their Co content is presented in Figure IV.8. It is observed that the pure Ni coating exhibits a wear rate of about $12 \cdot 10^{-4} \text{ mm}^3/\text{Nm}$. However, the wear rate is dramatically reduced to less than half with the addition of a high Co content of about 63 wt.% to the coating. The wear rate of the electrodeposited coating continues to decrease gradually with increasing Co content in the coating to reach a value of about $1.85 \cdot 10^{-4} \text{ mm}^3/\text{Nm}$ in the Ni-Co alloy with 87% Co content, more than six times lower than that of the pure Ni coating. This reduction in the wear rate of electrodeposited coatings despite the decrease in their hardness (see Figure IV.5) contradicts Archard's law (eq.III.7) which correlates inversely between wear rate and hardness of the worn surface. The inverse Archard law can be explained by the change of the crystal structure from α (fcc) to the special

ϵ (hcp) phase which exhibit excellent tribological behavior. The reduction in wear rate with increasing Co content is in good agreement with the reduction and stabilization of the friction coefficient (Figure IV.7).

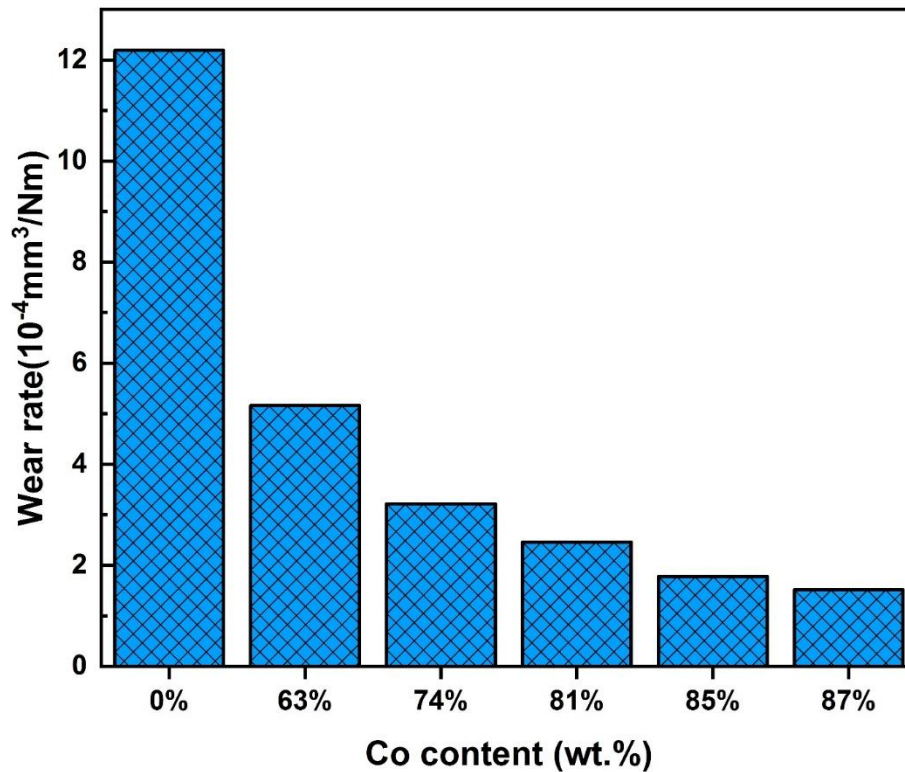


Figure IV.8: Wear rate vs. Co content of the electrodeposited Ni-Co coatings.

To further understanding of the wear behavior of the elaborated coatings, the worn surfaces morphologies can be observed by SEM as shown in Figure IV.9. The pure Ni coating with α -phase structure shows a discontinuous tribofilm resulting from the severe adhesive wear in the rubbing direction (Figure IV.9 a-b). This tribofilm, which consists of both the wear debris of the coating and the transferred debris from the pin, is the reason for the high and unstable friction coefficient and the higher wear rate of the pure Ni and nickel-rich Ni-Co coatings, as explained in detail in section (III.3). Alloying Ni with high Co content leads to a dense and smooth worn surface with very slight adhesion, as can be clearly seen on the worn surface of the Ni₂₆-Co₇₄ coating with a mixed ($\alpha+\epsilon$) crystal structure (Figure IV.9 (c)-(d)), leading to a relatively low and stable friction coefficient and a lesser wear rate compared to the pure Ni deposit. While Ni-Co coatings with Co content > 74 wt.%, which are characterized by a particular crystal structure ϵ (hcp), show smaller damaged regions with a very smooth and dense surface exempt of any tribofilms, adherent debris or transfers from the pin (Figure IV.9 (e)-(f)),

which corresponds to a very low wear rate and a very stable friction coefficient. Hence, it can be concluded that the more ϵ (hcp) phase is dominant, the better the anti-wear behavior will be.

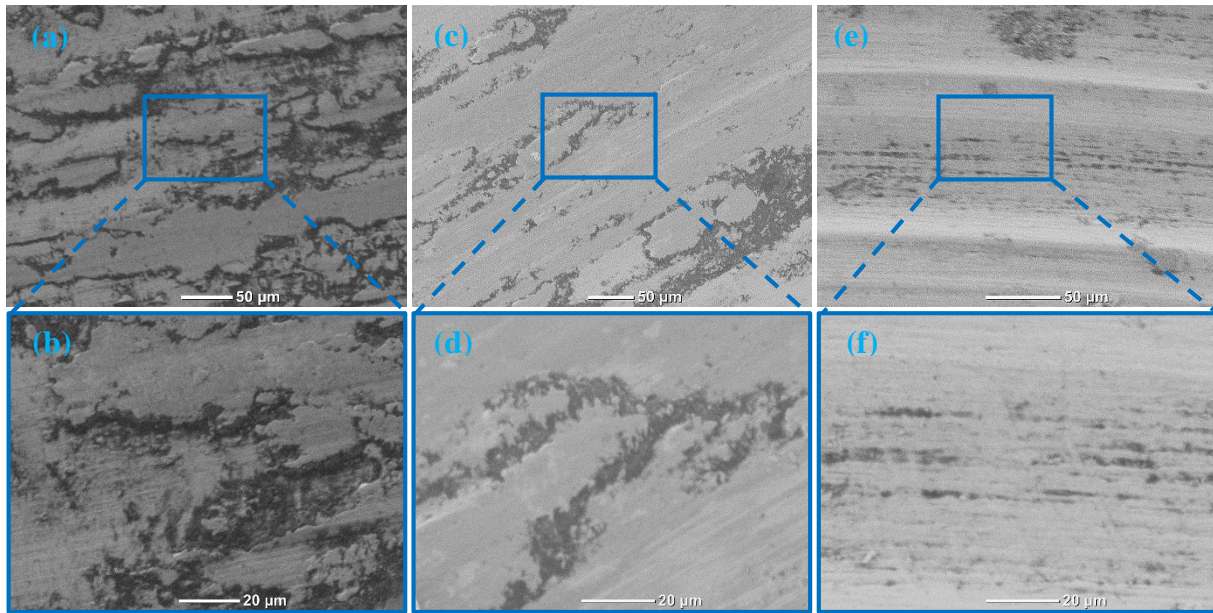


Figure IV.9: Worn surface morphologies of the electrodeposited Ni-Co coatings (a) (b) pure Ni coating, (c) (d) Ni-Co coating with 74 wt.% Co, (e) (f) Ni-Co with 87 wt.% Co.

The wear tracks of steel balls used as pins are also observed by SEM as can be seen in [Figure IV.10](#). The wear tracks of the pin rubbed against the pure Ni coating are relatively wide ([Figure IV.10 \(a\)](#)) and show many pores caused by the detachment of the material as a result of severe adhesive wear. These detachments adhere to the surface of the Ni coating during rubbing and form a tribofilm as shown in [Figure IV.9 \(a\)-\(b\)](#). As the Co content increases to about 63 wt.%, the wear track of the pin becomes narrower and shows the least amount of detachments. Whereas a Co content ≥ 74 wt.% resulted in much narrower wear scars on the pin that are free of any detached particles or debris being transferred to the coating ([Figure IV.10 \(c\)](#)). Thus, it can be concluded that the sizes of the pin wear tracks are in agreement with the wear rate of the Ni-Co coated substrates (disks) presented in [Figure IV.8](#).

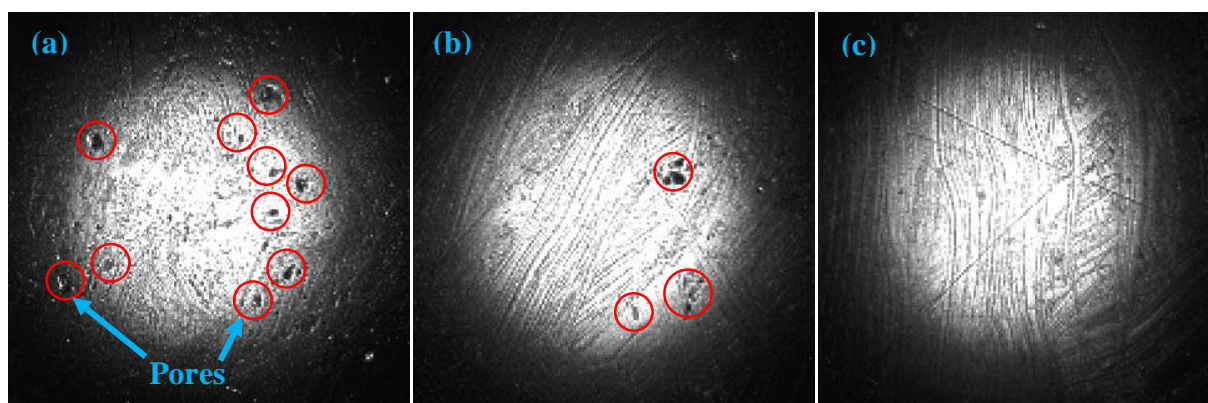


Figure IV.10: Wear tracks of the pins rubbed against (a) pure Ni coating, (b) Ni-Co coating with 63 wt.% Co, (c) Ni-Co coating with 87 wt.% Co.

IV.3.2 Effect of the bath temperature on the properties of the electrodeposited Ni-Co coatings

From the previous section, it was concluded that the morphostructural and anti-wear properties of Ni-Co coatings were significantly influenced by their Co content, which can be controlled mainly by the Co content of the bath. However, previous studies have concluded that the Co content of the coatings can also be influenced by other plating parameters, such as bath temperature [122,123]. To our knowledge, the question of the effect of temperature on the anti-wear properties of Ni-Co coatings has not been the subject of any previous study. For this purpose, it is important to study in detail the variations in composition and morphostructural properties of electrodeposited Ni-Co coatings as a function of bath temperature and to understand their relation with the anti-wear properties. This section of the study examines the effect of bath temperature on the composition and morphostructural properties of Ni-Co coatings, which are directly related to their mechanical and tribological behavior, in order to fully understand the effect of the electrodeposition bath temperature on the anti-wear properties of the electrodeposited coatings.

IV.3.2.a) Effect on the deposition potential

Figure IV.11 shows the galvanostatic curves for the deposition of Ni-Co alloy at different electroplating bath temperatures. It can be clearly seen that the reduction potential of Ni^{2+} and Co^{2+} ions gradually decreases and becomes less cathodic with increasing bath temperature. The measured potential is an indication of the reactions that occur at the substrate-electrolyte interface. Thus, the variation of the potential occurs in response to the variation of the electrical

resistivity of the substrate surface as a function of the nucleation and growth phenomena of the deposit [190,191]. Initially, a fast decrease in the reduction potential due to the charge of the double electrical layer can be observed, until the reduction potential of the Ni^{2+} and Co^{2+} ions is reached. Thereafter, the potential becomes quasi-stable and does not fluctuate until the end of the deposition operation, indicating a uniform deposition of the coating on the steel surface, regardless of the bath temperature [192]. As the concentration of electroactive species near the substrate becomes close to zero, the potential becomes more negative to compensate the capacitive effect [193]. Increasing bath temperature may provide higher diffusion coefficients, more kinetic energy and ions mobility, resulting in less near substrate impoverishment by the Ni^{2+} and Co^{2+} ions; therefore, the capacitor formed between the substrate and the metal ions does not require much charge for compensation, which resulted in the decrease of the overpotential required to create nucleus with increasing temperature. The decrease in deposition potential can also be explained by the increase in current efficiency with increasing bath temperature, as concluded in previous studies dealing with the electrodeposition of Ni-Co layers [37,125]. At a lower bath temperatures ($<40^\circ\text{C}$), a considerable amount of current is consumed by the hydrogen evolution reaction (HER) which competes with the reduction reaction of Ni^{2+} and Co^{2+} ions [125], resulting in a relatively high required overpotential. However, an increase in bath temperature makes the hydrogen evolution less intense, improves the efficiency of the current and, consequently, the potential required for the co-deposition of the Ni-Co alloy becomes lower. Thus, it can be concluded that the bath temperature is a factor that facilitates the diffusion of ions through the electric double layer formed on the substrate-electrolyte interface, decreases the reduction potential and consequently accelerates the deposition rate of the Ni-Co alloy. It should be noted that the same behavior of deposition potential decrease with increasing bath temperature was noticed by Sarac et al for Ni-Co [192] and Ni-Cu [194] electrodeposition on an ITO substrate.

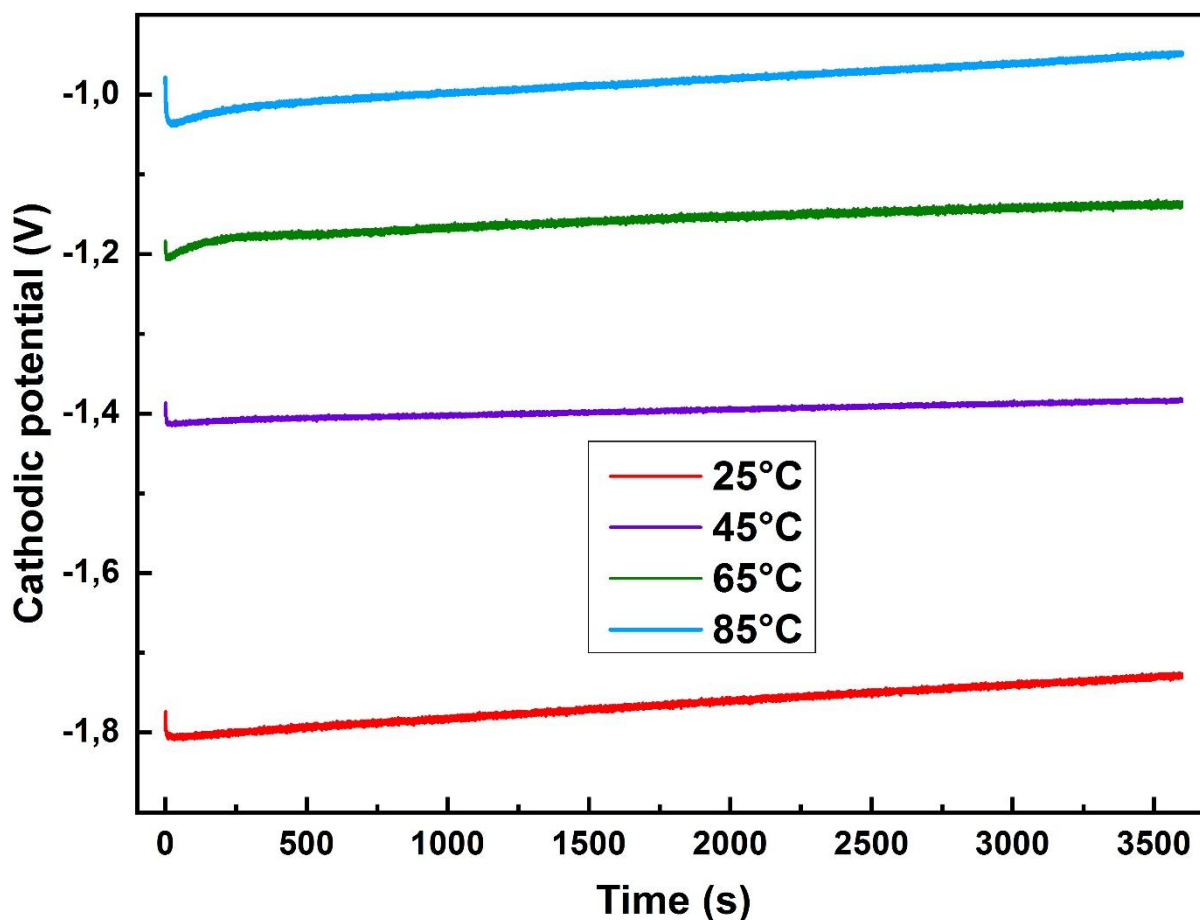


Figure IV.11: Cathodic potential as a function of time at different electroplating bath temperatures.

IV.3.2.b) Effect on the composition of coatings

The concentration of Co and Ni in Ni-Co coatings electrodeposited at a constant concentration of cobalt sulfate in the bath (20g/l) is plotted against bath temperature in [Figure IV.12](#). It is clear that the bath temperature strongly influences the composition of the deposits, where it can be seen that the concentration of the Co and Ni elements varies with the variation of the bath temperature. The deposits produced at ambient temperature (25°C) contain the maximum cobalt content (48 wt.%), this Co content decreases with increasing bath temperature to reach its minimum value (30.7 wt.%) at a bath temperature of 65°C, then it undergoes an increase towards (39.3 wt.%) with increasing bath temperature to 85°C. Thus, it is noticed that the percentage of Co in the electrodeposits at all the studied bath temperatures is higher than that in the electrolyte (8.33 wt.%), which means that the anomalous co-deposition mechanism of the Ni-Co alloy explained extensively in section [\(III.3.1.a\)](#) still exists regardless of the bath temperature. However, the calculation of the abnormality degree by the relationship mentioned in section [\(IV.3.1.a\)](#) shows that the bath temperature has a significant influence on it. While it

decreases from 5.76 to 3.69 following the increase in temperature up to 65°C and then increases to 4.72 when the temperature rises to 85°C. It is worth mentioning that to the present day, the literature reports different results concerning the effect of bath temperature on the composition of Ni-Co alloy electrodeposits. Although there are no previous studies covering the full range of bath temperature variations taken in this study (25 to 85°C), but findings in good agreement with the results of this study in the range of 30 to 60°C are revealed for Ni-Co alloys electroplated in a chloride bath [125], in a chloride-sulfate bath [195] and also in a chloride-sulfamate bath [196]. In contrast, the Co content was found to be unaffected meaningfully by the change of bath temperature in the range of room temperature (22-37°C) [192]. On the other hand, a slight increase in the Co content of Ni-Co alloy deposited from a gluconate bath was detected by M.Kamel [123] when increasing the bath temperature from 5 to 60°C. These contradictory results can be attributed to the use of different electrodeposition parameters such as applied current density and electrodeposition bath composition.

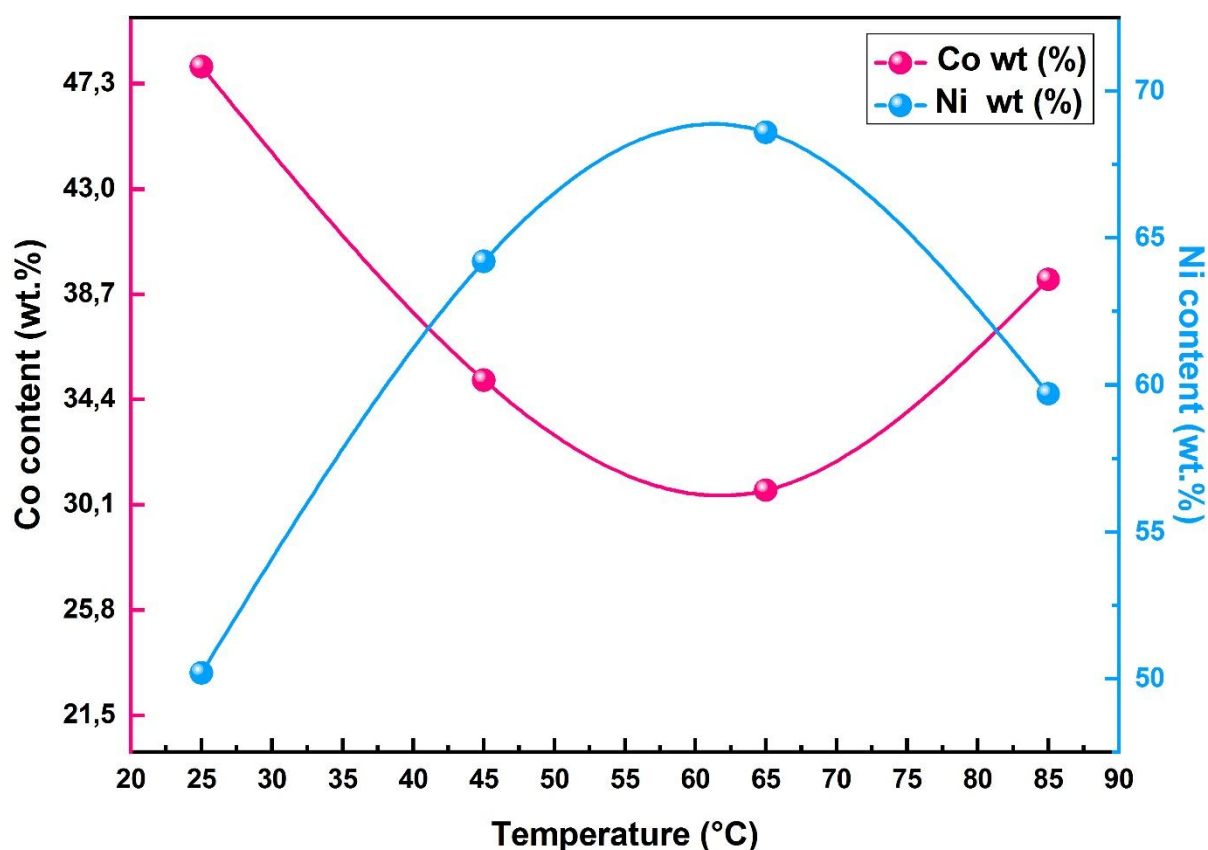


Figure IV.12: Co and Ni contents in the electrodeposited Ni-Co coatings vs. the bath temperature.

IV.3.2.c) Effect on the morphostructural properties of coatings

From SEM observations of the coating morphologies, the bath temperature does not appear to have a significant effect on the grains shape, which is consistent with some previous studies [192]. Moreover, the grain size is too fine to be resolved by SEM, so we focus in this section only on studying the bath temperature effect on the surface quality of electrodeposited Ni-Co coatings. Figure IV.13 shows the SEM observations of the Ni-Co coatings electrodeposited at different bath temperatures. It can be clearly seen that the coating electrodeposited at 25 °C is characterized by a dense, rough, crack-free and orange peel-like morphology (Figure IV.13 (a)). The electrodeposited coating at 45 °C seems to be as dense but rougher than that electrodeposited at 25 °C, where the rougher surface in this case can be attributed to the slight increase in crystallite size following the increase in bath temperature from 25 to 45 ° as can be seen in Figure IV.13 (b). Raising the bath temperature to 65°C results in relatively smooth but porous coating (Figure IV.13 (c)). A further increase in temperature to 85°C gives a coating with a high porosity rate, as shown in Figure IV.13 (d). The appearance of porosity on the surface of Ni-Co coatings deposited at the highest used bath temperatures (65 and 85°C) is possibly due to the effect of Cl⁻ and SO₄⁻ anions [134], where the coatings are deposited from a bath with a high contents of SO₄⁻ and Cl⁻ anions, these latter being able to attack the surface of coatings, preferably at high temperatures, resulting in holes, cracks and burning of the coatings. At the macroscopic scale, the coating brightness improves when the deposition temperature is increases from 25 to 65°C, while a higher bath temperature leads to dull grey deposits similar to the Ni-Co foil electrodeposited at 60°C by Y.F. Yang et al [125]. The improvement in the coatings brightness is due to the weakness of the hydrogen evolution reaction (HER) with the increase of the bath temperature. As explained in detail in section (IV.3.2.a), this competitive reaction to the reduction of Ni²⁺ and Co²⁺ ions, consumes a significant part of the current dedicated to the electroplating of Ni-Co alloy and causes the formation of hydrogen bubbles which translates into some micropores leading to the decrease of the brightness of coatings electrodeposited at low temperature (25 -45 °C). Furthermore, the weakness of HER leads to an increase in the current efficiency and subsequently to the increase of the deposit thickness from (48±5µm to 54±5µm) when the bath temperature increases from 25 to 85°C. On the other hand, the dull gray brittle deposits accompanied by the phenomenon of black burning are due to the effect of Cl⁻ and SO₄⁻ on the surface of coatings deposited at high temperatures (> 65 °C).

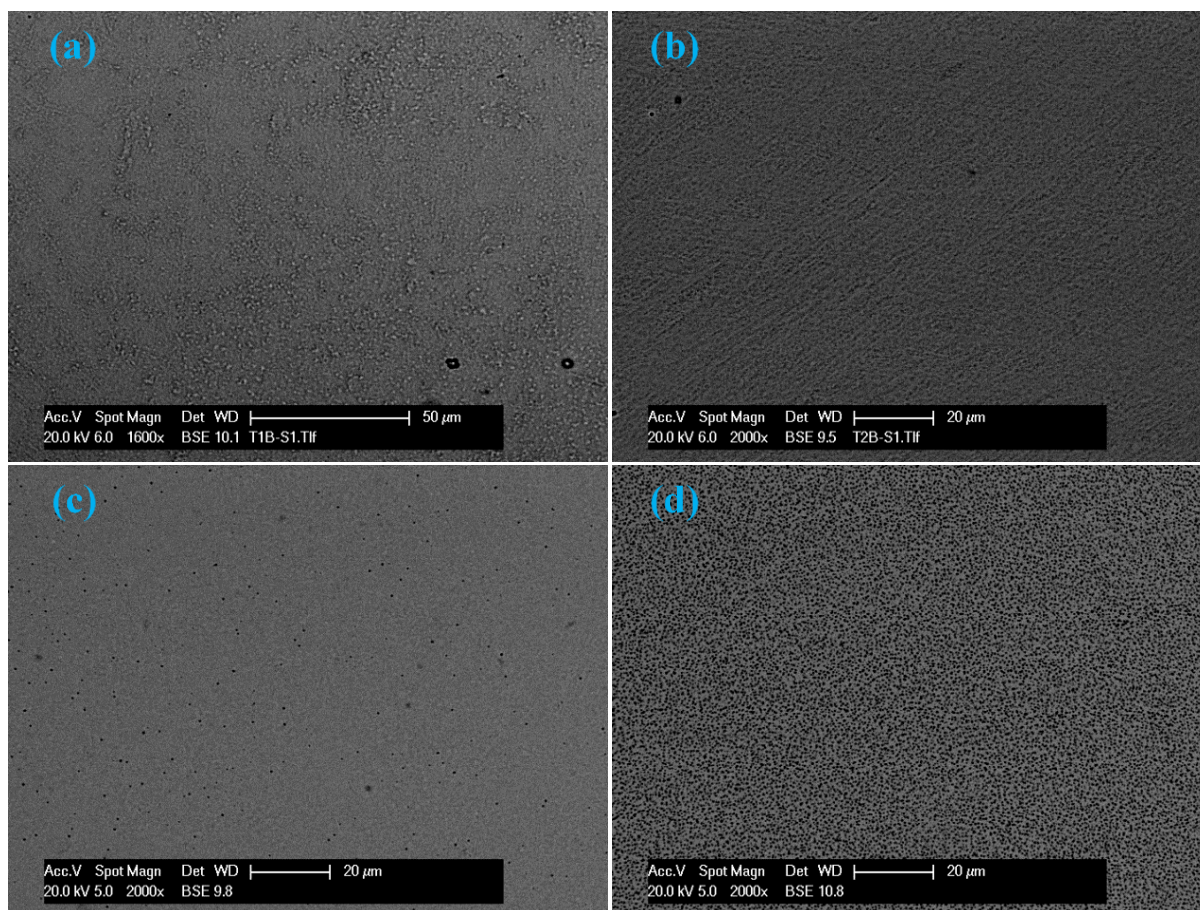


Figure IV.13: SEM micrographs of the Ni-Co coatings electrodeposited at: (a) 25°C, (b) 45°C, (c) 65°C, (d) 85°C.

XRD patterns of the Ni-Co coatings electrodeposited at different bath temperatures are shown in Figure IV.14. As clearly seen, all the peaks characterize the α (fcc) total Ni-Co solid solution with (111) preferential orientation, which is in good agreement with the results revealed in previous studies at this range of Co content (30 to 48 wt.% Co) in the presence of saccharin [29,194]. However, some changes can be observed in the XRD patterns of electrodeposits with increasing temperature. The first observed change is the gradual increase in peaks intensity as the bath temperature increases from 25 to 65°C, and its diminution by a further increase of temperature toward 85°C. These variations in peak intensity can be well correlated with the variation in Co content (Figure IV.12), as the peaks intensities becomes stronger with decreasing Co content, and weaken with increasing Co content. The increase of the intensity is a sign of the improvement of coatings crystallinity and vice versa [197]. A reasonable explanation for the improvement in crystallinity with increasing bath temperature is the decrease in Co content, as the large Co atoms (atomic radius = 152pm [170]) partially replace

small Ni atoms (atomic radius =149pm [170]) in the crystal lattice, as shown in Figure III.7, resulting in localized distortions in the Ni lattice. This hypothesis can be supported by the patterns of Ni-Co coatings electrodeposited in baths with different Co contents, where increasing the Co content in the coatings leads to a decrease in their crystallinity (Figure IV.3). A similar behavior with increasing Co content can be observed also in the study of C.Ma [29].

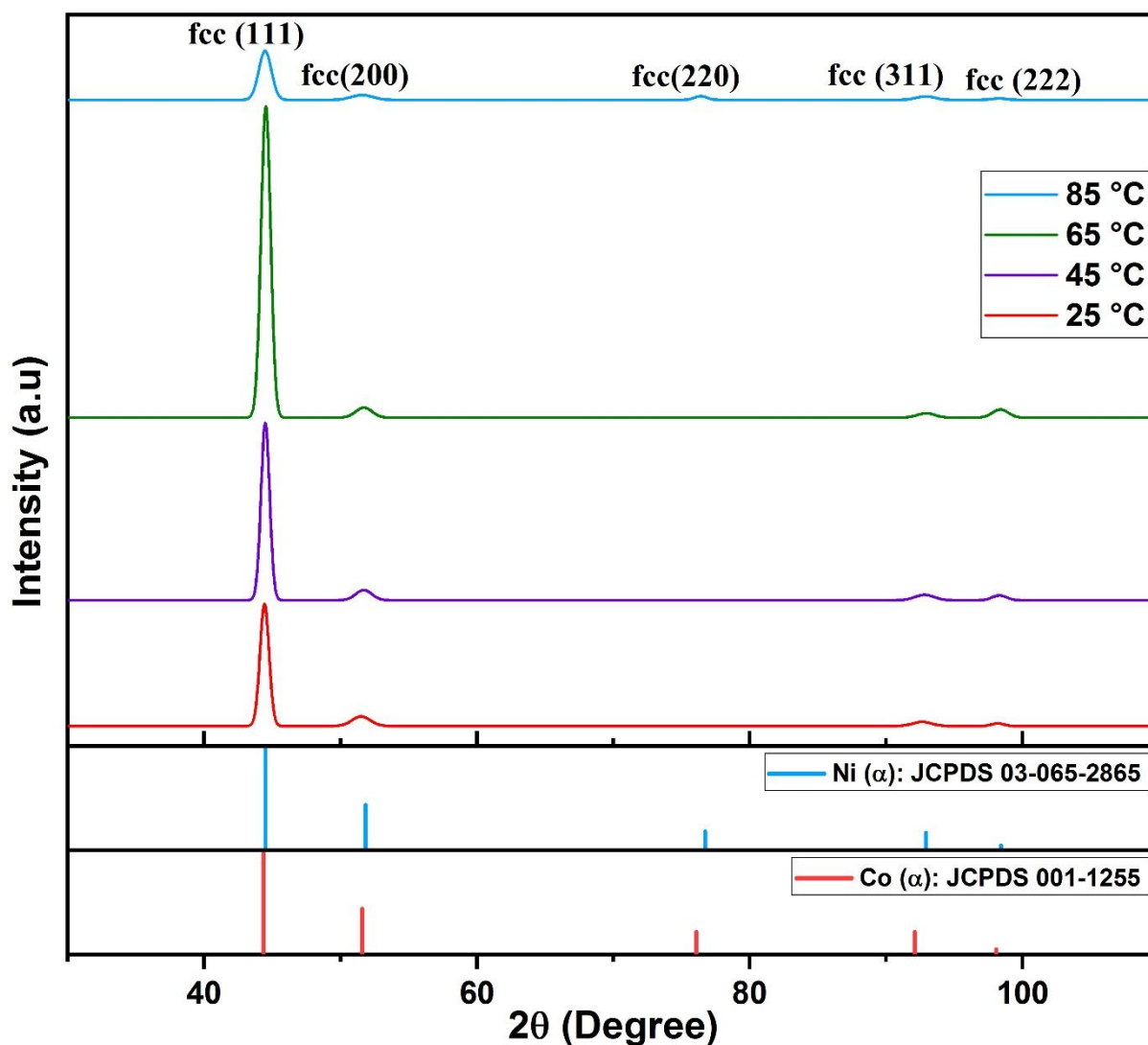


Figure IV.14: XRD patterns of the Ni-Co coatings electrodeposited at different bath temperatures.

The second change that can be observed is the appearance of the fcc (200) peak (at~76°) exclusively on the XRD pattern of the coating electrodeposited at 85°C. This additional peak is not due to another crystal impurity or the formation of a new phase, but is only caused by a slight change in the preferential crystallographic orientation of the electrodeposits, where this

characteristic peak coincides well with the one that appeared at the same position in the JCPDS cards of pure Ni (α) and Co (α), as shown in Figure IV.14.

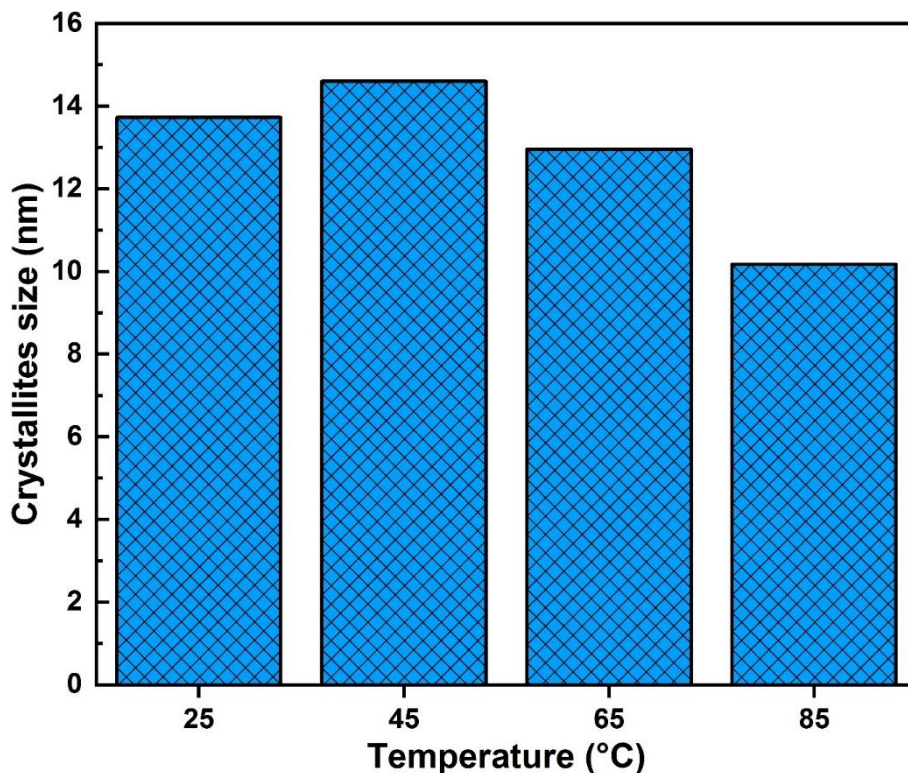


Figure IV.15: Crystallites size of the electrodeposited Ni-Co coatings vs. the bath temperature.

IV.3.2.d) Effect on the microhardness of coatings

Figure IV.16 shows the average microhardness of the Ni-Co coatings electrodeposited at different bath temperatures. It is obvious that the bath temperature has a slight effect on the microhardness of the electrodeposited coatings. The Ni-Co coating deposited at room temperature (25°C) shows the highest hardness value among the elaborated coatings, i.e., 781.66 HV, which is attributed to its dense pore-free surface and its relatively fine crystallites size, as shown in Figure IV.13 (a) and Figure IV.15, respectively. This value decreases to 761 HV in the coating deposited at 45°C, which can be explained according to the Hall-Petch effect by the increase in the crystallites size (Figure IV.16). The hardness increases slightly to 777 HV with a further increase in bath temperature to 65°C, which can be correlated with the decrease in the crystallites size. However, the coating deposited at this temperature has low hardness compared to that deposited at 25°C, despite its relatively smaller crystallite size, and this can be attributed to its porous surface (Figure IV.13 (c)). While the coating deposited at 85

°C exhibits the lowest hardness in this study despite its smaller crystallite size among the electrodeposited coatings, this may also be related to the high rate of porosity appearing on its surface as shown by SEM observations (Figure IV.13 (d)).

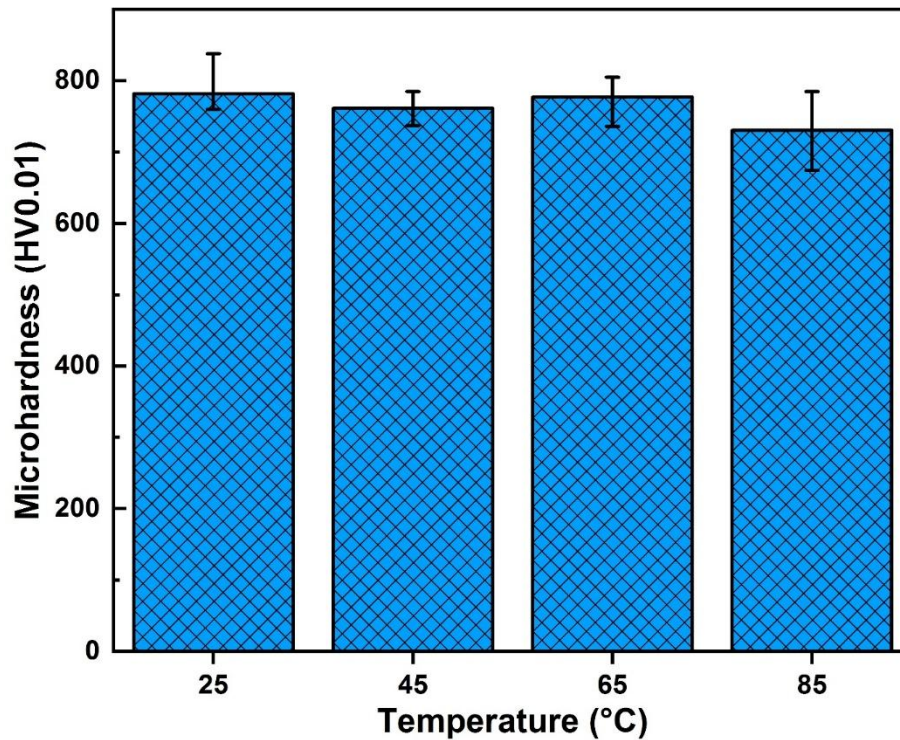


Figure IV.16: Microhardness of the electrodeposited Ni-Co coatings vs. the bath temperature.

To further verify the relationship between hardness, crystallites size and porosity of coatings, the measured hardness is plotted as function of the inverse square root of crystallites size ($d^{-0.5}$) in the form of Hall-Petch relationship as shown in Figure IV.17. It is clear that the variation of the coating hardness following the variation of the bath temperature is consistent partially with the Hall-Petch relationship (eq.III.6). The electrodeposits prepared at 25 °C have a higher hardness than the Ni-Co coating electrodeposited at 45 °C (781.66 vs. 761 HV) due to its finer crystallite size (13.73 vs. 14.6 nm). However, a deviation from the Hall-Petch gradient is noticed below a crystallite size of about 14 nm, where anomalously low microhardnesses of 777 and 730 HV can be observed for the coatings electrodeposited at 65 and 85 °C despite their relatively finer crystallite sizes (12.96 and 10.17 nm, respectively) compared to the coating electrodeposited at room temperature with a crystallite size of (13.73 nm).

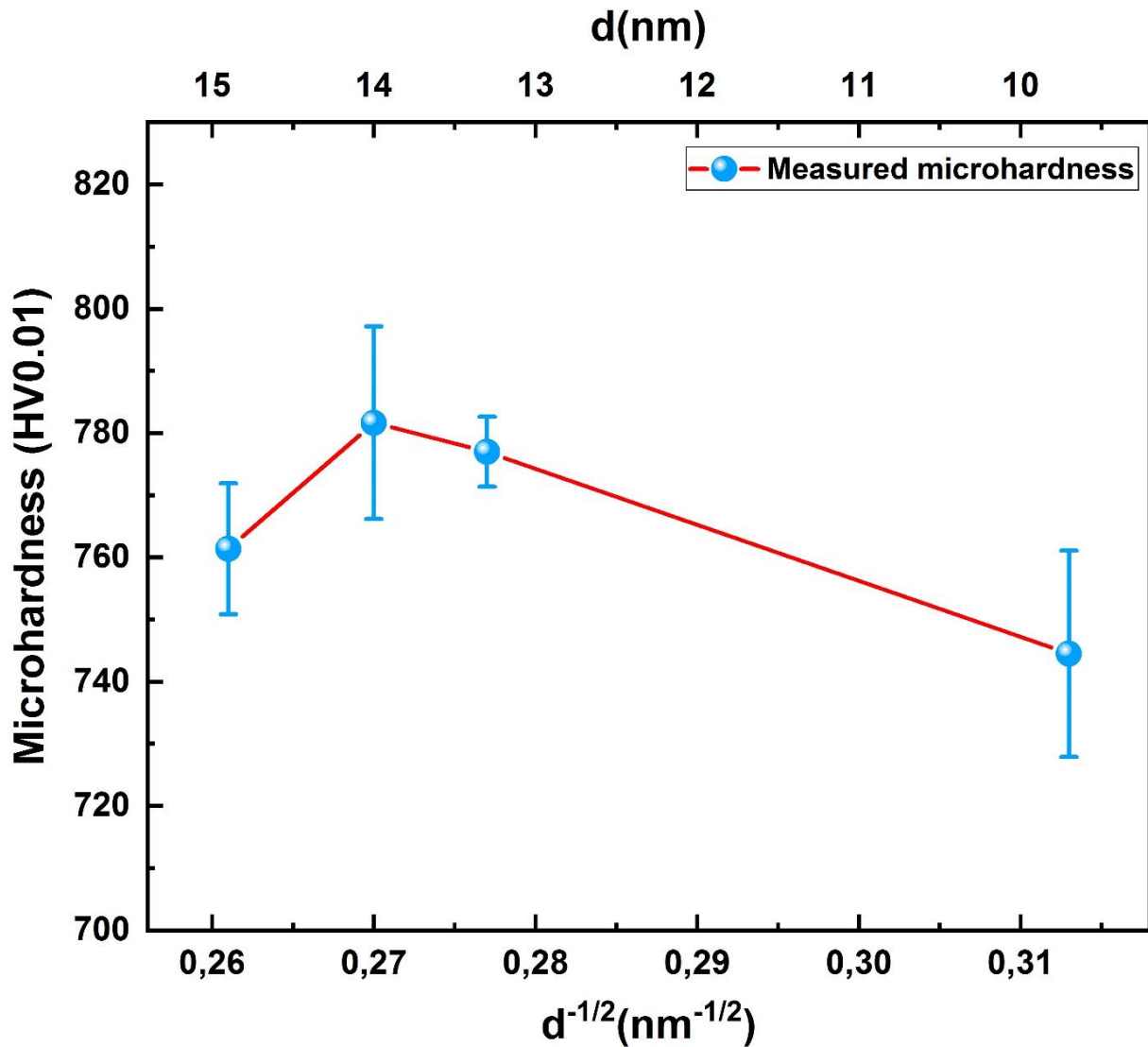


Figure IV.17: Microhardness vs. the inverse square root of crystallites size of the Ni-Co coatings electrodeposited at different bath temperatures.

This deviation from the Hall-Petch gradient occurs almost at the same crystallite size value (14 nm) obtained for coatings deposited in baths with different Co concentrations (Figure IV.6). Thus, it can be concluded that the Hall-Petch hardening (grain-boundary hardening) is not the decisive criterion for the hardness of the nanocrystalline Ni-Co coatings electrodeposited under such bath temperature conditions. The failure of the Hall-Petch relationship in the case of nanocrystalline electrodeposits is attributed to the texture effect [199], to the increased porosity [134] and others factors as shown in section (I.5.5.b). However, the effect of porosity seems to be predominant in this study, as all coatings have almost the same texture as can be seen in Figure IV.14, while their porosity rates are not the same, where the coating electroplated at 65 °C and to a larger extent the one electroplated at 85 °C have exclusively loose microstructures

containing a high porosity rate (Figure IV.13 (c) and (d)). This high porosity which owing to the negligible effect of the grains size. Thus, it can be concluded that for the pore-free coatings, the hardness-crystallites size relationship can satisfy the Hall-Petch effect, while the porosity effect must be taken into account in the case of porous coatings. Similar results in bath temperature range 45 to 60 °C were reported by C.K.Chung et al [196] for the Ni-Co films electrodeposited at sulfamate-chloride bath, where the microhardness decreased by increasing bath temperature. Nevertheless, the effect of porosity was not taken as an explanation for the decrease in microhardness in this study, despite the porosity clearly observed in the SEM micrographs of their electrodeposited Ni-Co films. On the other hand, L.Feng et al [199] found that nanocrystalline pure Ni coatings electrodeposited at a bath temperature ranging from 45 to 60 °C follow the Hall-Petch effect well, but with pore-free coatings in this case, which may well support our suggestions.

IV.3.2.e) Effect on the tribological behavior of coatings

The friction coefficients as function of sliding time of the Ni-Co coatings electrodeposited at different bath temperatures are shown in Figure IV.18. The coating electrodeposited at 25 °C has the lower and the more stable friction coefficient among the electrodeposited coatings with an average value of 0.38. The friction coefficient increases and becomes unstable with the increase of the deposition temperature towards 45°C and continues its increase and instability with further increase of the bath temperature up to 65°C, while it decreases significantly for coatings deposited at 85°C. This later coating, unlike other coatings, shows four phases in the friction coefficient evolution during the sliding time. The first contact phase (from 0 to 30 s of rubbing) governed by surface roughness that is a common step for all samples (as explained in detail in section (III.3.1.d)). The second phase of smoothing (30 to about 120 s), which has a direct relationship with the surface hardness and wear mechanism. The third phase (from 120 to 300 s) specific to this coating, which can be attributed to the harsh abrasion of this porous burnt deposit. The final phase (from the fifth minute until the end of the wear test), which is characterized by a decrease and stabilization of the friction coefficient due in this case to the total deterioration of the burnt porous coating and the penetration of the pin to the level of the substrate surface, where the evolution of the friction coefficient becomes at the same level as that of the bare substrate shown in Figure III.9. Referring to Figure IV.12, it can be noted that the variation in the friction coefficient of Ni-Co coatings electrodeposited at different bath temperatures is inversely related to the Co content in the coating. In other words, the friction

coefficient of coatings decreases as their Co content increases. This result confirms the lubricating effect of Co (friction-reduction effect) suggested in the sections (III.3.2.d) and (IV.3.1.d) of this thesis and also in some previous studies [28,29,39,177].

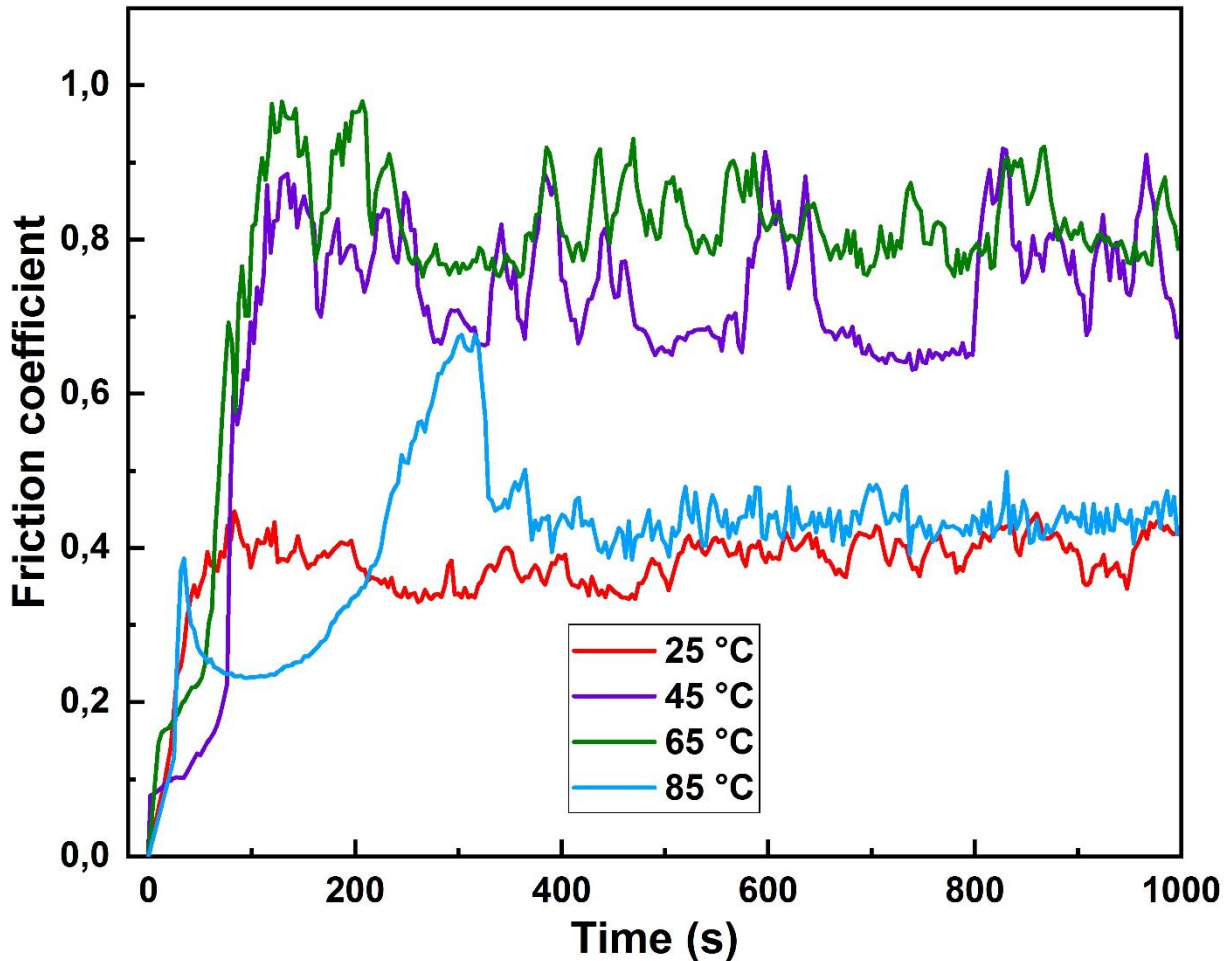


Figure IV.18: Friction coefficient of the Ni-Co electrodeposited at different bath temperatures vs. sliding time.

After the completion of the wear test, the wear rate of Ni-Co coatings is estimated by mass loss using the equation (II.9 [43]). Figure IV.19 shows the wear rate of the coatings electrodeposited at different bath temperatures. It is evident that the wear rate of the coatings becomes higher as the temperature of the plating bath increases.

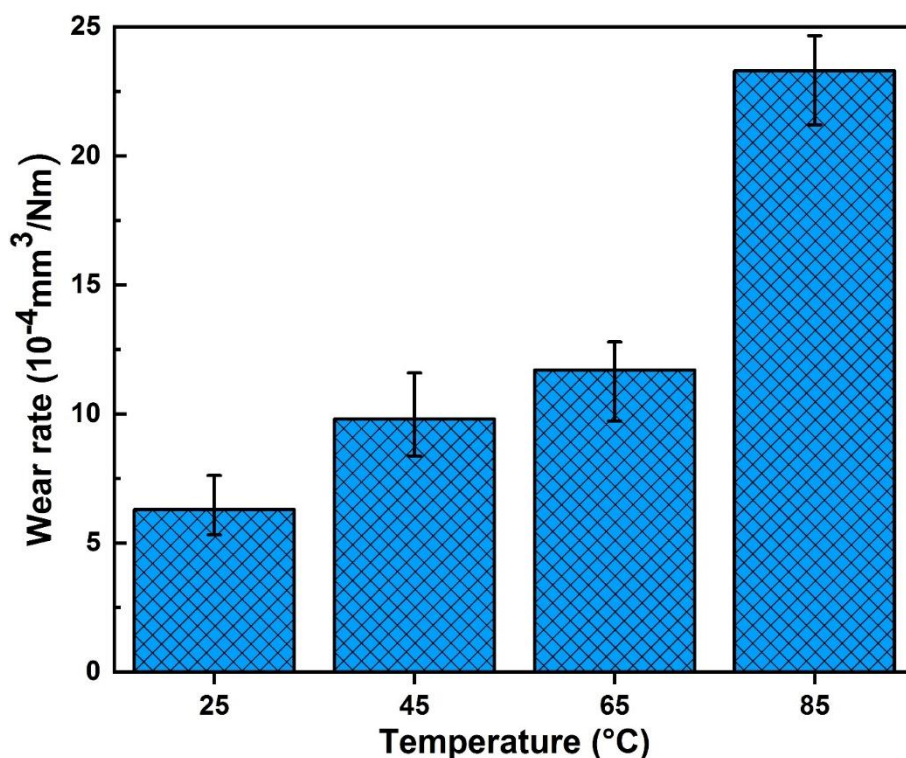


Figure IV.19: Wear rate of the Ni-Co coatings electrodeposited at different bath temperatures.

The nanocrystalline Ni-Co alloy coating electroplated at room temperature (25 °C) has the lowest wear rate ($6.3 \cdot 10^{-4} \text{ mm}^3 \text{N}^{-1} \text{m}^{-1}$) and the highest wear resistance among the electroplated coatings, thanks to its relatively higher hardness and lower friction coefficient as shown in [Figure IV.16](#) and [Figure IV.18](#). The wear rate increases by 55% for the coatings deposited at 45°C, due to the diminution of hardness and the increase in friction coefficient about two times compared to that of the coatings deposited at 25°C, as illustrated in [Figure IV.16](#) and [Figure IV.18](#), respectively. The Ni-Co coating electrodeposited at 65 °C exhibits a higher wear rate than the coating deposited at 45 °C, despite its slightly higher hardness ([Figure IV.16](#)), which can be attributed to its higher friction coefficient among the deposited coatings and also to its porous surface. The wear rate continues to increase and becomes almost double in the worn coatings electrodeposited at 85 °C compared to the coating deposited at 65 °C, and this despite its friction coefficient being almost half of the latter coating ([Figure IV.18](#)). This can be attributed mainly to the decrease in hardness and high porosity of the coating deposited at 85°C, due to its burning and embrittlement by Cl^- and SO_4^- anions during electrodeposition, which are assisted by the high bath temperature as explained in detail in section (IV.3.2.c). Hence, it can be concluded that the wear rate of the nanocrystalline Ni-Co coatings electrodeposited under

such bath temperature conditions follows Archard's law (eq.III.7) which establishes an inverse correlation between the wear rate and the hardness of the worn surface, except for the coating electrodeposited at 65°C that exhibits an anomaly due to its high friction coefficient.

The microscopic observation of the worn surfaces morphology helps to better understand the wear and friction behavior of the prepared coatings. SEM observations of the worn surfaces of the coatings electrodeposited at different bath temperatures are given in Figure IV.20. It can be clearly seen that Ni-Co coatings electrodeposited at temperatures between 25 and 65 °C exhibit a mixed adhesive-abrasive wear mechanism (Figure IV.20 (a)-(c)), which is a commonly observed mechanism in the wear of this type of Ni-rich (< 50 wt.% Co) Ni-Co coatings as shown in sections (III.3.1.d) and (IV.3.1.d) of this study and as concluded by some previous studies [39,66,177]. The Ni-Co coating deposited at 25°C with the highest Co content shows a discontinuous tribofilm on its worn surface with the highest adhesion rate of removable material. This tribofilm rich in Co lubricant component (48 wt.%) is responsible for the lowest friction coefficient and the highest anti-wear performance of this Ni-Co coating among the elaborated coatings, as this tribofilm acts as a barrier separating the two surfaces in contact. Tribofilms consisting of the adhered matter can also be observed on the worn surfaces of the coatings electrodeposited at 45° and 65°C. However, these tribofilms contain less Co lubricant than the first coating (35.2 and 30.7 wt.%, respectively), leading to a higher friction coefficient of these deposits (Figure IV.18). In addition, the tribofilm formed in this case covers less surface area, resulting in more damaged areas and a higher wear rate, since the effectiveness of the tribofilm as a barrier between two contacting surfaces decreases with decreasing surface area covered by it (see section III.3.1.d). This finding is noticed especially for the Ni-Co coating electrodeposited at 65 °C that shows the dominance of the abrasive wear mechanism with a very slight adhesion (Figure IV.20 (c)). Unlike coatings electrodeposited in the 25-65°C temperature range, the coating electrodeposited at 85°C exhibits only a single abrasive wear mechanism. This severe abrasive wear is responsible for the total deterioration of this brittle layer and the penetration of the pin up to the substrate surface (Figure IV.20 (d)). This wear behavior is also at the origin of the particular evolution of the friction coefficient of this coating different from that of the other coatings deposited in the bath temperature range of 25 to 65 °C, especially its final friction phase that shows a friction coefficient comparable to that of the bare substrate as stated in Figure III.9. On the other hand, it can be clearly seen that the higher the temperature of the plating bath, the wider and deeper the wear track becomes, which is

consistent with the wear rate results presented as a function of bath temperature in [Figure IV.19](#). Hence, it can be assumed that the room temperature (25 °C) is the best bath temperature for the electrodeposition of such Ni-Co coatings designed for anti-wear applications. This requires a revision of the 45 °C temperature used in many previous studies [\[29,29,33,39,177\]](#) in the elaboration of Ni-Co coatings for tribological applications.

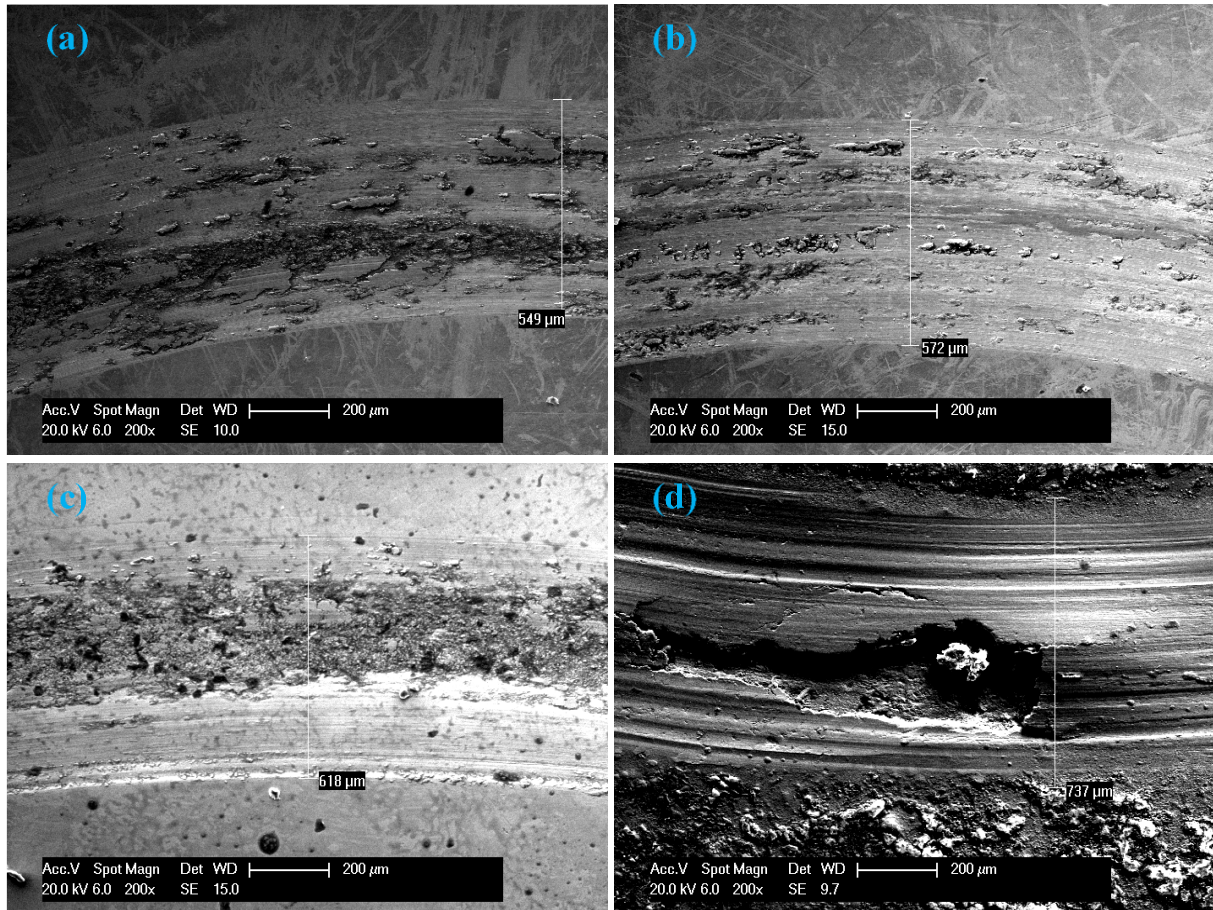


Figure IV.20: Worn surface morphologies of the Ni-Co coatings electrodeposited at: (a) 25°C, (b) 45°C, (c) 65°C and (d) 85°C.

IV.3.3 Other parameters that seem to have a slight effect on the properties of the electrodeposited Ni-Co coatings

In the previous sections, it has been shown that the concentration of Co and the bath temperature have a significant effect that should be taken into account when preparing an anti-wear Ni-Co coating. The objective of this section is complementary to the previous ones, where the maintenance of microstructural, mechanical and anti-wear properties of nanocrystalline Ni-Co

alloy coatings is tested on different metallic substrates (StW24 steel, copper and brass) and with different coating thicknesses (43.2, 79.8 and 110.6 μm).

IV.3.3.a) Effect on the deposition potential

Figure IV.21 shows as a function of deposition time the evolution of the deposition potential on the different materials used as substrates; namely StW24 steel, copper and brass. It can be seen that the deposition potential varies according to the type of substrate between -1.39 and -1.43 V. This variation of about -0.04V is a very slight deviation and can even be considered as a measurement error, especially when compared to the variation of the deposition potential as a function of bath temperature (Figure IV.11), which shows a large variation between -1 and -1.8V. Thus, it can be concluded that the effect of the type of the metal used as substrate on the deposition potential of nanocrystalline Ni-Co alloy coatings is negligible.

IV.3.3.b) Effect on the composition of coatings

Figure IV.22 shows the Co content in the electrodeposition bath and in the coatings electrodeposited on different substrates (Figure IV.22 (a)) and during different deposition times (Figure IV.22 (b)). The first remark that can be taken is the fact that the Co content in the coatings is higher than that in the bath whatever the nature of substrate or the deposition duration. This indicates that the anomalous codeposition mechanism of Ni-Co alloy explained in detail in section (III.3.1) still occurs, regardless of the type of substrate or the electroplating duration. Furthermore, if we compare with the effects of bath Co content and bath temperature, as shown in Figures IV.2 and IV.12, respectively, we can conclude that the type of metal substrate and the deposition time have a very small or even negligible effect on the Co content of the electrodeposited Ni-Co coatings.

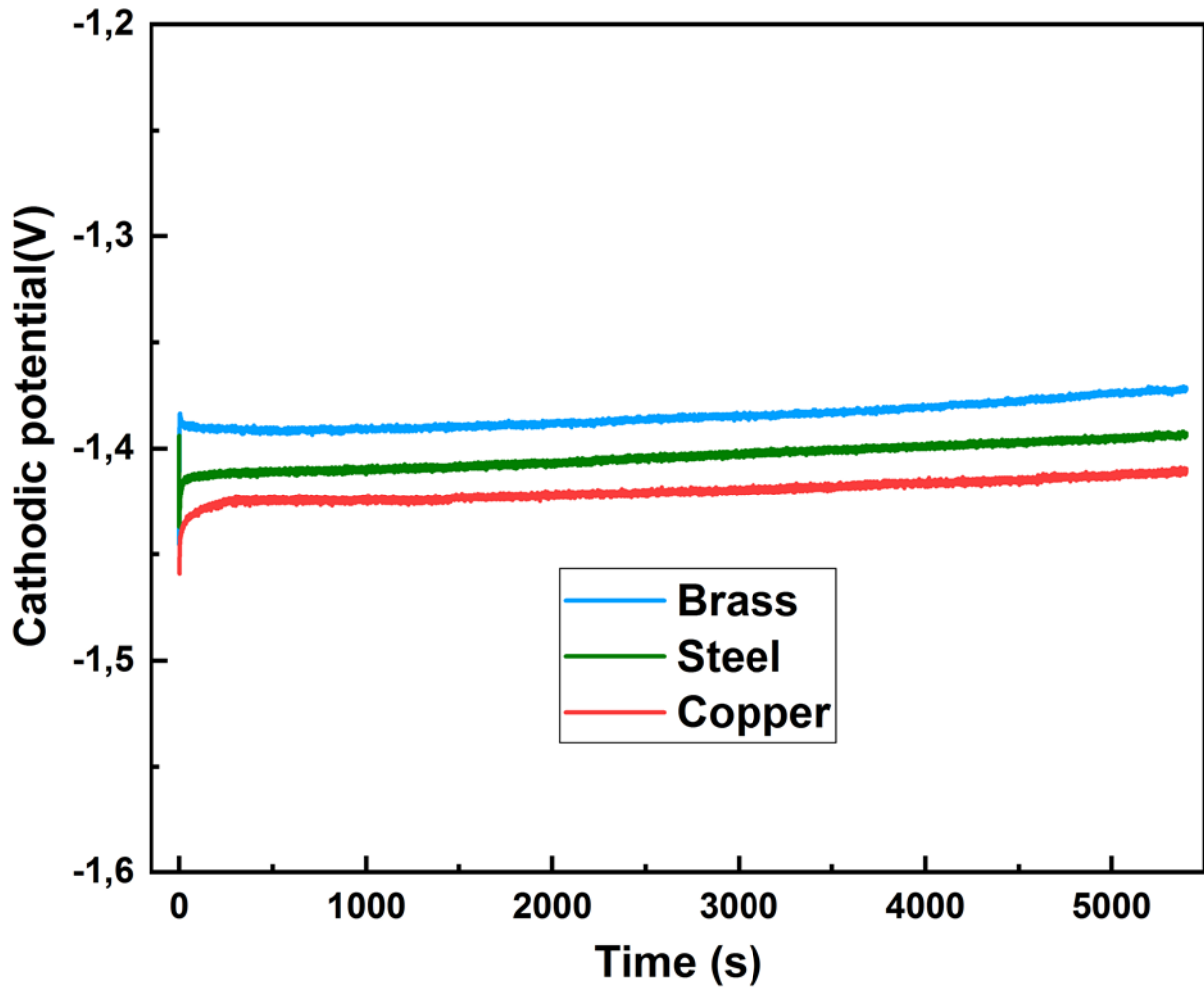


Figure IV.21: Deposition potential on the different used substrates as a function of deposition time.

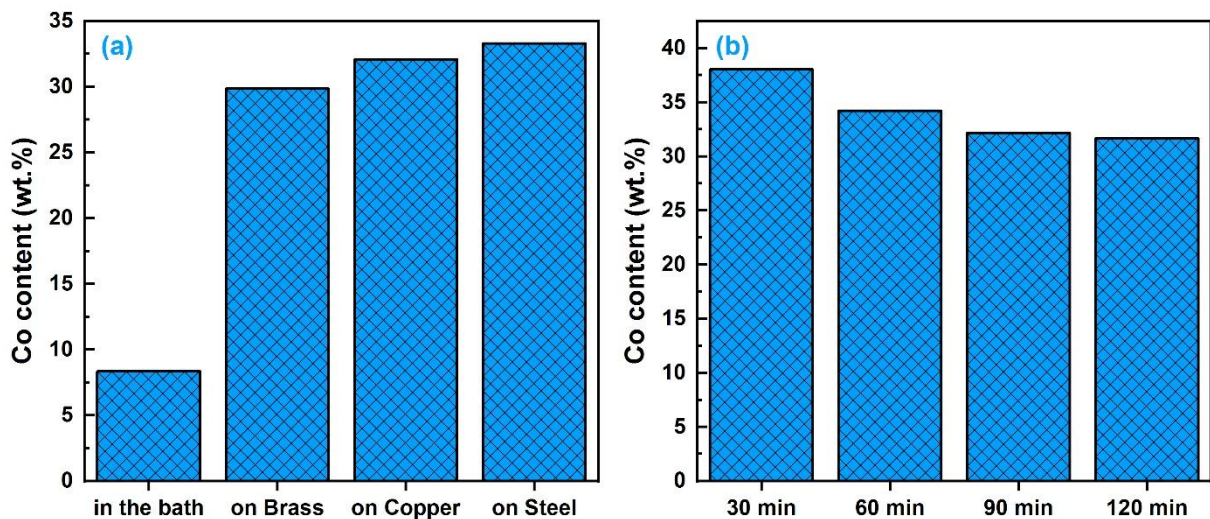


Figure IV.22: Co content in the electrodeposition bath and in the coatings deposited on different substrates (a) and during different deposition times (b).

IV.3.3.c) Effect on the thickness of coatings

The thickness of the elaborated Ni-Co coatings as a function of type of substrate and electrodeposition duration is shown in Figure IV.23. It is evident that the electrodeposited coatings show only a slight variation in thickness with the variation of the type of the used metallic substrate (Figure IV.23 (a)). As the coatings deposited on copper and brass have almost the same thickness of about 45.2 and 44.5 μm respectively, while the coating deposited on StW24 steel has a slightly higher thickness of about 47.6 μm .

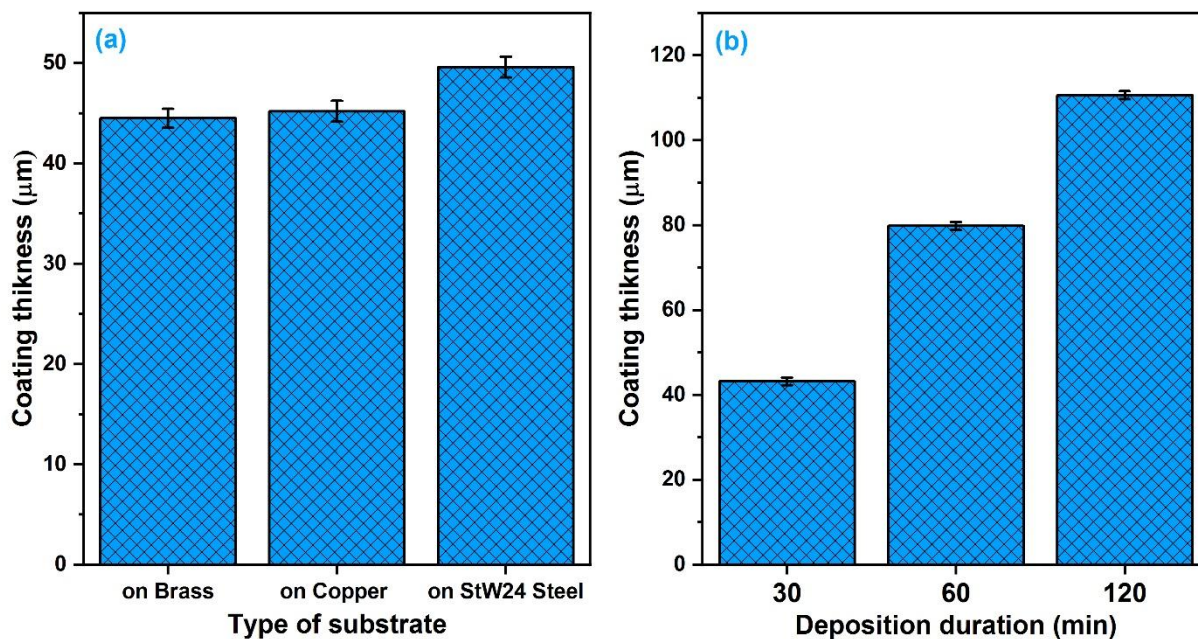


Figure IV.23: Thickness of coatings as a function of type of substrate (a) and deposition duration (b).

In contrast, the thickness of the electrodeposited Ni-Co coatings increases significantly with increasing deposition time (Figure IV.23 (b)). The deposition time of 30 min results in coatings with a thickness of about 43.2 μm , the thickness increases towards 79.8 μm after one hour of deposition and to about 110.6 μm after two hours of deposition. Hence, it can be concluded that the deposition rate decreases with increasing deposition time from 1.44 $\mu\text{m}/\text{min}$ after half an hour of deposition to 1.33 $\mu\text{m}/\text{min}$ after one hour and then to 0.92 $\mu\text{m}/\text{min}$ after 2 hours of deposition. This is mainly attributed to the relative impoverishment of the electrodeposition bath by Co^{2+} and Ni^{2+} ions with the extension of the deposition time. Moreover, the thickness of the coatings deposited on the different substrates has a direct relationship with their Co

content, supporting our proposal that the deposition rate has a proportional relationship with the degree of anomalous codeposition of the Ni-Co alloy (see section IV.3.1.b).

IV.3.3.d) Effect on the microstructural properties of coatings

Figure IV.24 displays the XRD spectra of the coatings deposited on the different substrates and with different thicknesses. It is clear that regardless of the nature of the substrate or the thickness of the coating, all the peaks characterize the total solid solution of the Ni-Co alloy with α (fcc) crystal structure known for such Ni-Co coatings with a Co content < 50 wt.%, as shown in sections (I.5.6.a) and (III.3.1.b). The substrate type and the layer thickness also do not show a significant influence on the crystallographic texture of the coatings, since all the prepared coatings exhibit the same crystallographic orientations (111), (200), (311) and (222) with the consolidation of (111) as preferred orientation. The only change that can be observed in the XRD patterns of the prepared coatings with the change of substrate and coating thickness is the slight variation in the peaks intensities. Referring to Figure IV.22, it can be seen that the peak intensity has an inverse relationship with the Co content in the coatings, as the peak intensity becomes stronger with decreasing Co content and vice versa. This supports our previous suggestion (see section III.3.1.c and IV.3.2.c) concerning the decrease in the crystallinity of Ni-Co coatings with increasing Co content due to the mismatches in the Ni crystal lattice created by Co atoms with relatively larger atomic radius.

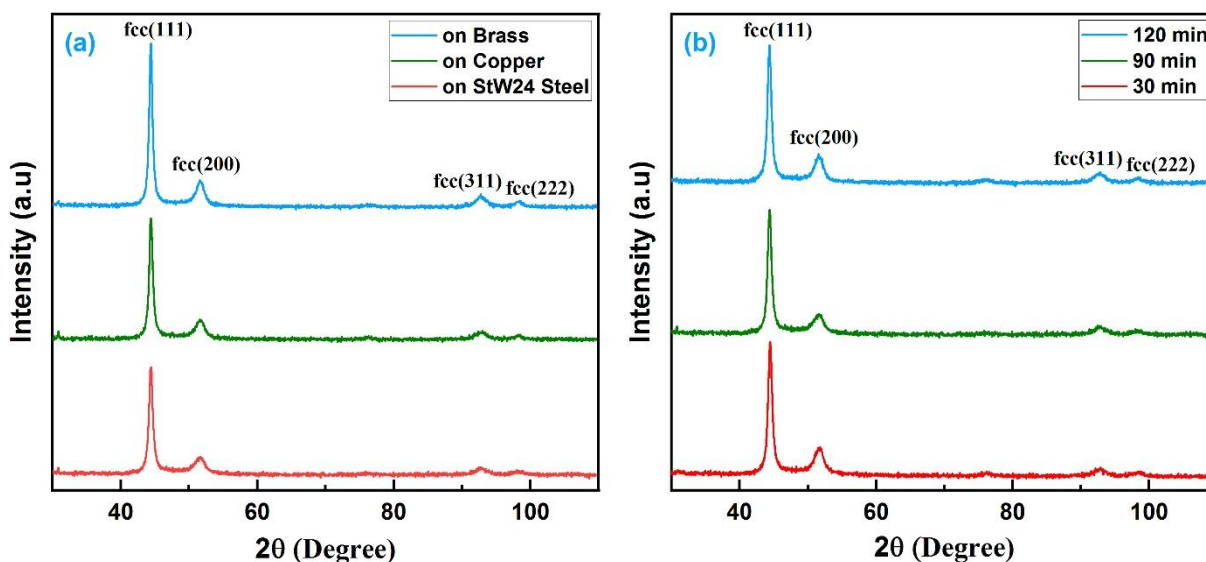


Figure IV.24: XRD patterns of Ni-Co coatings electrodeposited on different substrates (a) and with different thicknesses (b).

IV.3.3.e) Effect on the hardness of coatings

The nano-indentation (instrumented indentation) technique is used exclusively in this part of the study to avoid the effect of the substrate interaction on the measured hardness values, since different substrates and coating thicknesses are used. The advantage of this technique is that very low indentation loads can be applied, as the hardness measurement of the coatings can be distorted by substrate deformation when high loads are applied. In general, the depth of the indentation should be no more than 10-20% of the total coating thickness to confine the plastic flow region caused by the indenter penetrating the coating, thereby eliminating the effect of the substrate on the measured hardness [200–202]. According to the load-displacement curves of nano-indentation (Figure IV.25 (b) and (d)), the penetration depth of the indenter in all the measurements does not exceed 0.14 μm , while the thickness of the prepared Ni-Co layers is between 43 and 110 μm , which means that the indenter penetration does not exceed 0.33% of the coating thickness. Therefore, it can be stated that the effect of the substrate deformation on the measured hardness values is completely excluded.

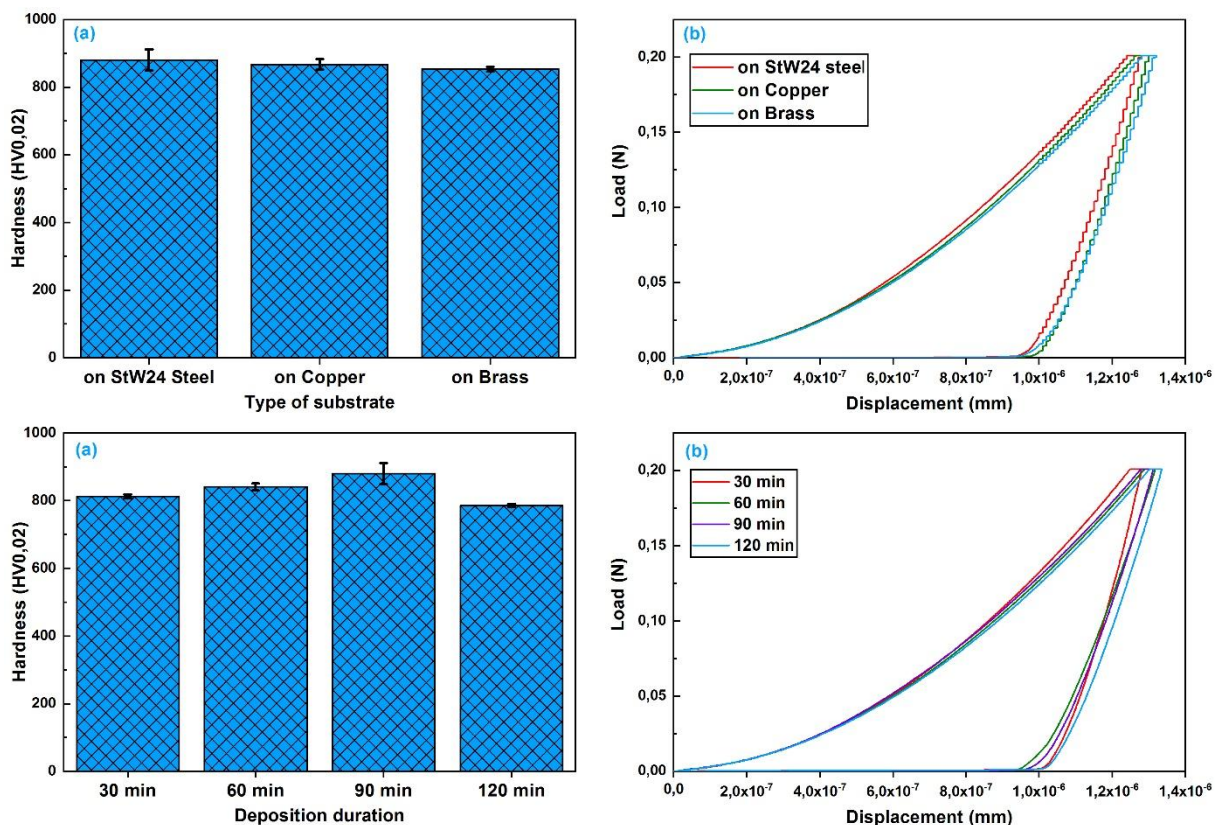


Figure IV.25: Nanohardness of the coatings deposited at different substrates and with different thicknesses (a) (c) and their indentation load-displacements curves (b) (d).

On the other hand, it can be clearly seen that the variation of the hardness of the coatings depending on the type of the used metallic substrate does not present a very significant evolution (Figure IV.25 (a)). Since the hardness varies between about 853HV for the coating on brass to about 880HV for the coating on StW24 steel. While the Ni-Co alloy coatings deposited with different deposition times show a more significant change in hardness with the increase in their thickness (Figure IV.25 (b)). Where the hardness increases from about 813 to 880 HV as a result of increasing the thickness of the layer from about 43 to about 80 μm and then decreases to about 785 HV with further increase in thickness to about 110 μm . Thus, it can be suggested that the type of substrate and, to a greater extent, the thickness of the layer has a slight effect on the hardness of nanocrystalline Ni-Co alloy coatings.

IV.3.3.f) Effect on the tribological behavior of coatings

We want to investigate the tribological properties of the coatings by scratch test in this part of the work to test in addition to the anti-wear properties of the coatings, their adhesion to the substrates. Since different metal substrates and coating thicknesses are applied in this part, this is what could affect the coating/substrate adhesion force. Recording the normal force (F_N) acting on the scratch stylus and the tangential force (F_T) acting in the direction of the scratch is potentially used to determine the critical load (L_C) characterizing the substrate/coating adhesion force. Tangential force monitoring, in particular, can provide information on the adhesion loss and the frictional resistance that can be used with microscopic observations to accurately determine the critical load (L_C) [203]. The variation of the tangential force (F_T) as a function of the applied normal force (F_N) in the scratch tests of Ni-Co coatings deposited on different substrates and having different thicknesses are presented in Figure IV.26. As expected, the curves show a continuous increase in tangential force F_T with increasing applied load F_N . There is also some fluctuations in the F_T vs F_N curve, which are explained by the presence of asperities, pores and roughness on the surface of the elaborated Ni-Co coatings. These deform when the stylus comes into contact with the coating to give a smooth and polished intermediate layer [204]. However, no transition points that might be indicative of the critical delamination force (L_C) of the Ni-Co coating on the substrate can be observed in the frictional behavior of the system from the (F_T vs F_N) graphs.

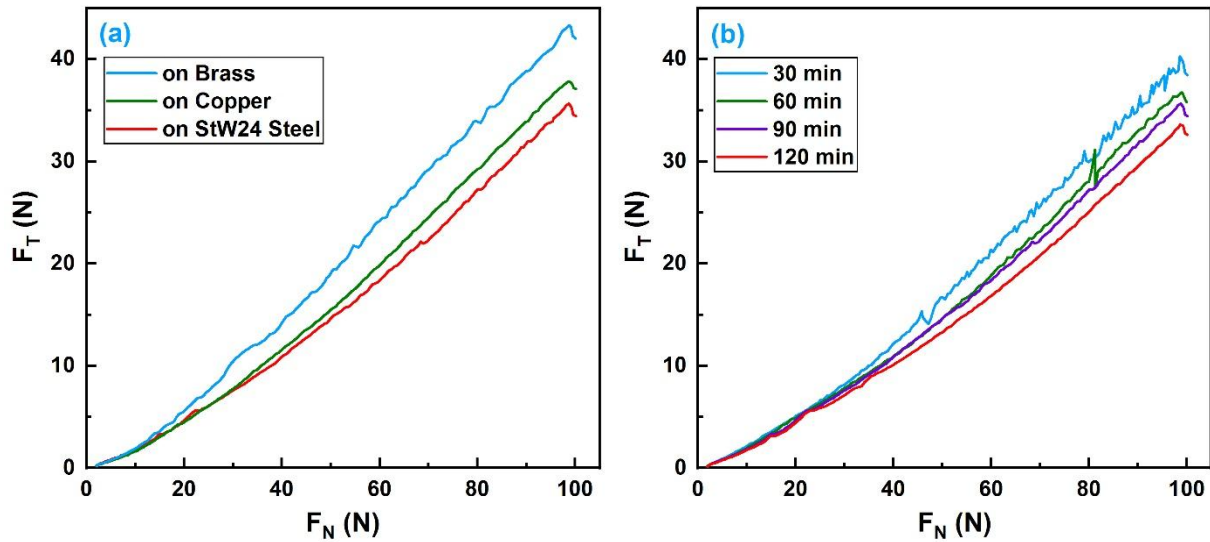


Figure IV.26: F_T vs. F_N monitoring during the scratch test of Ni-Co coatings deposited on different substrates (a) and with different thicknesses (b).

The plot of friction coefficient ($\mu = F_T/F_N$) versus the normal force (F_N) may be more useful than the (F_T vs. F_N) plots in the determination of the critical load (L_C) [204]. Figure IV.27 shows the variation of the friction coefficient as a function of the applied normal load.

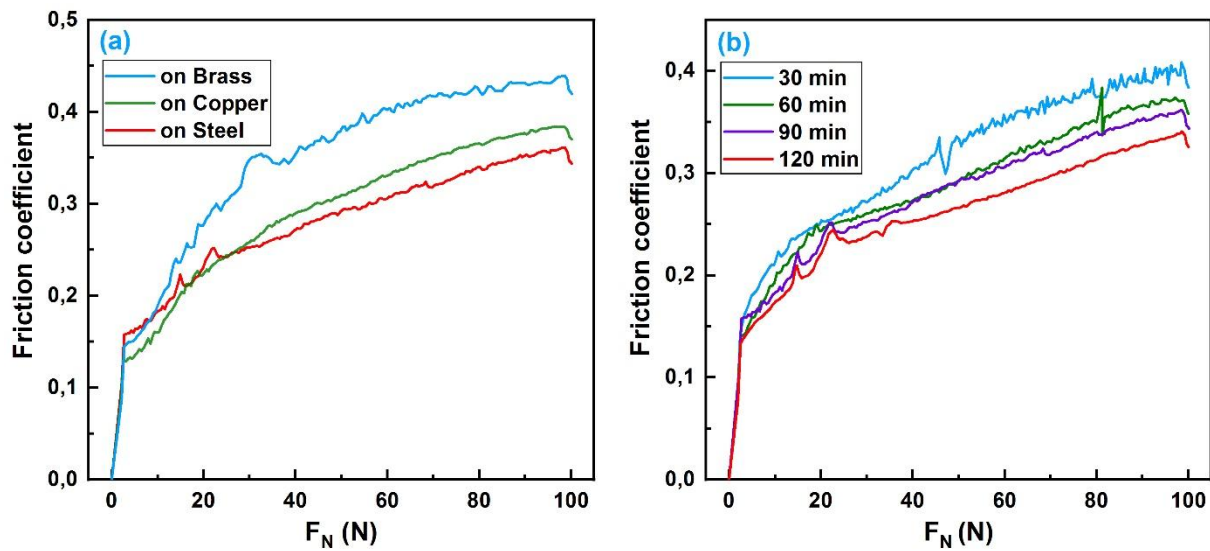


Figure IV.27: Friction coefficient vs. F_N monitoring during the scratch test of Ni-Co coatings deposited on different substrates (a) and with different thicknesses (b).

Except the first transition due to the first contact of the stylus with the coating surface, no transition points can be observed in the frictional behavior of all the electrodeposited nanocrystalline Ni-Co coatings. This means that under these test conditions, the deposited Ni-

Co layers do not delaminate from the substrate surface, whatever the type of the used metallic substrate or the thickness of the deposited layer. These results can be attributed to the thickness and hardness of the coating. Indeed, when the coating is relatively hard and too thick, the penetrator cannot reach the coating/substrate interface in order to delaminate the coating from the substrate. However, despite the fact that the stylus could not reach the substrate due to the thickness of the deposited layers ($\geq 43 \mu\text{m}$), it can be stated that the adhesion of the deposited layers is strong on all the studied substrates and with all the applied thicknesses insofar as the layers do not delaminate despite the application of a normal load up to 100 N. On the other hand, if we refer to [Figure IV.23](#), it can be noticed that the friction coefficient of the deposited Ni-Co coatings is decreases with the increase of their thickness.

The monitoring of critical loads and friction coefficients is not a sufficient parameter to study the adhesion and tribological properties of the elaborated coatings. Optical microscopy observations of scratch test scars can provide additional information on the adhesion and tribological behavior of the layers [205]. Optical micrographs taken along the length of the scratch channels produced on the different electrodeposited Ni-Co coatings are shown in [Figure IV.28](#) and [Figure IV.29](#).

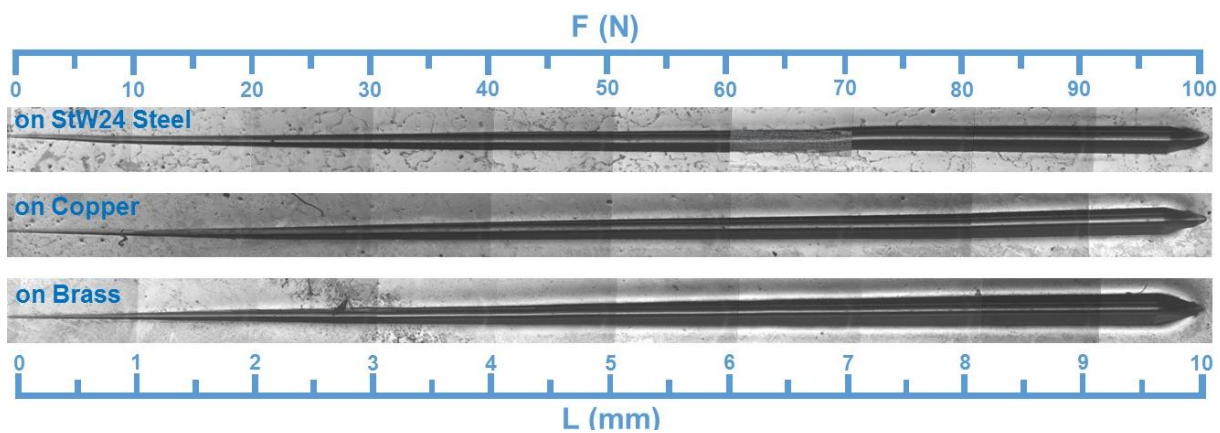


Figure IV.28: Optical micrographs of the scratches performed on the Ni-Co coatings deposited on StW24 steel, copper and brass.

It appears that all the coatings behave as ductile materials and exhibit significant plastic deformation in the direction of the stylus, which deformation increases with the penetration of the stylus into the coating as a result of the increase in the applied normal load. However, no cracks, fragmentation or spalling that could characterize critical loads can be observed along the scratch channel on all the examined Ni-Co coatings, these observations are also confirmed

by SEM observations on one of the realized scratches, as shown in Figure IV.30. Accordingly, the scratch test under such conditions on ductile Ni-Co alloy coatings can be operated more as an abrasion test than as an adherence test.

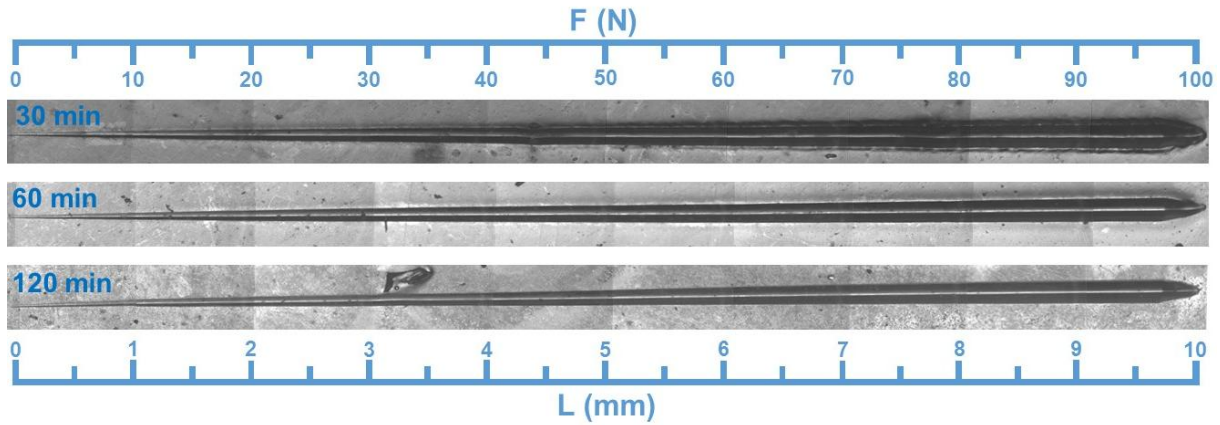


Figure IV.29: Optical micrographs of the scratches performed on Ni-Co coatings of different thicknesses.

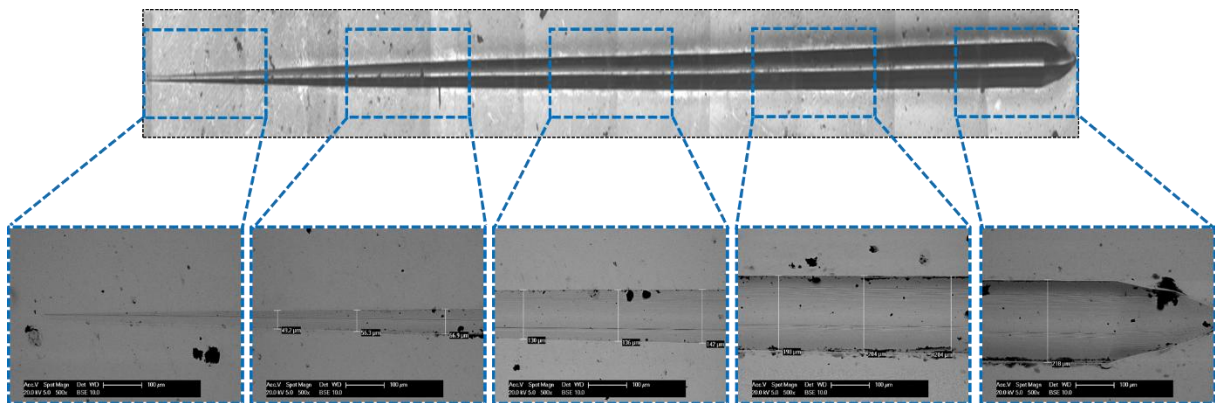


Figure IV.30: SEM micrographs of a scratch made on one of the electrodeposited Ni-Co coatings.

The scratch test is not only reserved to the characterization of the adhesion of coatings on substrates, but it can also be exploited to obtain information about the tribological performances and the wear resistance of the coatings. Profiles on the largest width of the scratch channel are made by mechanical profiler in order to qualitatively evaluate the abrasion resistance of the various elaborated Ni-Co layers as illustrated in Figure IV.31. As can be clearly observed, there are slight variations (in the micrometer range) in the width and depth of the scratches, which correspond to the differences in abrasion resistance and plastic deformation of the different prepared coatings. As the scratch test is a two-dimensional indentation test [206,207], these

slight differences in wear resistance can be attributed mainly to the slight differences in hardness of the examined Ni-Co coatings. Accordingly, by comparing the results in [Figure IV.25](#) with those in [Figure IV.31](#), we can conclude that the hardness of the coating is the decisive parameter in the scratch resistance of the coating. It can be seen that narrower and shallower scratches corresponding to less plastic deformation and higher abrasion resistance can be observed with the increase in hardness following the change of substrate or the variation in coating thickness.

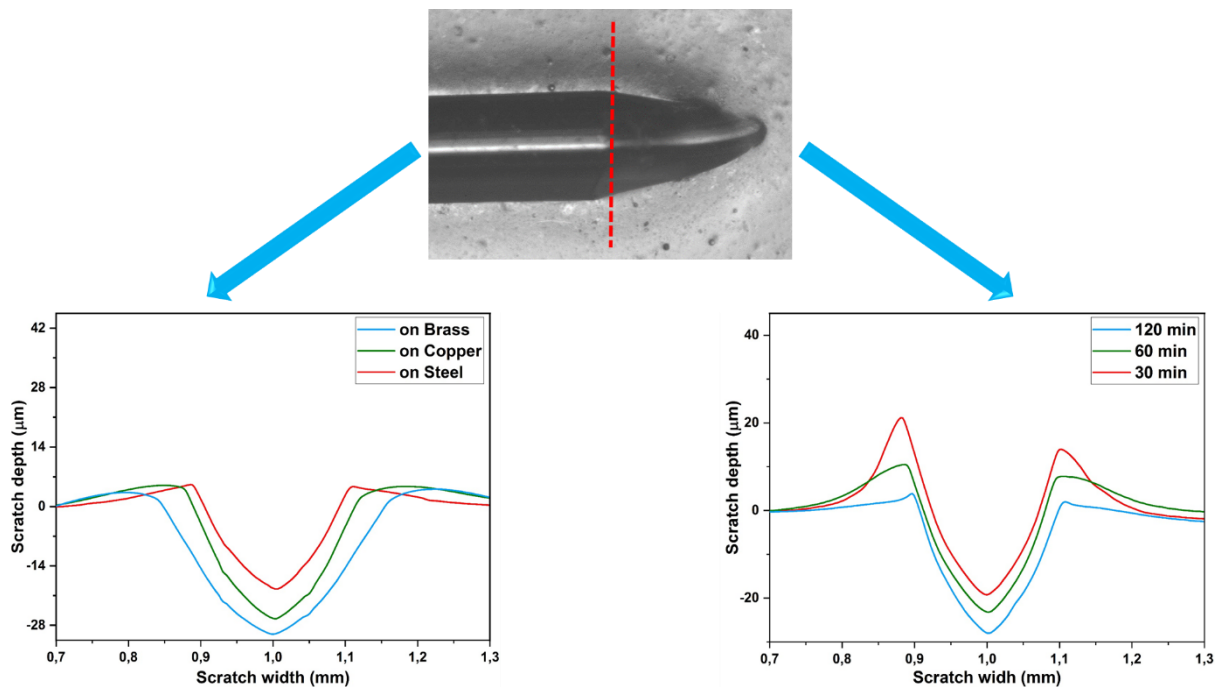


Figure IV.31: Cross-sectional profiles on the largest width of the scratches made on the different studied coatings.

IV.4 CONCLUSIONS

In order to optimize the electrodeposition conditions of anti-wear Ni-Co coatings, this chapter was devoted to the examination of the effect of some experimental parameters of their electrodeposition, namely the Co content of the electrolyte and the bath temperature on their composition and on their morphostructural, mechanical and tribological properties. The maintenance of the properties of the Ni-Co coatings, in particular their tribological performances, was also tested on different substrates, namely StW24 steel, copper and brass and using different coating thicknesses (43.2, 79.8 and 110.6 µm). The following important conclusions can be drawn from these different investigations.

(1) The analysis of the chemical composition of the electrodeposited Ni-Co coatings showed that the anomalous codeposition mechanism of Ni-Co alloy (discussed in detail in the previous chapter) was always present, regardless of the concentration of Co in the electrolyte, the bath temperature, the substrate type or the deposition time. Varying these parameters can only affect the degree of the anomalous codeposition.

(2) The variation of Co concentration in the electrolyte had a great influence on the composition and the properties of the electrodeposited Ni-Co coatings. Since, the Co content in the coatings has gradually increased, in parallel with its gradual increase in the electrolyte. This gradual increase in Co content has led to a gradual change in morphology, from granular smooth to branched-porous, passing through a mixture of both, and a change in the crystal structure from α (fcc) to ϵ (hcp) passing by a mixed α (fcc) + ϵ (hcp) structure. The formation of the branched-porous morphology and the increase in crystallite size with increasing Co content led to a significant decrease in the hardness of the Ni-Co coatings according to a quasi-Hall-Petch gradient. However, the formation of ϵ (hcp) phase with excellent friction reduction behavior in Co-rich Ni-Co nanocrystalline coatings resulted in their very good wear resistance despite their relatively low hardness.

(3) The bath temperature also showed a significant effect on the composition and on the different properties of the elaborated Ni-Co coatings. The Co content in the coatings changed as the bath temperature varied. Increasing the bath temperature did not appear to have a significant effect on the grains shape, but led to a significant porosity rate in the coatings electrodeposited at a bath temperature $\geq 65^\circ\text{C}$. It did not cause any change in the crystalline phases of the deposits but resulted in a slight variation in the crystallites size. The variation of the coatings hardness with the variation of the crystallites size exhibited a deviation from Hall-Petch gradient in this case, due to the appearance of a significant porosity rate in the coatings deposited at a bath temperature $\geq 65^\circ\text{C}$. The frictional and anti-wear properties of the coatings also varied due to the variation in the composition, microstructure and microhardness with the variation of the bath temperature. The Ni-Co coating deposited at 25°C demonstrated the better tribological performances among the elaborated coatings, which implies a review of the use of higher temperatures in the electroplating of Ni-Co coatings for anti-wear applications.

(4) The electrodeposited Ni-Co coatings showed a strong adhesion on all the studied substrates and with all the applied thicknesses. They also maintained their good tribological properties

and showed only a slight change in the anti-wear performances despite the change in the type of metal substrate and the layer thickness, which could allow to extend the fields of their applications.

*General conclusions and
perspectives*

GENERAL CONCLUSIONS AND PERSPECTIVES

1. GENERAL CONCLUSIONS

As recent studies have shown, the electrodeposited microcrystalline Ni-Co alloy coatings have better tribological properties than pure microcrystalline Ni coatings. However, the microhardness must be further increased by decreasing the crystallite size according to the Hall-Petch effect. The objective of this thesis was to study the tribological performances of Ni-Co coatings with reduced nanometric crystallite size elaborated under different electrodeposition conditions, on different substrates and with different thicknesses, aiming at improving their mechanical and tribological properties as economical and eco-friendly alternatives to the environmentally harmful hard chromium coatings commonly used in anti-wear applications. The objective was also to investigate the disputed and poorly understood role of tribofilms and wear debris on the different tribological behaviors of these coatings.

For this purpose, nanocrystalline Ni and Ni-Co coatings were electrodeposited on a StW24 mild steel substrate in the presence of 2-butyne-1,4-diol (BD) and saccharin as crystallites refiners. Special attention being paid to the effect of the latter on the morphostructural characteristics of these coatings. Chemical, morphological, structural and mechanical characterizations on the worn and unworn surfaces of the substrate and electroplated coatings were conducted by different surface analysis techniques. The performances of the nanocrystalline Ni-Co coatings as anti-wear coating on StW24 mild steel was examined. The anti-wear performances of these coatings were compared also with the commonly used coating for such applications, namely the electrodeposited nanocrystalline pure Ni coating. Furthermore, the wear mechanisms, the wear debris, the tribofilms and their roles on the tribological behavior of all studied materials have been thoroughly investigated. The results showed that the nanocrystalline electrodeposited Ni and Ni-Co coatings exhibit a very good hardness-toughness combination and a strong adhesion to the StW24 mild steel substrate. The nanocrystalline Ni-Co coatings showed superior anti-wear performance compared to the uncoated StW24 steel substrate and to the pure nanocrystalline Ni coating. However, it was noticed that the Ni-rich Ni-Co coating (63 wt.% Ni) exhibited a relatively high friction coefficient, while the Co-rich Ni-Co coating (87 wt.% Co) showed a relatively low hardness, which means that the Co content in the coatings has a very significant effect on their mechanical and tribological properties.

Therefore, in the second part of this thesis, we focused on the study of the different parameters that can affect the Co content of Ni-Co coatings and consequently their mechanical and anti-

wear performances, namely the Co^{2+} concentration and the temperature of the electrodeposition bath. The results showed that the gradual addition of Co^{2+} to the electrolyte resulted in the gradual increase of the Co content in the electrodeposited coatings. This led to the substantial change of the crystal structure from α (fcc) to ϵ (hcp) passing by a mixed α (fcc) + ϵ (hcp), and a gradual change in morphology from granular smooth to branched-porous, passing through a mixture of both, which translated by the gradual decrease in the hardness according to a quasi-Hall-Petch gradient. The friction coefficient of the Ni-Co coatings was also decreased sensibly to the increase of their Co content, which could be explained by the lubricant effect of Co, the gradual change of crystal structure toward ϵ (hcp) phase with excellent friction reduction behavior and the disappearance of tribofilms on the worn surfaces of Co-rich Ni-Co coatings. The dramatic decrease in the friction coefficient resulted to a decrease in the wear rate and an improvement in the wear resistance, despite the decrease in the hardness of the coatings, what contradicts the Archard's law.

The bath temperature has also showed a significant effect on the composition and on the different properties of the elaborated Ni-Co coatings. The Co content in the coatings changed as the bath temperature varied. Increasing the bath temperature did not appear to have a significant effect on the grains shape, but led to a significant porosity rate in the coatings electrodeposited at a bath temperature $\geq 65^\circ\text{C}$. It did not cause any change in the crystalline phases of the deposits but resulted in a slight variation in the crystallites size. The variation of the coatings hardness with the variation of the crystallites size exhibited a deviation from Hall-Petch gradient in this case, due to the appearance of a significant porosity rate in the coatings deposited at a bath temperature $\geq 65^\circ\text{C}$. The frictional and anti-wear properties of the coatings also varied due to the variation in the composition, microstructure and microhardness with the variation of the bath temperature. The Ni-Co coating deposited at 25°C demonstrated the better tribological performances among the elaborated coatings, which implies a review of the use of higher temperatures in the electroplating of Ni-Co coatings for anti-wear applications.

The mechanical and anti-wear properties of the electrodeposited Ni-Co coatings were also tested on different metal substrates (StW24 steel, copper and brass) and with different thicknesses (43.2, 79.8 and 110.6 μm). The results indicated that the electrodeposited Ni-Co coatings showed strong adhesion on all the substrates studied and with all the thicknesses applied. They also retained almost the same structure, mechanical properties and good tribological properties and showed only a slight change in their anti-wear performances despite the change in their thicknesses and the type of metal substrate.

The outcomes of this thesis also revealed that whatever the various conditions applied in this thesis (bath composition, temperature, type of the substrate, and deposition time):

- The electrodeposition of Ni-Co alloys maintained an anomalous codeposition mechanism where the less noble metal (Co) deposited preferentially to the more noble metal (Ni).
- The coefficient of friction of Ni-Co coatings showed always an inverse relationship with their Co content.

The above results allowed us to conclude that:

- Nanocrystalline Ni-Co alloy coatings exhibit very good tribological performances better than that of pure Ni.
- There is considerable scope to further improve the anti-wear performances of nanocrystalline Ni-Co alloy coatings to exceed those of hard chromium, simply by optimizing the electrodeposition conditions.
- The tribological applications of these coatings can be very broad, as their properties vary only slightly when varying their thickness and the type of metallic substrate.

2. PERSPECTIVES

Through this study, we have concluded that the Co-rich Ni-Co coatings (more than 50 wt.% Co) exhibit the best tribological properties of friction reduction and wear resistance. However, the hardness of these coatings is decreased with increasing Co content. Therefore, the subject of increasing the hardness of this kind of coatings without altering their desirable tribological properties is a subject that can be of great interest. The approach that we have considered for the increase of the hardness of these coatings is their reinforcement by hard micro or nano particles. [Figure 1](#) illustrates macroscopic observations of Ni-Co-SiO₂ nanocomposite coatings deposited in the presence of different amounts of 2-butyne-1,4-diol (BD) and saccharin as grain refiners and sodium dodecyl sulfates (SDS) as surfactant. We find that the coatings with a microcrystalline Ni-Co metal matrix, deposited in the absence of grain refiners (0 BD 0Saccharine) exhibit the highest homogeneity among the deposited coatings and the best dispersion of SiO₂ nanoparticles. The addition of 0.5 g/l BD leads to inhomogeneous coatings (0.5BD 0Saccharin), where the majority of SiO₂ nanoparticles were concentrated on a single part of the coating surface. But the progressive addition of saccharin leads to increasingly homogeneous coatings. It is also observed that the coatings electrodeposited in the absence of SDS show a very poor homogeneity, but the progressive addition of SDS to the bath leads to

the progressive improvement in the homogeneity of the deposits. Thus, it can be concluded that the used additives have a great influence on the homogeneity and quality of the electrodeposited Ni-Co-SiO₂ nanocomposite coatings. For this purpose, we wish in our next work to optimize the concentration of the different additives in the electroplating bath to obtain more homogeneous and harder Ni-Co-SiO₂ nanocomposite coatings with tribological performances better than that of Co-rich nanocrystalline Ni-Co coatings.

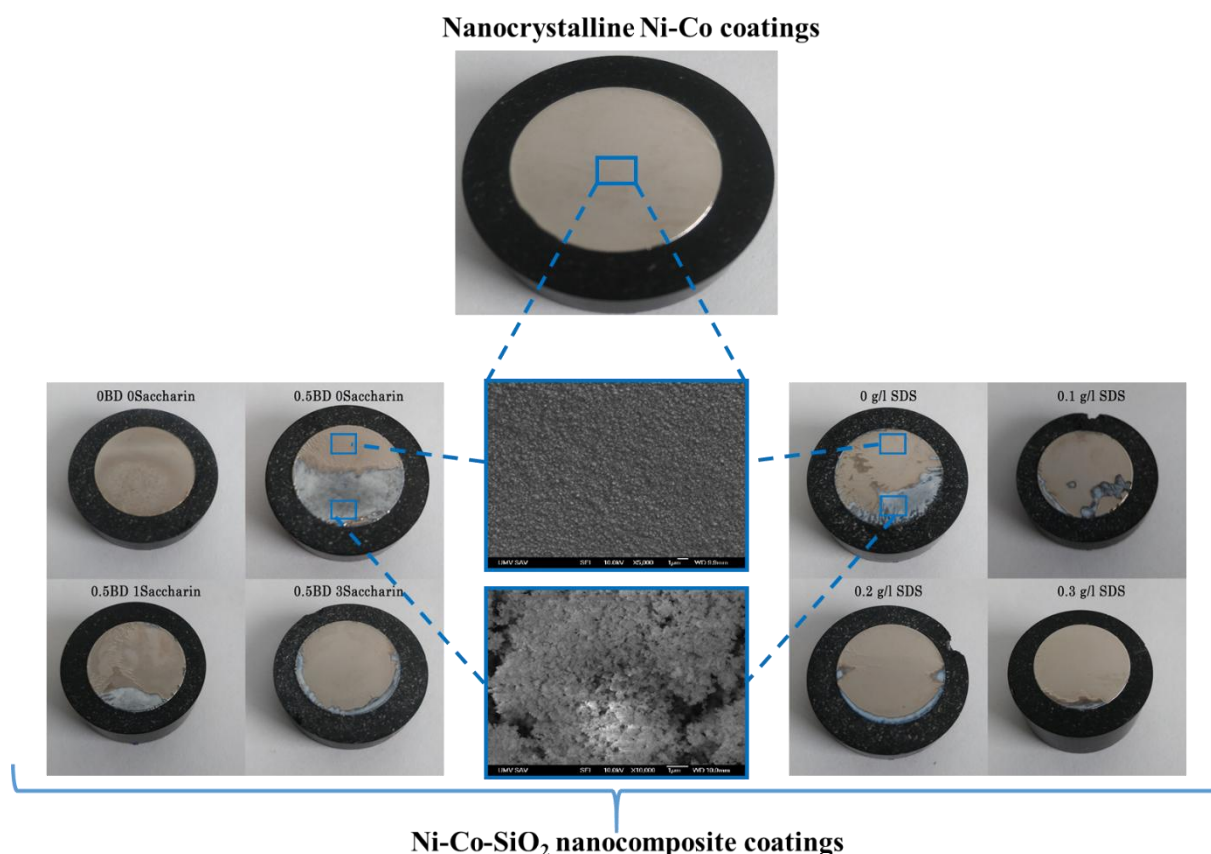


Figure 1: Macroscopic observations of Ni-Co-SiO₂ nanocomposite coatings deposited in the presence of different additives amounts.

*Bibliographical
references*

References:

- [1] I. Hutchings, P. Shipway, *Tribology: Friction and wear of engineering materials*, Elsevier Science, 2017.
- [2] T. Mang, K. Bobzin, T. Bartels, *Industrial Tribology: Tribosystems, Friction, Wear and Surface Engineering, Lubrication*, Wiley-VCH Verlag GmbH & Co. KGaA, Weinheim, Germany, 2010. <https://doi.org/10.1002/9783527632572>.
- [3] J. Frêne, La tribologie de l'antiquité à nos jours, *Mécanique & Industries*. 2 (2001) 263-282.
- [4] K.-H.Z. Gahr, *Microstructure and Wear of Materials*, Elsevier, North Holland, 1987.
- [5] D.J.G. Speight, A review of "Surface Science Investigations in Tribology, Experimental Approaches" Yip-Wah Chung, A.M. Homola, and G. Bryan Street, Editors, *Fuel Science and Technology International*. 10 (1992) 1561-1561. <https://doi.org/10.1080/08843759208905362>.
- [6] G. Darut, *Élaboration de revêtements à structure sub-micrométrique pour applications tribologiques par projection plasma de suspensions*, PhD thesis, University of Limoges, 2010.
- [7] A. Bahari, *Investigation into Tribological Performance of Vegetable Oils as Biolubricants at Severe Contact Conditions*, PhD thesis, University of Sheffield, 2017.
- [8] D. Luo, *Selection of coatings for tribological applications*, PhD thesis, Ecully, Ecole centrale de Lyon, 2009.
- [9] B.G. Mellor, *Surface coatings for protection against wear*, CRC Press, Cambridge, 2006.
- [10] O. Wånstrand, *Wear resistant low friction coatings for machine elements*, PhD thesis, Acta Universitatis Upsaliensis, 2000.
- [11] B. Swain, S. Bhuyan, R. Behera, S.S. Mohapatra, A. Behera, *Wear: A Serious Problem in Industry*, IntechOpen, 2020. <https://doi.org/10.5772/intechopen.94211>.
- [12] K. Holmberg, A. Matthews, *Coatings tribology: properties, mechanisms, techniques and applications in surface engineering*, Elsevier, 2009.
- [13] A.A.-K.H. Abu-Ein, S.M. Fayyad, M. Al-Rashdan, G. Al-Marahle, *Data-Base System of Tribological Coating Materials*, *Contemporary Engineering Sciences*. 5 (2012) 315-324.
- [14] Y. Ibaliden, *Etude du comportement d'un revêtement anti-usure en milieu hydrogène*, Magister thesis, University of Mostaganem, 2010.
- [15] S.N. Naik, S.M. Walley, The Hall-Petch and inverse Hall-Petch relations and the hardness of nanocrystalline metals, *J Mater Sci*. 55 (2020) 2661-2681. <https://doi.org/10.1007/s10853-019-04160-w>.
- [16] S.C. Tjong, H. Chen, *Nanocrystalline materials and coatings*, *Materials Science and Engineering: R: Reports*. 45 (2004) 1-88. <https://doi.org/10.1016/j.mser.2004.07.001>.
- [17] G.-M. Chow, I.A. Ovid'ko, T. Tsakalakos, eds., *Nanostructured Films and Coatings*, Springer Netherlands, 2000. <https://doi.org/10.1007/978-94-011-4052-2>.
- [18] V. Viswanathan, T. Laha, K. Balani, A. Agarwal, S. Seal, *Challenges and advances in nanocomposite processing techniques*, *Materials Science and Engineering: R: Reports*. 54 (2006) 121-285. <https://doi.org/10.1016/j.mser.2006.11.002>.
- [19] J.W. Dini, *Electrodeposition: the materials science of coatings and substrates*, Noyes Publications, Park Ridge, N.J., U.S.A., 1993.
- [20] J. James, G.G. Heiniger, Meeting the pollution prevention challenge at tinker air force base, *Federal Facilities Environmental Journal*. 6 (1995) 35-48. <https://doi.org/10.1002/ffej.333006030-5>.
- [21] C. Ould, X. Badiche, P. Montmitonnet, Y. Gachon, *Tests Tribologiques et mécaniques de différents revêtements PVD pour cylindres de laminoirs à bandes en acier Haut Carbone*, in: Presses des Mines, 2012.
- [22] S. Wang, C. Ma, F.C. Walsh, *Alternative tribological coatings to electrodeposited hard chromium: a critical review*, *Transactions of the IMF*. 98 (2020) 173-185. <https://doi.org/10.1080/00202967.-2020.1776962>.
- [23] D. Jeong, F. Gonzalez, G. Palumbo, K. Aust, U. Erb, The effect of grain size on the wear properties of electrodeposited nanocrystalline nickel coatings, *Scripta Materialia*. 44 (2001) 493-499. [https://doi.org/10.1016/S1359-6462\(00\)00625-4](https://doi.org/10.1016/S1359-6462(00)00625-4).

- [24] M. Surender, B. Basu, R. Balasubramaniam, Wear characterization of electrodeposited Ni-WC composite coatings, *Tribology International*. 37 (2004) 743-749. <https://doi.org/10.1016/j.triboint.2004.04.003>.
- [25] S. Özkan, G. Hapçı, G. Orhan, K. Kazmanlı, Electrodeposited Ni/SiC nanocomposite coatings and evaluation of wear and corrosion properties, *Surface and Coatings Technology*. 232 (2013) 734-741. <https://doi.org/10.1016/j.surfcoat.2013.06.089>.
- [26] Z. Mahidashti, M. Aliofkhaezrai, N. Lotfi, Review of Nickel-Based Electrodeposited Tribocoatings, *Transactions of the Indian Institute of Metals*. 71 (2017). <https://doi.org/10.1007/s12666-017-1175-x>.
- [27] J. Yu, Y. Wang, X. Zhao, Q. Li, Q. Qiao, J. Zhao, S. Zhai, Wear Resistance of Ni-Based Alloy Coatings, *Advances in Materials Science and Engineering*. 2019 (2019) 1–7. <https://doi.org/10.1155/2019/2548285>.
- [28] M. Hamidouche, N. Khennafi-Benghalem, Comparison between the microstructural, morphological, mechanical and tribological characteristics of nanocrystalline Ni and Ni-Co electrodeposited coatings, *JNTM*. 7 (2017) 33-38.
- [29] C. Ma, Electrodeposited nanocrystalline Ni-Co and Co-Ni-P coatings for hard chromium replacement, PhD thesis, University of Southampton, 2013.
- [30] Sh. Hassani, K. Raeissi, M.A. Golozar, Effects of saccharin on the electrodeposition of Ni-Co nanocrystalline coatings, *Journal of Applied Electrochemistry*. 38 (2008) 689-694. <https://doi.org/10.1007/s10800-008-9488-4>.
- [31] S.L. Wang, L.L. Hong, W.W. Yu, Influence of 2-butyne-1, 4-diol on the structure and performance of the Co-Ni alloy plated by electrodeposition, *Acta Metallurgica Sinica*. 21 (2008) 50-56. [https://doi.org/10.1016/S1006-7191\(08\)60019-8](https://doi.org/10.1016/S1006-7191(08)60019-8).
- [32] L.D. Rafailović, H.P. Karnthaler, T. Trišović, D.M. Minić, Microstructure and mechanical properties of disperse Ni-Co alloys electrodeposited on Cu substrates, *Materials Chemistry and Physics*. 120 (2010) 409-416. <https://doi.org/10.1016/j.matchemphys.2009.11.029>.
- [33] L. Wang, Y. Gao, Q. Xue, H. Liu, T. Xu, Graded composition and structure in nanocrystalline Ni-Co alloys for decreasing internal stress and improving tribological properties, *Journal of Physics D: Applied Physics*. 38 (2005) 1318-1324. <https://doi.org/10.1088/0022-3727/38/8/033>.
- [34] L. Tian, J. Xu, S. Xiao, The influence of pH and bath composition on the properties of Ni-Co coatings synthesized by electrodeposition, *Vacuum*. 86 (2011) 27-33. <https://doi.org/10.1016/j.vacuum.2011.03.027>.
- [35] Y. Li, H. Jiang, W. Huang, H. Tian, Effects of peak current density on the mechanical properties of nanocrystalline Ni-Co alloys produced by pulse electrodeposition, *Applied Surface Science*. 254 (2008) 6865-6869. <https://doi.org/10.1016/j.apsusc.2008.04.087>.
- [36] R. Oriňáková, A. Oriňák, G. Vering, I. Talian, R.M. Smith, H.F. Arlinghaus, Influence of pH on the electrolytic deposition of Ni-Co films, *Thin Solid Films*. 516 (2008) 3045-3050. <https://doi.org/10.1016/j.tsf.2007.12.081>.
- [37] C. Lupi, D. Pilone, Electrodeposition of nickel-cobalt alloys: the effect of process parameters on energy consumption, *Minerals Engineering*. 14 (2001) 1403-1410. [https://doi.org/10.1016/S0892-6875\(01\)00154-6](https://doi.org/10.1016/S0892-6875(01)00154-6).
- [38] T.R. Mahmood, J.K. Dennis, P.L. Barrett, Effect of ultrasonic agitation on Ni-Co and Ni-Fe deposition, *Surface Technology*. 22 (1984) 219-239. [https://doi.org/10.1016/0376-4583\(84\)9010-80](https://doi.org/10.1016/0376-4583(84)9010-80).
- [39] C. Ma, S.C. Wang, L.P. Wang, F.C. Walsh, R.J.K. Wood, The role of a tribofilm and wear debris in the tribological behaviour of nanocrystalline Ni-Co electrodeposits, *Wear*. 306 (2013) 296-303. <https://doi.org/10.1016/j.wear.2013.01.121>.
- [40] L. Wang, Y. Gao, Q. Xue, H. Liu, T. Xu, Microstructure and tribological properties of electrodeposited Ni-Co alloy deposits, *Applied Surface Science*. 242 (2005) 326-332. <https://doi.org/10.1016/j.apsusc.2004.08.033>.
- [41] Sh. Hassani, K. Raeissi, M. Azzi, D. Li, M.A. Golozar, J.A. Szpunar, Improving the corrosion and tribocorrosion resistance of Ni-Co nanocrystalline coatings in NaOH solution, *Corrosion Science*. 51 (2009) 2371-2379. <https://doi.org/10.1016/j.corsci.2009.06.026>.

- [42] Y. Li, H. Jiang, D. Wang, H. Ge, Effects of saccharin and cobalt concentration in electrolytic solution on microhardness of nanocrystalline Ni-Co alloys, *Surface and Coatings Technology*. 202 (2008) 4952-4956. <https://doi.org/10.1016/j.surfcoat.2008.04.093>.
- [43] N. Fenineche, C. Coddet, A. Saida, Effect of electrodeposition parameters on the microstructure and mechanical properties of Co-Ni alloys, *Surface and Coatings Technology*. 41 (1990) 75-81. [https://doi.org/10.1016/0257-8972\(90\)90131-U](https://doi.org/10.1016/0257-8972(90)90131-U).
- [44] Brevier Technical Ceramics, http://www.keramverband.de/brevier_engl/5/7/1/5_7_1_2.htm (accessed January 20, 2021).
- [45] C.P. Massola, A.P. Chaves, E. Albertin, A discussion on the measurement of grinding media wear, *Journal of Materials Research and Technology*. 5 (2016) 282-288. <https://doi.org/10.1016/j.jmrt.2015.12.003>.
- [46] J.-P. Deville, A. Cornet, *Physique et ingénierie des surfaces*, EDP Sciences, 2012.
- [47] A. KHERRAF, Propriétés mécaniques et biomécaniques de dépôts obtenus par projection thermique « Application de l'Emission Acoustique », PhD thesis, University of Batna 2, 2014.
- [48] C.M. Taylor, Automobile engine tribology-design considerations for efficiency and durability, *Wear*. 221 (1998) 1-8. [https://doi.org/10.1016/S0043-1648\(98\)00253-1](https://doi.org/10.1016/S0043-1648(98)00253-1).
- [49] B. Bhushan, B.K. Gupta, *Handbook of Tribology: Materials, Coatings, and Surface Treatments*, McGraw-Hill, 1991.
- [50] S. Korcek, R. K. Jensen, Fuel Efficient Engine Oils, Additive Interactions, Boundary Friction, and Wear, in: *Tribology Series*, Elsevier, 1999: pp. 13-24. [https://doi.org/10.1016/S0167-8922\(99\)80024-8](https://doi.org/10.1016/S0167-8922(99)80024-8).
- [51] G.W. Stachowiak, ed., *Wear: materials, mechanisms and practice*, Wiley, Chichester, England, 2005.
- [52] E. Harea, I. Lapsker, A. Laikhtman, L. Rapoport, Bauschinger's Effect and Dislocation Structure Under Friction of LiF Single Crystals, *Tribol Lett*. 52 (2013) 205-212. <https://doi.org/10.1007/s11249-013-0206-y>.
- [53] T.B. Torgerson, M.D. Harris, S.A. Alidokht, T.W. Scharf, S.M. Aouadi, R.R. Chromik, J.S. Zabinski, A.A. Voevodin, Room and elevated temperature sliding wear behavior of cold sprayed Ni-WC composite coatings, *Surface and Coatings Technology*. 350 (2018) 136-145. <https://doi.org/10.1016/j.surfcoat.2018.05.090>.
- [54] J. Mystkowska, D. Łysik, M. Klekotka, Effect of Saliva and Mucin-Based Saliva Substitutes on Fretting Processes of 316 Austenitic Stainless Steel, *Metals*. 9 (2019) 178. <https://doi.org/10.3390/met9020178>.
- [55] M. Bouderbala, Analyse du comportement tribologique des ceramiques Application aux engrenages cylindriques, Magister thesis, University of Boumerdes, 2006.
- [56] O. Laidi, Caractérisation de la résistance à l'usure des aciers "HSLA X52 et X70," Magister thesis, University of Laghouat, 2013.
- [57] M.F. Ashby, S.C. Lim, Wear-mechanism maps, *Scripta Metallurgica et Materialia*. 24 (1990) 805-810. [https://doi.org/10.1016/0956-716X\(90\)90116-X](https://doi.org/10.1016/0956-716X(90)90116-X).
- [58] N. Fillot, Etude mécanique de l'usure : Modélisation par Eléments Discrets des débits de troisième corps solide, PhD thesis, INSA, Lyon, 2004.
- [59] What is Friction?, Kyowa Interface Science Co.,Ltd. https://www.face-kyowa.co.jp/english/en_science/en_what_friction.html (accessed February 21, 2021).
- [60] T.A. Stolarski, S. Tobe, The effect of spraying distance on wear resistance of molybdenum coatings, *Wear*. 249 (2001) 1096-1102. [https://doi.org/10.1016/S0043-1648\(01\)00842-0](https://doi.org/10.1016/S0043-1648(01)00842-0).
- [61] E. Rabinowicz, *Friction and Wear of Materials*, 2nd ed., Wiley, Chichester, England, 1995.
- [62] L. Ke, L. Jian, Surface nanocrystallization (SNC) of metallic materials-presentation of the concept behind a new approach, *Journal of Materials Science and Technology*. 15 (1999) 193-197.
- [63] F. Nasirpouri, *Electrodeposition of Nanostructured Materials*, Springer International Publishing, 2017. <https://doi.org/10.1007/978-3-319-44920-3>.
- [64] Y.D. Gamburg, G. Zangari, *Theory and Practice of Metal Electrodeposition*, Springer-Verlag, New York, 2011. <https://doi.org/10.1007/978-1-4419-9669-5>.
- [65] A. Akarapu, Surface property modification of copper by nanocomposite coating, Master thesis, National Institute of Technology, 2011.

- [66] M. Hamidouche, N. Khennafi-Benghalem, S. Jacomet, M. Fidès, P. Hvizdoš, Study of Ni₆₃-Co₃₇ nanocrystalline electrodeposited alloy as anti-wear coating on mild steel substrate, *Mater. Res. Express*. 6 (2019) 126557. <https://doi.org/10.1088/2053-1591/ab580f>.
- [67] L.J. Durney, *Electroplating Engineering Handbook*, 4th ed., Springer US, 1996. <https://www.springer.com/gp/book/9780412741104> (accessed June 21, 2021).
- [68] I. Gurrappa, L. Binder, Electrodeposition of nanostructured coatings and their characterization-A review, *Sci Technol Adv Mater*. 9 (2008) 043001. <https://doi.org/10.1088/1468-6996/9/4/043001>.
- [69] The Electroplating Process and Applications, PRV Engineering Blog. (2017). <https://blog.prv-engineering.co.uk/electroplating-process-applications/> (accessed June 28, 2020).
- [70] The Different Applications of Electroplating, Gold Plating Services. <https://www.goldplating.com/blogs/news/the-different-applications-of-electroplating> (accessed February 22, 2021).
- [71] C.C. Koch, *Nanostructured materials: processing, properties and applications*, Enlarged 2nd edition, William Andrew, Norwich, 2007.
- [72] H. Gleiter, Nanocrystalline materials, *Progress in Materials Science*. 33 (1989) 223-315. [https://doi.org/10.1016/0079-6425\(89\)90001-7](https://doi.org/10.1016/0079-6425(89)90001-7).
- [73] D. Clark, D. Wood, U. Erb, Industrial applications of electrodeposited nanocrystals, *Nanostructured Materials*. 9 (1997) 755-758. [https://doi.org/10.1016/S0965-9773\(97\)00163-3](https://doi.org/10.1016/S0965-9773(97)00163-3).
- [74] G.T. Rogers, K.J. Taylor, The effects of coumarin on the electrodeposition of nickel, *Electrochimica Acta*. 8 (1963) 887-904. [https://doi.org/10.1016/0013-4686\(62\)87045-5](https://doi.org/10.1016/0013-4686(62)87045-5).
- [75] J.O. Bockris, *Fundamental Aspects of ELECTROCRYSTALLIZATION*, Springer US, 1967. <https://doi.org/10.1007/978-1-4684-0697-9>.
- [76] L.P. Bicelli, B. Bozzini, C. Mele, L. D'Urzo, A Review of Nanostructural Aspects of Metal Electrodeposition, *Int. J. Electrochem. Sci*. 3 (2008) 53.
- [77] U. Erb, Electrodeposited nanocrystals: Synthesis, properties and industrial applications, *Nanostructured Materials*. 6 (1995) 533-538. [https://doi.org/10.1016/0965-9773\(95\)00114-X](https://doi.org/10.1016/0965-9773(95)00114-X).
- [78] A.E. Fetohi, R.M. Abdel Hameed, K.M. El-Khatib, E.R. Souaya, Study of different aluminum alloy substrates coated with Ni-Co-P as metallic bipolar plates for PEM fuel cell applications, *International Journal of Hydrogen Energy*. 37 (2012) 10807-10817. <https://doi.org/10.1016/j.ijhydene.2012.04.066>.
- [79] C. Ma, S.C. Wang, C.T.J. Low, L.P. Wang, F.C. Walsh, Effects of additives on microstructure and properties of electrodeposited nanocrystalline Ni-Co alloy coatings of high cobalt content, *Transactions of the IMF*. 92 (2014) 189-195. <https://doi.org/10.1179/0020296713Z.00000000011-5>.
- [80] B. Ranjith, G. Paruthimal Kalaignan, Ni-Co-TiO₂ nanocomposite coating prepared by pulse and pulse reversal methods using acetate bath, *Applied Surface Science*. 257 (2010) 42-47. <https://doi.org/10.1016/j.apsusc.2010.06.029>.
- [81] L.-K. Wu, X.-Y. Liu, J.-M. Hu, Electrodeposited SiO₂ film: a promising interlayer of a highly active Ti electrode for the oxygen evolution reaction, *J. Mater. Chem. A*. 4 (2016) 11949-11956. <https://doi.org/10.1039/C6TA03931F>.
- [82] O. US EPA, *Health Effects Notebook for Hazardous Air Pollutants*, US EPA. (2016). <https://www.epa.gov/haps/health-effects-notebook-hazardous-air-pollutants> (accessed February 24, 2021).
- [83] Regulation (EC) No 1272/2008 of the European Parliament and of the Council of 16 December 2008 on classification, labelling and packaging of substances and mixtures, amending and repealing Directives 67/548/EEC and 1999/45/EC, and amending Regulation (EC) No 1907/2006 (Text with EEA relevance), 2008. <http://data.europa.eu/eli/reg/2008/1272/oj/eng> (accessed February 25, 2021).
- [84] Z. Zeng, J. Zhang, Anti-wear properties of Cr-C and Ni-Co alloy coatings as substitutes for conventional nanocrystalline Cr coatings, *J. Phys. D: Appl. Phys.* 41 (2008) 185303. <https://doi.org/10.1088/0022-3727/41/18/185303>.
- [85] W.E.G. Hansal, B. Tury, M. Halmdienst, M.L. Varsányi, W. Kautek, Pulse reverse plating of Ni-Co alloys: Deposition kinetics of Watts, sulfamate and chloride electrolytes, *Electrochimica Acta*. 52 (2006) 1145-1151. <https://doi.org/10.1016/j.electacta.2006.07.012>.
- [86] J.R. Davis, *Nickel, Cobalt, and Their Alloys*, ASM International, 2000.

- [87] C. Gu, J. Lian, Z. Jiang, High Strength Nanocrystalline Ni-Co Alloy with Enhanced Tensile Ductility, *Advanced Engineering Materials*. 8 (2006) 252-256. <https://doi.org/10.1002/adem.200500197>.
- [88] A. Karimzadeh, M. Aliofkhaezaei, F.C. Walsh, A review of electrodeposited Ni-Co alloy and composite coatings: Microstructure, properties and applications, *Surface and Coatings Technology*. 372 (2019) 463-498. <https://doi.org/10.1016/j.surfcoat.2019.04.079>.
- [89] A. Brenner, *Electrodeposition of Alloys: PRINCIPLES and PRACTICE*, ACADEMIC PRESS INC, New York, 1963.
- [90] N. Zech, E.J. Podlaha, D. Landolt, Anomalous Codeposition of Iron Group Metals: II. Mathematical Model, *J. Electrochem. Soc.* 146 (1999) 2892-2900. <https://doi.org/10.1149/1.1392-025>.
- [91] H. Okamoto, T.B. Massalski, Alloy phase diagrams, in: *ASM Handbook*, ASM International, 1992.
- [92] J.K. Dennis, T.E. Such, *Nickel and Chromium Plating*, Elsevier, 1993.
- [93] K.R. Marikkannu, G.P. Kalaigan, T. Vasudevan, The role of additives in the electrodeposition of nickel-cobalt alloy from acetate electrolyte, *Journal of Alloys and Compounds*. 438 (2007) 332-336. <https://doi.org/10.1016/j.jallcom.2006.11.174>.
- [94] S. Shriram, S. Mohan, N.G. Renganathan, R. Venkatachalam, Electrodeposition of Nanocrystalline Nickel—a Brief Review, *Transactions of the IMF*. 78 (2000) 194-197. <https://doi.org/10.1080/00202967.2000.11871337>.
- [95] T. Kolonits, Z. Czigány, L. Péter, I. Bakonyi, J. Gubicza, Improved Hardness and Thermal Stability of Nanocrystalline Nickel Electrodeposited with the Addition of Cysteine, *Nanomaterials*. 10 (2020) 2254. <https://doi.org/10.3390/nano10112254>.
- [96] M.J.N.V. Prasad, A.H. Chokshi, Superplasticity in electrodeposited nanocrystalline nickel, *Acta Materialia*. 58 (2010) 5724-5736. <https://doi.org/10.1016/j.actamat.2010.06.047>.
- [97] M. Schlesinger, M. Paunovic, *Modern Electroplating*, John Wiley & Sons, 2011.
- [98] K.H.J. Buschow, *Encyclopedia of Materials: Science and Technology*, Elsevier, 2001.
- [99] D. Saraev, R.E. Miller, Atomic-scale simulations of nanoindentation-induced plasticity in copper crystals with nanometer-sized nickel coatings, *Acta Materialia*. 54 (2006) 33-45. <https://doi.org/10.1016/j.actamat.2005.08.030>.
- [100] Compound Metal Coatings Inc. (CMC), *ELECTROLESS NICKEL*, <https://www.cmcnickelplating.com/cms/index.php/coatings/electroless-nickel> (accessed February 26, 2021).
- [101] N.S. Mbugua, M. Kang, Y. Zhang, N.J. Ndiithi, G. V. Bertrand, L. Yao, Electrochemical Deposition of Ni, NiCo Alloy and NiCo-Ceramic Composite Coatings-A Critical Review, *Materials (Basel)*. 13 (2020) 3475. <https://doi.org/10.3390/ma13163475>.
- [102] M. Srivastava, V. Ezhil Selvi, V.K. William Grips, K.S. Rajam, Corrosion resistance and microstructure of electrodeposited nickel-cobalt alloy coatings, *Surface and Coatings Technology*. 201 (2006) 3051-3060. <https://doi.org/10.1016/j.surfcoat.2006.06.017>.
- [103] X. Yang, Q. Li, S. Zhang, H. Gao, F. Luo, Y. Dai, Electrochemical corrosion behaviors and corrosion protection properties of Ni-Co alloy coating prepared on sintered NdFeB permanent magnet, *J Solid State Electrochem.* 14 (2010) 1601-1608. <https://doi.org/10.1007/s10008-009-09-93-0>.
- [104] G.F. Wang, K.C. Chan, K.F. Zhang, Low temperature superplasticity of nanocrystalline electrodeposited Ni-Co alloy, *Scripta Materialia*. 54 (2006) 765-770. <https://doi.org/10.1016/j.scriptamat.2005.11.024>.
- [105] B. Bakhit, A. Akbari, A comparative study of the effects of saccharin and β -SiC nano-particles on the properties of Ni and Ni-Co alloy coatings, *Surface and Coatings Technology*. 253 (2014) 76-82. <https://doi.org/10.1016/j.surfcoat.2014.05.016>.
- [106] Y. Xuetao, W. Yu, S. Dongbai, Y. Hongying, Influence of pulse parameters on the microstructure and microhardness of nickel electrodeposits, *Surface and Coatings Technology*. 202 (2008) 1895-1903. <https://doi.org/10.1016/j.surfcoat.2007.08.023>.
- [107] L. Wang, Y. Gao, T. Xu, Q. Xue, A comparative study on the tribological behavior of nanocrystalline nickel and cobalt coatings correlated with grain size and phase structure, *Materials Chemistry and Physics*. 99 (2006) 96-103. <https://doi.org/10.1016/j.matchemphys.2005.10.014>.

- [108] B. Bakhit, A. Akbari, Nanocrystalline Ni-Co alloy coatings: electrodeposition using horizontal electrodes and corrosion resistance, *Journal of Coatings Technology and Research*. 10 (2013) 285-295. <https://doi.org/10.1007/s11998-012-9437-3>.
- [109] M. Alizadeh, A. Teymuri, E. Salahinejad, F. Alijani, A novel method to enhance silicon incorporation into nickel electrodeposited coatings, *Vacuum*. 134 (2016) 103-109. <https://doi.org/10.1016/j.vacuum.2016.10.006>.
- [110] G. Zhao, Y. Zhou, H. Zhang, Sliding wear behaviors of electrodeposited Ni composite coatings containing micrometer and nanometer Cr particles, *Transactions of Nonferrous Metals Society of China*. 19 (2009) 319-323. [https://doi.org/10.1016/S1003-6326\(08\)60271-X](https://doi.org/10.1016/S1003-6326(08)60271-X).
- [111] M. Zamani, A. Amadeh, S.M. Lari Baghal, Effect of Co content on electrodeposition mechanism and mechanical properties of electrodeposited Ni-Co alloy, *Transactions of Nonferrous Metals Society of China*. 26 (2016) 484-491. [https://doi.org/10.1016/S1003-6326\(16\)64136-5](https://doi.org/10.1016/S1003-6326(16)64136-5).
- [112] B. Kucharska, A. Krawczyńska, K. Roźniatowski, J. Zdunek, K. Poplawski, J. Sobiecki, The effect of current types on the microstructure and corrosion properties of Ni/Nano Al₂O₃ composite coatings, *Materiali in Tehnologije*. 51 (2017) 403-411. <https://doi.org/10.17222/mit.2015.347>.
- [113] A.M. Rashidi, A. Amadeh, The effect of saccharin addition and bath temperature on the grain size of nanocrystalline nickel coatings, *Surface and Coatings Technology*. 204 (2009) 353-358. <https://doi.org/10.1016/j.surfcoat.2009.07.036>.
- [114] A. Abdel Aal, H.A. Gobran, F. Muecklich, Electrodeposition of Ni-Ru-Al composite coating on steel surface, *Journal of Alloys and Compounds*. 473 (2009) 250-254. <https://doi.org/10.1016/j.jallcom.2008.05.050>.
- [115] J.X. Kang, W.Z. Zhao, G.F. Zhang, Influence of electrodeposition parameters on the deposition rate and microhardness of nanocrystalline Ni coatings, *Surface and Coatings Technology*. 203 (2009) 1815-1818. <https://doi.org/10.1016/j.surfcoat.2009.01.003>.
- [116] R. Mishra, B. Basu, R. Balasubramaniam, Effect of grain size on the tribological behavior of nanocrystalline nickel, *Materials Science and Engineering: A*. 373 (2004) 370-373. <https://doi.org/10.1016/j.msea.2003.09.107>.
- [117] J. Schiøtz, F.D. Di Tolla, K.W. Jacobsen, Softening of nanocrystalline metals at very small grain sizes, *Nature*. 391 (1998) 561-563. <https://doi.org/10.1038/35328>.
- [118] G.C. Hadjipanayis, R.W. Siegel, eds., *Nanophase Materials: Synthesis - Properties - Applications*, Springer Netherlands, 1994. <https://doi.org/10.1007/978-94-011-1076-1>.
- [119] C.K. Chung, W. Chang, Effect of pulse frequency and current density on anomalous composition and nanomechanical property of electrodeposited Ni-Co films, *Thin Solid Films*. 517 (2009) 4800-4804. <https://doi.org/10.1016/j.tsf.2009.03.087>.
- [120] A. Karpuz, H. Kockar, M. Alper, Electrodeposited Co-Ni Films: Electrolyte pH—Property Relationships, *Journal of Superconductivity and Novel Magnetism*. 26 (2013) 651-655. <https://doi.org/10.1007/s10948-012-1774-z>.
- [121] J. Vazquez-Arenas, M. Pritzker, Effect of electrolyte and agitation on the anomalous behavior and morphology of electrodeposited Co-Ni alloys, *J Solid State Electrochem*. 17 (2013) 419-433. <https://doi.org/10.1007/s10008-012-1932-z>.
- [122] T. Baskar, A.S. George, P.S.B. Aremu, Effect of Bath Temperature on Properties of Electrodeposited Nickel-Cobalt, *Journal of University of Shanghai for Science and Technology*. 22 (2020) 87-94. <https://doi.org/10.51201/Jusst12679>.
- [123] M.M. Kamel, Anomalous codeposition of Co-Ni: alloys from gluconate baths, *J Appl Electrochem*. 37 (2007) 483-489. <https://doi.org/10.1007/s10800-006-9279-8>.
- [124] D. Golodnitsky, Y. Rosenberg, A. Ulus, The role of anion additives in the electrodeposition of nickel-cobalt alloys from sulfate electrolyte, *Electrochimica Acta*. 47 (2002) 2707-2714. [https://doi.org/10.1016/S0013-4686\(02\)00135-4](https://doi.org/10.1016/S0013-4686(02)00135-4).
- [125] Y.Y. Yang, B. Deng, Preparation of Ni-Co Alloy Foils by Electrodeposition, *Advances in Chemical Engineering and Science*. 01 (2011) 27-32. <https://doi.org/10.4236/aces.2011.12005>.
- [126] G. Qiao, T. Jing, N. Wang, Y. Gao, X. Zhao, J. Zhou, W. Wang, High-speed jet electrodeposition and microstructure of nanocrystalline Ni-Co alloys, *Electrochimica Acta*. 51 (2005) 85-92. <https://doi.org/10.1016/j.electacta.2005.03.050>.

- [127] Q.S. Chen, Z.Y. Zhou, G.C. Guo, S.G. Sun, Electrodeposition of nanostructured CoNi thin films and their anomalous infrared properties, *Electrochimica Acta*. 113 (2013) 694-705. <https://doi.org/10.1016/j.electacta.2013.09.114>.
- [128] A. Sharma, S. Chhangani, R. Madhavan, S. Suwas, Correlation between crystallographic texture, microstructure and magnetic properties of pulse electrodeposited nanocrystalline Nickel-Cobalt alloys, *Journal of Magnetism and Magnetic Materials*. 434 (2017) 68-77. <https://doi.org/10.1016/j.jmmm.2016.12.146>.
- [129] C. Lupi, A. Dell'Era, M. Pasquali, P. Imperatori, Composition, morphology, structural aspects and electrochemical properties of Ni-Co alloy coatings, *Surface and Coatings Technology*. 205 (2011) 5394-5399. <https://doi.org/10.1016/j.surfcoat.2011.06.002>.
- [130] G.D. Hibbard, K.T. Aust, U. Erb, Thermal stability of electrodeposited nanocrystalline Ni-Co alloys, *Materials Science and Engineering: A*. 433 (2006) 195-202. <https://doi.org/10.1016/j.msea.2006.06.096>.
- [131] J. Kong, M. Sabatini, L. Monaco, J. Tam, J.L. McCrea, G. Palumbo, J. Howe, U. Erb, Characterization of a nanocrystalline NiCo electroformed sheet metal, *J Mater Sci*. 56 (2021) 1749-1767. <https://doi.org/10.1007/s10853-020-05325-8>.
- [132] I.Z. Rahman, M.V. Khaddem-Mousavi, A.A. Gandhi, T.F. Lynch, M.A. Rahman, Growth of Electrodeposited Ni-Co and Fe-Co Magnetic Films on Cu Substrates, *Journal of Physics: Conference Series*. 61 (2007) 523-528. <https://doi.org/10.1088/1742-6596/61/1/106>.
- [133] I. Kharmachi, L. Dhouibi, P. Berçot, M. Rezrazi, B. Lakard, Electrodeposition Behavior, Physico-chemical Properties and Corrosion Resistance of Ni-Co Coating Modified by Gelatin Additive, *Prot Met Phys Chem Surf*. 53 (2017) 1059-1069. <https://doi.org/10.1134/S2070205117-060132>.
- [134] C. Ma, S.C. Wang, R.J.K. Wood, J. Zekonyte, Q. Luo, F.C. Walsh, Hardness of porous nanocrystalline Co-Ni electrodeposits, *Met. Mater. Int*. 19 (2013) 1187-1192. <https://doi.org/10.1007/s12540-013-6006-y>.
- [135] I.A. Inman, Compacted oxide layer formation under conditions of limited debris retention at the wear interface during high temperature sliding wear of superalloys, PhD thesis, Northumbria University, 2004.
- [136] W.A. Brainard, D.H. Buckley, Preliminary Friction and Wear Studies of Cobalt-rhenium Solid Solution Alloy in Air and in Vacuum, National Aeronautics and Space Administration, 1971.
- [137] Y. Tsuru, M. Nomura, F.R. Foulkes, Effects of boric acid on hydrogen evolution and internal stress in films deposited from a nickel sulfamate bath, *Journal of Applied Electrochemistry*. 32 (2002) 629-634. <https://doi.org/10.1023/A:1020130205866>.
- [138] S. Lal, D. Gautam, K.M. Razeeb, The Impact of Surfactant Sodium Dodecyl Sulfate on the Microstructure and Thermoelectric Properties of p-type $(\text{Sb}_{1-x}\text{Bi}_x)_2\text{Te}_3$ Electrodeposited Films, *ECS J. Solid State Sci. Technol*. 6 (2017) 3017-3021. <https://doi.org/10.1149/2.0041703jss>.
- [139] X-Ray Fluorescence Spectroscopy - The Next Generation of Wear Debris Analysis, *Machinery Lubrication*, <https://www.machinerylubrication.com/Read/86/x-ray-fluorescence-spectroscopy> - (accessed August 21, 2020).
- [140] W.L. Bragg, W.H. Bragg, The structure of some crystals as indicated by their diffraction of X-rays, *Proceedings of the Royal Society of London. Series A, Containing Papers of a Mathematical and Physical Character*. 89 (1913) 248-277. <https://doi.org/10.1098/rspa.1913.0083>.
- [141] Techbriefs Media Group, X-ray Diffraction (XRD) Characterization Methods for Sigma=3 Twin Defects in Cubic Semiconductor (100) Wafers, . <https://www.techbriefs.com/component/content/article/tb/pub/techbriefs/electronics-and-computers/25972> (accessed June 21, 2021).
- [142] B.J. Inkson, Scanning electron microscopy (SEM) and transmission electron microscopy (TEM) for materials characterization, in: G. Hübschen, I. Altpeter, R. Tschuncky, H.-G. Herrmann (Eds.), *Materials Characterization Using Nondestructive Evaluation (NDE) Methods*, Woodhead Publishing, 2016: pp. 17-43. <https://doi.org/10.1016/B978-0-08-100040-3.00002-X>.
- [143] Confocal microscope instrument, *Encyclopedia Britannica*. <https://www.britannica.com/technology/confocal-microscope> (accessed June 13, 2020).
- [144] S.A. James, L.C. Powell, C.J. Wright, Atomic Force Microscopy of Biofilms-Imaging, Interactions, and Mechanics, *IntechOpen*, 2016. <https://doi.org/10.5772/63312>.

- [145] W.C. Oliver, G.M. Pharr, Measurement of hardness and elastic modulus by instrumented indentation: Advances in understanding and refinements to methodology, *Journal of Materials Research*. 19 (2004) 3. <https://doi.org/10.1557/jmr.2004.19.1.3>.
- [146] S.K. Gürel, İ.A. Yüksel, T. O. Kılınc, Uncertainty calculations and calibration of metal hardness testing equipment, in: S. Gazal (Ed.), 19th International Congress of Metrology (CIM2019), EDP Sciences, Paris, France, 2019: p. 12002. <https://doi.org/10.1051/metrology/201912002>.
- [147] E. Broitman, Indentation Hardness Measurements at Macro-, Micro-, and Nanoscale: A Critical Overview, *Tribol Lett.* 65 (2016) 23. <https://doi.org/10.1007/s11249-016-0805-5>.
- [148] D.J. Shuman, A.L.M. Costa, M.S. Andrade, Calculating the elastic modulus from nanoindentation and microindentation reload curves, *Materials Characterization*. 58 (2007) 380-389. <https://doi.org/10.1016/j.matchar.2006.06.005>.
- [149] R.J.K. Wood, P. Ramkumar, L. Wang, T.J. Wang, K. Nelson, E.S. Yamaguchi, J.J. Harrison, H.E.G. Powrie, N. Otin, Electrostatic monitoring of the effects of carbon black on lubricated steel/steel sliding contacts, in: D. Dowson, M. Priest, G. Dalmaz, A.A. Lubrecht (Eds.), *Tribology and Interface Engineering Series*, Elsevier, 2005: pp. 109-121. [https://doi.org/10.1016/S0167-892-2\(05\)80013-6](https://doi.org/10.1016/S0167-892-2(05)80013-6).
- [150] K. Yang, X. Shi, W. Zhai, A.M. Mahmoud Ibrahim, Wear rate of a TiAl matrix composite containing 10 wt% Ag predicted using the Newton interpolation method, *RSC Adv.* 5 (2015) 67102-67114. <https://doi.org/10.1039/C5RA11086F>.
- [151] H. Dahms, I.M. Croll, The Anomalous Codeposition of Iron-Nickel Alloys, *J. Electrochem. Soc.* 112 (1965) 771-775. <https://doi.org/10.1149/1.2423692>.
- [152] W.C. Grande, J.B. Talbot, Electrodeposition of Thin Films of Nickel-Iron II. Modeling, *J. Electrochem. Soc.* 140 (1993) 675-681. <https://doi.org/10.1149/1.2056141>.
- [153] A. Bai, C.C. Hu, Effects of electroplating variables on the composition and morphology of nickel-cobalt deposits plated through means of cyclic voltammetry, *Electrochimica Acta*. 47 (2002) 3447-3456. [https://doi.org/10.1016/S0013-4686\(02\)00281-5](https://doi.org/10.1016/S0013-4686(02)00281-5).
- [154] M. Rojas, C.L. Fan, H.J. Miao, D.L. Piron, Characterization of hydrogen evolution on cobalt electrodeposits in water electrolysis, *Journal of Applied Electrochemistry*. 22 (1992) 1135-1141. <https://doi.org/10.1007/BF01297414>.
- [155] M. Palomar-Pardavé, B.R. Scharifker, E.M. Arce, M. Romero-Romo, Nucleation and diffusion-controlled growth of electroactive centers, *Electrochimica Acta*. 50 (2005) 4736-4745. <https://doi.org/10.1016/j.electacta.2005.03.004>.
- [156] C.E. Dávalos, J.R. López, H. Ruiz, A. Méndez, R. Antaño-López, G. Trejo, Study of the Role of Boric Acid During the Electrochemical Deposition of Ni in a Sulfamate Bath, *Int. J. Electrochem. Sci.* 8 (2013) 16.
- [157] J.S. Santos, R. Matos, F. Trivinho-Strixino, E.C. Pereira, Effect of temperature on Co electrodeposition in the presence of boric acid, *Electrochimica Acta*. 53 (2007) 644-649. <https://doi.org/10.1016/j.electacta.2007.07.025>.
- [158] N. Wang, W.C. Hu, Y.H. Lu, Y.F. Deng, X.B. Wan, Y.W. Zhang, K. Du, L. Zhang, Role of surfactants in construction of porous copper film by electrodeposition approach, *Transactions of the IMF*. 89 (2013) 261-267. <https://doi.org/10.1179/174591911x13119320025636>.
- [159] S.H. Jeon, W.I. Choi, G.D. Song, Y.H. Son, D. Hur, Influence of Surface Roughness and Agitation on the Morphology of Magnetite Films Electrodeposited on Carbon Steel Substrates, *Coatings*. 6 (2016) 62. <https://doi.org/10.3390/coatings6040062>.
- [160] L. Tian, J. Xu, C. Qiang, The electrodeposition behaviors and magnetic properties of Ni-Co films, *Applied Surface Science*. 257 (2011) 4689-4694. <https://doi.org/10.1016/j.apsusc.2010.12.123>.
- [161] O.K. von Goldbeck, Iron-Carbon Fe-C, in: O.K. von Goldbeck (Ed.), *IRON-Binary Phase Diagrams*, Springer Berlin Heidelberg, Berlin, Heidelberg, 1982: pp. 23-26. https://doi.org/10.1007/978-3-662-08024-5_12.
- [162] U. Holzwarth, N. Gibson, The Scherrer equation versus the “Debye-Scherrer equation,” *Nature Nanotechnology*. 6 (2011) 534-534. <https://doi.org/10.1038/nnano.2011.145>.
- [163] B. Tury, M. Lakatos-Varsányi, S. Roy, Ni-Co alloys plated by pulse currents, *Surface and Coatings Technology*. 200 (2006) 6713-6717. <https://doi.org/10.1016/j.surfcoat.2005.10.008>.
- [164] S. Mordechay, P. Milan, *MODERN ELECTROPLATING*, 5th ed., John Wiley & Sons, Hoboken, New Jersey, 2010.

- [165] J. Amblard, I. Epelboin, M. Froment, G. Maurin, Inhibition and nickel electrocrystallization, *Journal of Applied Electrochemistry*. 9 (1979) 233-242. <https://doi.org/10.1007/bf00616093>.
- [166] H. Li, F. Czerwinski, J.A. Szpunar, Monte-Carlo simulation of texture and microstructure development in nanocrystalline electrodeposits, *Nanostructured Materials*. 9 (1997) 673-676. [https://doi.org/10.1016/S0965-9773\(97\)00148-7](https://doi.org/10.1016/S0965-9773(97)00148-7).
- [167] A. Karpuz, H. Kockar, M. Alper, O. Karaagac, M. Hacıismailoglu, Electrodeposited Ni-Co films from electrolytes with different Co contents, *Applied Surface Science*. 258 (2012) 4005-4010. <https://doi.org/10.1016/j.apsusc.2011.12.088>.
- [168] D. Tabor, *The Hardness of Metals*, Oxford University Press, Oxford, New York, 2000.
- [169] Vickers Hardness for all the elements in the Periodic Table, <http://periodictable.com/Properties/A/VickersHardness.v.log.html> (accessed April 13, 2019).
- [170] Atomic Radius for all the elements in the Periodic Table, <http://periodictable.com/Properties/A/AtomicRadius.v.html> (accessed April 13, 2019).
- [171] H.U. Rehman, *Solid Solution Strengthening and Diffusion in Nickel- and Cobalt-based Superalloys*, PhD thesis, FAU University, 2016.
- [172] A.S. Taha, F.H. Hammad, Application of the Hall-Petch Relation to Microhardness Measurements on Al, Cu, Al-MD 105, and Al-Cu Alloys, *physica status solidi (a)*. 119 (1990) 455-462. <https://doi.org/10.1002/pssa.2211190207>.
- [173] S. Kamran, K. Chen, L. Chen, *Ab initio* examination of ductility features of fcc metals, *Physical Review B*. 79 (2009) 024106. <https://doi.org/10.1103/PhysRevB.79.024106>.
- [174] D.M. Nuruzzaman, M.A. Chowdhury, *Friction and Wear of Polymer and Composites, Composites and Their Properties*. (2012). <https://doi.org/10.5772/48246>.
- [175] D. Muhammad Nuruzzaman, M. Asaduzzaman Chowdhury, M. Lutfar Rahaman, Effect of duration of rubbing and normal load on friction coefficient for polymer and composite materials, *Industrial Lubrication and Tribology*. 63 (2011) 320-326. <https://doi.org/10.1108/0036879111111-54931>.
- [176] N. Malatji, P.A.I. Popoola, Tribological and Corrosion Performance of Electrodeposited Nickel Composite Coatings, *Electrodeposition of Composite Materials*. (2016). <https://doi.org/10.5772/6-2170>.
- [177] L. Wang, Y. Gao, Q. Xue, H. Liu, T. Xu, Microstructure and tribological properties of electrodeposited Ni-Co alloy deposits, *Applied Surface Science*. 242 (2005) 326-332. <https://doi.org/10.1016/j.apsusc.2004.08.033>.
- [178] Z. Zhou, W.M. Rainforth, C.C. Tan, P. Zeng, J.J. Ojeda, M.E. Romero-Gonzalez, P.Eh. Hovsepian, The role of the tribofilm and roll-like debris in the wear of nanoscale nitride PVD coatings, *Wear*. 263 (2007) 1328-1334. <https://doi.org/10.1016/j.wear.2006.12.059>.
- [179] F. Svahn, Å. Kassman-Rudolph, E. Wallén, The influence of surface roughness on friction and wear of machine element coatings, *Wear*. 254 (2003) 1092-1098. [https://doi.org/10.1016/S0043-1648\(03\)00341-7](https://doi.org/10.1016/S0043-1648(03)00341-7).
- [180] M. Godet, The third-body approach: A mechanical view of wear, *Wear*. 100 (1984) 437-452. [https://doi.org/10.1016/0043-1648\(84\)90025-5](https://doi.org/10.1016/0043-1648(84)90025-5).
- [181] Q. Luo, Z. Zhou, W.M. Rainforth, M. Bolton, Effect of Tribofilm Formation on the Dry Sliding Friction and Wear Properties of Magnetron Sputtered TiAlCrYN Coatings, *Tribol Lett*. 34 (2009) 113-124. <https://doi.org/10.1007/s11249-009-9415-9>.
- [182] S.K. Biswas, Some mechanisms of tribofilm formation in metal/metal and ceramic/metal sliding interactions, *Wear*. 245 (2000) 178-189. [https://doi.org/10.1016/S0043-1648\(00\)00477-4](https://doi.org/10.1016/S0043-1648(00)00477-4).
- [183] H. Kato, K. Komai, Tribofilm formation and mild wear by tribo-sintering of nanometer-sized oxide particles on rubbing steel surfaces, *Wear*. 262 (2007) 36-41. <https://doi.org/10.1016/j.wear.-2006.03.046>.
- [184] S. Gupta, D. Filimonov, V. Zaitsev, T. Palanisamy, M.W. Barsoum, Ambient and 550°C tribological behavior of select MAX phases against Ni-based superalloys, *Wear*. 264 (2008) 270-278. <https://doi.org/10.1016/j.wear.2007.03.011>.
- [185] J. Vilana, E. Gómez, E. Vallés, Influence of the composition and crystalline phase of electrodeposited CoNi films in the preparation of CoNi oxidized surfaces as electrodes for urea electro-oxidation, *Applied Surface Science*. 360 (2016) 816-825. <https://doi.org/10.1016/j.apsusc.2015.11.072>.

- [186] I. Kharmachi, L. Dhouibi, P. Bercot, E.M. Rezrazi, Co-deposition of Ni-Co alloys on carbon steel and corrosion resistance, *Journal of Materials and Environmental Science*. 6 (2015) 1807-1812.
- [187] I.A. Inman, P.S. Datta, Studies of high temperature sliding wear of metallic dissimilar interfaces III: Incoloy MA956 versus Incoloy 800HT, *Tribology International*. 43 (2010) 2051-2071. <https://doi.org/10.1016/j.triboint.2010.05.010>.
- [188] A. Dolati, M. Sababi, E. Nouri, M. Ghorbani, A study on the kinetic of the electrodeposited Co-Ni alloy thin films in sulfate solution, *Materials Chemistry and Physics*. 102 (2007) 118-124. <https://doi.org/10.1016/j.matchemphys.2006.07.009>.
- [189] K. Lu, M.L. Sui, An explanation to the abnormal Hall-Petch relation in nanocrystalline materials, *Scripta Metall. Mater.* (1993) 1465-1470.
- [190] A.J. Bard, L.R. Faulkner, *Electrochemical Methods: Fundamentals and Applications*, 2nd ed., Hoboken: John Wiley & Sons, 2001.
- [191] A.M.A. Mohamed, Y. Ahmad, Electrodeposition of Nanostructured Nickel-Ceramic Composite Coatings: A review, *International Journal of Electrochemical Science*. 9 (2014) 1942-1963.
- [192] U. Sarac, M. Kaya, M.C. Baykul, Bath temperature-dependent structural properties, coercive force, surface morphology and surface texture of electrochemically grown nanostructured Ni-Co/ITO thin films, *Appl. Phys. A*. 126 (2020) 239. <https://doi.org/10.1007/s00339-020-3423-x>.
- [193] R.F. da C. Pereira, E.S.D. de Oliveira, M.R.S. Vieira, M.A.G. de A. Lima, S.L. Urtiga, Evaluation of Co-Ni/SiC Nanocomposite Coating Obtained by Electrodeposition on the Corrosion Resistance of API 5L X80 Steel, *Mat. Res.* 20 (2017) 221-230. <https://doi.org/10.1590/1980-5373-MR-2017-0025>.
- [194] U. Sarac, M.C. Baykul, Morphological and microstructural properties of two-phase Ni-Cu films electrodeposited at different electrolyte temperatures, *Journal of Alloys and Compounds*. 552 (2013) 195-201. <https://doi.org/10.1016/j.jallcom.2012.10.071>.
- [195] Y.F. Yang, Z.H. Wen, Q.G. Li, Electrodeposition of Ni-Co alloy films onto titanium substrate, *Rare Met.* 33 (2014) 442-447. <https://doi.org/10.1007/s12598-013-0197-8>.
- [196] C.K. Chung, R.X. Zhou, W.T. Chang, The anomalous behavior and properties of Ni-Co films codeposited in the sulfamate-chloride electrolyte, *Microsyst Technol.* 14 (2008) 1279-1284. <https://doi.org/10.1007/s00542-007-0509-8>.
- [197] M. Inoue, I. Hirasawa, The relationship between crystal morphology and XRD peak intensity on CaSO₄·2H₂O, *Journal of Crystal Growth*. 380 (2013) 169-175. <https://doi.org/10.1016/j.jcrysgro.2013.06.017>.
- [198] A.M. Rashidi, A. Amadeh, Effect of Electroplating Parameters on Microstructure of Nanocrystalline Nickel Coatings, *Journal of Materials Science & Technology*. 26 (2010) 82-86. [https://doi.org/10.1016/S1005-0302\(10\)60013-8](https://doi.org/10.1016/S1005-0302(10)60013-8).
- [199] L. Feng, Y.Y. Ren, Y.H. Zhang, S. Wang, L. Li, Direct Correlations among the Grain Size, Texture, and Indentation Behavior of Nanocrystalline Nickel Coatings, *Metals*. 9 (2019) 188. <https://doi.org/10.3390/met9020188>.
- [200] T.Y. Tsui, G.M. Pharr, Substrate effects on nanoindentation mechanical property measurement of soft films on hard substrates, *Journal of Materials Research*. 14 (1999) 292-301. <https://doi.org/10.1557/JMR.1999.0042>.
- [201] R. Saha, W.D. Nix, Effects of the substrate on the determination of thin film mechanical properties by nanoindentation, *Acta Materialia*. 50 (2002) 23-38. [https://doi.org/10.1016/S1359-6454\(01\)00328-7](https://doi.org/10.1016/S1359-6454(01)00328-7).
- [202] X. Chen, J.J. Vlassak, Numerical study on the measurement of thin film mechanical properties by means of nanoindentation, *Journal of Materials Research*. 16 (2001) 2974-2982. <https://doi.org/10.1557/JMR.2001.0408>.
- [203] P.J. Burnett, D.S. Rickerby, The scratch adhesion test: An elastic-plastic indentation analysis, *Thin Solid Films*. 157 (1988) 233-254. [https://doi.org/10.1016/0040-6090\(88\)90006-5](https://doi.org/10.1016/0040-6090(88)90006-5).
- [204] D.K. Marjolaine, Adhesion Characterization of Hard Ceramic Coatings by the Scratch Test, Master thesis, Queen's University at Kingston, 1999.
- [205] B. Etcheverry, Adhérence, mécanique et tribologie des revêtements composites NiP/Talc multifonctionnels à empreinte écologique réduite, PhD thesis, 2006.
- [206] R. (Romain M.) Bard, Analysis of the scratch test for cohesive-frictional materials, Master thesis, Massachusetts Institute of Technology, 2010.

[207] N. Rajendhran, P. De Baets, S. Huang, J. Vleugels, J. Sukumaran, Single-point scratch testing for understanding particle engagement in abrasion of multiphase materials, *Wear*. (2021) 203689. <https://doi.org/10.1016/j.wear.2021.203689>.

Abstract

The objective of this thesis was the electrodeposition and the characterization of the eco-friendly and the cost-effective Ni-Co alloy coatings intended to replace the eco-harmful hard chromium coatings in the tribological applications. In the first part, an attempt was done to prove the performances of Ni-Co alloy nanocrystals as anti-wear coatings through their electrodeposition on StW24 mild steel, and then comparing their tribological behavior with those of the uncoated StW24 steel substrate and a coating used commonly against wear, i.e. the electrodeposited nanocrystalline Ni coating. The results of the mechanical and tribological analysis have shown that the nanocrystalline Ni-Co coatings have better anti-wear performances compared to the uncoated substrate and the nanocrystalline pure Ni coating. However, it has been noticed that the Ni-rich nanocrystalline Ni-Co coating presents a higher friction coefficient than the uncoated substrate, while the Co-rich Ni-Co coating exhibits a lower hardness than the pure Ni coating, which means that the Co content in the coating has a great influence on its properties. For this purpose, we aimed in the second part of this thesis to study the effect of two essential parameters of electrodeposition, namely the Co^{2+} ions concentration in the bath and the bath temperature on the Co content in the coatings. It was observed that the Co content in the coatings varied proportionally to the variation of the Co^{2+} ions concentration in the bath, resulting in significant changes in their morphology, structure and consequently significant changes in their mechanical and tribological properties. The hardness of the coatings decreased with the increase of their Co content, but in spite of this, the wear resistance increased, which is attributed to the lubricating effect of Co and to the progressive variation of the crystalline structure from the α (fcc) phase to the ϵ (hcp) phase that has an excellent friction-reduction behavior. The bath temperature also showed its influence on the composition and properties of the elaborated coatings. It has significantly affected their Co content, their crystallite size as well as their porosity rate, resulting in a change in their hardness, their friction coefficient, as well as their wear resistance. It has been concluded also that the coatings deposited at room temperature (25°C) have the best anti-wear performances thanks to their low porosity rate, their high hardness and thanks to their low friction coefficient compared to the other coatings. The ability of Ni-Co alloy nanocrystalline coatings to maintain its anti-wear performances on different metal substrates (StW24 steel, copper and brass) and with different thicknesses (43.2, 79.8 and 110.6 μm) was also examined. The results showed only a slight effect of the latter parameters on the properties of the coatings. In addition, these coatings have proven to have a high adhesion capacity on all the studied substrates and with the different thicknesses, which would offer the possibility of their use in many industrial applications.

ملخص

كان الهدف من خلال هذه الأطروحة الترسيب الكهروكيميائي وتوصيف طلاءات سبيكة النيكل-كوبالت الصديقة للبيئة والاقتصادية بهدف تطبيقها في الحماية من التآكل الميكانيكي كبديل لطلاءات الكروم الصلب الضارة بالبيئة. تم في القسم الأول محاولة اظهار كفاءة البنى النانو بلورية لهذه السبيكة كطلاءات مضادة للتآكل الميكانيكي وذلك من خلال ترسيبها كهروكيميائيا على ركيزة من الفولاذ اللين ثم مقارنة سلوكها الترابولوجي بركيزة من الفولاذ اللين غير المطلي وأيضاً بطلاء يستعمل عادة كمضاد للتآكل الميكانيكي وهو طلاء النيكل النانو بلوري الذي تم ترسيبه أيضاً كهروكيميائياً. وقد اثبتت نتائج الاختبارات الميكانيكية والترابولوجية ان طلاء سبيكة النيكل-كوبالت النانو بلوري يتمتع بمقاومة تآكل عالية مقارنة بركيزة الفولاذ غير المطلية ومقارنة أيضاً بطلاء النيكل النانو بلوري النقي. لكننا لاحظنا ان طلاء النيكل-كوبالت الغني بالنيكل أظهر معامل احتكاك أعلى من ركيزة الفولاذ غير المطلية، كما لاحظنا ان طلاء النيكل-كوبالت الغني بالكوبالت اظهر صلادة اقل من غطاء النيكل النقي وهو ما يعني ان نسبة الكوبالت في الطلاء لها تأثير كبير على خصائصه. لهذا قررنا في القسم الثاني أن ندرس تأثير شرطين هامين من شروط الترسيب الكهروكيميائي المتمثلان في تركيز ايونات الكوبالت في حمام الطلاء الكهروكيميائي وايضا درجة حرارة الحمام على نسبة الكوبالت في الطلاء النانو بلوري لسبيكة النيكل-كوبالت. وقد وجدنا ان تركيز الكوبالت في الطلاءات المترسبة يتغير وفق علاقة طردية مع تركيز ايونات الكوبالت في الحمام مما يؤدي الى تغيرات هامة في مورفولوجيتها وبنيتها البلورية ونتيجة لذلك تغيرات هامة في خصائصها الميكانيكية والترابولوجية، حيث ان صلابتها تتناقص باستمرار مع ارتفاع نسبة الكوبالت لكن على الرغم من ذلك فإن مقاومتها للتآكل الميكانيكي تزداد وهذا ما يعزى الى الانحدار الكبير في معامل الاحتكاك الخاص بها بفضل التحول التدريجي للبنية البلورية من البنية α (fcc) الى البنية ϵ (hcp) المعروفة بخاصية تقليل الاحتكاك. اظهرت أيضاً درجة حرارة الحمام تأثيرها على الخصائص البنيوية، الميكانيكية والترابولوجية للطلاءات المنجزة، حيث اثرت بشكل كبير على نسبة الكوبالت في الطلاءات المنجزة وحجم بلوراتها وأيضاً نسبة المسامية فيها مما أدى الى التغير في صلابتها، معامل احتكاكها وايضا مقاومتها للتآكل الميكانيكي. وقد لوحظ ان الطلاءات المترسبة في درجة حرارة الغرفة (25 درجة مئوية) تمتلك أفضل فعالية ضد التآكل بفضل نسبة مساميتها المنعدمة تقريبا، صلابتها الكبيرة وايضا بفضل معامل احتكاكها المنخفض مقارنة بالطلاءات الأخرى. تم أيضاً امتحان قدرة الطلاءات النانو بلورية لسبيكة النيكل-كوبالت في الحفاظ على فعاليتها ضد التآكل على ركائز معدنية مختلفة وهي الفولاذ اللين، النحاس والتيمباك وبسماكة مختلفة (43.2، 79.8 و 110.6 مايكرومتر). وقد اظهرت الطلاءات المنجزة حفاظها على فعاليتها ضد الاحتكاك والتآكل الميكانيكي، حيث لم تؤثر هذه العوامل الأخيرة الا بشكل طفيف على خصائص هذه الطلاءات. بالإضافة الى ذلك اثبتت هذه الطلاءات قدرة التصاق عالية مع جميع الركائز وفي جميع الحالات ما من شأنه أن يوفر امكانية لاستعمالها في العديد من التطبيقات الصناعية.